FRACTURE BEHAVIOR OF SINGLE MASON SAND PARTICLES UNDER UNIAXIAL COMPRESSION

A Thesis Presented for the
Master of Science
Degree
The University of Tennessee, Knoxville

Thuy Thanh Trieu
August 2017

ACKNOWLEDGEMENTS

This thesis is a result of two years of research during graduate school at the University of Tennessee. The preparation and completion of this thesis is made possible with the assistance, guidance, and support of countless individuals. I would like to express my deepest gratitude for their time, patience and endless effort through this journey.

First and foremost, I would like to thank my advisor, Dr. Khalid Alshibli, for the patience and guidance that he has given me these past years to help me succeed and survive the thesis route of graduate school. Without his inexhaustible help in providing valuable references, information, and advice, I would be lost in a sea of information. Thank you Dr. Alshibli.

I would like to thank my thesis committee members, Dr. Claudia Rawn and Dr. Angel Palomino, for the valuable discussions and support in my research.

A special thanks to the Engineering Fundamental Department, Dr. Richard Bennett, Dr. Amy Biegalski, Dr. Isaac Jeldes, Dr. Rachel McCord, and Professor Will Schleter for giving me an opportunity to help guide the young minds of our future, and for providing me financial support to attend graduate school. A super special thanks to Ms. Janet Coward and Mr. Michael Allen for being the best at what you do.

A special thanks to Karen Lee for being my graduate school buddy, study buddy, thesis buddy, stress buddy, roommate, and friend through these years.

Lastly, and most important, I would like to extend a sincere thanks to members of my family, especially my mom and Kristi Trieu, and my boyfriend, Darrion Lipscomb for their constant and unyielding support, always reminding me to work on or asking me about my thesis when I procrastinate or want to forget about it, and for letting me know and reminding me that hard-work pays off in the end.

ABSTRACT

Tensile strength of granular materials under one-dimensional (1D) compression is often examined because granular materials fracture in many applications where the soil mass experience high compression stresses. Through methods such as 1D compression, three-dimensional (3-D) imaging, and discrete element modeling, researchers had determined that the Weibull distribution is a good model to represent the tensile strengths of granular material and the fracturing strength of granular materials is dependent on mineralogy, morphology, grain-size, loading rate, gradation, coordination number, and moisture content. Uniaxial compression experiments were performed on Mason sand particles retained between US sieve #10 (2 mm) and #20 (0.84 mm) and retained by sieve #10 (2 mm) to measure fracture loads, particle diameter in the loading direction (d_L), tensile strengths, and fracture modes. Visual mineral inspections of particles provided pre-fracture and post-fracture particle descriptions, particle shape, morphology, and mineralogy, which is classified based on particle color collaborated with x-ray diffraction analysis of particle mineralogy. Synchrotron micro-tomography (SMT) imaging is performed on 14 mason sand particles to examine the effects of fracture modes and internal structure on particle tensile strength. The Weibull distribution model is utilized to examine the characteristic tensile strength, the tensile strength at which 37% of particles had a probability surviving, and correlation between particle size and tensile strength; an in-depth analysis is provided to examine the accuracy of the characteristic tensile strength of the Weibull model to the tensile strength at which 63% of particles fracture. The influences of particle size, mineralogy, shape, morphology, surface texture, fracture mode, and internal structure on the tensile strength of single sand particles are examined. Particles with smaller d_L, were platy

shaped, subangular, smooth, and had less internal flaws generally fractured at higher tensile strengths; particle mineralogy influenced tensile strength in all factors.

TABLE OF CONTENT

CHAPTER ONE: INTRODUCTION 1

1.1 MOTIVATION 1
1.2 OBJECTIVES 3
1.3 THESIS OUTLINE 4
CHAPTER TWO: LITERATURE REVIEW 5

2.1 INTRODUCTION 5
2.2 PROBABILITY OF PARTICLE FRACTURE 11
2.3 PARTICLE FRACTURE 12
2.3.1 Types and Modes of Particle Damage 14
2.3.2 Fracture Patterns 15
2.4 METHODS FOR ANALYSIS 15
2.4.1 Weibull Statistics 16
2.4.2 Discrete Element Modeling (DEM) 16
2.4.3 High-Speed Microscope Camera 16
2.4.4 3D Imaging: Computed Tomography (CT) 17
CHAPTER THREE: MATERIALS AND METHODS 18

3.1 INTRODUCTION 18
3.2 MATERIAL 18
3.3 EXPERIMENTS 24
3.3.1 Uniaxial Compression 24
3.3.2 Synchrotron Micro-computed Tomography (SMT) 27
CHAPTER FOUR: RESULTS AND DISCUSSION 29

4.1 INTRODUCTION 29
4.2 UNIAXIAL UNCONFINED COMPRESSION 30
4.2.1 Weibull Statistical Distribution Model 31
4.2.2 Tensile Strength 48
4.2.2.1 Effects of Particle Size 48
4.2.2.2 Effects of Particle Mineralogy 60
4.2.2.3 Effects of Particle Shape 81
4.2.2.4 Effects of Particle Morphology 129

4.2.2.5 Effects of Particle Surface Texture 149
4.2.2.6 Effects of Particle Fracture Mode 171
4.3 SYNCHROTRON MICRO-TOMOGRAPHY (SMT) IMAGING 193
4.3.1 Weibull Model and Tensile Strength 194
4.3.2 Fracture Mode 197
4.3.3 Internal Structure 201
CHAPTER FIVE: CONCLUSIONS AND RECOMMENDATIONS 206

5.1 CONCLUSION 206
5.2 RECOMMENDATIONS 209
REFERENCES 210

APPENDICES 218

APPENDIX A 219
APPENDIX B 235
APPENDIX C 250
APPENDIX D 262
APPENDIX E 275
APPENDIX F 284
APPENDIX G 301
APPENDIX H 313
APPENDIX I 326
APPENDIX J 352
VITA..... 355

LIST OF TABLES

Table 3-1. Parameters for the data collection of diffraction in the Bruker D2Phaser bench top diffractometer 21

Table 3-2. Major and minor compounds for the red/pink, clear/translucent, black/brown, and white/tan subgroups 23

Table 4-1. Weibull distribution parameters for particles retained between sieves #10 (2 mm) and #20 (0.84 mm) and by sieve #10 (2 mm) for all subgroups 42

Table 4-2. Number of red/pink, black/brown , white/tan, and clear translucent particles retained between sieve #10 (2 mm) and #20 (0.84 mm) based on particle diameter in the loading direction (mm). 53

Table 4-3. Number of red/pink, brown/black, white/tan, and clear/translucent particles retained by sieve #10 (2 mm) based on particle diameter in the loading direction (mm). 54

Table 4-4. Particle diameter in the loading direction (mm), properties for particles retained between sieve #10 (2 mm) and #20 (0.84 mm) and by sieve #10 (2 mm) 56

Table 4-5. Tensile strength properties for red/pink (major and secondary compounds: quartz, potassium feldspar, and plagioclase feldspar) particles retained between sieve #10 (2 mm) and #20 (0.84 mm) and by sieve #10 (2 mm) 63

Table 4-6. Tensile strength properties for black/brown (major and secondary compounds: quartz, mica (biotite), tridymite, plagioclase feldspar, potassium feldspar, and calcite) particles retained between sieve #10 (2 mm) and #20 (0.84 mm) and by sieve #10 (2 mm) 67

Table 4-7. Tensile stress properties for white/tan (major and secondary compounds: quartz, plagioclase feldspar, potassium feldspar, and mica (muscovite)) particles retained between sieve #10 (2 mm) and #20 (0.84 mm) and by sieve #10 (2 mm) 71

Table 4-8. Tensile stress properties for clear/translucent (major and secondary compounds: quartz and plagioclase feldspar) particles retained between sieve #10 (2 mm) and #20 (0.84 mm) and by sieve #10 (2 mm) 76

Table 4-9. Calculated and estimated characteristic tensile strength particles retained between sieve #10 (2 mm) and #20 (0.84 mm) and by sieve #10 (2 mm) in all subgroups 79

Table 4-10. Number of particles, average d_L, and average tensile strengths for platy shaped particles retained between sieve #10 (2 mm) and #20 (0.84 mm) and by sieve #10 (2 mm) subdivided into colored subgroups. 87

Table 4-11. Number of particles, average d_L, and average tensile strengths for rectangular prismatic shaped particles retained between sieve #10 (2 mm) and #20 (0.84 mm) and by sieve #10 (2 mm) subdivided into colored subgroups. 97

Table 4-12. Number of particles, average d_L, and average tensile strengths for spherical shaped particles retained between sieve #10 (2 mm) and #20 (0.84 mm) and by sieve #10 (2 mm) subdivided into colored subgroups. 105

Table 4-13. Number of particles, average d_L, and average tensile strengths for triangular prismatic shaped particles retained between sieve #10 (2 mm) and #20 (0.84 mm) and by sieve #10 (2 mm) subdivided into colored subgroups. 114

Table 4-14. Number of particles, average d_L, and average tensile strengths for other shaped particles retained between sieve #10 (2 mm) and #20 (0.84 mm) and by sieve #10 (2 mm) subdivided into colored subgroups. 122

Table 4-15. Summary of particles angularity for particles retained between sieve #10 (2 mm) and #20 (0.84 mm) based on colored subgroups 135

Table 4-16. Summary of particles angularity for particles retained by sieve #10 (2 mm) based on colored subgroups 144

Table 4-17. Summary of particles surface texture properties for particles retained between sieve #10 (2 mm) and #20 (0.84 mm) 156

Table 4-18. Summary of particles surface texture properties for particles retained by sieve #10 (2 mm) 165

Table 4-19. Number of particles and average tensile strengths based on fracture modes for red/pink (major and secondary compounds: quartz, potassium feldspar, and plagioclase feldspar) particles retained between sieve #10 (2 mm) and #20 (0.84 mm) and by sieve #10 (2 mm) 174

Table 4-20. Number of particles and average tensile strengths based on fracture modes for black/brown (major and secondary compounds: quartz, mica (biotite), tridymite, plagioclase feldspar, potassium feldspar, and calcite) particles retained between sieve #10 (2 mm) and #20 (0.84 mm) and by sieve #10 (2 mm) 179

Table 4-21. Number of particles and average tensile strengths based on fracture modes for white/tan (major and secondary compounds: quartz, plagioclase feldspar, potassium feldspar, and mica (muscovite)) particles retained between sieve #10 (2 mm) and #20 (0.84 mm) and by sieve #10 (2 mm) 185

Table 4-22. Number of particles and average tensile strengths based on fracture modes for clear/translucent (major and secondary compounds: quartz and plagioclase feldspar) particles retained between sieve #10 (2 mm) and #20 (0.84 mm) and by sieve #10 (2 mm) 189

Table A-1. The label (C or J), particle number, peak load (N), compressive displacement (mm), d_L (mm), tensile strength (MPa), fracture mode, and particle description prior to and post fracture for red/pink (major and secondary compounds: quartz, potassium feldspar, and plagioclase feldspar) particles retained between sieve #10 (2 mm) and #20 (0.84 mm) 220

Table B-1. The label (C or J), particle number, peak load (N), compressive displacement (mm), d_L (mm), tensile strength (MPa), fracture mode, and particle description prior to and post fracture for black/brown (major and secondary compounds: quartz, mica (biotite), tridymite, plagioclase

feldspar, potassium feldspar, and calcite) particles retained between sieve #10 (2 mm) and #20 (0.84 mm)..... 236

Table C-1. The label (C or J), particle number, peak load (N), Compressive displacement (mm), d_L (mm), tensile strength (MPa), fracture mode, and particle description prior to and post fracture for white/tan (major and secondary compounds: quartz, plagioclase feldspar, potassium feldspar, and mica (muscovite)) particles retained between sieve #10 (2 mm) and #20 (0.84 mm) 251

Table D-1. The label (C or J), particle number, peak load (N), compressive displacement (mm), particle d_L (mm), tensile strength (MPa), fracture mode, and particle description prior to and post fracture clear/translucent (major and secondary compounds: quartz and plagioclase feldspar) particles retained between sieve #10 (2 mm) and #20 (0.84 mm)..... 263

Table E-1. The label (C or J), particle number, peak load (N), Compressive displacement (mm), d_L (mm), tensile strength (MPa), fracture mode, and particle description prior to and post fracture for red/pink (major and secondary compounds: quartz, potassium feldspar, and plagioclase feldspar) particles retained by sieve #10 (2 mm) 276

Table F-1. The label (C or J), particle number, peak load (N), Compressive displacement (mm), d_L (mm), tensile strength (MPa), fracture mode, and particle description prior to and post fracture for black/brown (major and secondary compounds: quartz, mica (biotite), tridymite, plagioclase feldspar, potassium feldspar, and calcite) particles retained by sieve #10 (2 mm)..... 285

Table G-1. The label (C or J), particle number, peak load (N), Compressive displacement (mm), d_L (mm), tensile strength (MPa), fracture mode, and particle description prior to and post fracture for white/tan (major and secondary compounds: quartz, plagioclase feldspar, potassium feldspar, and mica (muscovite)) particles retained by sieve #10 (2 mm) 302

Table H-1. The label (C or J), particle number, peak load (N), Compressive displacement (mm), d_L (mm), tensile strength (MPa), fracture mode, and particle description prior to and post fracture for

clear/translucent (major and secondary compounds: quartz and plagioclase feldspar) particles retained by sieve #10 (2 mm)..... 314

Table J-1. Color, size, label, d_L (mm), fracture load (N), peak load (N), tensile strength (MPa), fracture mode, and internal structure mode for 14 mason sand particles obtained through 3-D x-ray imaging from synchrotron micro-tomography..... 353

LIST OF FIGURES

Figure 1-1. Definition of Particle Breakage Potential (Hardin 1985) 2

Figure 2-1. Uniaxial compression curves for uniformly and well graded sands (Nakata et al. 2001). 7

Figure 2-2. 1-D compression of an irregular particle (Cavarretta and O'Sullivan 2012). 9

Figure 2-3. 1-D compression of an irregular particle (Cavarretta and O'Sullivan 2012). 9

Figure 3-1. Scanning Electron Microscope Image of Mason Sand 19

Figure 3-2. Grain Size Distribution for Mason Sand 19

Pressure 21

Figure 3-3. Full Spectrum of Mason Sand as obtained by XRD and Quantified by RockJock (Druckrey 2016) 22

Figure 3-4. Unconfined Uniaxial Single Particle Compression Apparatus 25

Figure 3-5. Single Sand Particle Prior to Loading 27

Figure 4-1. Weibull distribution of characteristic tensile strength for red/pink (major and secondary compounds: quartz, potassium feldspar, and plagioclase feldspar) particles retained between sieve #10 (2 mm) and #20 (0.84 mm) 33

Figure 4-2. Weibull distribution of characteristic tensile strength for black/brown particles (major and secondary compounds: quartz, mica (biotite), tridymite, plagioclase feldspar, potassium feldspar, and calcite) retained between sieve #10 (2 mm) and #20 (0.84 mm) 34

Figure 4-3. Weibull distribution of characteristic tensile strength for white/tan (major and secondary compounds: quartz, plagioclase feldspar, potassium feldspar, and mica (muscovite)) particles retained between sieve #10 (2 mm) and #20 (0.84 mm) 35

Figure 4-4. Weibull distribution of characteristic tensile strength for clear/translucent (major and secondary compounds: quartz and plagioclase feldspar) particles retained between sieve #10 (2 mm) and #20 (0.84 mm) 36

Figure 4-5. Weibull distribution of characteristic tensile strength for red/pink (major and secondary compounds: quartz, potassium feldspar, and plagioclase feldspar) particles retained by sieve #10 (2 mm)..... 37

Figure 4-6. Weibull distribution of characteristic tensile strength for black/brown (major and secondary compounds: quartz, mica (biotite), tridymite, plagioclase feldspar, potassium feldspar, and calcite) particles retained by sieve #10 (2 mm) 38

Figure 4-7. Weibull distribution of characteristic tensile strength for white/tan (major and secondary compounds: quartz, plagioclase feldspar, potassium feldspar, and mica (muscovite)) particles retained by sieve #10 (2 mm)..... 39

Figure 4-8. Weibull distribution of characteristic tensile strength for clear/translucent (major and secondary compounds: quartz and plagioclase feldspar) particles retained by sieve #10 (2 mm). 40

Figure 4-9. Relationship between tensile strength and d_L for the red/pink (major and secondary compounds: quartz, potassium feldspar, and plagioclase feldspar), the black/brown (major and secondary compounds: quartz, mica (biotite), tridymite, plagioclase feldspar, potassium feldspar, and calcite), the white/tan (major and secondary compounds: quartz, plagioclase feldspar potassium feldspar, and mica (muscovite)) , and the clear/translucent (major and secondary compounds: quartz and plagioclase feldspar) particles retained between sieve #10 (2 mm) and #20 (0.84 mm)..... 50

Figure 4-10. Relationship between tensile strength and d_L for the red/pink (major and secondary compounds: quartz, potassium feldspar, and plagioclase feldspar), the black/brown (major and secondary compounds: quartz, mica (biotite), tridymite, plagioclase feldspar, potassium feldspar,

and calcite), the white/tan (major and secondary compounds: quartz, plagioclase feldspar potassium feldspar, and mica (muscovite)) , and the clear/translucent (major and secondary compounds: quartz and plagioclase feldspar) particles retained by sieve #10 (2 mm). 51

Figure 4-11. μ±σ for red/pink (major and secondary compounds: quartz, potassium feldspar, and plagioclase feldspar), black/brown (major and secondary compounds: quartz, mica (biotite), tridymite, plagioclase feldspar, potassium feldspar, and calcite), white/tan (major and secondary compounds: quartz, plagioclase feldspar, potassium feldspar, and mica (muscovite)) and clear/translucent (major and secondary compounds: quartz and plagioclase feldspar) particles retained between sieve #10 (2 mm) and #20 (0.84 mm) 58

Figure 4-12. μ±σ for red/pink (major and secondary compounds: quartz, potassium feldspar, and plagioclase feldspar), black/brown (major and secondary compounds: quartz, mica (biotite), tridymite, plagioclase feldspar, potassium feldspar, and calcite), white/tan (major and secondary compounds: quartz, plagioclase feldspar, potassium feldspar, and mica (muscovite)) and clear/translucent (major and secondary compounds: quartz and plagioclase feldspar) particles retained by sieve #10 (2 mm) 59

Figure 4-13. The tensile strength histograms for red/pink (major and secondary compounds: quartz, potassium feldspar, and plagioclase feldspar) particles retained (a) between sieve #10 (2 mm) and #20 (0.84 mm) and (b) by sieve #10 (2 mm) 62

Figure 4-14. The tensile strength histograms for brown/black (major and secondary compounds: quartz, mica (biotite), tridymite, plagioclase feldspar, potassium feldspar, and calcite) particles retained (a) between sieve #10 (2 mm) and #20 (0.84 mm) and (b) by sieve #10 (2 mm) 66

Figure 4-15. The tensile stress histograms for white/tan (major and secondary compounds: quartz, plagioclase feldspar, potassium feldspar, and mica (muscovite)) particles retained (a) between sieve #10 (2 mm) and #20 (0.84 mm) and (b) by sieve #10 (2 mm). 70

Figure 4-16. The tensile stress histograms for clear/translucent (major and secondary compounds: quartz and plagioclase feldspar) particles retained (a) between sieve #10 (2 mm) and #20 (0.84 mm) and (b) by sieve #10 (2 mm). 75

Figure 4-17. Classification based on visual inspection for (a) platy shaped, (b) rectangular prismatic shaped, (c) spherical shaped, (d) triangular prismatic shaped, and (e) (f) other shaped particles.. 82

Figure 4-18. Platy shaped red/pink (major and secondary compounds: quartz, potassium feldspar, and plagioclase feldspar), black/brown (major and secondary compounds: quartz, mica (biotite), tridymite, plagioclase feldspar, potassium feldspar, and calcite), white/tan (major and secondary compounds: quartz, plagioclase feldspar, potassium feldspar, and mica (muscovite)) and clear/translucent (major and secondary compounds: quartz and plagioclase feldspar) particles retained between sieve #10 (2 mm) and #20 (0.84 mm) (a) with outliers (b) without outliers..... 84

Figure 4-19. Platy shaped red/pink (major and secondary compounds: quartz, potassium feldspar, and plagioclase feldspar), black/brown (major and secondary compounds: quartz, mica (biotite), tridymite, plagioclase feldspar, potassium feldspar, and calcite), white/tan (major and secondary compounds: quartz, plagioclase feldspar, potassium feldspar, and mica (muscovite)) and clear/translucent (major and secondary compounds: quartz and plagioclase feldspar) particles retained by sieve #10 (2 mm) (a) with outliers (b) without outliers. 85

Figure 4-20. Average d_L within one standard deviation, without outliers, for platy shaped red/pink (major and secondary compounds: quartz, potassium feldspar, and plagioclase feldspar), black/brown (major and secondary compounds: quartz, mica (biotite), tridymite, plagioclase feldspar, potassium feldspar, and calcite), white/tan (major and secondary compounds: quartz, plagioclase feldspar, potassium feldspar, and mica (muscovite)) and clear/translucent (major and secondary compounds: quartz and plagioclase feldspar) particles retained between sieve #10 (2 mm) and #20 (0.84 mm) and by sieve #10 (2 mm) 90

Figure 4-21. Average tensile strength within one standard deviation, without outliers, for platy shaped red/pink (major and secondary compounds: quartz, potassium feldspar, and plagioclase feldspar), black/brown (major and secondary compounds: quartz, mica (biotite), tridymite, plagioclase feldspar, potassium feldspar, and calcite), white/tan (major and secondary compounds: quartz, plagioclase feldspar, potassium feldspar, and mica (muscovite)) and clear/translucent (major and secondary compounds: quartz and plagioclase feldspar) particles retained between sieve #10 (2 mm) and #20 (0.84 mm) and by sieve #10 (2 mm)..... 91

Figure 4-22. Rectangular prismatic shaped particles red/pink (major and secondary compounds: quartz, potassium feldspar, and plagioclase feldspar), black/brown (major and secondary compounds: quartz, mica (biotite), tridymite, plagioclase feldspar, potassium feldspar, and calcite), white/tan (major and secondary compounds: quartz, plagioclase feldspar, potassium feldspar, and mica (muscovite)) and clear/translucent (major and secondary compounds: quartz and plagioclase feldspar) retained between sieve #10 (2 mm) and #20 (0.84 mm) (a) with outliers (b) without outliers. 93

Figure 4-23. Rectangular prismatic shaped red/pink (major and secondary compounds: quartz, potassium feldspar, and plagioclase feldspar), black/brown (major and secondary compounds: quartz, mica (biotite), tridymite, plagioclase feldspar, potassium feldspar, and calcite), white/tan (major and secondary compounds: quartz, plagioclase feldspar, potassium feldspar, and mica (muscovite)) and clear/translucent (major and secondary compounds: quartz and plagioclase feldspar) particles retained by sieve #10 (2 mm)..... 94

Figure 4-24. Average d_L within one standard deviation, without outliers, for rectangular prismatic shaped red/pink (major and secondary compounds: quartz, potassium feldspar, and plagioclase feldspar), black/brown (major and secondary compounds: quartz, mica (biotite), tridymite, plagioclase feldspar, potassium feldspar, and calcite), white/tan (major and secondary compounds: quartz, plagioclase feldspar, potassium feldspar, and mica (muscovite)) and clear/translucent (major and

secondary compounds: quartz and plagioclase feldspar) particles retained between sieve #10 (2 mm) and #20 (0.84 mm) and by sieve #10 (2 mm)..... 99

Figure 4-25. Average tensile strength within one standard deviation, without outliers, for rectangular prismatic shaped red/pink (major and secondary compounds: quartz, potassium feldspar, and plagioclase feldspar), black/brown (major and secondary compounds: quartz, mica (biotite), tridymite, plagioclase feldspar, potassium feldspar, and calcite), white/tan (major and secondary compounds: quartz, plagioclase feldspar, potassium feldspar, and mica (muscovite)) and clear/translucent (major and secondary compounds: quartz and plagioclase feldspar) particles retained between sieve #10 (2 mm) and #20 (0.84 mm) and by sieve #10 (2 mm) 100

Figure 4-26. Spherical shaped red/pink (major and secondary compounds: quartz, potassium feldspar, and plagioclase feldspar), black/brown (major and secondary compounds: quartz, mica (biotite), tridymite, plagioclase feldspar, potassium feldspar, and calcite), white/tan (major and secondary compounds: quartz, plagioclase feldspar, potassium feldspar, and mica (muscovite)) and clear/translucent (major and secondary compounds: quartz and plagioclase feldspar) particles retained between sieve #10 (2 mm) and #20 (0.84 mm). 103

Figure 4-27. Spherical shaped red/pink (major and secondary compounds: quartz, potassium feldspar, and plagioclase feldspar), black/brown (major and secondary compounds: quartz, mica (biotite), tridymite, plagioclase feldspar, potassium feldspar, and calcite), white/tan (major and secondary compounds: quartz, plagioclase feldspar, potassium feldspar, and mica (muscovite)) and clear/translucent (major and secondary compounds: quartz and plagioclase feldspar) particles retained by sieve #10 (2 mm)..... 104

Figure 4-28. Average d_L within one standard deviation, without outliers, for spherical shaped red/pink (major and secondary compounds: quartz, potassium feldspar, and plagioclase feldspar), black/brown (major and secondary compounds: quartz, mica (biotite), tridymite, plagioclase feldspar, potassium feldspar, and calcite), white/tan (major and secondary compounds: quartz,

plagioclase feldspar, potassium feldspar, and mica (muscovite)) and clear/translucent (major and secondary compounds: quartz and plagioclase feldspar) particles retained between sieve #10 (2 mm) and #20 (0.84 mm) and by sieve #10 (2 mm)..... 107

Figure 4-29. Average tensile strength within one standard deviation, without outliers, for spherical shaped red/pink (major and secondary compounds: quartz, potassium feldspar, and plagioclase feldspar), black/brown (major and secondary compounds: quartz, mica (biotite), tridymite, plagioclase feldspar, potassium feldspar, and calcite), white/tan (major and secondary compounds: quartz, plagioclase feldspar, potassium feldspar, and mica (muscovite)) and clear/translucent (major and secondary compounds: quartz and plagioclase feldspar) particles retained between sieve #10 (2 mm) and #20 (0.84 mm) and by sieve #10 (2 mm)..... 108

Figure 4-30. Triangular prismatic shaped red/pink (major and secondary compounds: quartz, potassium feldspar, and plagioclase feldspar), black/brown (major and secondary compounds: quartz, mica (biotite), tridymite, plagioclase feldspar, potassium feldspar, and calcite), white/tan (major and secondary compounds: quartz, plagioclase feldspar, potassium feldspar, and mica (muscovite)) and clear/translucent (major and secondary compounds: quartz and plagioclase feldspar) particles retained between sieve #10 (2 mm) and #20 (0.84 mm)..... 111

Figure 4-31. Triangular prismatic shaped red/pink (major and secondary compounds: quartz, potassium feldspar, and plagioclase feldspar), black/brown (major and secondary compounds: quartz, mica (biotite), tridymite, plagioclase feldspar, potassium feldspar, and calcite), white/tan (major and secondary compounds: quartz, plagioclase feldspar, potassium feldspar, and mica (muscovite)) and clear/translucent (major and secondary compounds: quartz and plagioclase feldspar) particles retained by sieve #10 (2 mm) (a) with outliers (b) without outliers. 112

Figure 4-32. Average d_L within one standard deviation, without outliers, for triangular prismatic shaped red/pink (major and secondary compounds: quartz, potassium feldspar, and plagioclase feldspar), black/brown (major and secondary compounds: quartz, mica (biotite), tridymite, plagioclase

feldspar, potassium feldspar, and calcite), white/tan (major and secondary compounds: quartz, plagioclase feldspar, potassium feldspar, and mica (muscovite)) and clear/translucent (major and secondary compounds: quartz and plagioclase feldspar) particles retained between sieve #10 (2 mm) and #20 (0.84 mm) and by sieve #10 (2 mm)..... 116

Figure 4-33. Average tensile strength within one standard deviation, without outliers, for triangular prismatic shaped red/pink (major and secondary compounds: quartz, potassium feldspar, and plagioclase feldspar), black/brown (major and secondary compounds: quartz, mica (biotite), tridymite, plagioclase feldspar, potassium feldspar, and calcite), white/tan (major and secondary compounds: quartz, plagioclase feldspar, potassium feldspar, and mica (muscovite)) and clear/translucent (major and secondary compounds: quartz and plagioclase feldspar) particles retained between sieve #10 (2 mm) and #20 (0.84 mm) and by sieve #10 (2 mm) 117

Figure 4-34. Other shaped red/pink (major and secondary compounds: quartz, potassium feldspar, and plagioclase feldspar), black/brown (major and secondary compounds: quartz, mica (biotite), tridymite, plagioclase feldspar, potassium feldspar, and calcite), white/tan (major and secondary compounds: quartz, plagioclase feldspar, potassium feldspar, and mica (muscovite)) and clear/translucent (major and secondary compounds: quartz and plagioclase feldspar) particles retained between sieve #10 (2 mm) and #20 (0.84 mm)..... 120

Figure 4-35. Other shaped red/pink (major and secondary compounds: quartz, potassium feldspar, and plagioclase feldspar), black/brown (major and secondary compounds: quartz, mica (biotite), tridymite, plagioclase feldspar, potassium feldspar, and calcite), white/tan (major and secondary compounds: quartz, plagioclase feldspar, potassium feldspar, and mica (muscovite)) and clear/translucent (major and secondary compounds: quartz and plagioclase feldspar) particles retained by sieve #10 (2 mm)..... 121

Figure 4-36. Average d_L within one standard deviation for other shaped red/pink (major and secondary compounds: quartz, potassium feldspar, and plagioclase feldspar), black/brown (major and

secondary compounds: quartz, mica (biotite), tridymite, plagioclase feldspar, potassium feldspar, and calcite), white/tan (major and secondary compounds: quartz, plagioclase feldspar, potassium feldspar, and mica (muscovite)) and clear/translucent (major and secondary compounds: quartz and plagioclase feldspar) particles retained between sieve #10 (2 mm) and #20 (0.84 mm) and by sieve #10 (2 mm) 125

Figure 4-37. Average tensile strength within one standard deviation for other shaped red/pink (major and secondary compounds: quartz, potassium feldspar, and plagioclase feldspar), black/brown (major and secondary compounds: quartz, mica (biotite), tridymite, plagioclase feldspar, potassium feldspar, and calcite), white/tan (major and secondary compounds: quartz, plagioclase feldspar, potassium feldspar, and mica (muscovite)) and clear/translucent (major and secondary compounds: quartz and plagioclase feldspar) particles retained between sieve #10 (2 mm) and #20 (0.84 mm) and by sieve #10 (2 mm) 126

Figure 4-38. Particle classified as (a) subangular and (b) subrounded. 130

Figure 4-39. Angularity of particles retained between sieve #10 (2 mm) and #20 (0.84 mm) for particles in the (a) red/pink (major and secondary compounds: quartz, potassium feldspar, and plagioclase feldspar), (b) black/brown(major and secondary compounds: quartz, mica (biotite), tridymite, plagioclase feldspar, potassium feldspar, and calcite), (c) white/tan white/tan (major and secondary compounds: quartz, plagioclase feldspar, potassium feldspar, and (d) clear/translucent major and secondary compounds: quartz and plagioclase feldspar)subgroups..... 131

Figure 4-40. Average d_L within one standard deviation for subangular and subrounded particles, without outliers, retained between sieve #10 (2 mm) and #20 (0.84 mm) based on the red/pink (major and secondary compounds: quartz, potassium feldspar, and plagioclase feldspar), black/brown (major and secondary compounds: quartz, mica (biotite), tridymite, plagioclase feldspar, potassium feldspar, and calcite), white/tan (major and secondary compounds: quartz, plagioclase feldspar,

potassium feldspar, and mica (muscovite)) and clear/translucent (major and secondary compounds: quartz and plagioclase feldspar) subgroups 138

Figure 4-41. Average tensile strength within one standard deviation for subangular and subrounded particles, without outliers, retained between sieve #10 (2 mm) and #20 (0.84 mm) based on the red/pink (major and secondary compounds: quartz, potassium feldspar, and plagioclase feldspar), black/brown (major and secondary compounds: quartz, mica (biotite), tridymite, plagioclase feldspar, potassium feldspar, and calcite), white/tan (major and secondary compounds: quartz, plagioclase feldspar, potassium feldspar, and mica (muscovite)) and clear/translucent (major and secondary compounds: quartz and plagioclase feldspar) subgroups 139

Figure 4-42. Angularity of particles retained by sieve #10 (2 mm) for particles in the (a) red/pink (major and secondary compounds: quartz, potassium feldspar, and plagioclase feldspar), (b) black/brown (major and secondary compounds: quartz, mica (biotite), tridymite, plagioclase feldspar, potassium feldspar, and calcite), (c) white/tan (major and secondary compounds: quartz, plagioclase feldspar, potassium feldspar, and mica (muscovite)) and (d) clear/translucent (major and secondary compounds: quartz and plagioclase feldspar) subgroups 141

Figure 4-43. Average d_L within one standard deviation for subangular and subrounded particles, without outliers, retained by sieve #10 (2 mm) based on the red/pink (major and secondary compounds: quartz, potassium feldspar, and plagioclase feldspar), black/brown (major and secondary compounds: quartz, mica (biotite), tridymite, plagioclase feldspar, potassium feldspar, and calcite), white/tan (major and secondary compounds: quartz, plagioclase feldspar, potassium feldspar, and mica (muscovite)) and clear/translucent (major and secondary compounds: quartz and plagioclase feldspar) subgroups 147

Figure 4-44. Average tensile strength within one standard deviation for subangular and subrounded particles, without outliers, retained by sieve #10 (2 mm) based on the red/pink (major and secondary compounds: quartz, potassium feldspar, and plagioclase feldspar), black/brown (major

and secondary compounds: quartz, mica (biotite), tridymite, plagioclase feldspar, potassium feldspar, and calcite), white/tan (major and secondary compounds: quartz, plagioclase feldspar, potassium feldspar, and mica (muscovite)) and clear/translucent (major and secondary compounds: quartz and plagioclase feldspar) subgroups 148

Figure 4-45. Particles classified as rough. 150

Figure 4-46. Particles classified as smooth. 150

Figure 4-47. Surface texture of particles retained between sieve #10 (2 mm) and #20 (0.84 mm) for particles in the (a) red/pink (major and secondary compounds: quartz, potassium feldspar, and plagioclase feldspar), (b) black/brown (major and secondary compounds: quartz, mica (biotite), tridymite, plagioclase feldspar, potassium feldspar, and calcite), (c) white/tan (major and secondary compounds: quartz, plagioclase feldspar, potassium feldspar, and mica (muscovite)) and (d) clear/translucent (major and secondary compounds: quartz and plagioclase feldspar) subgroups. 152

Figure 4-48. Average d_L within one standard deviation for rough and smooth particles, without outliers, retained between sieve #10 (2 mm) and #20 (0.84 mm) based on the red/pink (major and secondary compounds: quartz, potassium feldspar, and plagioclase feldspar), black/brown (major and secondary compounds: quartz, mica (biotite), tridymite, plagioclase feldspar, potassium feldspar, and calcite), white/tan (major and secondary compounds: quartz, plagioclase feldspar, potassium feldspar, and mica (muscovite)) and clear/translucent (major and secondary compounds: quartz and plagioclase feldspar) subgroups 159

Figure 4-49. Average tensile strength within one standard deviation for rough and smooth particles, without outliers, retained between sieve #10 (2 mm) and #20 (0.84 mm) based on the red/pink (major and secondary compounds: quartz, potassium feldspar, and plagioclase feldspar), black/brown (major and secondary compounds: quartz, mica (biotite), tridymite, plagioclase feldspar, potassium feldspar, and calcite), white/tan (major and secondary compounds: quartz,

plagioclase feldspar, potassium feldspar, and mica (muscovite)) and clear/translucent (major and secondary compounds: quartz and plagioclase feldspar) subgroups..... 160

Figure 4-50. Surface texture of particles retained by sieve #10 (2 mm) for particles in the (a) red/pink (major and secondary compounds: quartz, potassium feldspar, and plagioclase feldspar), (b) black/brown (major and secondary compounds: quartz, mica (biotite), tridymite, plagioclase feldspar, potassium feldspar, and calcite), (c) white/tan (major and secondary compounds: quartz, plagioclase feldspar, potassium feldspar, and mica (muscovite)) and (d) clear/translucent (major and secondary compounds: quartz and plagioclase feldspar) subgroups. 162

Figure 4-51. Average d_L within one standard deviation for rough and smooth particles, without outliers, retained by sieve #10 (2 mm) based on the red/pink (major and secondary compounds: quartz, potassium feldspar, and plagioclase feldspar) particles, black/brown (major and secondary compounds: quartz, mica (biotite), tridymite, plagioclase feldspar, potassium feldspar, and calcite) particles, white/tan (major and secondary compounds: quartz, plagioclase feldspar, potassium feldspar, and mica (muscovite)) particles, and clear/translucent (major and secondary compounds: quartz and plagioclase feldspar) particles subgroups 168

Figure 4-52. Average tensile strength within one standard deviation for rough and smooth particles, without outliers, retained by sieve #10 (2 mm) based on the red/pink (major and secondary compounds: quartz, potassium feldspar, and plagioclase feldspar) particles, black/brown (major and secondary compounds: quartz, mica (biotite), tridymite, plagioclase feldspar, potassium feldspar, and calcite) particles, white/tan (major and secondary compounds: quartz, plagioclase feldspar, potassium feldspar, and mica (muscovite)) particles, and clear/translucent (major and secondary compounds: quartz and plagioclase feldspar) particles subgroups. 169

Figure 4-53. Particle classification based on fracture (a) Mode 1, (b) Mode 2, (c) Mode 3, (d) Mode 4, and (e) Mode 5..... 172

Figure 4-54. Fracture mode vs. tensile strengths for red/pink (major and secondary compounds: quartz, potassium feldspar, and plagioclase feldspar) particles retained (a) between sieve #10 (2 mm) and #20 (0.84 mm) and (b) by sieve #10 (2 mm) 173

Figure 4-55. Average tensile strengths, without outliers, of the fracture modes within one standard deviation for the red/pink (major and secondary compounds: quartz, mica (biotite), tridymite, plagioclase feldspar, potassium feldspar, and calcite) particles retained between sieve #10 (2 mm) and #20 (0.84 mm) and by sieve #10 (2 mm). 176

Figure 4-56. Fracture mode vs. tensile strengths for black/brown (major and secondary compounds: quartz, mica (biotite), tridymite, plagioclase feldspar, potassium feldspar, and calcite) particles retained (a) between sieve #10 (2 mm) and #20 (0.84 mm) and (b) by sieve #10 (2 mm) 178

Figure 4-57. Average tensile strengths, without outliers, of the fracture modes within one standard deviation for the black/brown (major and secondary compounds: quartz, mica (biotite), tridymite, plagioclase feldspar, potassium feldspar, and calcite) particles retained between sieve #10 (2 mm) and #20 (0.84 mm) and by sieve #10 (2 mm). 181

Figure 4-58. Fracture mode vs. tensile strengths for white/tan (major and secondary compounds: quartz, plagioclase feldspar, potassium feldspar, and mica (muscovite)) particles retained (a) between sieve #10 (2 mm) and #20 (0.84 mm) and (b) by sieve #10 (2 mm) 183

Figure 4-59. Average tensile strengths, without outliers, of the fracture modes within one standard deviation for the white/tan (major and secondary compounds: quartz, plagioclase feldspar, potassium feldspar, and mica (muscovite)) particles retained between sieve #10 (2 mm) and #20 (0.84 mm) and by sieve #10 (2 mm). 186

Figure 4-60. Fracture mode vs. tensile strengths for clear/translucent (major and secondary compounds: quartz and plagioclase feldspar) particles retained (a) between sieve #10 (2 mm) and #20 (0.84 mm) and (b) by sieve #10 (2 mm) 188

Figure 4-61. Average tensile strengths, without outliers, of the fracture modes within one standard deviation for the clear/translucent (major and secondary compounds: quartz and plagioclase feldspar) particles retained between sieve #10 (2 mm) and #20 (0.84 mm) and by sieve #10 (2 mm). 191

Figure 4-62. Weibull distribution of characteristic tensile strength for mason sand particles retained between sieve #10 (2 mm) and #20 (0.84 mm) and by sieve #10 (2 mm) 195

Figure 4-63. Tensile histogram for mason sand particles retained between sieve #10 (2 mm) and #20 (0.84 mm) and by sieve #10 (2 mm) 196

Figure 4-64. Particle classification based on fracture (a) Mode 1, (b) Mode 3, (c) Mode 3.5, and (d) Mode 4. 199

Figure 4-65. Fracture mode vs. tensile strengths for red/pink (major and secondary compounds: quartz, potassium feldspar, and plagioclase feldspar), black/brown (major and secondary compounds: quartz, mica (biotite), tridymite, plagioclase feldspar, potassium feldspar, and calcite), white/tan (major and secondary compounds: quartz, plagioclase feldspar, potassium feldspar, and mica (muscovite)) and clear/translucent (major and secondary compounds: quartz and plagioclase feldspar) particles retained between sieve #10 (2 mm) and #20 (0.84 mm) and by sieve #10 (2 mm) 200

Figure 4-66. Particle classifications based on internal structure (a) rating 1, (b) rating 2, (c) rating 3 (d) rating 4, (e) rating 5, and (f) Mode 6. 202

Figure 4-67. Internal structure rating vs. tensile strengths for red/pink (major and secondary compounds: quartz, potassium feldspar, and plagioclase feldspar), black/brown (major and secondary compounds: quartz, mica (biotite), tridymite, plagioclase feldspar, potassium feldspar, and calcite), white/tan (major and secondary compounds: quartz, plagioclase feldspar, potassium feldspar, and mica (muscovite)) and clear/translucent (major and secondary compounds: quartz

and plagioclase feldspar) particles retained between sieve #10 (2 mm) and #20 (0.84 mm) and by sieve #10 (2 mm) 203

Figure 4-9a. Relationship between tensile strength and d_L for red/pink (major and secondary compounds: quartz, potassium feldspar, and plagioclase feldspar) particles retained between sieve #10 (2 mm) and #20 (0.84 mm).σ..... 327

Figure 4-9b. Relationship between tensile strength and d_L for black/brown (major and secondary compounds: quartz, mica (biotite), tridymite, plagioclase feldspar, potassium feldspar, and calcite) particles retained between sieve #10 (2 mm) and #20 (0.84 mm)..... 328

Figure 4-9c. Relationship between tensile strength and d_L for white/tan (major and secondary compounds: quartz, plagioclase feldspar, potassium feldspar, and mica (muscovite)) particles retained between sieve #10 (2 mm) and #20 (0.84 mm)..... 329

Figure 4-9d. Relationship between tensile strength and d_L for clear/translucent (major and secondary compounds: quartz and plagioclase feldspar) particles retained between sieve #10 (2 mm) and #20 (0.84 mm)..... 330

Figure 4-10a. Relationship between tensile strength and d_L for red/pink (major and secondary compounds: quartz, potassium feldspar, and plagioclase feldspar) particles retained by sieve #10 (2 mm). .. 331

Figure 4-10b. Relationship between tensile strength and d_L for black/brown (major and secondary compounds: quartz, mica (biotite), tridymite, plagioclase feldspar, potassium feldspar, and calcite) particles retained by sieve #10 (2 mm). 332

Figure 4-10c. Relationship between tensile strength and d_L for white/tan (major and secondary compounds: quartz, plagioclase feldspar, potassium feldspar, and mica (muscovite)) particles retained by sieve #10 (2 mm)..... 333

Figure 4-10d. Relationship between tensile strength and d_L for clear/translucent (major and secondary compounds: quartz and plagioclase feldspar) particles retained by sieve #10 (2 mm). 334

Figure 4-13b.1. The uniaxial compression of particle Red/Pink 25-11_J retained by sieve #10 (2 mm) with a particle diameter in loading direction of 1.25 mm. 335

Figure 4-13b.2. The tensile strength histograms for red/pink (major and secondary compounds: quartz, potassium feldspar, and plagioclase feldspar) particles retained by sieve #10 (2 mm) with the exclusion of the outlier..... 336

Figure 4-14a.1. The uniaxial compression curve for black/brown particle 25-21_C retained between sieve #10 (2 mm) and #20 (0.84 mm) with a particle diameter in loading direction of 0.80 mm..... 337

Figure 4-14a.2. The tensile strength histograms for black/brown (major and secondary compounds: quartz, mica (biotite), tridymite, plagioclase feldspar, potassium feldspar, and calcite) particles retained between sieve #10 (2 mm) and #20 (0.84 mm) with the exclusion of the outlier. 338

Figure 4-14b.1. The uniaxial compression curve for clear/translucent particle 25-36_J retained by sieve #10 (2 mm) with a particle diameter in loading direction of 0.90 mm. 339

Figure 4-14b.2. The uniaxial compression curve for clear/translucent particle 25-33_C retained by sieve #10 (2 mm) with a particle diameter in loading direction of 0.95 mm. 339

Figure 4-14b.3. The tensile strength histograms for black/brown (major and secondary compounds: quartz, mica (biotite), tridymite, plagioclase feldspar, potassium feldspar, and calcite) particles retained by sieve #10 (2 mm) with the exclusion of outliers. 340

Figure 4-15a.1. The uniaxial compression curve for white/tan particle retained between sieve #10 (2 mm) and #20 (0.84 mm) with a particle diameter in loading direction of 0.50 mm 341

Figure 4-15a.2. The tensile strength histograms for white/tan (major and secondary compounds: quartz, plagioclase feldspar, potassium feldspar, and mica (muscovite)) particles retained between sieve #10 (2 mm) and #20 (0.84 mm) with the exclusion of the outlier. 342

Figure 4-15a.3. The uniaxial compression curve for white/tan particle retained between sieve #10 (2 mm) and #20 (0.84 mm) with a particle diameter in loading direction of 1.00 mm 343

Figure 4-15a.4. The uniaxial compression curve for white/tan particle retained between sieve #10 (2 mm) and #20 (0.84 mm) with a particle diameter in loading direction of 1.20 mm 343

Figure 4-15a.5. The tensile strength histograms for white/tan (major and secondary compounds: quartz, plagioclase feldspar, potassium feldspar, and mica (muscovite)) particles retained between sieve #10 (2 mm) and #20 (0.84 mm) with further exclusions of the outliers. 344

Figure 4-15b.1. The uniaxial compression curve for white/tan particle retained by sieve #10 (2 mm) with a particle diameter in loading direction of 1.60 mm. 345

Figure 4-15b.2. The tensile strength histograms for white/tan (major and secondary compounds: quartz, plagioclase feldspar, potassium feldspar, and mica (muscovite)) particles retained by sieve #10 (2 mm) with the exclusion of the outlier. 346

Figure 4-16a.1. The uniaxial compression curve for clear/translucent particle 25-38_J retained between sieve #10 (2 mm) and #20 (0.84 mm) with a particle diameter in loading direction of 0.70 mm. 347

Figure 4-16a.2. The tensile strength histograms for clear/translucent (major and secondary compounds: quartz and plagioclase feldspar) particles retained between sieve #10 (2 mm) and #20 (0.84 mm) with the exclusion of the outlier..... 348

Figure 4-22a.1. The uniaxial compression curve for red/pink particle 25-22_C retained between sieve #10 (2 mm) and #20 (0.84 mm) with a particle diameter in loading direction of 1.00 mm..... 349

Figure 4-22a.2. The uniaxial compression curve for red/pink particle 25-2_J retained between sieve #10 (2 mm) and #20 (0.84 mm) with a particle diameter in loading direction of 1.00 mm..... 349

Figure 4-22a.3. The uniaxial compression curve for clear/translucent particle 25-42_J retained between sieve #10 (2 mm) and #20 (0.84 mm) with a particle diameter in loading direction of 0.80 mm. 350

Figure 4-31a.1. The uniaxial compression curve for black/brown particle 25-9_J retained by sieve #10 (2 mm) with a particle diameter in loading direction of 1.20 mm. 350

Figure 4-39a.1. The uniaxial compression curve for clear/translucent particle 25-26_C retained between sieve #10 (2 mm) and #20 (0.84 mm) with a particle diameter in loading direction of 0.80 mm. 351

CHAPTER ONE: INTRODUCTION

1.1 MOTIVATION

The constitutive behavior and deformation characteristics of granular materials are highly influenced by the fracturing behavior of the particles (Lade et al. 1996; Nakata et al. 2001; McDowell and Amon 2000; McDowell 2002; Todisco et al. 2016; Wang and Coop 2016). The fracture strength of granular materials is commonly investigated because particle fracture occurs most often when high stresses are applied to the soil (Lade et al. 1996). In recent years, one-dimensional (1D) compression of granular particles has been widely used to relate the fracture strength of individual particles to the bulk material constitutive and deformation characteristics for a better understand of the impact of compression of granular materials. Researchers had proposed different techniques to measure particle fracture.

In 1967, Marsal developed the breakage index, (B), based on the change of individual particle sizes in a grain size distribution from large-scale triaxial compression experiments. The breakage index is defined as the sum of the positive difference between final and initial grain size distributions and sum of the negative difference between final and initial grain size distributions. Lee and Farhoomand (1967) tested granular particles via isotropic and anisotropic triaxial compression to examine compression and fracture behavior of various sands and gravels and proposed a breakage factor to convey the change in diameter of a single sand particle. Hardin (1985) developed breakage potential, total breakage, and relative breakage factors based on the grain size distribution. Breakage potential factor, (B_p), is defined as the area between the grain size distribution curve and the vertical line at the particle diameter of 0.074 mm, as shown in Figure 1-1, in which the area is defined as the unit area of 1 log cycle.

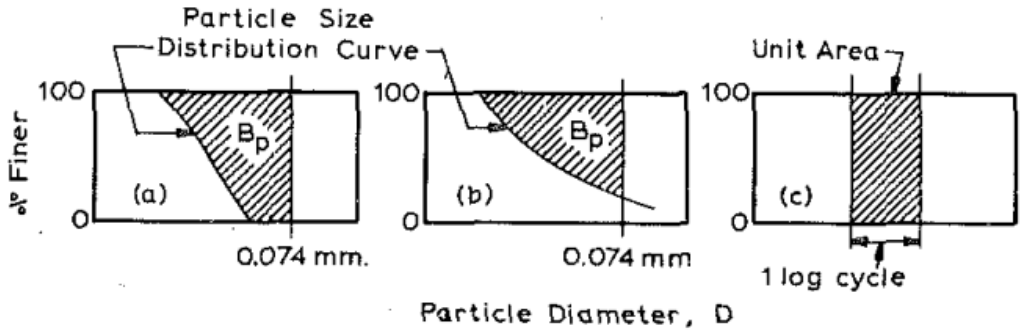


Figure 1-1. Definition of Particle Breakage Potential (Hardin 1985)

Breakage potential factor represents the likelihood of all particles in the grain-size distribution fracturing to a size smaller than No. 200 sieve size. Total breakage factor (B_t) is the difference between the grain size distribution before and after loading. Relative breakage factor (B_r) is the ratio between total breakage and breakage potential and is independent of grain size distribution. Nakata et al. (1999) compared particles fractured in single-particle crushing tests to colored particles in triaxial samples, first compressed under high pressure and then subjected to isotropic consolidation and shearing, by recording the particle images before and after testing with a camera that had a microscopic attachment; this allowed for the examination of the probability of survival of the particles. From the single-particle crushing experiments, a breakage factor is developed based on the grain size distribution after loading. The breakage factor (B_f) is defined as the percentage of particles smaller than the minimum particle size prior to loading.

Through technological advances, researchers are able to investigate the micromechanical properties of particles during in-situ testing using non-destructive methods such as high speed microscopic cameras and x-ray computed tomography. In 2001, Nakata el at. captured digital images of colored particles prior to and post particle fracture, under 1D compression, using a camera with a microscope to determine the yielding characteristics of the sand particles. Zhao et al. (2015) utilized a novel mini-loading apparatus coupled with three-dimensional (3D) X-ray

micro-computer tomography (μCT) to fracture, capture images of, and analyze two types of sand particles. Al Mahbub and Haque (2016) investigated micromechanic properties of sand particles under high pressure 1D compression through the use of X-ray computed tomography (CT) imaging. Wang and Coop (2016) and Todisco et al. (2016) recorded particle fracture under uniaxial compression of various types of sand using a high-speed microscopic camera to investigate the breakage behavior of single sand particles. Cil and Alshibli (2012), Wang and Arson (2016), and Druckrey (2016) utilized discrete element methods (DEM) to model the fracture of granular materials using agglomerate concepts to obtain engineering properties of sand particles.

While many researchers had investigated the impact of high stress compression, varying strain rates, and yield stresses on granular material, few had examined methods to predict the fracture forces of individual particles under compression given the particle minerology and morphology, size, and loading criteria on the fracturing of individual sand particles (Hagerty et al. 1993; McDowell and Bolton 1998; Nakata et al. 2001; McDowell 2002; Parab et al. 2014; Mahbub and Haque 2016). This thesis aims to relate particle minerology, morphology, size, deformation, and loading criteria to determine how these factors influence the fracture behavior of individual particles to provide micromechanical insights on particle fracturing using uniaxial compression tests and 3D imaging.

1.2 OBJECTIVES

The objective of the thesis is to:

a) Examine the effects of particle size and composition on the fracture behavior of single sand particles using uniaxial compression

b) Utilize powdered x-ray diffraction to determine the Mason sand mineralogy and its influence on particle fracture

c) Investigate the influence of particle shape, morphology, internal flaws, loading geometry, particle size, and particle composition to the force required to fracture a particular particle.

The outcome of the analysis will provide a better understanding of the fracture behavior of individual particles as a key element in understanding the fracturing behavior of a bulk sand.

1.3 THESIS OUTLINE

The thesis contains five Chapters. The first Chapter is an introduction to the thesis. The second Chapter presents a literature review of 1-D compression. It includes factors that affect grain fracture under compression and methods to analyze fractured particles. Chapter 3 describes the experimental work which includes a description of the materials used, apparatus set up, and experimental procedures for powdered x-ray diffraction, 1-D compression, and the procedure to conduct the scans at the Advanced Photon Source, the scanning process, and image reconstruction. The analysis for the synchrotron microtomography (SMT) is also presented in Chapter 3, which includes the analysis steps in AVIZO code. The results of analysis for the 1D compression experiments and SMT images are discussed in Chapter 4. The conclusions and recommendations for future research in this particular topic are presented in Chapter 5.

CHAPTER TWO: LITERATURE REVIEW

2.1 INTRODUCTION

This Chapter presents a literature review of uniaxial compressions of particles. A brief history of uniaxial compression and how it has been used to obtain granular properties of sand particles is discussed. Factors that affect how granular particles fracture under compression will also be examined. Finally, the methods used to analyze particle fractures post-compression is presented and discussed.

Prior to World War II, investigations of sand fracturing under high pressures and great depths were discouraged because such occurrences were unlikely and the results were insignificant. Interest in granular compression re-emerged due to findings from high pressure 1-D compression tests on sands that were conducted by Terzaghi and Peck (1948). They discovered that the yield stress point, the stress point where the compression index changes, was an important component pertaining to particle fracture and it was affected by the morphology and engineering properties of the particles. Terzaghi and Peck (1948) and Harremoes (1959) reported that relative density was proportional to the yield point stress. Particles with more pronounced cleavage were extensively fractured compared to particles with less cleavage at high pressures and changes in particle size and mineralogy did not influence the yield point stress. Hagerty et al. (1993) concluded that the increase in particle angularity and size resulted in more particles fracturing.

Uniaxial compression is a widely-used test to determine the fracturing behavior of granular particles since it can control the load and deformation applied onto the particle, which can be used to determine engineering properties, such as tensile strengths (Tavares 2007). Under uniaxial compression, the failure of granular material occurred after the onset of elastic yielding through tensile failure (Lade et al. 1996; McDowell and Bolton 1998; McDowell and Amon

2000; Nakata et al. 2001; McDowell 2002). Tensile strength of the particle is a function of the particle size (McDowell and Bolton 1998; McDowell and Amon 2000; McDowell 2002). As particle size increases, tensile strength decreases (Nakata et al. 1999; Wang and Coop 2016). The characteristic tensile strength of a particle is defined as

$$\sigma_{tensile} = \frac{F}{d^2} \tag{1}$$

where $\sigma_{tensile}$ is the tensile stress, F is the force on the particle, and d is the particle size, defined as the initial distance between the two flat platens at the start of the particle-fracturing test (Jaeger 1967). Elastic yielding occurs in the yield region, a region where irrecoverable fracturing occurs and is initiated with the yield stress point (McDowell and Bolton, 1998).

The yield stress point, defined as the point of maximum curvature on a logarithm vertical stress versus void ratio relationship and marks where particle fracturing initiates. Figure 2-1 displays a typical void ratio versus logarithm effective stress relationship for uniformly and well graded silica sand under uniaxial compression. Point P represents the yield stress point; the dashed and solid lines represent the uniformly graded sand and well-graded sand, respectively (Nakata et al., 2001). The yield stress point is affected by initial void ratio, angularity, gradation, and particle size. Loose granular materials had higher initial void ratios, resulting in more particle rearrangement occurring prior to fracturing and a higher yield stress point (Hagerty et al. 1993; McDowell and Bolton 1998). An increase in particle angularity resulted in a lower yield stress point (Hagerty et al. 1993). Materials with a uniform gradation had a higher yield stress point (Nakata et al. 2001). The yield stress point increases with decreasing particle size (McDowell and Bolton 1998; Nakata et al. 2001; McDowell 2002; Cil and Alshibli 2014). As shown in Figure 2, the uniformly graded silica sand has a steeper normal compression line in the

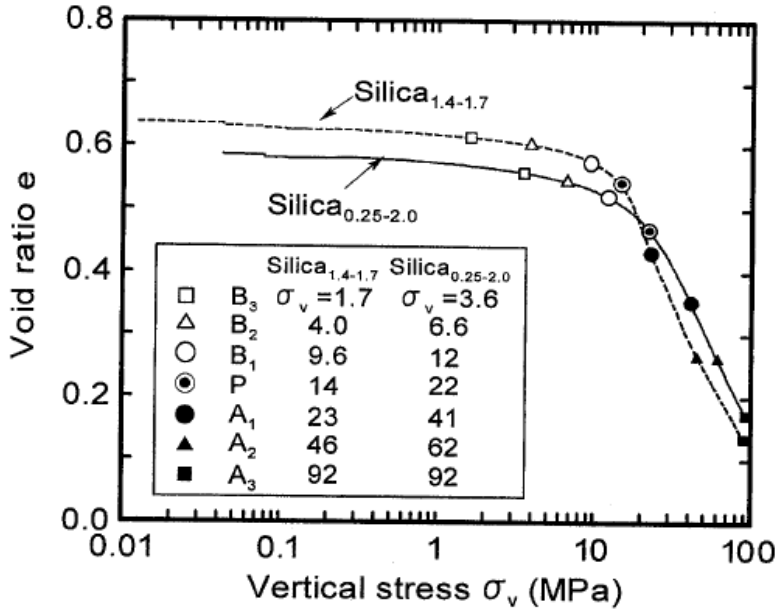


Figure 2-1. Uniaxial compression curves for uniformly and well graded sands (Nakata et al. 2001).

plastic hardening region after the yield stress point compared to the well-graded silica sand. The steeper curve indicates more particles fracturing occurring (McDowell and Bolton 1998; Nakata et al. 2001; McDowell 2002). For a particle under 1-D compression, the yield stress is proportional to grain tensile strength (McDowell and Bolton 1998).

Particle position, morphology, and internal structure influence the fracture mode of granular particles. Cavarretta et al. (2010) and Cavarretta and O'Sullivan (2012) utilized uniaxial compression tests and simple analytical models and noted that the contact area between the flat platen and the irregular shaped particle during particle displacement is caused by flattening the asperity; the contact are can also can change due to particle rotation known as kinetic degradation, which is the reduction in stiffness of a particle that can affect the rotation and stress distribution within the particle.

Figure 2-2 illustrates the compression of an irregular particle under force (*F*) with a particle size of d_3 (Cavarretta and O'Sullivan 2012). Point *A* represents the point of contact between the particle and the top loading platen. Points *CDE* represent the points of contact between the particle and the bottom platen; these points form a triangle. Point *G* represents the center of gravity for the particle. Point *A'* and G' represent the vertical projects of point *A* and *G*, respectively, and are within the triangle *CDE*. When the vertical projection of the top compression point, *A'*, falls within triangle *CDE*, the particle will not rotate or slip and be compressed under the applied vertical force. When *A*' falls on the other side of line *CD*, outside of triangle *CDE*, the particle will slip and rotate along line *CD*, the axis of rotation, until the next tallest point on the particle, represented by point *B*, comes into contact with the top loading plate. At this point, line *AB* will be in contact with the top loading platen and line *CD* will be in contact with the bottom loading platen, stabilizing the particle. The susceptibility of a particle to rotation and slippage upon initial compression depends on its geometry and the number and strength of contact points on its contact surface. This concept can be related to force chains in a granular media for the bulk of the material.

Figure 2-3 displays a spherical and irregular particle under compression and an irregular particle within a granular media under compression (Cavarretta and O'Sullivan 2012). Particles shown in Figure 2-3a and b experience a strong vertical force, synonymous with a chain reaction. The irregular particle has four contact points because of neighboring particles. The vertical particles impart strong forces, creating a force chain that can resist buckling, while the non-vertical particles impart weak orthogonal forces onto the particle, which can provide lateral support. The uniaxial compression of the single particles can be analogous to the compression of

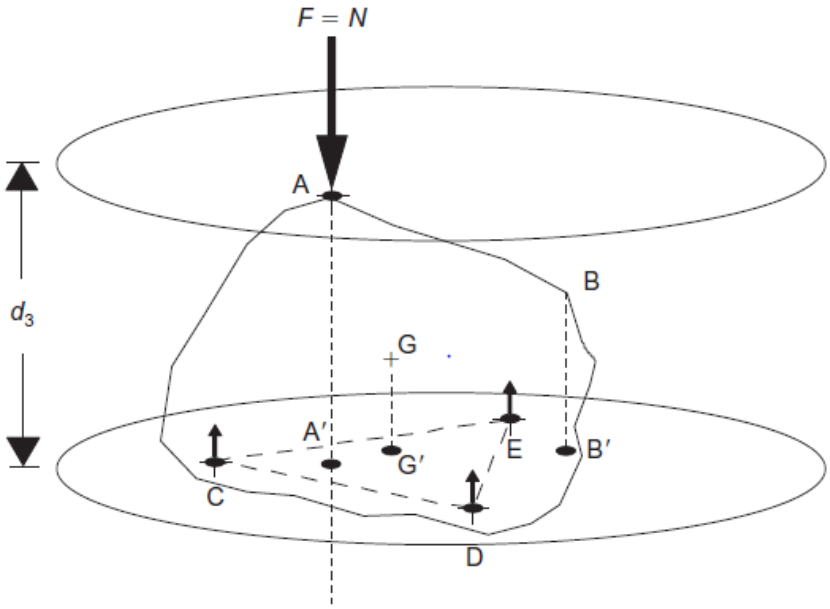


Figure 2-2. 1-D compression of an irregular particle (Cavarretta and O'Sullivan 2012).

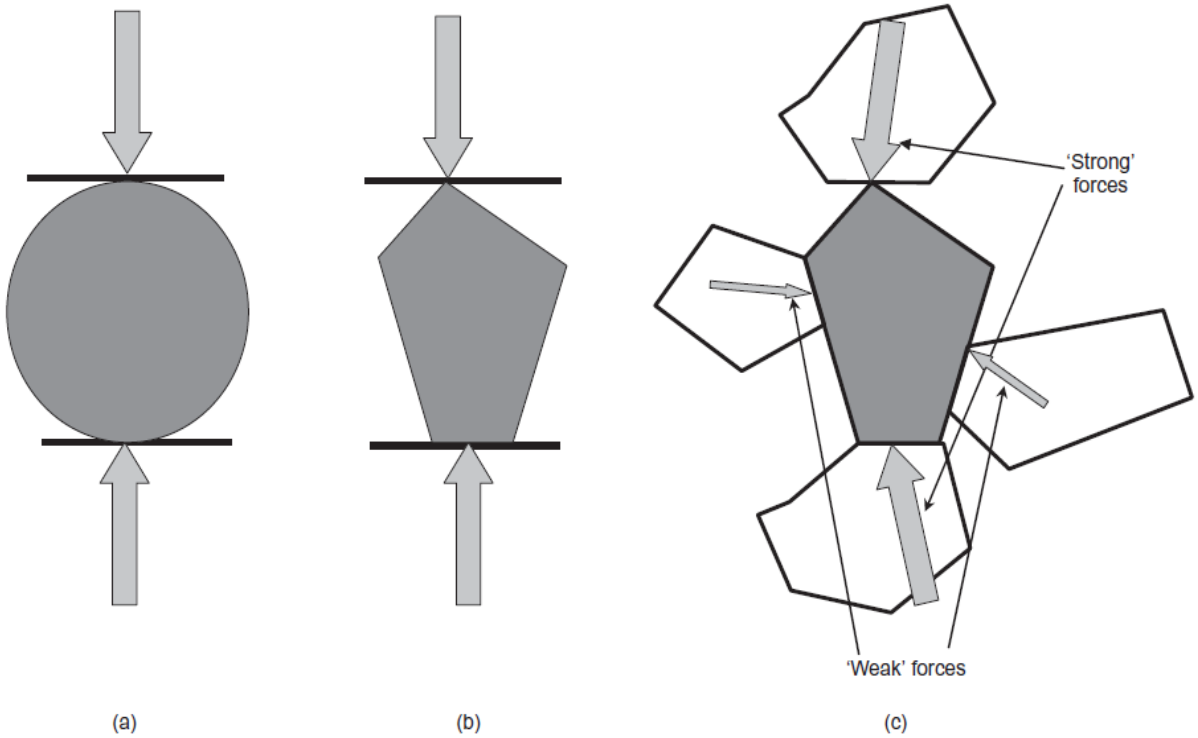


Figure 2-3. 1-D compression of an irregular particle (Cavarretta and O'Sullivan 2012).

a granular media and can be used to model the compression, fracture, or rearrangement of granular media (Cavarretta et al. 2010; Cavarretta and O'Sullivan 2012). Cil and Alshibli (2014) investigated fracturing of silica sand specimens using 3-D synchrotron micro-tomography (SMT) and DEM and found that fracturing occurred more frequently at the end plates and that fractured particles will continue to sustain load and cause fractures to propagate to neighboring particles. Druckrey and Alshibli (2015) utilized 3D SMT and synchrotron x-ray radiography to collect images and information on fracture modes of single sand particles undergoing unconfined compression to create extended finite element method (XFEM) models similar to the experiments to compare experimental and modeled fracture modes. Zhao et al. (2015) utilize 3D x-ray micro-computed tomography (μCT) to examine the fracture patterns of single sand particles under compression. Druckrey and Alshibli (2015) and Zhao et al. (2015) found that particle fracture initiates at the point of contact with the loading platen.

The morphology of the particle affects the contact between the particle and loading platens, and the fracture pattern. As modeled by Druckrey and Alshibli (2015), spherical particles do not produce results similar to the irregular shaped particles that were in the experiments. This is due to the difference in particle surface to platen contact during loading.

The internal structure of a particle can also affect its fractural behavior based on mineralogy and internal flaws. Types of internal flaws within the particle can be voids, micro-cracks, inclusions, defined as foreign substances within the particles, and cleavage, referring to how minerals fracture along low bonding crystallographic planes; these flaws can influence the fracturing pattern of the particle (Harremoes 1959; Hagerty et al. 1993; Zhao et al. 2015; Wang and Coop 2016; Druckrey 2016). Utilizing x-ray μCT, Zhao et al. (2015) noted that particles containing initial voids fractured at smaller stresses and contribute to the size effect of particle

strength. Zhao et al. (2015) and Wang and Coop (2016) conducted particle compression experiments and founded that heterogeneous particles, either naturally occurring or due to inclusions and weathering, fractured at lower stresses. Particles with pronounced cleavages fractured along the cleavage and at lower stresses (Harremoes 1959; Zhao et al. 2015). Predominately quartz particles lack cleavages and develop conchoidal fractures that was not influenced by internal flaws and, therefore, fractures at higher stresses (Zhao et al. 2015; Todisco et al. 2016).

The strength of a particle is influenced by the coordination number (CN), or number of inter-particle contacts (Jaegar 1967; Oda 1977; McDowell et al. 1996; McDowell and Bolton 1998; Todisco et al. 2016). Oda (1977) experimentally determined that the CN is influenced by the void ratio and can be used to describe how close in proximity the particles are to each other and the heterogeneity in a granular media. McDowell et al. (1996) determined that CN can be utilized to determine fracture probability, in which fracture probability increases with an increase in CN. Jaegar (1967) found that particles with higher CN fractured at lower tensile strengths. Todisco et al. (2016) utilized a microscopic high speed camera to examine the influence of CN on particle strength and noted that the change in CN does not affect the fracturing behavior of granular material and particles having higher CN fractured at higher loads.

2.2 PROBABILITY OF PARTICLE FRACTURE

During compression, particles rearrange regardless of how densely packed the specimen. Particles can rearrange to interlock more and become densely packed or rearrange to be more loosely packed due to inter-particle slip, rotation or particle damage causing particle fracturing will occur (McDowell and Bolton 1998; Mesri and Vardhanabhuti 2009). The probability of particle fracture [$P_f(d)$] is based on three criteria: applied macroscopic stress, particle size, and

number of contact points with neighboring particles, or CN. The probability of particle fracture will increase with increasing applied macroscopic stress, decrease with decreasing particle size, and decrease with increasing CN. The probability of fracture decreases with increasing CN due to the decrease in stress on the particle. Larger particles had higher CN because they are surrounded by smaller particles while smaller grains had lower CN. The largest grains are more likely to fracture due to an increase in contact stress (McDowell et al. 1996; McDowell and Bolton 1998).

2.3 PARTICLE FRACTURE

Particle fracture occurs when stresses created by applied forces cause cracks that propagate through the particle causing it to fracture. Factors that can affect particle fracture include: morphology, gradation, mineral hardness, moisture, contact area and loading rate.

Particle morphology refers to the size and shape of the particle. Tavares (2007) and Wang and Coop (2016) noted that larger particles had a higher probability of fracturing at lower tensile strength because they are more susceptible to be internally flawed or had defects or cleavage. The shape of the particle is described based on its sphericity and roundness. Sphericity (*s*) as defined by Cavaretta et al. (2010) is "the ratio of the surface area of a sphere with the same volume as a particle to its actual surface area". Roundness (*r*) as defined be Cavaretta et al. (2010) "is calculated by drawing in-scribed circles within each corner of a 2-D image of a particle and then taking the ratio of the average radius of those circles to the radius of the largest circle that may be inscribed within the particle outline"; it describes how sharp a particle can be. Cavaretta et al. (2010) and Todisco et al. (2016) founded that under uniaxial compression of single particles, particles that are less spherical are stronger while angular particles had a higher probability of fracturing due to the increase in contact stresses concentrated at angular contact

points; thus, there was less stress redistribution and particle failure occurs at lower loads. Wang and Coop (2016) concluded that particles with rounded surfaces had a higher probability of pulverizing because they can sustain higher loads due to a lower stress concentration on the surface of the particle.

Lade et al. (1996) founded that well-graded particles are less likely to fracture because the relative density was higher; therefore, densely packed particles had a lower average contact stress and can withstand higher load. Mineral hardness, investigated by Lade et al. (1996) and Todisco et al. (2016), was noted to be dependent on the internal and external structure of the particle and can affect the strength of the particle through contact deformation. As mineral hardness increased, particle fracture decreases because the particle is harder or stronger. As mineral hardness decreased, due to internal structural flaws, particle fracture increased. Cavarretta et al. (2010) performed uniaxial compression on ballotini of various sizes and textures and founded that surface hardness and Young's modulus was altered due to etching, in which the etching increased the surface hardness of the particles.

Environmental conditions affect the surface energy of sand particles, which can influence the tensile strength, as explained by Orowan (1955) through the following equation:

$$\sigma_t \approx \sqrt{\frac{E\alpha}{2c}} \tag{2}$$

where σ_t is tensile strength of an ideal brittle material, E is the elastic Young's modulus, c is the surface crack depth, and α is the surface energy. E and c are not affected by environmental conditions while an increase in α will result in an increase in σ_t. Miura and Yamanouchi (1975) found that sand particles with wet surfaces, under confined uniaxial compression, had lower surface energy compared to dry particles and, therefore, had lower tensile strength. Oldecop and

Alonso (2001, 2003) developed a conceptual model to explore the effects of moisture content on compressed rockfill material and noted a decrease in particle strength as moisture content increased. Parab et al. (2014) observed that wet sand fractured at higher peak loads compared to dry sand, under static compression. Wang and Coop (2016) examined single particle strengths under uniaxial compression in wet and dry conditions and noted negligible difference in strength between the two conditions. The particle fracture energy and strength decreases with increasing moisture content.

As noted by Cil and Alshibli (2014), particles fractured more frequently at the loading platens, in which particles experience stress concentration prior to failure. Druckrey (2016) noted that particle fracture strength was dependent on loading rate; an increase in loading rate resulted in an increase in tensile strength for all particles, therefore particle fracture was rate dependent. Parab et al. (2014) found that particles experiencing dynamic compressions generally pulverized at varying peak loads while particles experiencing static compression generally fractured through interfacial cracks and into sub-particles.

2.3.1 Types and Modes of Particle Damage

Particle fracture can be classified into approximately three types of damage and four modes of failure. The three types of damage are: (1) abrasion or grinding of particle surface asperities, (2) fracturing of fragments, and (3) fracturing, splitting, or shattering of whole particles (Nakata et al. 1999; Nakata et al. 2001; Mesri and Vardhanabhuti 2009; Druckrey 2016). The four modes are: splitting, explosive, chipping, and mixed mode, with an occasional fifth mode labeled as core-remaining mode. Particle minerology influenced the failure mode while particle size did not. Splitting occurs when the particle splits into two or three large pieces without the creation of asperities. The explosive mode of failure occurs when the particle is

obliterated into tiny fragments. Chipping is not a mode of failure; rather, it occurs when a piece of the particle if broken off as the particle is still undergoing compression until failure. Because chipping can cause movement of the particle, it can cause a load change in the force being applied on the particle during compression. The mixed failure mode occurs when a small fragment of the particle is broken into many small fragments (explosive mode) and leaves a larger fragment in the loading platen (splitting mode). The core-remaining mode occurs when the left and right part of the particle is broken into small fragments (explosive mode), leaving only the middle portion of the particle (Todisco et al. 2016; Wang and Coop 2016).

2.3.2 Fracture Patterns

The fracture pattern of the particle can be classified into three categories: original fabric related, younger fabric related, or independent of fabric. Original fabric related fractures are fractures that occur as a result of the original structure of the particle, such as impurities of cleavages. Younger fabric related fractures pertain to fractures of parts of the particles that were altered due to weathering over time. Younger fabric fractures occur can greatly alter the strength of the particle and control induced fractures. Independent of fabric fracturing occurs at relatively high stresses (Zhao et al. 2015).

2.4 METHODS FOR ANALYSIS

Methods used to analyze particle fractures include: Weibull statistical approach, discrete element modeling (DEM), and experimental techniques such as a high-speed microscope camera or 3D imaging.

2.4.1 Weibull Statistics

The Weibull statistical model can be utilized as a tool to analyze particle tensile to quantify particle fracturing with the assumptions that: (1) failure occurs within the bulk of the material and (2) the particle fails under fast fracture under induced tensile strengths. A characteristic diameter is measured as the distance between two flat platens in order to obtain the characteristic tensile strength. The average tensile strength is proportional to the particle survival probability of 37%. Weibull modulus *m* is used to examine the variation in strength. Furthermore, it accounts for individual particle variability, such as internal structural flaws (McDowell et al. 1996; McDowell and Amon 2000; McDowell 2002; Druckrey et al. 2016).

2.4.2 Discrete Element Modeling (DEM)

The discrete element modeling (DEM) method utilized an agglomerate of small spheres bonded together to model a single or mass of sand particles to observe the various factors that affect the constitutive properties of the particles to simulate fracturing of granular particles (McDowell and Harireche 2002; Wang and Arson 2016). It allows for numerical fracturing of sand particles while incorporating material parameters hat account for variation in experimental tensile strength (Wang and Arson 2016). To create a realistic model of particle fracturing, the Weibull statistical model must be incorporated into the agglomerate to mimic the flaws and variations (McDowell and Harireche 2002).

2.4.3 High-Speed Microscope Camera

A high-speed microscope camera fitted with a microscopic lens to magnify the images of the particle can be used to provide clear, real-time images of the particles as they are being tested. The optimum frame rate and exposure is required to obtain the best quality images. From

the camera, the types of particle fractures and modes of failure can be accurately obtained (Todisco et al. 2016; Wang and Coop 2016).

2.4.4 3D Imaging: Computed Tomography (CT)

X-ray computed tomography (CT) is a non-destructive technique used to evaluate particle morphology, fracture behavior, internal structure and microstructural properties during in-situ compression. X-ray CT can yield high resolution 3D images to quantify microstructural properties of the particle, examine the fracturing behavior and its influence on particles, and quantify particle morphology at the micro-scale level. The technique consists of capturing high resolution x-ray CT images of the particle as the particle is being compressed in-situ. The types of x-rays used to capture these images can be from either industrial x-rays or a synchrotron light sources. The images are then reconstructed using image processing and analysis techniques to obtain quantitative information about the particle prior to and after fracture. Image processing procedures assist in noise reduction, segmenting different phases, and indemnification of individual fragments. Morphology parameters of the various components are obtained through image analysis techniques. X-ray CT provides insight on the fractured patterns of the particles during in-situ compression (Alshibli et al. 2014; Zhao et al. 2015; Al Mahbub and Haque 2016; Druckrey et al. 2016).

CHAPTER THREE: MATERIALS AND METHODS

3.1 INTRODUCTION

This Chapter presents an overview of the materials used in the experiments, describes the testing apparatuses used, and explains the experimental procedures. It also discusses specimen preparation for the powder diffraction analysis and the procedure for analyzing the synchrotron micro-computed tomography (SMT) images.

3.2 MATERIAL

Mason sand, a naturally occurring sand obtained from a quarry in Longmont, Colorado by Colorado Materials, Inc., was used in the experiments. Compared to uniform glass beads and ASTM 20-30 sand, mason sand is a heterogeneous mixture of various silicate minerals and, therefore, was selected to examine the engineering properties of natural sand deposits. A scanning electron microscope image and the grain size distribution for mason sand are shown in Figures 3-1 and 3-2, respectively. Based on ASTM-D2487, mason sand was classified as a poorly graded sand with effective particle size, D_{10} = 0.15 mm, D_{30} = 0.3 mm, D_{60} = 0.52 mm, C_c = 1.15, and C_u = 3.47.

Powder x-ray diffraction (XRD) was performed using a Bruker D2Phaser bench top diffractometer using a PMMA sample holder (model number C79298A3244D83), for all specimens. The PMMA sample holder ring was 8.5 mm high with a sample reception diameter of 40 mm. During diffraction, the sample must be flush with the surface of the sample holder to avoid peak shift due to sample surface displacement. Therefore, during sample preparations, the microscopic slide was then used to create a smooth and level sample surface by removing residual powder from the sample reception, helping to avoid peak shift due to sample surface

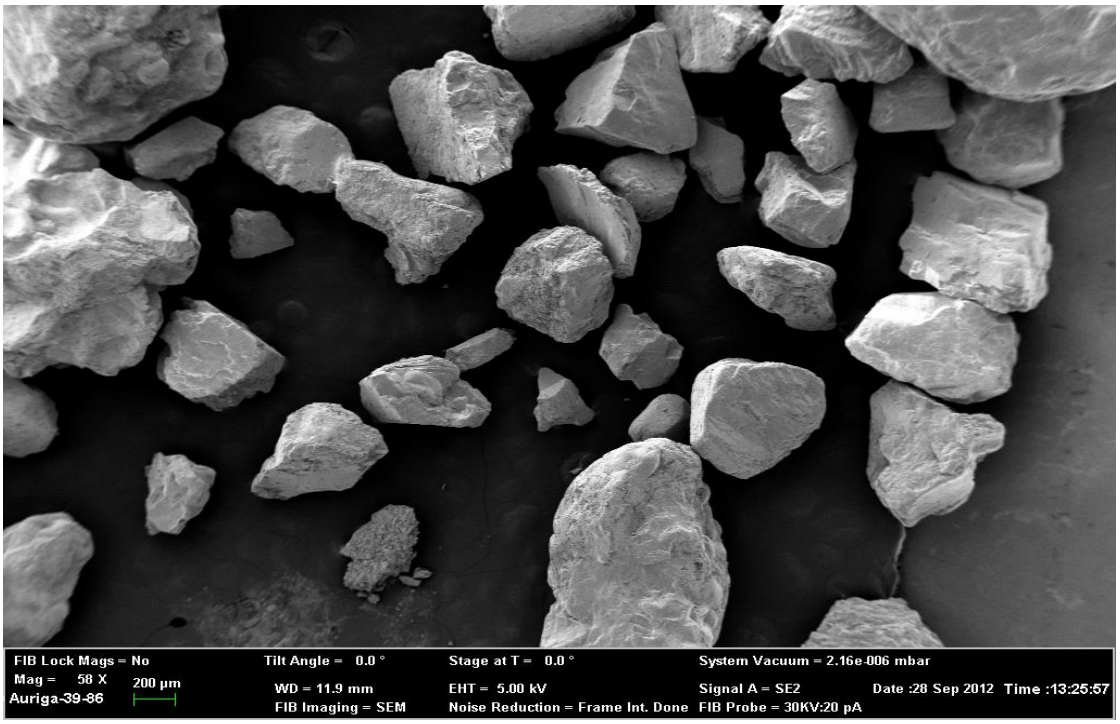


Figure 3-1. Scanning Electron Microscope Image of Mason Sand

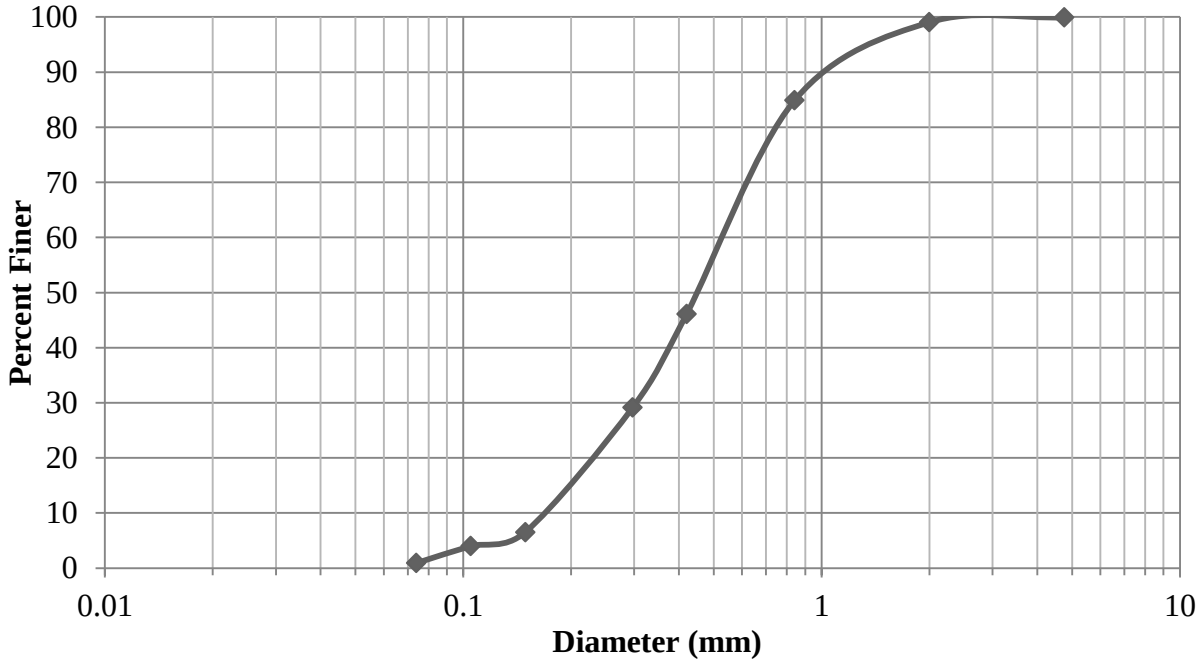


Figure 3-2. Grain Size Distribution for Mason Sand

displacement, however, this packing could introduce intensity differences due to preferred orientation. The sample is then placed into the diffractometer and powder diffraction data was collected. The data collection parameters are listed in Table 3-1. The collected data was analyzed using quantitative mineralogy analysis software to determine the phases present within the mason sand.

Powder x-ray diffraction was performed on the mason sand to identify particle mineral. Diffraction peaks were saved and analyzed using RockJock, quantitative mineralogy analysis software, to determine the fractions of various mineral components of the sand (Eberl 2003). Figure 3-3 displays a pie chart of the mason sand which shows that it was composed of 28% quartz, 25% tridymite, 16% plagioclase, 15% potassium feldspar (also known as Kspar), 6% ferrihydrite, 3% pyroxene, 2% mica, 2% psilomelane, 1% calcite, 1% hornblende, and 1% other.

A physical classification was performed based on color by dividing the sand into subgroups for testing as a method to examine the effect of particle mineralogy on fracture. The four subgroups are labeled as red/pink, clear/translucent, black/brown, and white/tan. It should be noted that classifying minerals using color as the identifying parameter can be problematic due to small amount of impurities having a profound effect on physical and optical properties such as color. For example, quartz can be clear, white, pink, purple, brown, green, grey, orange, yellow, blue, red, black, or multicolored. Powdered x-ray diffraction and a phase analysis software, HighScore Plus Version 4.0, were used to identify the major, secondary, and minor secondary phases in the subgroups, listed in Table 3-2. Based on the strongest peak, located at approximately 26.67 $^{o}2\theta$ corresponding to the (011) of quartz, the major phase in all four of the subgroups was identified as quartz. Additionally all subgroups contained plagioclase feldspar as

Table 3-1. Parameters for the data collection of diffraction in the Bruker D2Phaser bench top diffractometer.

Instrument	Bruker D2Phaser bench top diffractometer
Wavelength, [Å]	1.5406
Scan type	Couple 2θ/θ
Scan range, [°2θ]	$5 < 2\theta < 90$
Step size, [°2θ]	0.02
Step time, [s]	0.5
Accelerating voltage, [kV]	30
Current, [mA]	10
Temperature, [K]	298
Pressure	Atmospheric

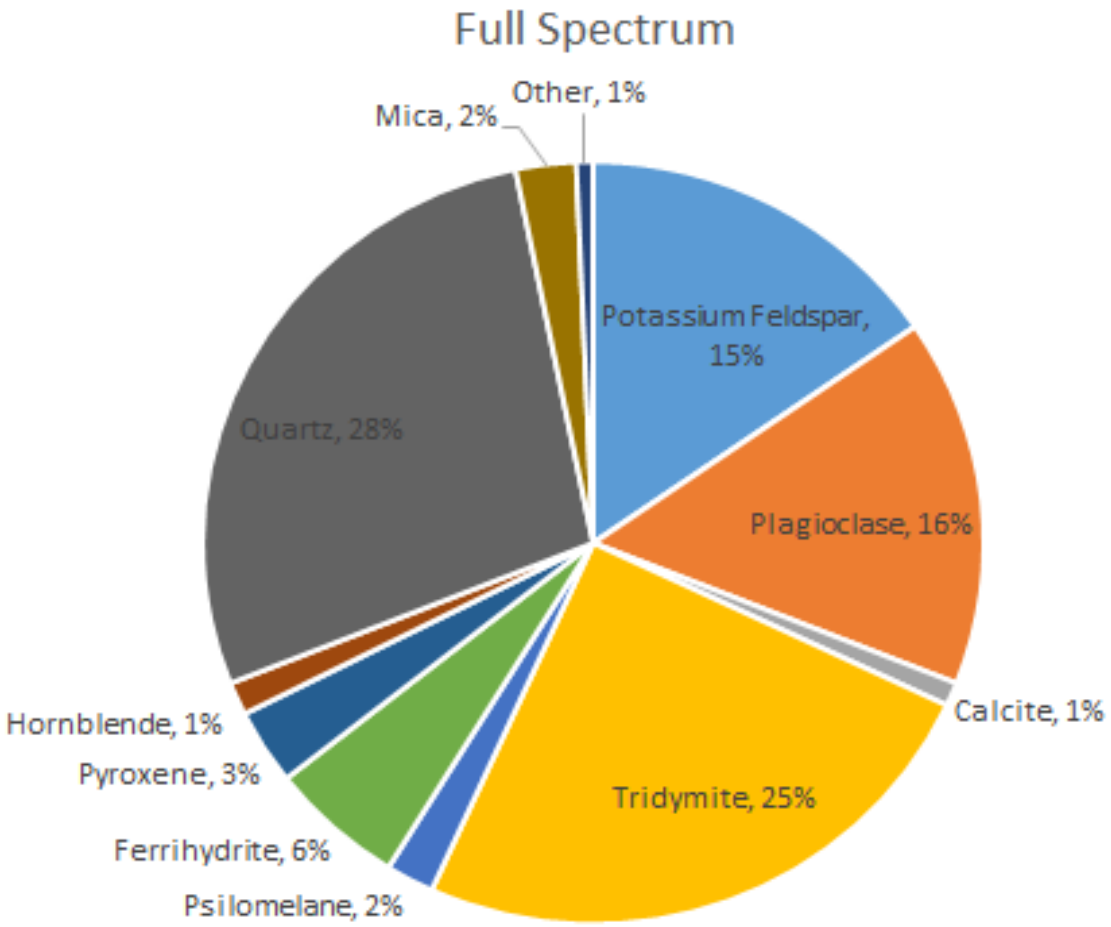


Figure 3-3. Full Spectrum of Mason Sand as obtained by XRD and Quantified by RockJock (Druckrey 2016)

Table 3-2. Major and minor compounds for the red/pink, clear/translucent, black/brown, and white/tan subgroups

Colored Subgroup	**Major**	**Secondary**	**Minor Secondary**
Red/Pink	Quartz	Potassium feldspar, Plagioclase feldspar	Mica, Calcite, Pyroxene
Black/Brown	Quartz	Mica (Biotite), Tridymite, Plagioclase feldspar, Potassium feldspar, Calcite	Psilomelane, Pyroxene, Hornblende, Ferrihydrite, Mica (Muscovite)
White/Tan	Quartz	Plagioclase feldspar, Potassium feldspar, Mica (Muscovite)	Mica (Biotite), Ferrihydrite, Pyroxene, Hornblende, Calcite
Clear/Translucent	Quartz	Plagioclase feldspar	Mica, Pyroxene, Ferrihydrite, Calcite, Tridymite

a secondary phase. Potassium feldspar was identified as a secondary phase in the red/pink subgroup. Secondary phases identified in the black/brown subgroup included mica (biotite), tridymite, potassium feldspar, and calcite. Secondary phases identified in the white/tan subgroup included potassium feldspar and mica (muscovite). To minimize confusion and maintain consistency, the subgroup will be referred to as red/pink, black/brown, white/tan, and clear/translucent. To examine the effect of particle size on fracturing, particles retained on US sieve #10 (2 mm) and particles passing sieve #10 (2 mm) and retained on sieve #20 (0.84 mm) were compressed. Appendices A through H contains Tables A-1 through H-1 that lists the particles, classified by particle and size.

3.3 EXPERIMENTS

3.3.1 Uniaxial Compression

Uniaxial compression of single mason sand particles was performed at a loading rate of 0.02 mm/min using an Omegadyne, Inc. LC101-25 model load cell with a range from 0 to 111.21 Newtons (N). Figure 3-4 shows the experimental setup of the uniaxial compression apparatus.

The motor was attached to a top plate, which was secured to the bottom plate using four aluminum rods with a diameter of 12.65 mm and length of 147.6 mm. The load cell was S-shaped with threaded holes at the top and bottom, which were used to directly attach the load cell to the motor at the top end, and top loading platen at the bottom end, using hollow head setscrews. Placed between the top loading platen and the load cell was a 3.27 mm thick aluminum plate used to measure the particle displacement during compression. The plate was 101.6 mm long with a width of 50.8 mm for half of its length and a width of 101.6 mm for the

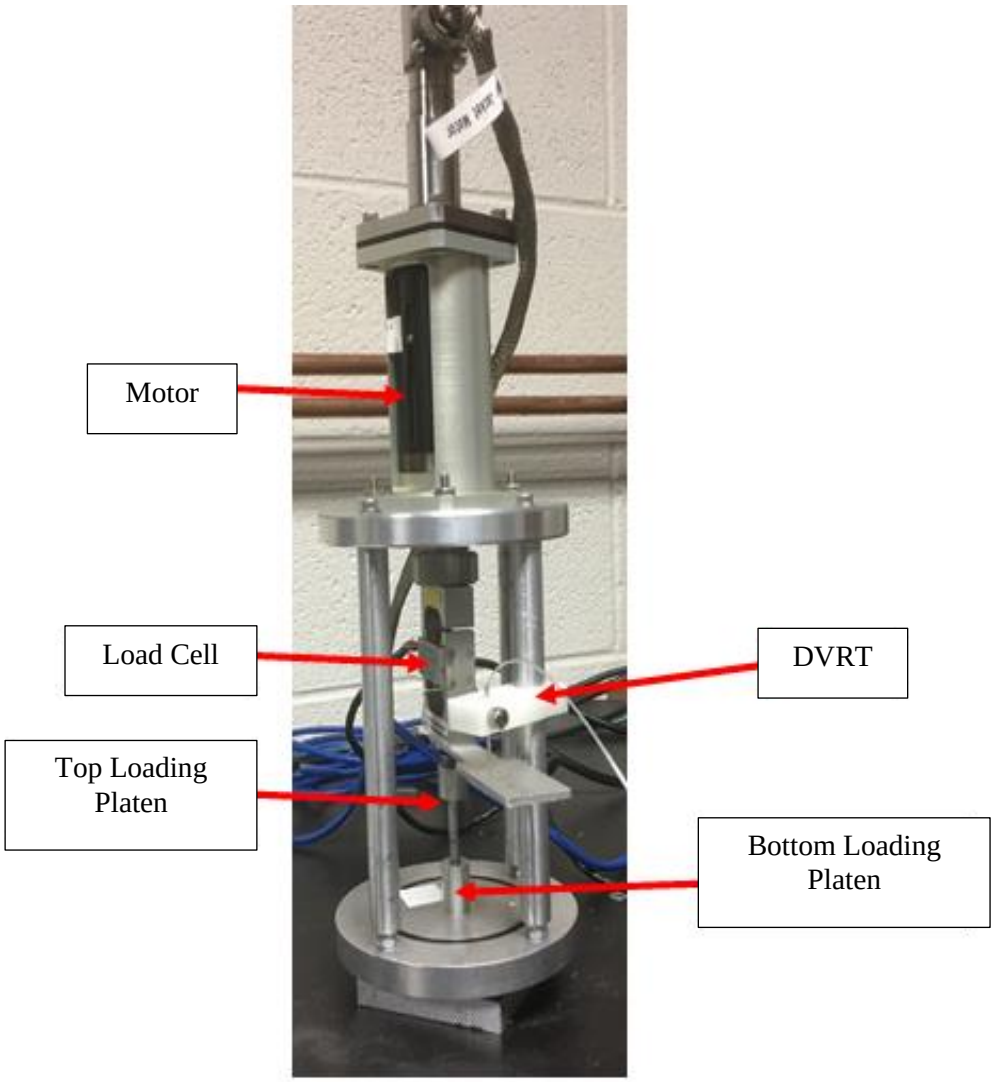


Figure 3-4. Unconfined Uniaxial Single Particle Compression Apparatus

remaining length. The smaller portion of the plate was directly attached onto the screw while the larger portion of the plate was positioned directly under the differential variable reluctance transducers (DVRT) to measure particle displacement. The particle displacement was measured using a Lord Sensing MicroStrain micro-miniature gauging DVRT, sensor part number 6103-0000. The DVRT was 4 mm long with a 1.5 mm spherical, ruby tip and has a body length of 24 mm with a diameter of 1.8034 mm. The DVRT can compress up to 3 mm and had a resolution of 1.5 µm. The body was placed into a small hole on a 50.89 mm by 19.13 mm by 11.40 mm acetyl rectangular prismatic and held into place with a steel allen bolt socket cap screw hex head allen key on one end (along the length). This rectangular prismatic was attached directly to the compression device through a 12.7 mm hole, drilled on the other end, in which the 12.65mm steel rod can be placed into. In order to secure the rectangular prismatic in place, a small hole was drilled at a height of 5.70 mm perpendicular to the 12.7 mm hole to attach an allen screw. This allows the user to move, position, and secure the DVRT along the rod, as necessary. The bottom platen was identical in size and material as the top platen and was attached to the bottom plate using a hollow head setscrew.

LabVIEW was the data acquisition (DAQ) program utilized to record the compressive displacement (in µm), and applied load (in N). During setup, the sand particle was placed on the bottom loading platen and the top loading platen was lowered until 0.2 N was exerted on the particle. This was controlled by the "Load Set Point" feature in LabView and allows the particle to be compressed between two platens, with a meniscal load being exerted, in order to obtain a d_L. The particle diameter in the loading direction, d_L, was the distance between the top and bottom loading platen prior to loading the particle. A ruler was placed behind the particle to measure the approximate d_L of the particle, as shown in Figure 3-5. The d_L is measured to the

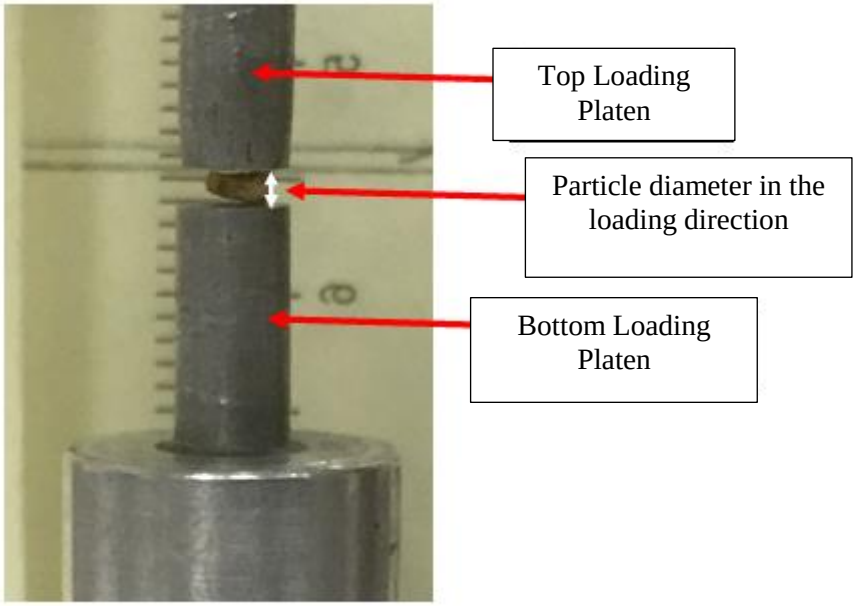


Figure 3-5. Single Sand Particle Prior to Loading

nearest 0.05 mm; a more accurate d_L was later obtained using the recorded compressive displacement values.

Once the approximate d_L was obtained, the DVRT was compressed prior to loading in order to measure displacement based on the expansion of the DVRT from its initial position. After the experiment was set up, the particle was loaded at a rate displacement of 0.02 mm/min. The displacement rates and loads were recorded every second and saved into a comma separated (CSV) file for further analysis. A total of 450 particles were tested; 223 were particles retained by US sieve #10 (2 mm) and 227 were particles passing sieve #10 (2 mm) and retained on sieve #20 (0.84 mm) (0.84 mm).

3.3.2 Synchrotron Micro-computed Tomography (SMT)

Synchrotron micro-computed tomography (SMT) was used to acquire x-ray images during single particle compression of 14 mason sand particles prior to loading, during loading, and at fracturing at a rate of 0.2 mm/min. The experiments were performed at the Advanced

Photon Source (APS), Argonne National Laboratory (ANL), Illinois, USA using the GeoSoilEnviroCARS (GSECARS) facility. Data was collected at beamline 13D using a beam size of 1.38 mm horizontal by 1.03 mm vertical. The particles were rotated between 0° to 180° with 1 second exposure times and scans were acquired at 0.20° rotation increments. The 3D images had a spatial resolution of 2.08 μm/voxel. For further details pertaining to the one-dimensional particle compression SMT imaging perform at ANL, refer to Druckrey and Alshibli (2015), Druckrey (2016) and Druckrey et al. (2016).

The SMT images were reconstructed and analyzed using Avizo Fire to measure the d_L, internal structures and fracture modes of 14 mason sand particle. Refer to Druckrey et al. (2014) for further information on the process of 3D imaging.

CHAPTER FOUR: RESULTS AND DISCUSSION

4.1 INTRODUCTION

This chapter discusses the results of the uniaxial compression and synchrotron micro-tomography (SMT) imaging of particles passing sieve #10 (2 mm) and retained on sieve #20 (0.84 mm) and retained by sieve #10 (2 mm) in the red/pink (major and secondary compounds: quartz, potassium feldspar, and plagioclase feldspar), black/brown (major and secondary compounds: quartz, mica (biotite), tridymite, plagioclase feldspar, potassium feldspar, and calcite), white/tan (major and secondary compounds: major and secondary compounds: quartz, plagioclase feldspar, potassium feldspar, and mica (muscovite)), and clear/translucent (major and secondary compounds: quartz and plagioclase feldspar) subgroups. Uniaxial compression results were used to calculate the tensile strength of all particles. The Weibull distribution model was applied to particles, in their respective subgroups and size categories, and its results were analyzed and discussed. The relationship between tensile strength and size, mineralogy, morphology, and fracture mode was investigated. Three-dimensional SMT imaging was utilized to examine d_L, internal structures, and fracture modes as it relates to tensile strength for 14 mason sand particles.

Through past research, it was predicted that particles with larger d_L (larger sized particles), spherical shaped, subrounded, subangular, and had more internal structure flaws will facture at lower tensile strengths (Lade et al. 1996; Tavares, 2007; Cavaretta et al. 2010; Todisco et al. 2016; Wang and Coop, 2016). Based on Mohs scale of mineral hardness, particle subgroups containing predominantly quartz, orthoclase, and plagioclase will contain harder minerals and fracture at higher tensile strengths; particle subgroups containing calcite and mica will contain softer minerals and fracture at lower tensile strengths (Mohs Scale of Mineral

Hardness, 1998; Mohs Hardness Scale, 2005). Fracture modes of the particle will be dependent on morphology and mineralogy.

4.2 UNIAXIAL UNCONFINED COMPRESSION

Uniaxial compression experiments provided fracture loads, compressive displacements, and particle diameters in the loading direction (d_L). The fracture load and diameter of particle in loading direction was used to calculate and examine the tensile strength of the particle; the Weibull statistical model was applied to examine the tensile strength statistical distribution and obtain the characteristic tensile strength of the particles. Pre-fracture descriptions, based on visual inspection, were recorded for each particle to determine the particle mineralogy and morphology to investigate how these factors influence the tensile strength of the particles. Post-fracture descriptions, based on visual inspection, are also recorded to aid in the classification of particle fracture modes and determine the relationship between fracture mode, particle mineralogy, and morphology. Visual inspection of the particle only provided front optical measurements of the particles, was, therefore, difficult to obtain contact area measurements between the particle and top and bottom loading platens. Therefore, while the effect of coordination number is a major contributor on particle tensile strength, it was not included due to equipment limitations.

The tensile strength (MPa), compressive displacement (mm), d_L (mm), fracture mode, and particle description prior to and post fracture are listed in Appendices A, B, C, and D, for red/pink (major and secondary compounds: quartz, potassium feldspar, and plagioclase feldspar), black/brown (major and secondary compounds: quartz, mica (biotite), tridymite, plagioclase feldspar, potassium feldspar, and calcite), white/tan (major and secondary compounds: quartz, plagioclase feldspar, potassium feldspar, and mica (muscovite)), and clear/translucent (major

and secondary compounds: quartz and plagioclase feldspar) particles passing sieve #10 (2 mm) and retained on sieve #20 (0.84 mm), respectively. The tensile strength (MPa), compressive displacement (mm), d_L (mm), fracture mode, and particle description prior to and post fracture are listed in Appendices E, F, G, and H red/pink (major and secondary compounds: quartz, potassium feldspar, and plagioclase feldspar), black/brown (major and secondary compounds: quartz, mica (biotite), tridymite, plagioclase feldspar, potassium feldspar, and calcite), white/tan (major and secondary compounds: quartz, plagioclase feldspar, potassium feldspar, and mica (muscovite)), and clear/translucent (major and secondary compounds: quartz and plagioclase feldspar) particles retained by sieve #10 (2 mm), respectively.

4.2.1 Weibull Statistical Distribution Model

The Weibull statistical model, developed by Weibull (1951), is a commonly used statistical distribution function to analyze the tensile strength of single particle fracture between two flat loading platens. Nakata et al. (1999) used the Weibull model to quantify particle fracture between two flat loading platens, with the exclusion of feldspar particles, and correlate the particle survival with the amount of particle fracture. Hyde and Nakata (1999) utilized the Weibull model to analyze plastic yielding of soil under oedometric compression. In 2000, McDowell and Amon found that Weibull statistics can successfully be applied to analyze the size effects of particles being fractured between two flat platens.

Weibull proposed that the probability of survival of a particle, (P_s), can be calculated based on the following equation:

$$P_s = e^{\left[-(\sigma_f/\sigma_{0f})\right]^{m_f}} \quad (3)$$

where $P_s = \frac{number\ of\ particles\ crushing\ at\ \sigma \geq \sigma_f}{total\ number\ of\ particles}$, σ_f is the tensile strength at failure, σ_{0f} is the characteristic tensile strength proportional to the particle survival probability of 37%, and m_f is the Weibull modulus (McDowell and Bolton 1998; McDowell and Amon 2000; Druckrey 2016). The characteristic tensile strength is a function of particle size and can be expressed as:

$$\sigma_{0f} \propto d^{-3/m_f} \tag{4}$$

where d is the particle diameter (McDowell and Bolton 1998; McDowell and Amon 2000). Since σ_{0f} is inversely proportional to (F), the force required to fracture the particle, and proportional to d^2, the particle diameter (based on (1)), then the relationship between the force to fracture the particle and the particle size can be expressed as:

$$F \propto d^{2-3/m_f} \tag{5}$$

A smaller Weibull modulus was expected from particles with larger diameters which implied a lower characteristic tensile strength, and therefore a lower force, was required to fracture the particle. Contrastingly, as noted by McDowell and Amon (2000), a small Weibull modulus indicated that there was a higher variability in the force required to fracture a particle and that this force was independent of particle size. Rather, the relationship between characteristic tensile strength and particle size of the particles, based on the Weibull statistical model, was a better indicator to determine the force required to fracture a particle.

Weibull statistical analysis was performed, based on colored subgroup and size, to examine the statistical distribution of tensile strength of the particle and to determine the characteristic tensile strength. Figures 4-1 through 4-8 displays the Weibull statistical model for the different colored subgroups in the two size categories. Figures 4-1 through 4-8 contain an R^2 value and Weibull modulus, m_f, of the data set; the characteristic tensile strength, σ_{0f}, calculated

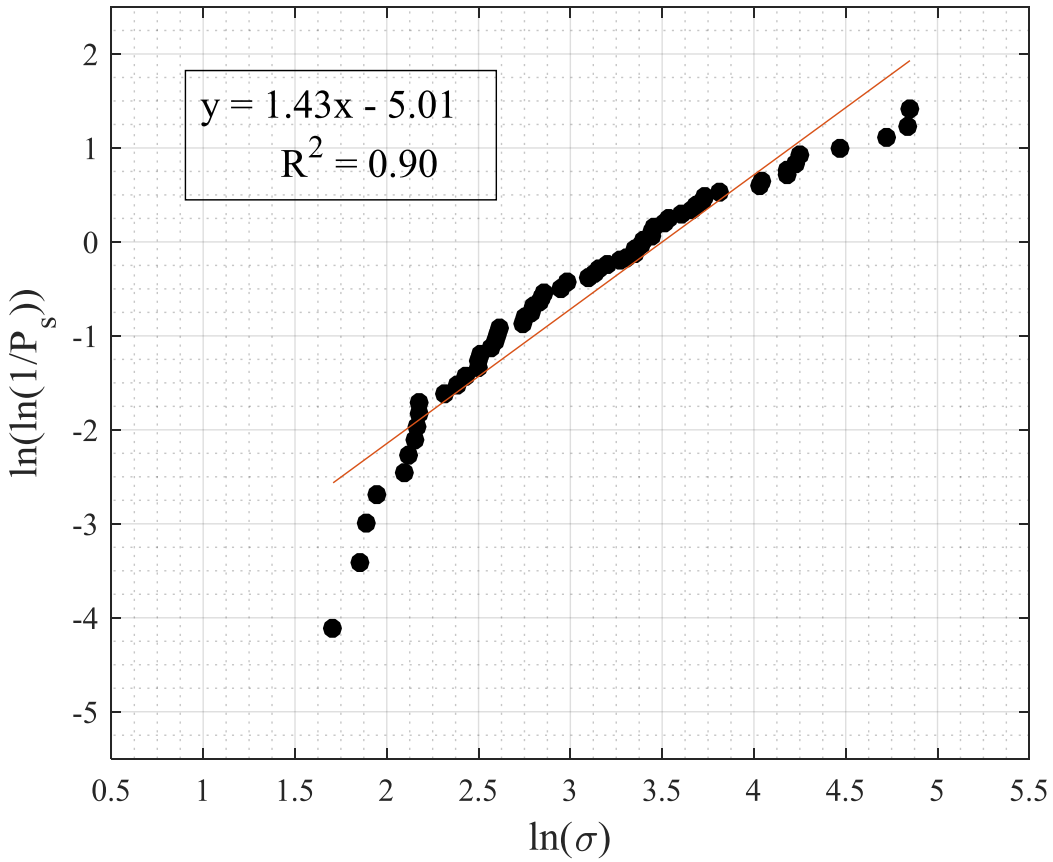


Figure 4-1. Weibull distribution of characteristic tensile strength for red/pink (major and secondary compounds: quartz, potassium feldspar, and plagioclase feldspar) particles retained between sieve #10 (2 mm) and #20 (0.84 mm)

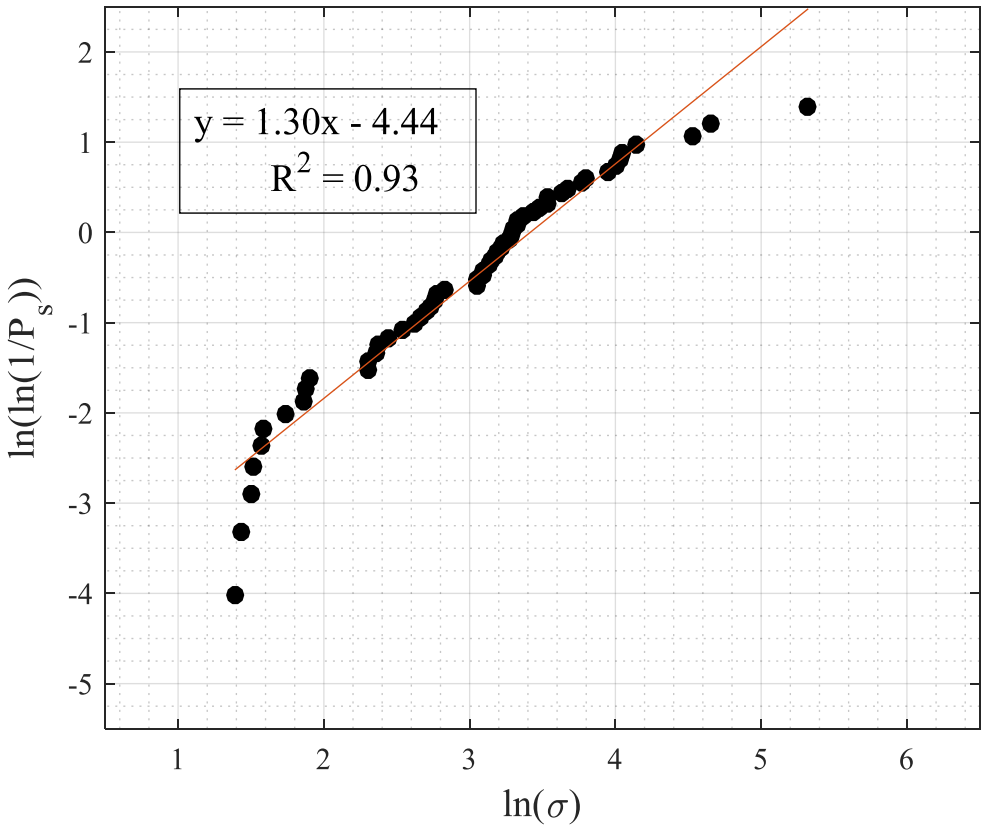


Figure 4-2. Weibull distribution of characteristic tensile strength for black/brown particles (major and secondary compounds: quartz, mica (biotite), tridymite, plagioclase feldspar, potassium feldspar, and calcite) retained between sieve #10 (2 mm) and #20 (0.84 mm)

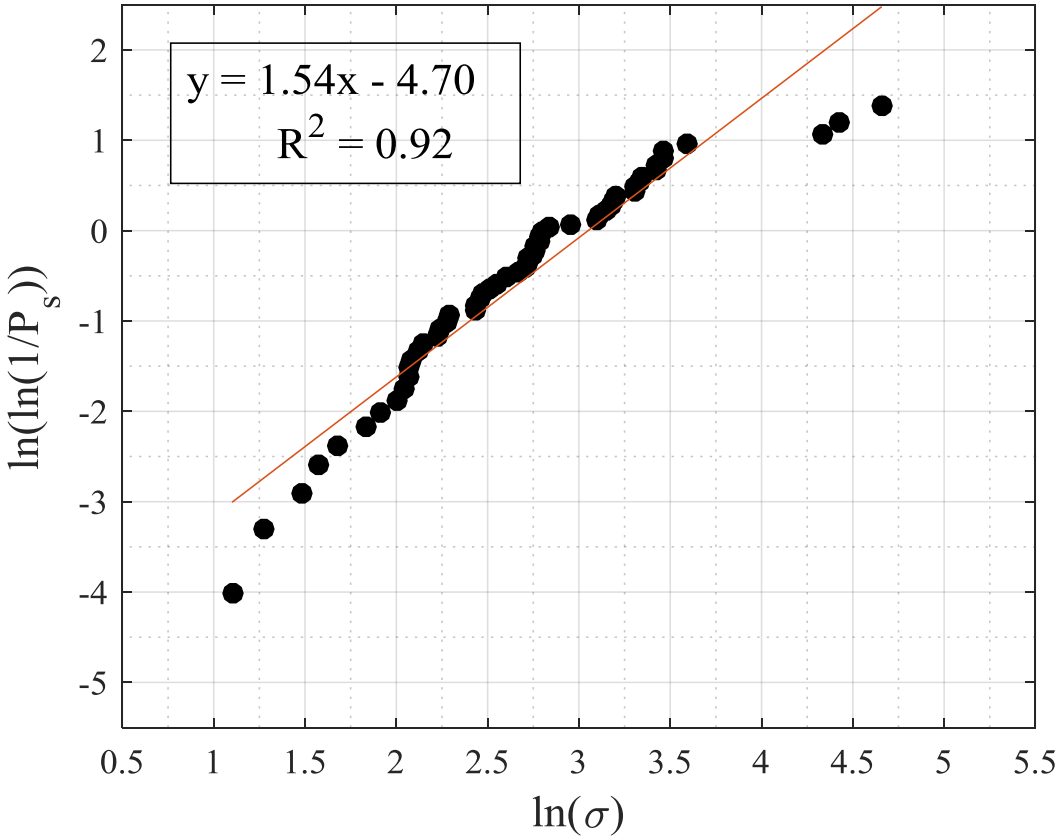


Figure 4-3. Weibull distribution of characteristic tensile strength for white/tan (major and secondary compounds: quartz, plagioclase feldspar, potassium feldspar, and mica (muscovite)) particles retained between sieve #10 (2 mm) and #20 (0.84 mm)

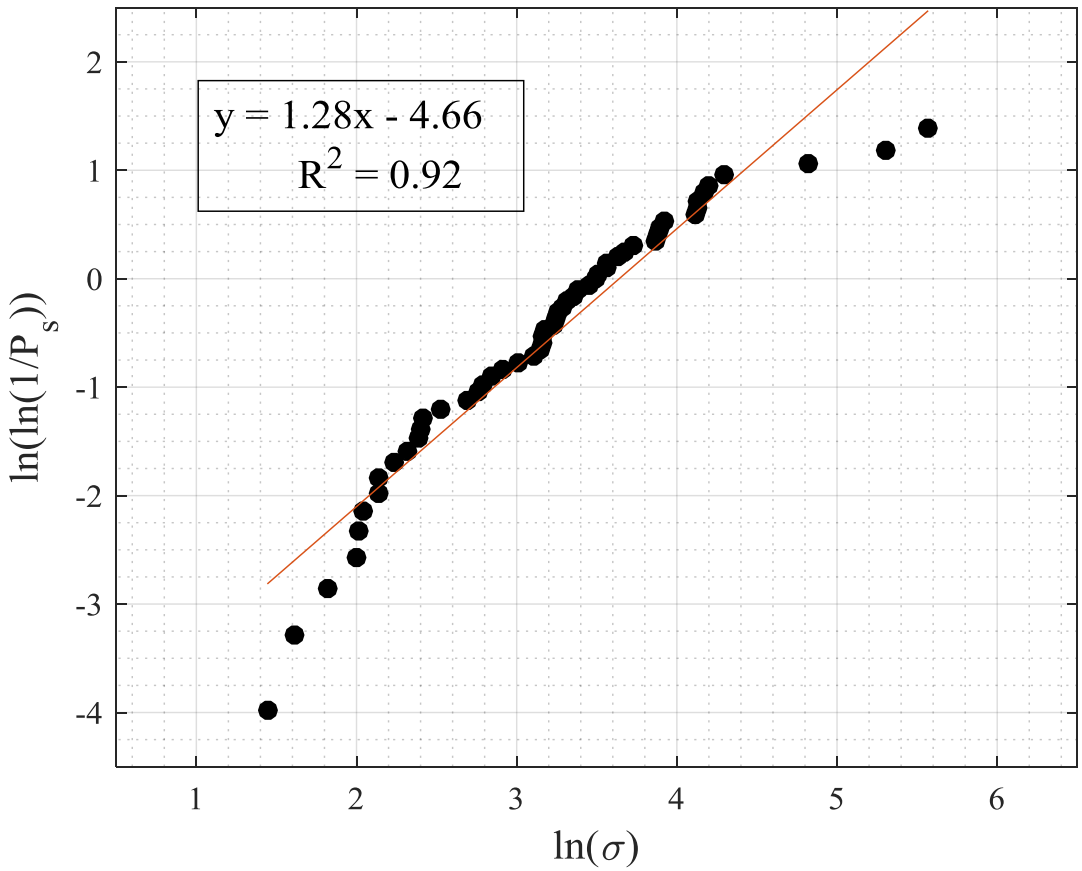


Figure 4-4. Weibull distribution of characteristic tensile strength for clear/translucent (major and secondary compounds: quartz and plagioclase feldspar) particles retained between sieve #10 (2 mm) and #20 (0.84 mm)

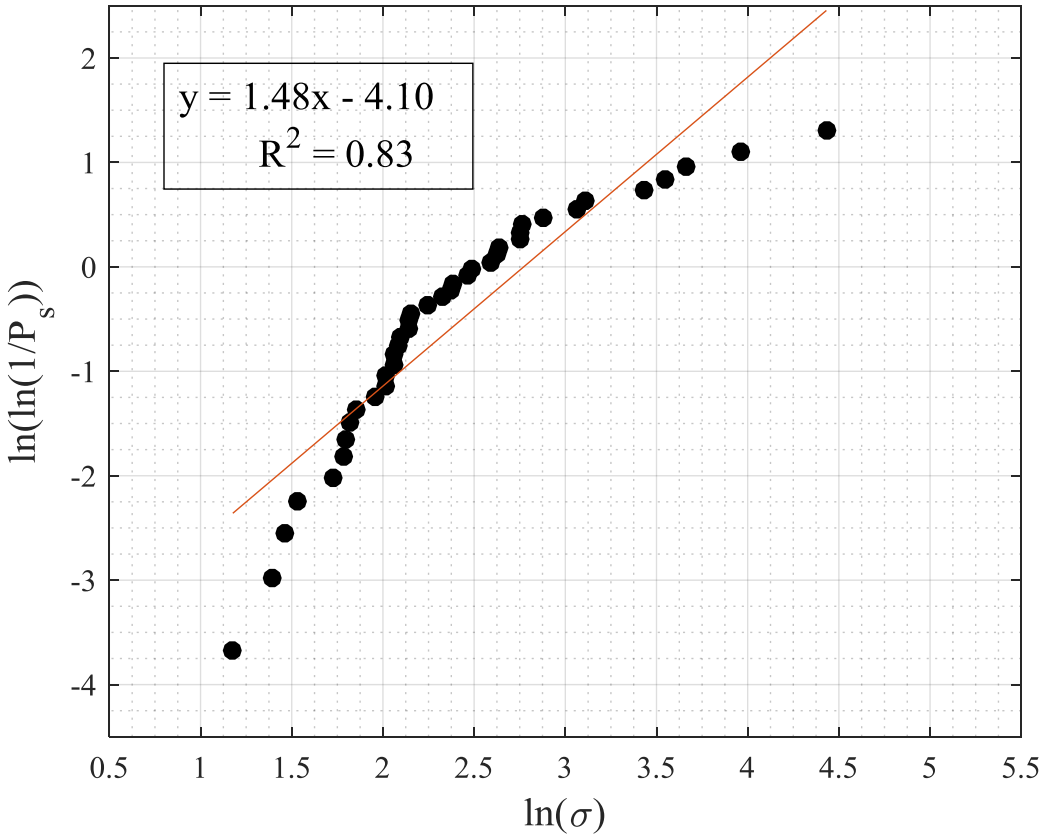


Figure 4-5. Weibull distribution of characteristic tensile strength for red/pink (major and secondary compounds: quartz, potassium feldspar, and plagioclase feldspar) particles retained by sieve #10 (2 mm)

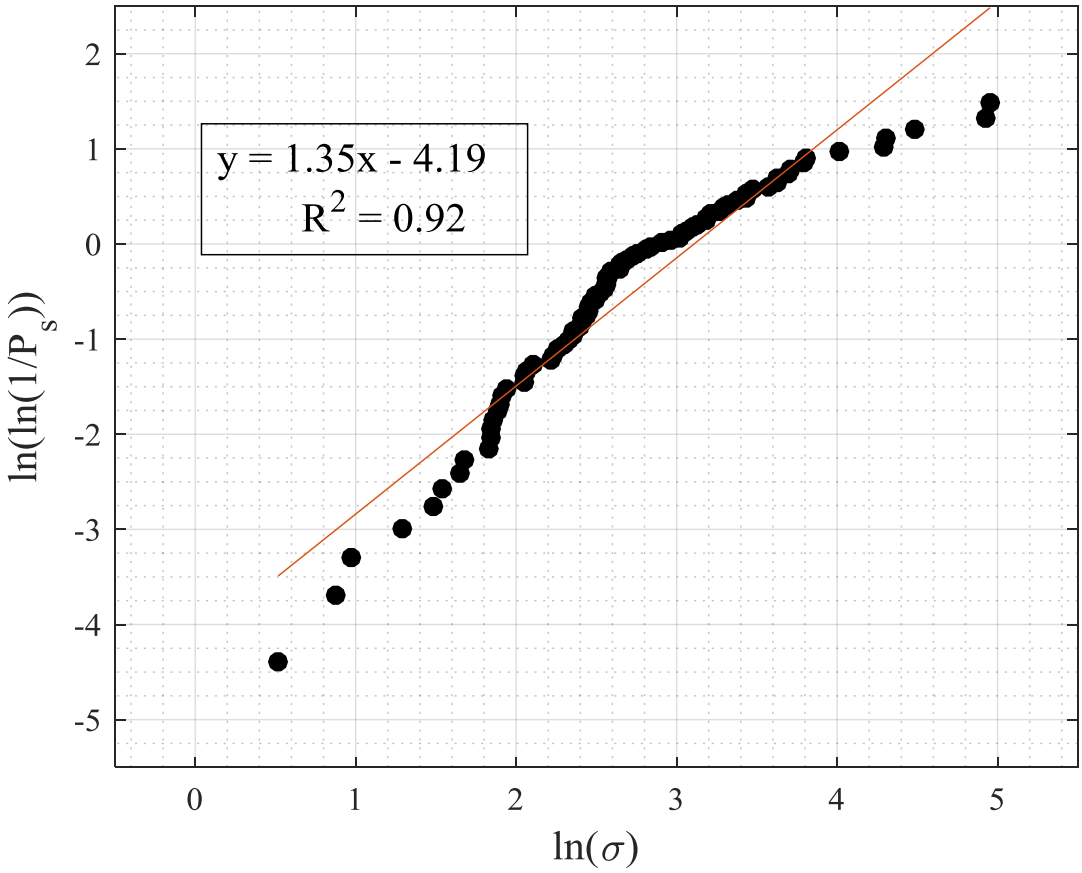


Figure 4-6. Weibull distribution of characteristic tensile strength for black/brown (major and secondary compounds: quartz, mica (biotite), tridymite, plagioclase feldspar, potassium feldspar, and calcite) particles retained by sieve #10 (2 mm)

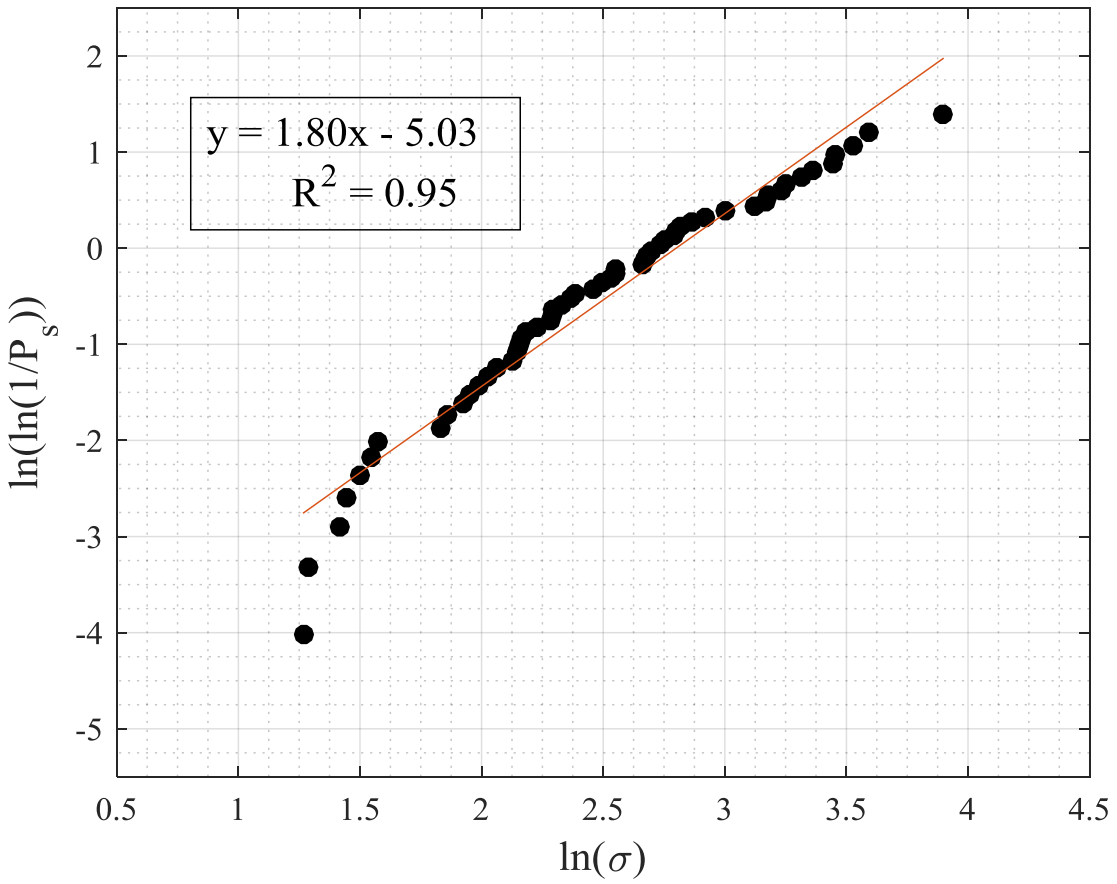


Figure 4-7. Weibull distribution of characteristic tensile strength for white/tan (major and secondary compounds: quartz, plagioclase feldspar, potassium feldspar, and mica (muscovite)) particles retained by sieve #10 (2 mm)

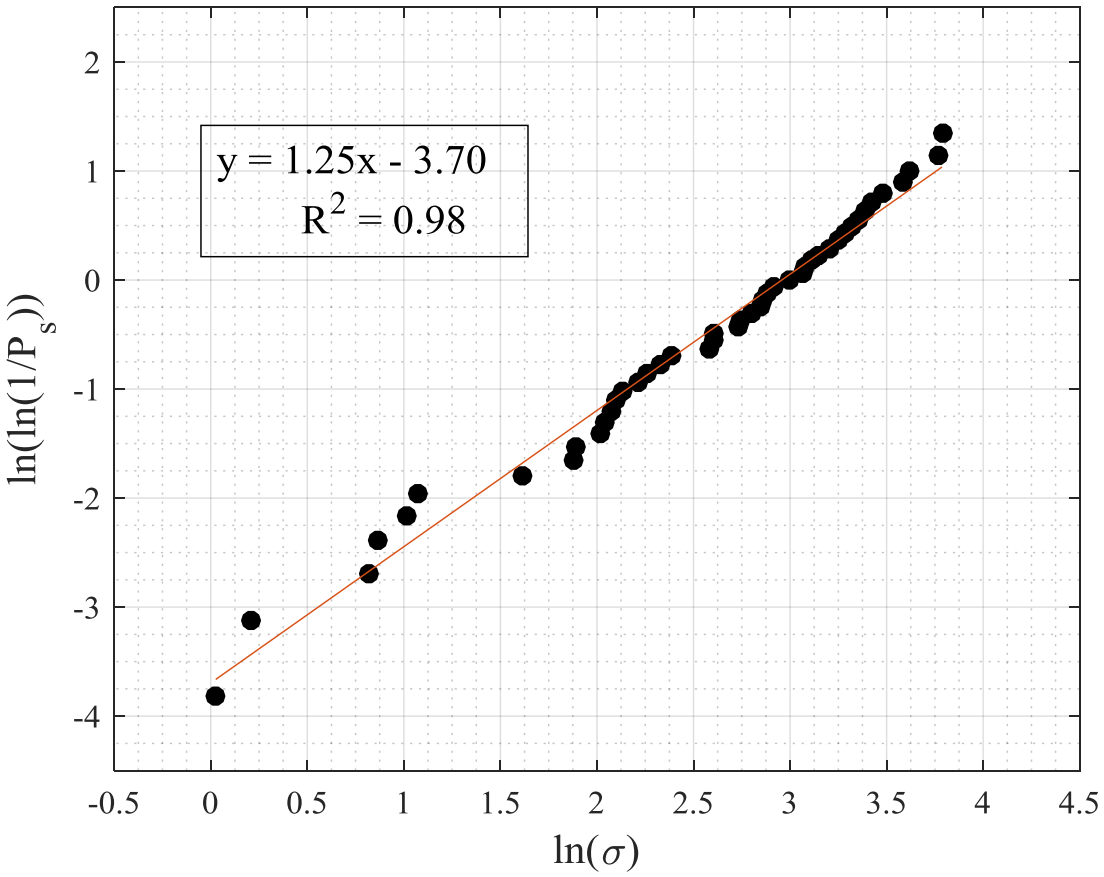


Figure 4-8. Weibull distribution of characteristic tensile strength for clear/translucent (major and secondary compounds: quartz and plagioclase feldspar) particles retained by sieve #10 (2 mm)

from the ln(ln(1/Ps)) versus ln(σ) relationship, was represented as the intersection between the fitted linear trend line and the x axis. The R^2 value signified how well the dataset correlated with the Weibull model fitted linear trend line and how accurate the characteristic tensile strength is to the tensile strength at the 63rd percentile; a higher value indicates a strong correlation between the data and fitted trendline and vice versa. The Weibull modulus, m_f, is the slope of the fitted linear trend line which describes the variation in particle strength. A smaller value signifies a high variation in strength. The characteristic tensile strength, σ_{0f}, is the stress in which 37% of particles will survive. This implies that at this tensile strength, approximately 63% of the particles will had already fractured (also referred to as the 63rd percentile tensile strength) and 37% of the particles can still sustain further tensile loading until the fracturing stage.

A summary of the R^2, m_f, and σ_{0f} for red/pink (major and secondary compounds: quartz, potassium feldspar, and plagioclase feldspar), black/brown (major and secondary compounds: quartz, mica (biotite), tridymite, plagioclase feldspar, potassium feldspar, and calcite), white/tan (major and secondary compounds: quartz, plagioclase feldspar, potassium feldspar, and mica (muscovite)), and clear/translucent (major and secondary compounds: quartz and plagioclase feldspar) particles retained between sieve #10 (2 mm) and #20 (0.84 mm) and by sieve #10 (2 mm) is given in Table 4-1. All colored subgroups within both size categories had relatively high R^2 values which implied an excellent statistical fit of the data sets to the fitted linear trend line, with the exception of red/pink particles retained by sieve #10 (2 mm); therefore, particles retained between sieve #10 (2 mm) and sieve #20 (0.84 mm) and by sieve #10 (2 mm) can be modeled using the Weibull distribution with slight deviations. For particles retained between sieve #10 (2 mm) and #20 (0.84 mm), the black/brown particles had the highest R^2 value and the red/pink particles had the lowest R^2 value, suggesting that the black/brown particles fit the

Table 4-1. Weibull distribution parameters for particles retained between sieves #10 (2 mm) and #20 (0.84 mm) and by sieve #10 (2 mm) for all subgroups

Colored Subgroups	**Particle sizes between sieves #10 (2 mm) and #20 (0.84 mm)**				**Particles retained on sieve #10 (2 mm)**			
	Number of Particles	R^2	m_f	σ_{0f} ***(MPa)***	***Number of Particles***	R^2	m_f	σ_{0f} ***(MPa)***
Red/Pink *(major and secondary compounds: quartz, potassium feldspar, and plagioclase feldspar)*	61	0.90	1.43	33.14	40	0.84	1.48	15.99
Black/Brown *(major and secondary compounds: quartz, mica (biotite), tridymite, plagioclase feldspar, potassium feldspar, and calcite)*	56	0.93	1.30	30.43	82	0.92	1.35	22.39

Table 4-1 Continued

Colored Subgroups	**Particle sizes between sieves #10 (2 mm) and #20 (0.84 mm)**				**Particles retained on sieve #10 (2 mm)**			
	Number of Particles	R^2	m_f	σ_{0f} ***(MPa)***	***Number of Particles***	R^2	m_f	σ_{0f} ***(MPa)***
White/Tan *(major and secondary compounds: quartz, plagioclase feldspar, potassium feldspar, and mica (muscovite))*	56	0.92	1.54	21.12	56	0.95	1.80	16.44
Clear/Translucent *(major and secondary compounds: quartz and plagioclase feldspar)*	54	0.92	1.28	38.09	46	0.98	1.25	19.24

Weibull distribution model better compared to the red/pink particles. For particles retained by sieve #10 (2 mm), the clear/translucent subgroup had the highest R^2 value while the red/pink subgroup had the lowest; the distribution of clear/translucent data points was closer to the trendline compared to the distribution of the red/pink data points, which are more scattered and farther away from the trend line, especially at the lower and upper ends, which indicated that the clear/translucent particles fit the Weibull distribution model better compared to the red/pink particles.

The white/tan particles, retained between sieve #10 (2 mm) and #20 (0.84 mm) and by sieve #10 (2 mm), had the highest m_f, but overall, m_f values were relatively low, implying high variations in particle strength and, therefore, no correlation between particle size and tensile strength. Based on the σ_{0f}, the clear/translucent particles had the highest σ_{0f} , at 38.09 MPa, while the white/tan particles had the lowest, at 21.12 MPa, for particles retained between sieve #10 (2 mm) and #20 (0.84 mm); this predicts that 63% of the clear/translucent particles will fracture prior to reaching a tensile strength of 38.09 MPa and 63% of the white/tan particles will fracture prior to reaching a tensile strength of 21.22 MPa. For particles retained by sieve #10 (2 mm), black/brown particles had the highest σ_{0f} , at 22.39 MPa, while the red/pink particles had the lowest σ_{0f} , at 15.99 MPa, inferring that 63% of the black/brown particles will fracture prior to reaching a tensile strength of 22.39 MPa and 63% of the red/pink particles will fracture prior to reaching a tensile strength of 15.99 MPa. This indicated that white/tan and red/pink particles were the weakest particles retained between sieve #10 (2 mm) and #20 (0.84 mm) and by sieve #10 (2 mm), respectively, while clear/translucent and black/brown particles were the strongest particles between sieve #10 (2 mm) and #20 (0.84 mm) and by sieve #10 (2 mm), respectively.

Referring to Tables 4-1, the Weibull distribution model is a good statistical indicator of the particle distribution based on tensile strength, as determined by many other researchers in the literature. Based on the high R^2 values for particle retained between sieve #10 (2 mm) and #20 (0.84 mm) and by sieve #10 (2 mm), the Weibull distribution was expected to be an excellent statistical indicator of tensile strength for black/brown, white/tan, and clear/translucent particles and a good statistical indicator of tensile strengths for the red/pink particles indicated by the lower R^2 values. The m_f of particles within the same colored subgroups, regardless of size category, was relatively similar, in which the particles retained by sieve #10 (2 mm) had higher Weibull moduli, with the exception of the clear/translucent particles. This indicated that the m_f was not affected by size, but only by particle mineralogy. The white/tan particles, retained by #10 sieve and between #10 and #20 (0.84 mm) sieves, had the highest Weibull modulus while the clear/translucent particles, retained by sieve #10 (2 mm) and between sieves #10 (2 mm) and #20 (0.84 mm), had the lowest m_f.

Overall, the m_f values of the four subgroups in the two sizes were relatively low and, therefore, it is probable that there was no correlation between fracture forces and particle size. As expected, the σ_{0f} and fracture loads of particle retained between sieve #10 (2 mm) and #20 (0.84 mm) were higher compared to particles retained by sieve #10 (2 mm) because smaller particles are less susceptible to having flaws or defects or cleavage (Tavares 2007; Wang and Coop 2016). For particles retained between sieve #10 (2 mm) and #20 (0.84 mm), the clear/translucent particles had the highest σ_{0f} and for particles retained by sieve #10 (2 mm), the black/brown particles had the highest σ_{0f}; this indicates that the σ_{0f} of a group of particles varies with size and mineralogy. While the results from the Weibull distribution coincide with findings already concluded in literature, this thesis will examine how accurately the Weibull distribution model

predicts the characteristic tensile strength based on mineralogy and size and analyze the model distribution.

Referring to Figures 4-1 through 4-8, the tensile strengths of the particles are not evenly distributed. Instead, tensile strength along the lower and upper ends of the distribution are scattered while the tensile strengths along the middle of the distribution are grouped into small clusters, which are defined as data points that are overlapping. It was determined that the data points are graphed based on increasing tensile strength, with the lowest tensile strength being excluded from the data based on calculations to obtain the Weibull distribution statistical model. The data points at the lower end of the distribution represented particles with lowest tensile strength, starting with the particle with the lowest tensile strength, while the upper end of the distribution consisted of data points representing particles with high tensile strength, ending with the particle with the highest tensile strength. At the lower end of the distribution, there was a tail consisted of a minimum of four scattered data points. The slope of these scattered points was steeper compared to the trend line and distance between the points decreased at a logarithmic rate as the scattered data points approached the first cluster, with the exception of clear/translucent particles retained on sieve # 10. The clusters within the middle of the distribution are formed based on tensile strengths and within each cluster, the difference in tensile strength rarely exceeded 1 MPa; when the tensile strength between two data point exceeded 1 MPa, the data points only slightly overlap, which made that area in the cluster more distinguishable. In most Figures, the difference in tensile strength between the clusters predominantly increased as the tensile strength of the data point increased. The wave-like pattern through the distribution and within the clusters denoted a gradual increase in tensile strength within ~1 MPa and the change from 1 MPa to the next 1 MPa. For instance, a cluster containing

data points of particles that had 15 to 17 MPa exhibited a gradual increase in tensile strength within 15 MPa followed by a slight decrease in the data points position to display the change from 15 MPa to 16 MPa. Excluding the lower end of the distribution, the amount of overlap between the data points was dictated by the difference between the tensile strength of the particles; a smaller difference in tensile strength between the particles was portrayed with more overlap between the data points while a greater different in tensile strength between the particles was portrayed with less overlap and more space between the data points. Similar to the lower end, the upper end of the distribution consisted of data points that are more scattered and the slope was less steep compared to the trend line, with the exception of clear/translucent particles retained on sieve #10 (2 mm). Furthermore, the distance between the data points also increased at a logarithmic rate.

The characteristics tensile strength, R^2, and Weibull modulus values can be utilized to evaluate the tensile strength of particles through single particle uniaxial compression and the relationship between tensile strength and particle. The characteristic tensile strength analysis showed that the particles retained between sieve #10 (2 mm) and #20 (0.84 mm) were stronger compared to the particles retained by sieve #10 (2 mm) but the strength based on mineralogy varied. For particles retained between sieve #10 (2 mm) and #20 (0.84 mm), the clear/translucent were expected to fracture at higher tensile strengths while the white/tan particles were expected to fracture at lower tensile strengths. For particles retained by sieve #10 (2 mm), the black/brown particles were predicted to be stronger while the white/tan particles were predicted to be weaker. The high R^2 values indicated that the Weibull model was a good indicator of the variability of the data and can be used to determine the tensile strength at which 37% of particles will survive. Based on the R^2 value, the characteristic tensile strength for the clear/translucent

particles retained by sieve #10 (2 mm) shall be more accurate while the characteristic tensile strength for the red/pink particles retained by sieve #10 (2 mm) shall be less accurate when compared to the 63rd percentile tensile strength. The Weibull modulus predicted that there will be no correlation between particle tensile strength and particle diameter in loading direction and there will be high variations in tensile strength. As a result of the Weibull distribution model, the data points of the particles that are relatively close in tensile strength were grouped together throughout the distribution while the weakest and strongest particles were scatter at the lower and upper limits of the distribution. Aside from the white/tan subgroup, the σ_{0f} for the remaining three subgroups fall within the largest cluster.

4.2.2 Tensile Strength

The effects of particle size, mineralogy, morphology, and fracture modes of 40 red/pink (major and secondary compounds: quartz, potassium feldspar, and plagioclase feldspar) particles, 82 black/brown (major and secondary compounds: quartz, mica (biotite), tridymite, plagioclase feldspar, potassium feldspar, and calcite) particles, 56 the white/tan (major and secondary compounds: quartz, plagioclase feldspar, potassium feldspar, and mica (muscovite)) particles, and 46 clear/translucent (major and secondary compounds: quartz and plagioclase feldspar) particles retained by sieve #10 (2 mm) and 61 red/pink particles, 56 black/brown particles, 56 white/tan particles, and 54 clear/translucent particles retained between sieve #10 (2 mm) and #20 (0.84 mm) on tensile strength were examined using uniaxial compression tests.

4.2.2.1 Effects of Particle Size

To examine the effects of particle size on tensile strength, the four subgroups were divided into two size categories, particles retained between sieves #10 (2 mm) and #20 (0.84 mm) and by sieve #10 (2 mm), and labeled based on particle diameter in loading direction (d_L).

Due to limitations in measurement tools, d_L values are approximated and had an accuracy of 0.01mm. If particle rotation occurred at the beginning, d_L was adjusted accordingly to accurately reflect the d_L of the particle where it began to stabilize and sustained loads with minimal rotation and particle rearrangement. It was predicted that particles with larger d_L will fracture at lower tensile strengths (Tavares 2007; Wang and Coop, 2016).

Figures 4-9 and 4-10 shows the relationship between particle d_L, in mm, and tensile strength, in MPa, for all particles retained between sieves #10 (2 mm) and #20 (0.84 mm) and particles retained by sieve #10 (2 mm), respectively. In Figures 4-9 and 4-10, the red/pink (major and secondary compounds: quartz, potassium feldspar, and plagioclase feldspar) particles are represented with red circles, the black/brown (major and secondary compounds: quartz, mica (biotite), tridymite, plagioclase feldspar, potassium feldspar, and calcite) particles are represented with blue squares, the white/tan (major and secondary compounds: quartz, plagioclase feldspar, potassium feldspar, and mica (muscovite)) particles are represented with green right sided triangles, and the clear/translucent (major and secondary compounds: quartz and plagioclase feldspar) particles are represented with black triangles; fitted least square regression lines, with colors corresponding to the color of the data points for each subgroup, are displayed. To examine the individual trends of each particle subgroup within the two size categories, Figures 4-9a through 4-9d are provided in Appendix I and display the tensile strength versus d_L relationship of red/pink, black/brown, white/tan, and clear/translucent particles retained between sieve #10 (2 mm) and #20 (0.84 mm). Figures 4-10a through 4-10d, provided in Appendix I, displays the tensile strength versus d_L relationship of red/pink, black/brown, white/tan, and clear/translucent particles retained by sieve #10 (2 mm). In Figures 4-9a through 4-10d, d_L, in mm, is represented on the x-axis and the tensile strength, in MPa, is represented on the log y-axis; the

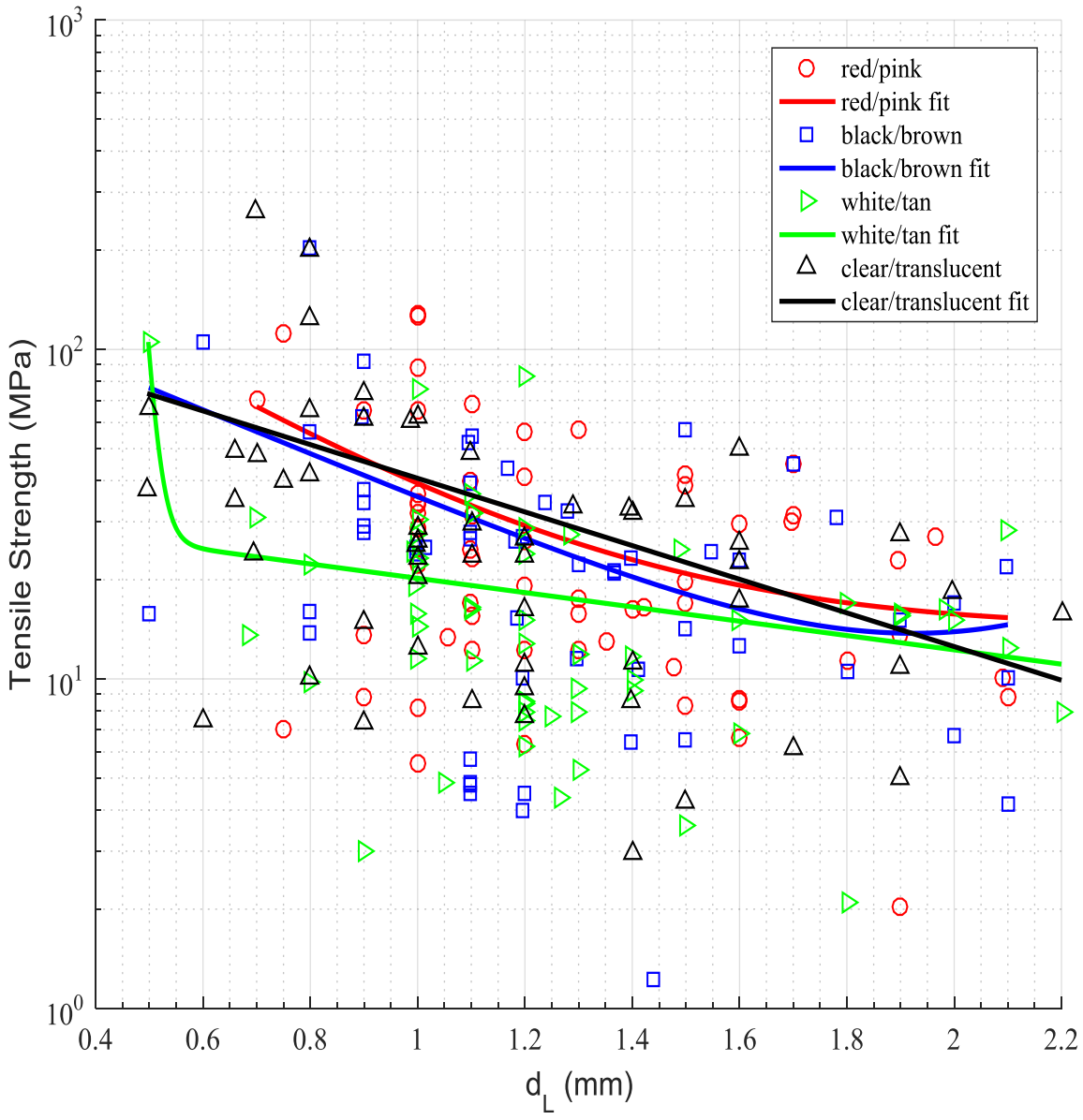


Figure 4-9. Relationship between tensile strength and d_L for the red/pink (major and secondary compounds: quartz, potassium feldspar, and plagioclase feldspar), the black/brown (major and secondary compounds: quartz, mica (biotite), tridymite, plagioclase feldspar, potassium feldspar, and calcite), the white/tan (major and secondary compounds: quartz, plagioclase feldspar potassium feldspar, and mica (muscovite)) , and the clear/translucent (major and secondary compounds: quartz and plagioclase feldspar) particles retained between sieve #10 (2 mm) and #20 (0.84 mm).

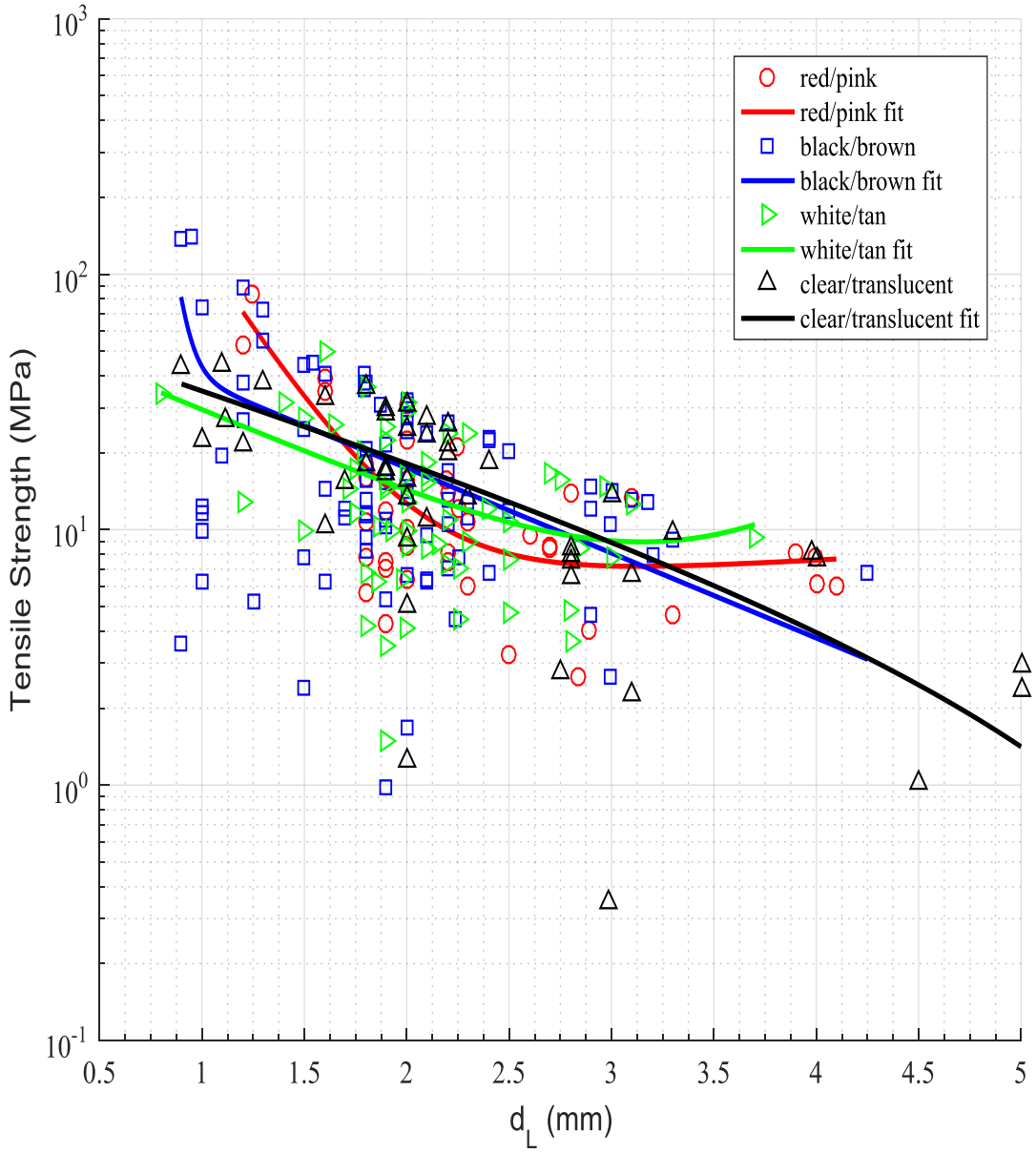


Figure 4-10. Relationship between tensile strength and d_L for the red/pink (major and secondary compounds: quartz, potassium feldspar, and plagioclase feldspar), the black/brown (major and secondary compounds: quartz, mica (biotite), tridymite, plagioclase feldspar, potassium feldspar, and calcite), the white/tan (major and secondary compounds: quartz, plagioclase feldspar potassium feldspar, and mica (muscovite)) , and the clear/translucent (major and secondary compounds: quartz and plagioclase feldspar) particles retained by sieve #10 (2 mm).

fitted least square regression line, μ, represented with a magenta dashed line, and (μ±σ), represented with black dashed lines, are shown.

As seen in Figure 4-9, particles retained between sieve #10 (2 mm) and #20 (0.84 mm) experienced tensile strengths between the range of 1 to 263 MPa with 196 particles fracturing prior to a tensile strength of 50 MPa. Exponential regression curves fitted to the data showed a negative correlation between tensile strength and d_L. The d_L ranged from approximately 0.50 mm to 2.20 mm, in which many particles had the same d_L. Table 4-2 displays the d_L, in increments of 0.20 mm, and the number of particles within those ranges, based on colored subgroups. As observed in Table 4-2, across the four colored subgroups, 106 particles had a d_L between 0.81 mm to 1.20 mm with less than 10 particles between 0.40 mm to 0.60 mm and 2.01 mm to 2.20 mm. Although many particles had the same d_L, the tensile strengths of the particles vary in which very few particles had the same d_L and tensile strengths, as shown in Figure 4-9.

Figure 4-10 displays the distribution of particles retained by sieve #10 (2 mm); 216 particles had a tensile strength between the ranges of 0.35 to 143 MPa and fractured prior to a tensile strength of 40 MPa. Exponential regression curves were fitted to the data and showed a negative correlation between tensile strength and d_L. The d_L ranged from approximately 0.70 mm to 5.00 mm, in which a majority of particles had the same diameter in loading direction. Table 4-3 displays the d_L, in ranges of 0.50 mm, and the number of particles within those ranges, based on colored subgroups. Based on Table 4-3, 144 particles from all subgroups had a d_L between 1.51 mm to 2.50 mm, 11 particles had a d_L less than 1.00 mm, and a total of 5 particles had a d_L larger than 4.00 mm. Similar to particles retained between sieve #10 (2 mm) and #20 (0.84 mm), many particles retained by sieve #10 (2 mm) had similar d_L but very few had similar tensile strengths.

Table 4-2. Number of red/pink, black/brown , white/tan, and clear translucent particles retained between sieve #10 (2 mm) and #20 (0.84 mm) based on particle diameter in the loading direction (mm).

d_L (mm)	**Number of particles**				
	Red/Pink *(major and secondary compounds: quartz, potassium feldspar, and plagioclase feldspar)*	***Brown/Black*** *(major and secondary compounds: quartz, mica (biotite), tridymite, plagioclase feldspar, potassium feldspar, and calcite)*	***White/Tan*** *(major and secondary compounds: quartz, plagioclase feldspar, potassium feldspar, and mica (muscovite))*	***Clear/ Translucent*** *(major and secondary compounds: quartz and plagioclase feldspar)*	**Total**
0.40 to 0.60	0	2	1	3	6
0.61 to 0.80	3	4	4	11	22
0.81 to 1.00	16	8	11	12	47
1.01 to 1.20	15	17	17	10	59
1.21 to 1.40	6	8	10	6	30
1.41 to 1.60	11	5	4	6	26
1.61 to 1.80	4	6	2	1	13
1.81 to 2.00	4	3	4	4	15
2.01 to 2.20	2	3	3	1	9

Table 4-3. Number of red/pink, brown/black, white/tan, and clear/translucent particles retained by sieve #10 (2 mm) based on particle diameter in the loading direction (mm).

d_L (mm)	**Number of Particles**				
	Red/Pink *(major and secondary compounds: quartz, potassium feldspar, and plagioclase feldspar)*	***Brown/Black*** *(major and secondary compounds: quartz, mica (biotite), tridymite, plagioclase feldspar, potassium feldspar, and calcite)*	***White/Tan*** *(major and secondary compounds: quartz, plagioclase feldspar, potassium feldspar, and mica (muscovite))*	***Clear/ Translucent*** *(major and secondary compounds: quartz and plagioclase feldspar)*	**Total**
0.50 to 1.00	0	8	1	2	11
1.01 to 1.50	2	11	4	4	21
1.51 to 2.00	17	34	26	17	94
2.01 to 2.50	8	18	16	8	50
2.51 to 3.00	6	6	7	7	26
3.01 to 3.50	2	4	1	3	10
3.51 to 4.00	3	0	1	2	6
4.01 to 4.50	1	1	0	1	3
4.51 to 5.00	0	0	0	2	2

Table 4-4 summarizes the μ, σ, and (μ±σ), in (mm), of d_L for particles retained between sieve #10 (2 mm) and #20 (0.84 mm) and by sieve #10 (2 mm). Figures 4-11 and 4-12 show $(\mu\pm\sigma)_{ld}$ for particles retained between sieve #10 (2 mm) and #20 (0.84 mm) and by sieve #10 (2 mm), respectively. As shown in Figure 4-11, the red/pink particles had larger d_L while the clear/translucent particles had smaller d_L, on average. The d_L ranges for the four colored subgroups were relatively similar. As shown in Figure 4-12, the clear/translucent particles had larger d_L while the black/brown particles had smaller d_L. The clear/translucent particles had the largest d_L range while the white/tan particles had the smallest d_L range, implying that the d_L for clear/translucent particles varied greatly while the white/tan particles had little variation. Referring to Figures 4-9a through 4-10d, 68% of particles had a d_L within μ±σ; based on Figures 4-10a through 4-10d, for red/pink particles and clear/translucent particles, particles with a d_L greater than $(\mu+\sigma)_{ld,10}$, had larger d_L and smaller tensile strengths while particles with a d_L less than $(\mu-\sigma)_{ld,10}$, had smaller d_L and larger tensile strengths.

Based on the Weibull model, particles retained between sieve #10 (2 mm) and #20 (0.84 mm) were stronger and there was a weak correlation between particle tensile strength and d_L. From the uniaxial compression experiments, particles retained between sieve #10 (2 mm) and #20 (0.84 mm) fractured at higher tensile strengths compared to the particles retained by sieve #10 (2 mm) and had a weak negative correlation between particle tensile strength and d_L, in which particles with larger d_L fractured at lower tensile strengths was observed. This trend was more apparent with the particles retained by sieve #10 (2 mm), as seen in Figure 4-10, especially with the red/pink and clear/translucent particles, compared to the particles retained between sieve #10 (2 mm) and #20 (0.84 mm), as seen in Figure 4-9. With the exclusion of particles within 68% of the $\mu_{ld,10}$, as d_L decreased, tensile strength increased. It can be seen in Figures 4-9a

Table 4-4. Particle diameter in the loading direction (mm), properties for particles retained between sieve #10 (2 mm) and #20 (0.84 mm) and by sieve #10 (2 mm)

Colored Subgroups	**Particles retained between sieve #10 (2 mm) and #20 (0.84 mm)**			**Particles retained by sieve #10 (2 mm)**		
	μ_{ld} ***(mm)***	σ_{ld} ***(mm)***	$(\mu \pm \sigma)_{ld}$ ***(mm)***	$\mu_{ld,10}$ ***(mm)***	$\sigma_{ld,10}$ ***(mm)***	$(\mu \pm \sigma)_{ld,10}$ ***(mm)***
Red/Pink *(major and secondary compounds: quartz, potassium feldspar, and plagioclase feldspar)*	1.29	0.346	0.944 to 1.64	2.34	0.721	1.62 to 3.06
Black/Brown *(major and secondary compounds: quartz, mica (biotite), tridymite, plagioclase feldspar, potassium feldspar, and calcite)*	1.27	0.383	0.887 to 1.65	1.96	0.636	1.32 to 2.60
White/Tan *(major and secondary compounds: quartz, plagioclase feldspar, potassium feldspar, and mica (muscovite))*	1.27	0.378	.892 to 1.65	2.10	0.496	1.60 to 2.60

Table 4-4 Continued

Colored Subgroups	**Particles retained between sieve #10 (2 mm) and #20 (0.84 mm)**			**Particles retained by sieve #10 (2 mm)**		
	μ_{ld} ***(mm)***	σ_{ld} ***(mm)***	$(\mu \pm \sigma)_{ld}$ ***(mm)***	$\mu_{ld,10}$ ***(mm)***	$\sigma_{ld,10}$ ***(mm)***	$(\mu \pm \sigma)_{ld,10}$ ***(mm)***
Clear/Translucent *(major and secondary compounds: quartz and plagioclase feldspar)*	1.15	0.405	.745 to 1.56	2.35	0.961	1.39 to 3.31

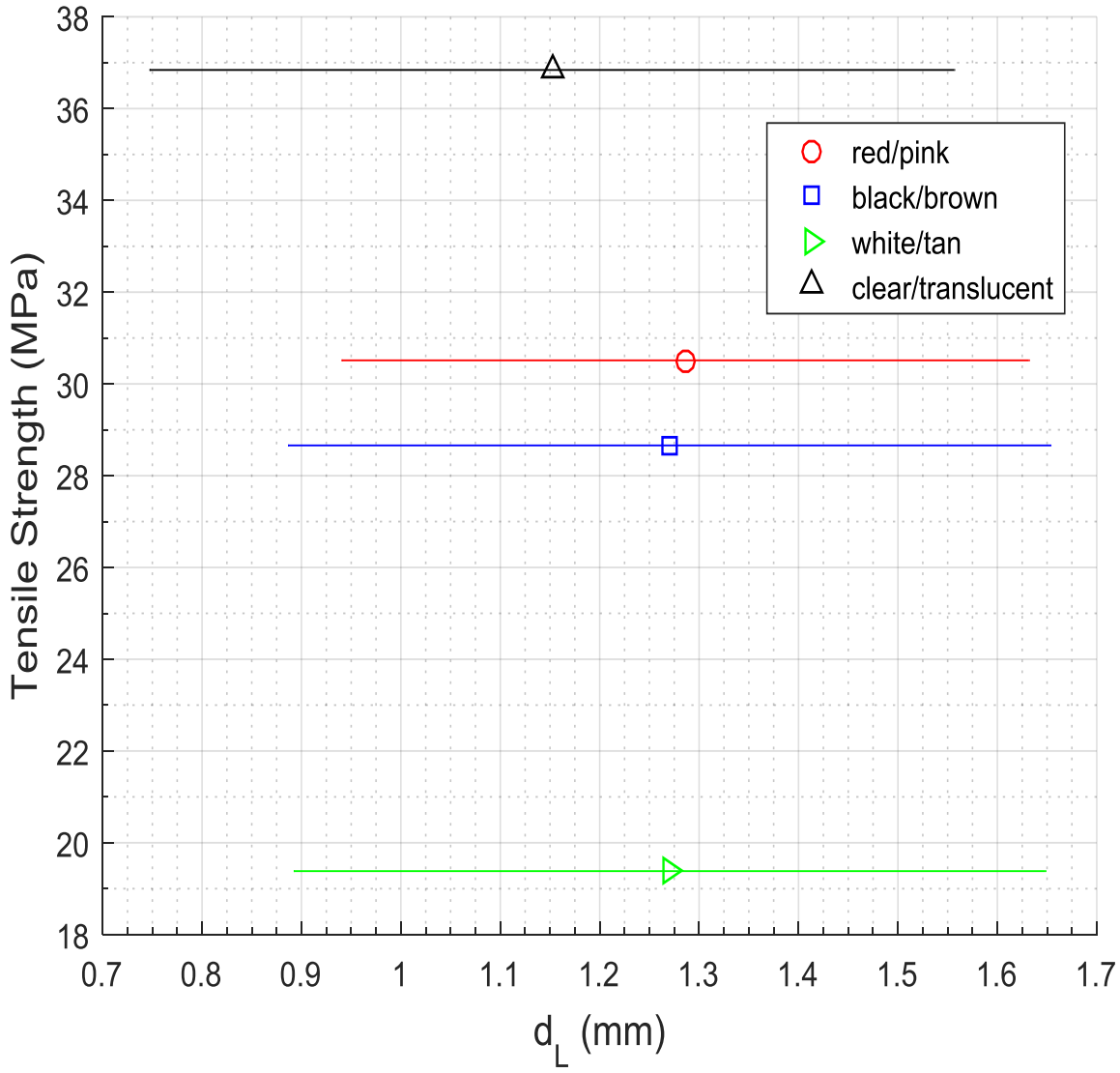


Figure 4-11. μ±σ for red/pink (major and secondary compounds: quartz, potassium feldspar, and plagioclase feldspar), black/brown (major and secondary compounds: quartz, mica (biotite), tridymite, plagioclase feldspar, potassium feldspar, and calcite), white/tan (major and secondary compounds: quartz, plagioclase feldspar, potassium feldspar, and mica (muscovite)) and clear/translucent (major and secondary compounds: quartz and plagioclase feldspar) particles retained between sieve #10 (2 mm) and #20 (0.84 mm)

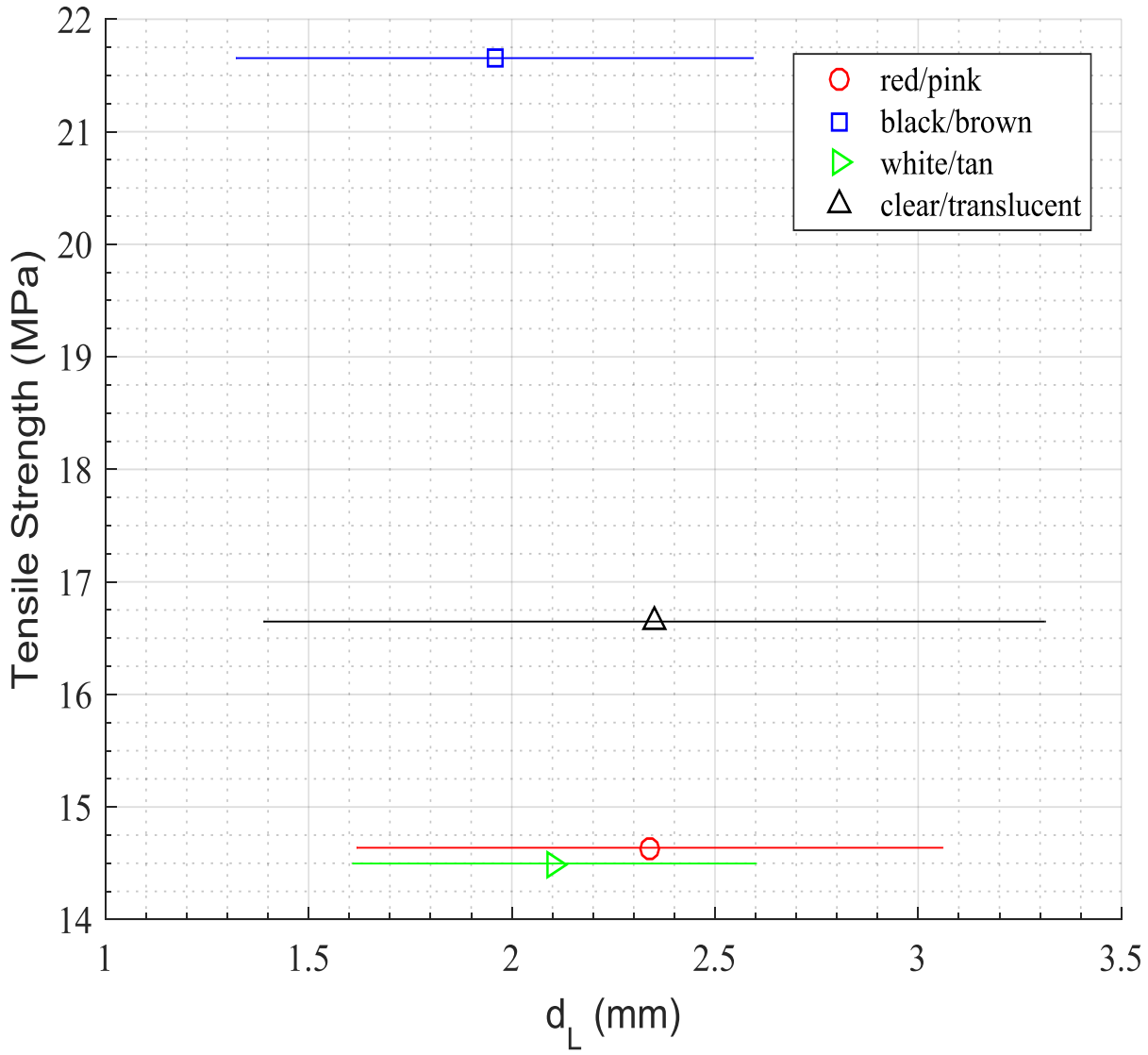


Figure 4-12. μ±σ for red/pink (major and secondary compounds: quartz, potassium feldspar, and plagioclase feldspar), black/brown (major and secondary compounds: quartz, mica (biotite), tridymite, plagioclase feldspar, potassium feldspar, and calcite), white/tan (major and secondary compounds: quartz, plagioclase feldspar, potassium feldspar, and mica (muscovite)) and clear/translucent (major and secondary compounds: quartz and plagioclase feldspar) particles retained by sieve #10 (2 mm)

through 4-9d and 4-10 through 4-10d that particles with smaller d_L fractured at higher tensile strengths while particles with larger d_L fractured at lower tensile strength. This implied that while there was a weak correlation between particle tensile strength and d_L, there was a high probability that larger sized particles and particles with larger d_L will fracture at lower tensile strengths compared to smaller particles, especially for particles retained by sieve #10 (2 mm). Furthermore, it can also be concluded, based on the tensile strength ranged from Figures 4-9 and 4-10, the particles retained between sieve #10 (2 mm) and #20 (0.84 mm) fractured at higher tensile strengths compared to particles retained by sieve #10 (2 mm).

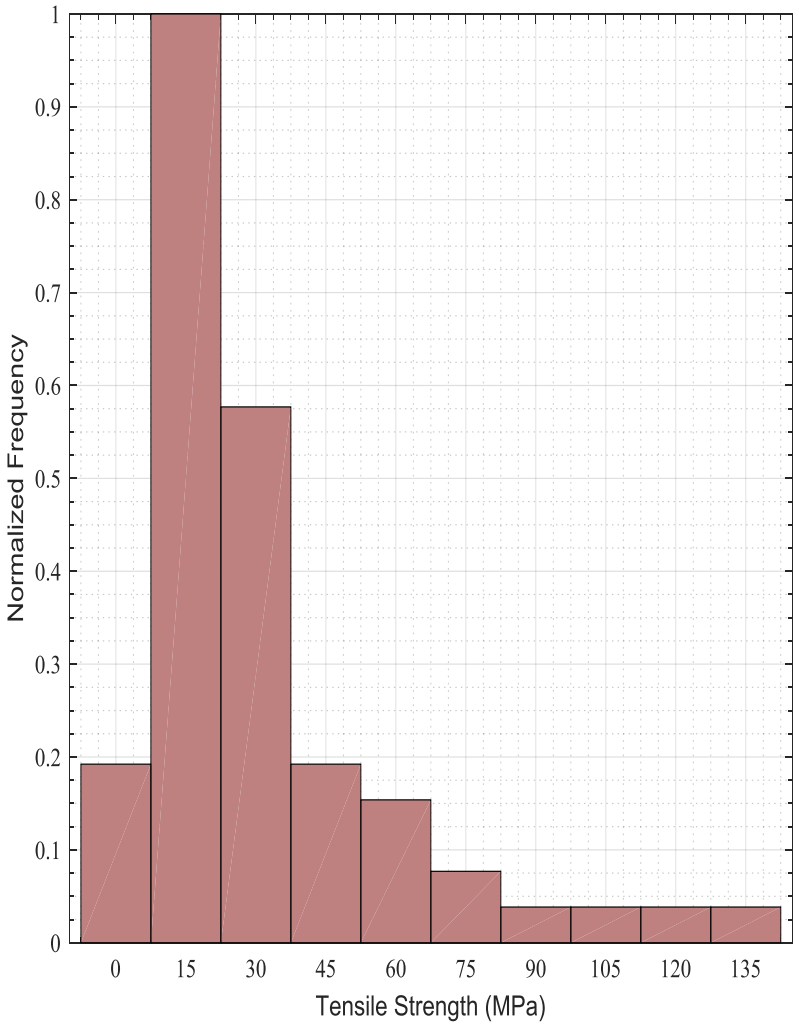
4.2.2.2 Effects of Particle Mineralogy

To examine the effects of particle mineralogy on tensile strength, Mason sand was divided into four subgroups based on visual classification of color (an approximate classification of mineralogy). The four colored subgroups are red/pink (major and secondary compounds: quartz, potassium feldspar, and plagioclase feldspar) particles, black/brown (major and secondary compounds: quartz, mica (biotite), tridymite, plagioclase feldspar, potassium feldspar, and calcite) particles, white/tan (major and secondary compounds: quartz, plagioclase feldspar, potassium feldspar, and mica (muscovite)) particles, and clear/translucent (major and secondary compounds: quartz and plagioclase feldspar) particles. To account for the effects of particle size, the four colored subgroups will be further divided into particles retained between sieve #10 (2 mm) and #20 (0.84 mm) and by sieve #10 (2 mm). The tensile strength histograms were created to examine the distribution of tensile strength based on mineralogy and size. The y-axis represents the frequency and the x-axis represents the tensile strength in MPa. Distribution, 97th and 63rd percentile strength, mean, and standard deviation tensile strength will be analyzed. The 97th percentile strength (σ_{97}) determines if there are outliers within the data set; if there are

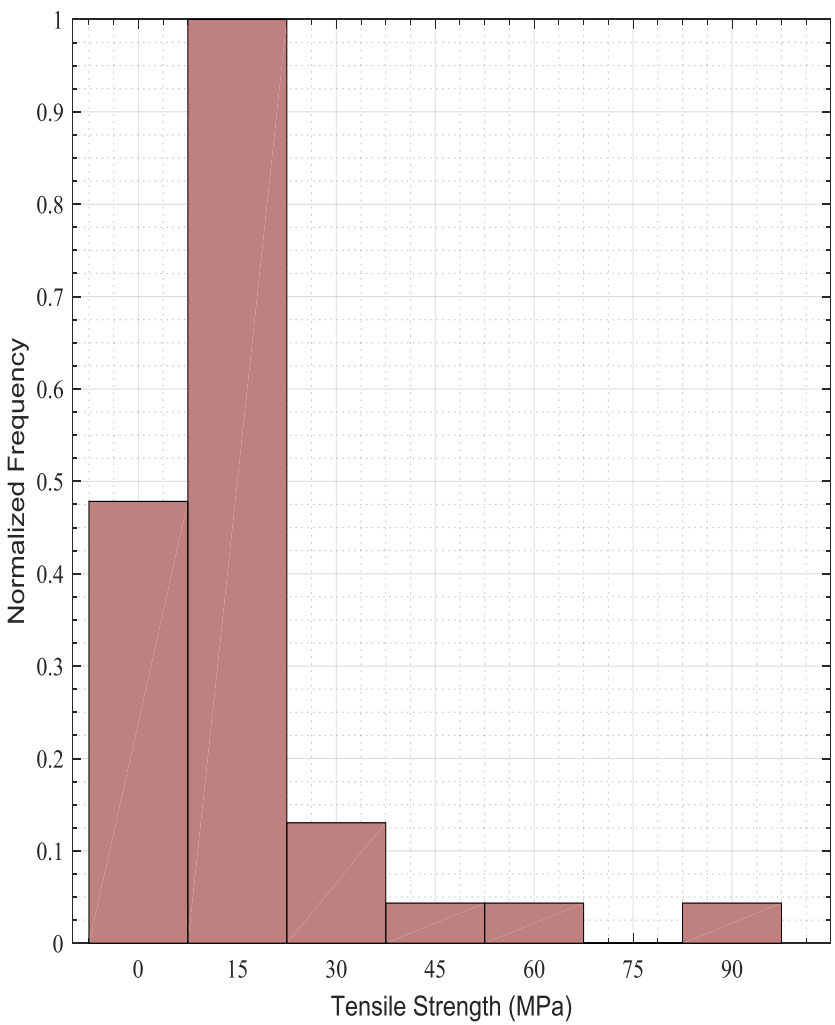
particles that had a tensile strength much greater than the σ_{97} (signified with a gap between the bin containing the σ_{97} and outlying tensile strength), then those particles will be considered as outliers. The outliers will be addressed but not removed from data analysis to illustrate the heterogeneity of the Mason sand. The 63rd percentile (σ_{63}) examines the tensile strength based on a probability of survival of 37%. The mean, μ_t, examines the strength at which 50% of particles fracture, and standard deviation (σ_t) was used to determine the range at which 68% of particles fracture $(\mu \pm \sigma)_t$. Changes to σ_{63}, σ_{97}, μ_t, σ_t, and $(\mu \pm \sigma)_t$ as a result of outliers will be reported in parentheses. Based on the Weibull model, it was predicted that the clear/translucent particles will fracture at higher tensile strengths and the white/tan particles will fracture at lower tensile strengths.

The major and secondary compounds of the red/pink particles were identified as quartz, potassium feldspar, and plagioclase feldspar. Based on the Weibull statistical distribution, this subgroup was predicted to had a probability of survival of 37% at a tensile strength of 33.14 and 15.99 MPa for the particles retained between sieve #10 (2 mm) and #20 (0.84 mm) and by sieve #10 (2 mm), respectively. This implied that 63% of particles retained between sieve #10 (2 mm) and #20 (0.84 mm) are predicted to fracture prior to a tensile strength of 33.14 MPa and 63% of particles retained by sieve #10 (2 mm) are predicted to fracture prior to a tensile strength of 15.99 MPa.

Figure 4-13 displays the distribution of tensile strengths for particles retained between sieve #10 (2 mm) and #20 (0.84 mm) and by sieve #10 (2 mm), respectively; Table 4-5 lists the σ_{63}, σ_{97}, μ_t, and σ_t for the distributions. The histogram distribution of Figure 4-13a and 4-13b are left skewed with a right tail, implying that the majority of particles will fracture at a lower tensile strength. Figure 4-13a had a σ_{97} of 121.42 MPa, which implied that 97% of particles will fracture



(a)



(b)

Figure 4-13. The tensile strength histograms for red/pink (major and secondary compounds: quartz, potassium feldspar, and plagioclase feldspar) particles retained (a) between sieve #10 (2 mm) and #20 (0.84 mm) and (b) by sieve #10 (2 mm)

Table 4-5. Tensile strength properties for red/pink (major and secondary compounds: quartz, potassium feldspar, and plagioclase feldspar) particles retained between sieve #10 (2 mm) and #20 (0.84 mm) and by sieve #10 (2 mm)

(MPa)	**Retained between sieve #10 (2 mm) and #20 (0.84 mm)**	**Retained by sieve #10 (2 mm)**
$\boldsymbol{\sigma_{63}}$	29.62	11.99 (11.83)
$\boldsymbol{\sigma_{97}}$	121.42	62.51 (43.75)
$\boldsymbol{\mu_t}$	30.51	14.64 (12.86)
$\boldsymbol{\sigma_t}$	28.07	15.33 (10.55)

prior to a tensile strength of 121.42 MPa. Though there are particles with a tensile strength slightly greater than the σ_{97}, those particles are grouped within the same tensile strength bin and are therefore not extraneous outliers. Compared to the predicted σ_{0f} of 33.14 MPa, the σ_{63} of 29.62 MPa, which represented the 37% probability of survival for particles, was smaller, which indicated that the red/pink particles retained between sieve #10 (2 mm) and #20 (0.84 mm) were weaker than predicted. Based on μ_t and σ_t, approximately half of the particles will fracture at a tensile strength less than 30.51 MPa and 68% of the particles will fracture at a tensile strength within the range of 2.44 and 58.58 MPa.

Figure 4-13b had a σ_{97} of 62.15 MPa, implying that 97% of particles will fracture prior to a tensile strength of 62.15 MPa. A σ_{63} of 14.64 MPa indicates that 63% of particles will fracture prior to this tensile strength. Compared to the σ_{0f} of 15.99 MPa, the particles fractured prior to reaching a tensile stress of 14.64 MPa and approximately 68% of particles will fracture at a tensile stress within the range of -0.69 and 289.97 MPa. A particle fracturing at a tensile strength

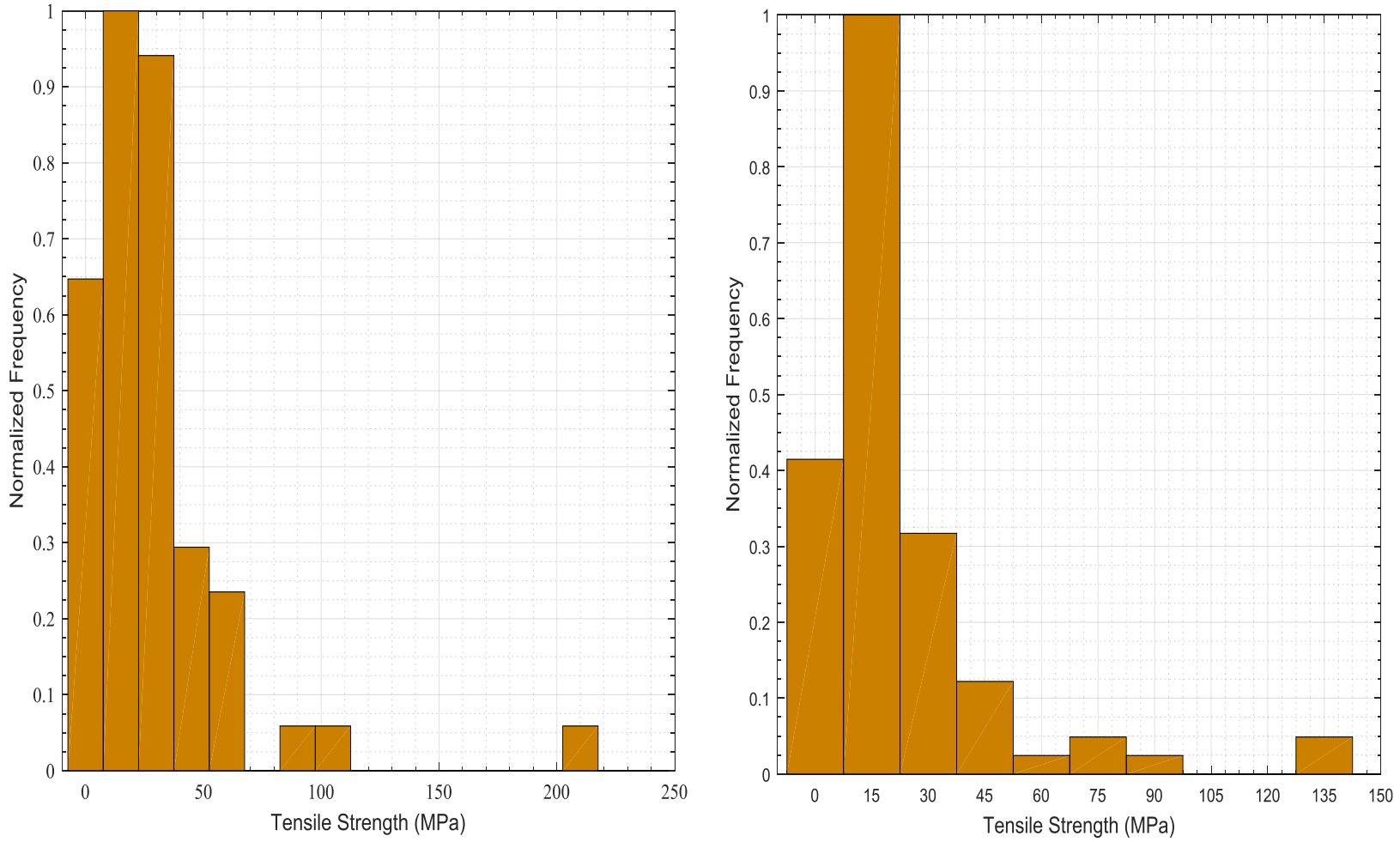
less than zero is impossible; the reason the lower limit of the tensile strength range was below zero was due to the outlying particle with a tensile stress of 84.05 MPa. Based on Table E-1 in Appendix E, the red/pink particle retained by sieve #10 (2 mm) associated with a tensile strength of 84.05 MPa was particle Red/Pink 25-11_J, shown in Figure 4-13b.1 in Appendix I. Figure 4-13b.1 displays the uniaxial compression curve, with load, in N, in the y-axis, and displacement, in mm, in the x-axis. As seen in Figure 4-13b.1, the particle experienced an exponential increase in load until it plateaued at 129N; the particle was unloaded at 130.29N because it sustained the load for double the time compared to other experiments. Based on the post fracture description, the particle sustained minor fractures of meniscal pieces.

Figure 4-13b.2 shows a tensile stress distribution with the exclusion of the outlier; the 97th and 63rd percentile stress, μ, and σ for this distribution was shown in Table 4-5 in parentheses. The tensile stress at which 97% and 63% of particles fractured was 43.57 and 11.83 MPa, respectively. Compared to the σ_{0f} of 15.99 MPa, σ_{63} is slightly smaller; 50% of the particles fractured prior to a tensile strength of 12.86 MPa and the range in which 68% of particles fractured was between 2.31 to 23.41 MPa. A majority of particles within both size categories fractured prior to 15 MPa. Compared to the red/pink particles retained by sieve #10 (2 mm), the particles retained between sieve #10 (2 mm) and #20 (0.84 mm) had a higher mean, standard deviation, 63rd, and 97th percentile, which indicated that the smaller particles were stronger and had a higher probability of fracturing at higher tensile strengths.

The major and secondary compounds of the black/brown particles were identified as quartz, mica (biotite), tridymite, plagioclase feldspar, potassium feldspar, and calcite. Based on the Weibull statistical distribution, the black/brown particles retained between sieve #10 (2 mm) and #20 (0.84 mm) had a characteristic tensile strength of 29.57 MPa while the particles retained

by sieve #10 (2 mm) had a characteristic strength of 22.39 MPa. This indicated that 63% of particles retained between sieve #10 (2 mm) and #20 (0.84 mm) were predicted to fracture prior to a tensile strength of 30.14 MPa and 63% of particles retained by sieve #10 (2 mm) were predicted to fracture prior to a tensile strength of 22.39 MPa. Based on the Weibull model, the black/brown particles retained by sieve #10 (2 mm) were predicted to had the strongest particles within this size category.

Figure 4-14 displays the distribution of tensile strengths for black/brown particles retained between sieve #10 (2 mm) and #20 (0.84 mm) and by sieve #10 (2 mm), respectively. Table 4-6 summarizes the σ_{63}, σ_{97}, μ_t, and σ_t for the distributions. Figures 4-14a and 4-14b display a strongly left skewed distribution with a right tail, which indicated that the majority of particles fractured at lower tensile strengths. A σ_{97} of 103.20 MPa in Figure 4-14a indicated that 97% of particles fractured at a tensile strength lower than 103.20 MPa. Based on this tensile strength, there was one outlier at a tensile stress of 204.97 MPa. From Table B-1 in Appendix B, the particle associated with a tensile strength of 204.97 MPa was Black/Brown 25-21_C, as shown in Figure 4-14a.1 in Appendix I. As shown in Figure 4-14a.1, particle Black/Brown 25-21_C experienced a relatively exponential increase in load until a decrease in load occurred at approximately 107 N, followed by a relatively linear increase in load that reached a plateau at approximately 131 N and fractured. It was possible that the particle fractures at the first peak, but due to difficulty in ability to perceive particle fracture with the current experiment set-up, the particle continued to sustain load until a sudden and drastic decrease in load was observed. Figure 4-14a.2 shows a distribution without the outlier and the σ_{63}, σ_{97}, μ_t, and σ_t for the new distribution is shown in Table 4-6. For the new distribution, 97% of particles fractured prior



(a) (b)

Figure 4-14. The tensile strength histograms for brown/black (major and secondary compounds: quartz, mica (biotite), tridymite, plagioclase feldspar, potassium feldspar, and calcite) particles retained (a) between sieve #10 (2 mm) and #20 (0.84 mm) and (b) by sieve #10 (2 mm)

Table 4-6. Tensile strength properties for black/brown (major and secondary compounds: quartz, mica (biotite), tridymite, plagioclase feldspar, potassium feldspar, and calcite) particles retained between sieve #10 (2 mm) and #20 (0.84 mm) and by sieve #10 (2 mm)

(MPa)	**Retained between sieve #10 (2 mm) and #20 (0.84 mm)**	**Retained by sieve #10 (2 mm)**
$\boldsymbol{\sigma_{63}}$	26.47 (26.25)	17.28 (16.54)
$\boldsymbol{\sigma_{97}}$	103.20 (87.89)	90.87 (73.38)
$\boldsymbol{\mu_t}$	28.66 (25.45)	21.65 (18.71)
$\boldsymbol{\sigma_t}$	31.77 (21.04)	618.73 (16.55)

to a tensile strength of 87.89 MPa; though there are particles with a tensile strength greater than 87.89 MPa, they are not outliers because they are within the same bin or are in a bin next to the bin containing the 97th percentile strength.

Referring to Figure 4-14b, σ_{97} was 90.87 MPa, which implied that 97% of particles fractured prior to tensile strength of 90.87 MPa with a majority of particles fracturing at a lower tensile stress. Based on this 97th percentile, there were two outlying particles, with tensile strengths of 137.43 and 141.62 MP. Based on Table F-1 in Appendix F, the particles associated with tensile strengths of 137.43 and 141.62 MPa, are Black/Brown 25-36_J and Black/Brown 25-33_C, respectively. Particle Black/Brown 25-36_J and Black/Brown 25-33_C are shown in Appendix I as Figures 4-14b.1 and 4-14b.2, respectively. Figure 4-14b.1 displays a relatively linear increase in load until a sudden decrease in load occurred at approximately 33 N, followed by a linear increase in load until a second sudden drop in load occurred at approximately 37 N, followed by a relatively linear increase in load until fracture occurred at 110.82 N. Based on the

Figure 4-14b.1, it was possible that the particle fractured at the first or second peak but the fracture was not visible and therefore particle loading continued until a visible fracture occurred. Figure 4-14b.2 displays a relatively linear increase in load, until approximately 35N where the slope changed and became steeper, compared to the initial slope, signifying that, at the same loading rate, the particle was sustaining the applied load for a longer period of time causing greater displacement. At approximately 40 N, the slope reverted back to the initial load and the particle experienced a linear increase in load until it plateaued and was unloaded at 127.81 N because it sustained the load for approximately 2.5 minutes without fracturing. Once the particle was unloaded and removed, it had fractured into 2 large components, implying that the particle had fractured prior to unloading but the fracture was not apparent and visible. Figure 4-14b.3, in Appendix I, displays the data distribution without the outlier accounted for; Table 4-6 displays the σ_{63}, σ_{97}, μ_t, and σ_t for the new distribution in parentheses.

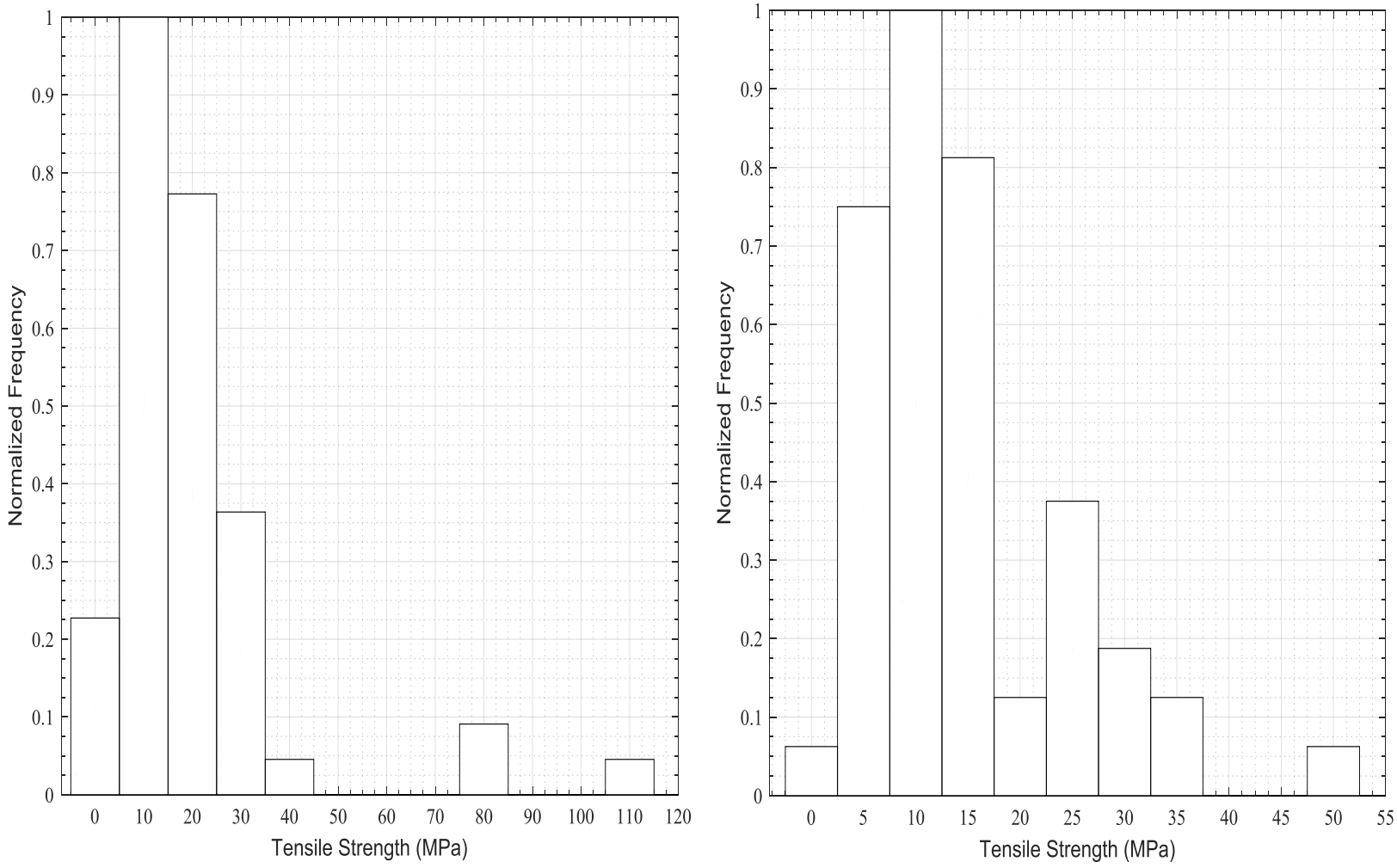
The 63rd percentile tensile strength indicates that 63% of particles will fracture prior to this tensile strength. Compared to the Weibull model predicted σ_{0f} of 29.57 and 22.39 MPa for particles retained between sieve #10 (2 mm) and #20 (0.84 mm) and by sieve #10 (2 mm), σ_{63}, with and without the outliers, are smaller, which indicated that the black/brown particles were weaker than predicted. The new σ_{97} decreased significantly but does not indicate that there were particles with tensile strengths much greater than the new σ_{97}.

The μ_t indicates the tensile strength at which 50% of particles will fracture. Figure 4-14 has a μ_t of 28.66 and 25.45 MPa, respectively. Referring to Figure 4-14, the particles had a 50% probability of fracturing prior to a tensile strength of 21.65 and 18.71 MPa, respectively. Both distributions experienced a decrease in μ_t once the outliers were removed. The tensile strength range where 68% of particles had are likely to fracture can be obtained from $\mu \pm \sigma$. Due to

incorrect σ for the distribution with the outliers, only the distribution without the outliers will be considered. Based on Figure 4-14a.2, 68% of particles were likely to fracture between a tensile strength range of 4.41 to 46.49 MPa; from Figure 4-14b.3, the tensile range in which 68% of particles were likely to fracture was between 2.16 to 35.26 MPa.

Compared to the black/brown particles retained by sieve #10 (2 mm), the particles retained between sieve #10 (2 mm) and #20 (0.84 mm) fractured at higher σ_{63}, σ_{97}, μ_t, and σ_t, with and without the outliers, which indicated that the smaller particles were stronger and had a higher probability of fracturing at higher tensile strengths. Furthermore, σ_{63}, μ_t, and σ_t changed by 0.75 MPa with the inclusion of outliers for particles retained by sieve #10 (2 mm); the 63rd percentile tensile strength did not change significantly for particles retained between sieve #10 (2 mm) and #20 (0.84 mm). This implied that the probability that 37% of particles survived based on σ_{63} was not influenced by outliers for the black/brown particles retained by sieve #10 (2 mm) and between sieve #10 (2 mm) and #20 (0.84 mm).

The major and secondary compounds of the white/tan particles were quartz, plagioclase feldspar, potassium feldspar, and mica (muscovite). Based on the Weibull statistical distribution, the white/tan particles retained between sieve #10 (2 mm) and #20 (0.84 mm) had a characteristic tensile strength of 21.12 MPa while the particles retained by sieve #10 (2 mm) had a characteristic tensile strength of 16.44 MPa. This indicated that 63% of particles retained between sieve #10 (2 mm) and #20 (0.84 mm) were predicted to fracture prior to a tensile stress of 21.12 MPa and 63% of particles retained by sieve #10 (2 mm) were predicted to fracture prior to a tensile strength of 16.44 MPa. Based on the Weibull model, the white/tan particles retained between sieve #10 (2 mm) and #20 (0.84 mm) were predicted be the weakest within this size category. Figure 4-15 displays the distribution of tensile strengths for these particles.



(a) (b)

Figure 4-15. The tensile stress histograms for white/tan (major and secondary compounds: quartz, plagioclase feldspar, potassium feldspar, and mica (muscovite)) particles retained (a) between sieve #10 (2 mm) and #20 (0.84 mm) and (b) by sieve #10 (2 mm).

Table 4-7. Tensile stress properties for white/tan (major and secondary compounds: quartz, plagioclase feldspar, potassium feldspar, and mica (muscovite)) particles retained between sieve #10 (2 mm) and #20 (0.84 mm) and by sieve #10 (2 mm)

(MPa)	**Retained between sieve #10 (2 mm) and #20 (0.84 mm)**	**Retained by sieve #10 (2 mm)**
σ_{63}	16.44 (16.31) [16.16]	18.84 (14.66)
σ_{97}	81.83 (69.91) [31.93]	35.97 (33.76)
μ_t	19.38 (17.82) [15.49]	14.50 (13.86)
σ_t	18.84 (14.89) [8.81]	9.75 (8.59)

Figure 4-15 displays a left skewed distribution with a right tail for white/tan particles retained between sieve #10 (2 mm) and #20 (0.84 mm) and by sieve #10 (2 mm); the σ_{63}, σ_{97}, μ_t, and σ_t for the distributions are listed in Table 4-7, respectively. Figure 4-15a has a 97th percentile tensile strength of 81.83 MPa; this implied that 97% of particles fractured at a tensile strength lower than 81.83 MPa with the particles fracturing predominantly at lower tensile strengths. Based on the 97th percentile, there was one outlier with a tensile stress of 105.43 MPa. From Table C-1 in Appendix C, the particle associated with a tensile stress of 105.43 MPa was particle White/Tan 25-17_J, showed in Figure 4-15a.1 in Appendix I. As depicted in Figure 4-15a.1, the particle experienced a relatively exponential increase in load that became momentarily constant, with a large increase in displacement, at approximately 5 N, followed by a non-uniform increase in load with minimal increase in loads coupled with large increase in displacements at approximately 10 N, followed by a relative linear increase until the particle sustained a small increase in load with a large increase in displacement and fractured at 26.13 N. The particle was

noted to had rotated and sustained asperity fractures at the first peak during loading; therefore, it was possible that the major fracture occurred at the first peak and was mistaken as an asperity fracture due to limitations in the ability to accurate perceive major particle fracture.

Figure 4-15a.2, shown in Appendix I, displays the data distribution with the exclusion of the outlier and Table 4-7 lists the σ_{63}, σ_{97}, μ_t, and σ_t for the new distribution in parentheses. The 97th percentile tensile stress in Figure 4-15a.2 implied that 97% of particles fractured prior to a tensile stress of 69.91 MPa, resulting in 2 outliers with tensile stress of 75.86 and 83.26 MPa. Referring to Table C-1 in Appendix C, the particles associated with a tensile stress of 75.86 and 83.26 MPa were particle White/Tan 25-15_J and particle White/Tan 25-6_C, respectively; Figure 4-15a.3 and 4-15a.4 in Appendix I depicted the uniaxial compression curve for particles White/Tan 25-15_J and White/Tan 25-6_C, respectively. Figure 4-15a.3 illustrates a relatively linear increase in load until approximately 60 N, in which a meniscal increase in load, coupled with large increase in displacements, occurred at approximately 60 N, followed by the linear increase in load until the particle fractured at 75.86 N . Figure 4-15a.4 shows a relatively linear increase in load with a sudden decrease, at approximately 18 N and 38 N, followed by relatively linear increase in loads until the particle plateaued and fractured at a load of 83.26 N. Figure 4-15a.5 in Appendix I displays the data distribution with the exclusion of the three outliers and the σ_{63}, σ_{97}, μ_t, and σ_t for the new distribution is shown in Table 4-6 in brackets. Furthermore, the distribution curve is not as strongly left skewed.

Referring to Figure 4-15b, σ_{97} was 35.97 MPa, connoting that 97% of fractured at a tensile stress lower than 35.97 MPa with the majority of the particles fracturing at a lower tensile. Based on the 97th percentile, there was one outlier with a tensile stress of 49.39 MPa. Table G-1 in Appendix G denotes that the particle associated with a tensile stress of 49.39 MPa

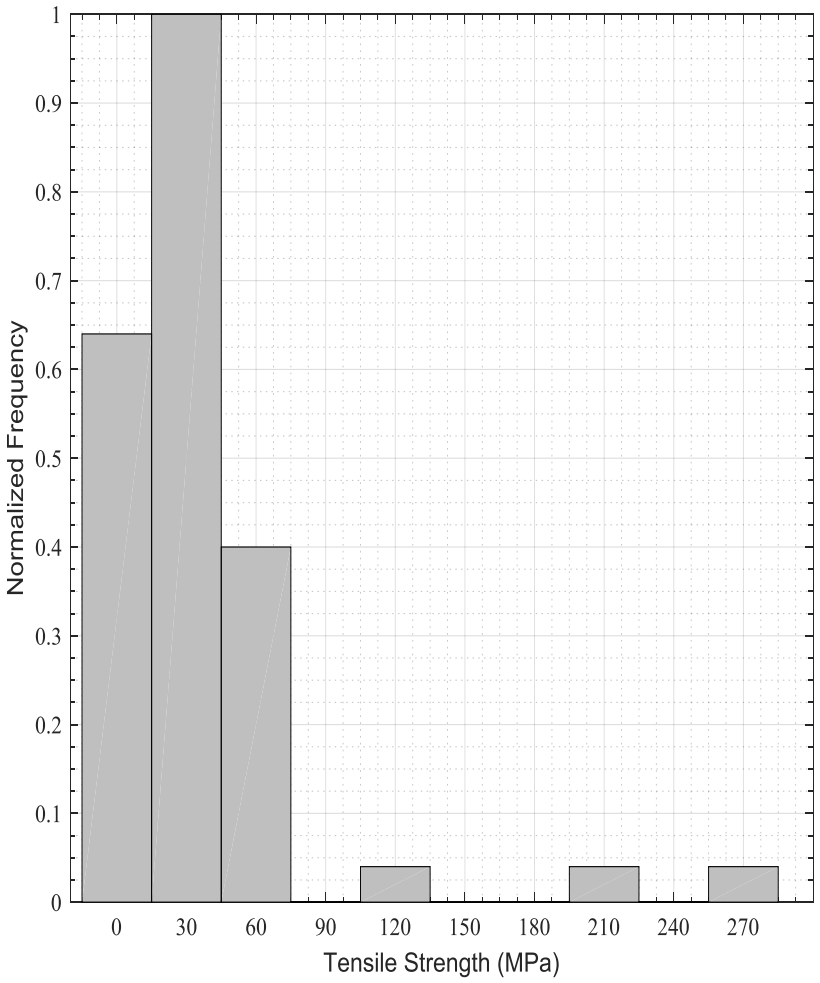
was particle White/Tan 25-3_C, shown in Figure 4-15b.1 in Appendix I. Figure 4-15b.1 displays the uniaxial compression curve; it can be seen that the particle experienced an exponential increase in load until approximately 70 N where the load remained constant with a large change in displacement, followed by a linear increase in load until the particle reached a plateau and fractured at 126.45 N. It was noted that the particle could had possible fractured at 70 N but, due to the inability to determine particle fracture as particle was being loaded without visible fracture, the particle continued to sustain load until a visible fracture occurred. Therefore, it was plausible that the particle fracture occurred at 70 N instead of 126.5 N. Figure 4-15b.2 in Appendix I displays the data distribution without the outlier accounted for and the new σ_{63}, σ_{97}, μ_t, and σ_t for the distribution without the outliers is shown in parentheses in Table 4-7. Based on the new σ_{97}, there were no outliers for the distribution in Figure 4-15b.2.

The 63rd percentile tensile strength indicates that 63% of particles will fracture prior to this tensile stress; compared to the Weibull model σ_{0f} of 21.12 and 16.44 MPa for particles retained between sieve #10 (2 mm) and #20 (0.84 mm) and by sieve #10 (2 mm), respectively, σ_{63} of 16.44, 16.31, 16.16, 18.84, and 14.66 MPa, based on Figures 4-15a, 4-15a.2, 4-15a.5, 4-15b, and 4-15b.2, were smaller, which indicated that the white/tan particles were weaker than predicted. It should be noted that the removal of outliers did not drastically affect the tensile stress of the probability of survival of 37%. The μ_t indicates the tensile stress at which 50% of particles will fracture. As the outliers were removed, the tensile stress at which 50% of particles survived decreased; due to the heterogeneity of Mason sand, the probability of survival for 50% of particles shall include the outliers; therefore, particles retained between sieve #10 (2 mm) and #20 (0.84 mm) and by sieve #10 (2 mm) had a 50% probability of fracturing prior to a tensile strength of 19.38 and 14.50 MPa, respectively. The tensile strength range in which 68% of

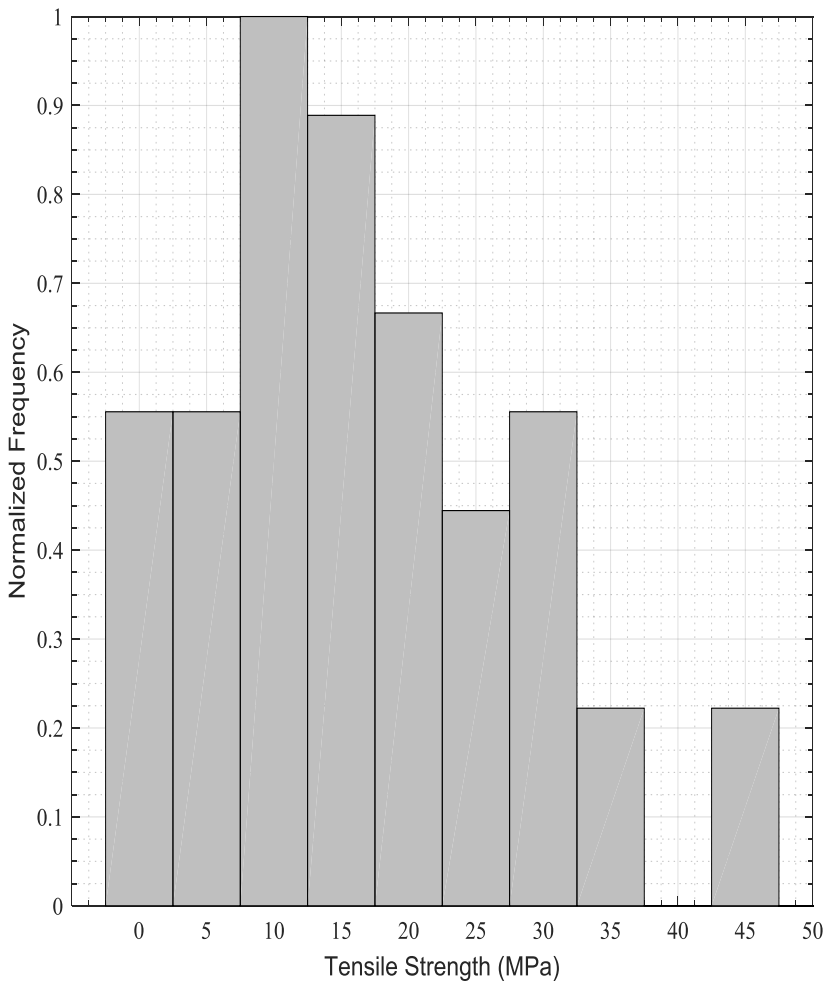
particles are likely to fracture can be obtained from $(\mu \pm \sigma)_t$; the removal of outliers decreased the tensile stress range. Due to the heterogeneity of the Mason sand, the tensile stress range based on the data from Figure 4-15a and 4-15b were preferred. Therefore, 68% of particles were most likely to fracture between a tensile stress range of 0.54 to 38.22 MPa and 4.75 to 24.25 MPa for particles retained between sieve #10 (2 mm) and #20 (0.84 mm) and by sieve #10 (2 mm), respectively.

Compared to the white/tan particles retained by sieve #10 (2 mm), the particles retained between sieve #10 (2 mm) and #20 (0.84 mm) had a higher σ_{63}, σ_{97}, μ_t, and σ_t, with and without the outliers, which indicated that the smaller particles were stronger and had a higher probability of fracturing at higher tensile strengths. Furthermore, σ_{63} did not change significantly, compared to μ_t and σ_t, with the inclusion or exclusion of outliers. This implied that the probability that 37% of particles will survive based on σ_{63} was not influenced by outliers for the white/tan particles.

The clear/translucent particles primarily consisted of quartz and plagioclase feldspar). Based on the Weibull statistical distribution, it as predicted that 63% of particles retained between sieve #10 (2 mm) and #20 (0.84 mm) were predicted to fracture prior to 38.09 MPa while 63% of particles retained by sieve #10 (2 mm) were predicted to fracture prior to 19.24 MPa. Furthermore, the Weibull model predicted that the clear/translucent particles retained between sieve #10 (2 mm) and #20 (0.84 mm) were the strongest within that size category. The tensile stress histograms for the clear/translucent particles retained between sieve #10 (2 mm) and #20 (0.84 mm) and by sieve #10 (2 mm) are shown in Figure 4-16, respectively; the σ_{63}, σ_{97}, μ_t, and σ_t for both distributions are shown in Table 4-8. Figure 4-16a had a strongly left skewed distribution with σ_{97} at 190.85 MPa, which indicated that there was an outlier at 262.11 MPa. From Table 4 in Appendix D, the particle associated



(a)



(b)

Figure 4-16. The tensile stress histograms for clear/translucent (major and secondary compounds: quartz and plagioclase feldspar) particles retained (a) between sieve #10 (2 mm) and #20 (0.84 mm) and (b) by sieve #10 (2 mm).

Table 4-8. Tensile stress properties for clear/translucent (major and secondary compounds: quartz and plagioclase feldspar) particles retained between sieve #10 (2 mm) and #20 (0.84 mm) and by sieve #10 (2 mm)

(MPa)	**Retained between sieve #10 (2 mm) and #20 (0.84 mm)**	**Retained by sieve #10 (2 mm)**
$\boldsymbol{\sigma_{63}}$	32.33 (31.51)	19.23
$\boldsymbol{\sigma_{97}}$	190.85 (119.85)	43.56
$\boldsymbol{\mu_t}$	33.84 (32.59)	16.65
$\boldsymbol{\sigma_t}$	44.90 (32.57)	11.57

with a tensile stress of 262.11 MPa was Clear/Translucent 25-38_J and is shown in Figure 4-16a.1 in Appendix I. Figure 4-16a.1 displays an exponential increase in load until 59N where a sudden drop in load occurred, followed by a relatively linear increase in load, in which the slope became steeper from 85 to 95N due to a gradual increase in load with larger increases in displacement; the particle reached a plateau at approximately 128N where it fractured at 128.03 MPa. It was noted that particle fracture could had occurred at first peak, but due to the difficulty in ability to perceive particle fracture with the current experimental set-up, the particles continued to sustain load until a sudden and drastic decrease in load as observed. Figure 4-16a.2 in Appendix I displays the new distribution without the outlier; the σ_{63}, σ_{97}, μ_t, and σ_t for the new distribution is shown in Table 4-8 in parentheses. Due to the outlier, the σ_t was greater than the μ_t, resulting in a tensile stress range of -11.06 to 78.74 MPa, which is impossible. The σ_{97} of 119.85 MPa for the new distribution connotes that there were no outliers. The σ_{63}, which was the tensile stress at which 63% of particles will fracture, decreased from 32.33 to 31.51 MPa as a

result of the outlier. Compared to the Weibull σ_{0f} of 38.09 MPa, the tensile strength at which 63% of particles fracture, and based on the distribution with and without outliers, was much lower, which indicated that the clear/translucent particles were weaker than predicted. Based on Figure 4-16a and 4-16a.2, 50% of particle fractured at the tensile stress of 33.84 and 32.59 MPa, respectively. The range at which 68% of particle fractured, based on Figure 4-16a.2, as between 0.02 to 65.16 MPa.

Figure 4-16b had a σ_{97} of 43.56 MPa, which implied that 97% of particles fractured prior to a tensile strength of 43.56 MPa and that there were no outliers present. The 63rd percentile stress indicated that 63% of particles fractured prior to a tensile strength of 19.23 MPa, which was very similar to the Weibull σ_{0f} of 19.24 MPa, which indicated that strength of the particle was as predicted by the Weibull model. A μ of 16.65 MPa implied that 50% of particles fractured at this tensile stress and, based on the σ, the tensile stress range in which 68% of particles fractured was between 5.08 to 28.22 MPa.

Referring to Figure 4-16, the clear/translucent particles retained between sieve #10 (2 mm) and #20 (0.84 mm) were more likely to sustain higher tensile strengths compared to particles retained by sieve #10 (2 mm). Furthermore, the characteristic tensile stress for the particles retained between sieve #10 (2 mm) and #20 (0.84 mm) were not affected by outliers and were expected to be weaker than predicted. Contrastingly, for the particles retained by sieve #10 (2 mm), the characteristic tensile stress and 63rd percentile tensile stress were the same values, which indicated the Weibull model correctly predicted the tensile stress at which 63% of particles will fracture.

In summary, the Weibull model characteristic tensile stress was generally higher compared to the 63rd percentile tensile stress obtained from the particle distribution, as shown in Table 4-9, and

was generally not greatly affected by outliers. Therefore, the Weibull model was a good indicator of the tensile stress of sand particles based on mineralogy and size but the characteristic tensile stress value obtained will be greater than the actual value at which 63% of particles fracture. The 63rd and 97th percentile and μ for particles retained between sieve #10 (2 mm) and #20 (0.84 mm) were generally higher compared to particles retained by sieve #10 (2 mm) and #20 (0.84 mm) in all four subgroups but varied within subgroups. This indicated that the smaller particles were stronger, agreeing with results from other researchers, and that within the size category, strength varies between the subgroups due to varying mineralogy. Although the μ was affected by the outliers and would change, the subgroup with the largest and lowest μ stayed consistent. For the particles retained between sieve #10 (2 mm) and #20 (0.84 mm), the clear/translucent particles had the highest μ while the white/tan particles had the lowest μ, which indicated that the clear/translucent particles were stronger while the white/tan particles were weaker. For the particles retained by sieve #10 (2 mm), the black/brown particles had the highest μ while the white/tan particles had the lowest μ, which indicated that the brown/black particles were stronger while the white/tan particles were weaker. The tensile stress range in which 68% of particles fractured was larger for the particles retained between sieve #10 (2 mm) and #20 (0.84 mm) but varied between subgroups. For particles retained between sieve #10 (2 mm) and #20 (0.84 mm), the tensile stress range for the red/pink, black/brown, white/tan, and clear/translucent were 56.14, 45.08, 37.68, and 65.14, MPa, respectively. The clear/translucent particles had the largest range while the white/tan particles had the smallest range, which indicated that the strength of the clear/translucent particles varies more while the white/tan particles had less variation in strength. For particles retained by sieve #10 (2 mm), the tensile stress range for the red/pink, black/brown, white/tan, and clear/translucent were 23.14, 33.10, 19.5/17.18, and 23.14 MPa,

Table 4-9. Calculated and estimated characteristic tensile strength particles retained between sieve #10 (2 mm) and #20 (0.84 mm) and by sieve #10 (2 mm) in all subgroups

Colored Subgroups	**Retained between sieve #10 (2 mm) and #20 (0.84 mm)**		**Retained by sieve #10 (2 mm)**	
	Histogram σ_{63} *(MPa)*	*Weibull* σ_{63} *(MPa)*	*Histogram* σ_{63} *(MPa)*	*Weibull* σ_{63} *(MPa)*
Red/Pink *(major and secondary compounds: quartz, potassium feldspar, and plagioclase feldspar)*	29.62	33.14	11.99 (11.83)	15.99
Black/Brown *(major and secondary compounds: quartz, mica (biotite), tridymite, plagioclase feldspar, potassium feldspar, and calcite)*	26.47 (26.25)	30.43	17.28 (16.54)	22.39
White/Tan *(major and secondary compounds: quartz, plagioclase feldspar, potassium feldspar, and mica (muscovite))*	16.44 (16.31) [16.16]	21.12	18.84 (14.66)	16.44

Table 4-9 Continued

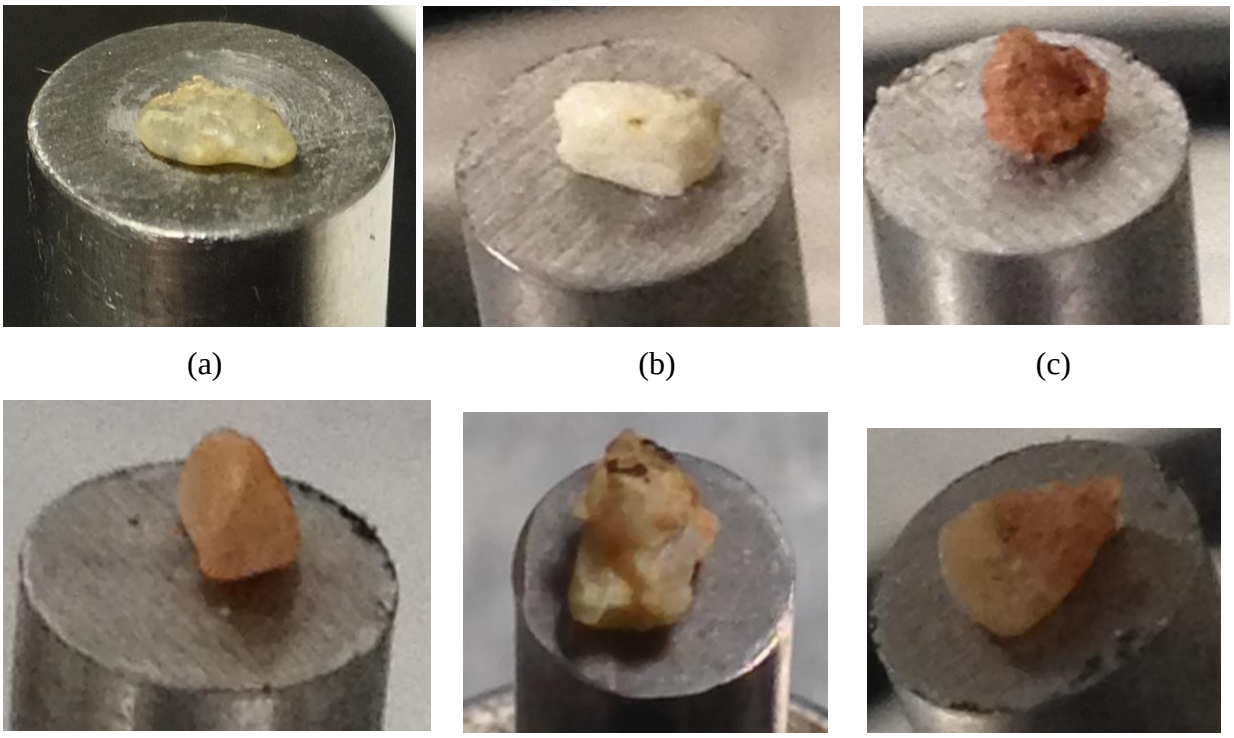
Colored Subgroups	**Retained between sieve #10 (2 mm) and #20 (0.84 mm)**		**Retained by sieve #10 (2 mm)**	
	Histogram σ_{63} *(MPa)*	*Weibull* σ_{63} *(MPa)*	*Histogram* σ_{63} *(MPa)*	*Weibull* σ_{63} *(MPa)*
Clear/Translucent *(major and secondary compounds: quartz and plagioclase feldspar)*	32.33 (31.51)	38.09	19.23	19.24

respectively. The black/brown particles had the largest range while the white/tan particles had the smallest range, which indicated that the black/brown particles had a higher variation in strength and the white/tan particles fractured at lower variation in strength compared to other subgroups.

Overall, the clear/translucent (major and secondary compounds: quartz and plagioclase feldspar) particles were stronger in particles retained between sieve #10 (2 mm) and #20 (0.84 mm) and the black/brown (major and secondary compounds: quartz, mica (biotite), tridymite, plagioclase feldspar, potassium feldspar, and calcite) particles were stronger in particles retained by sieve #10 (2 mm). The white/tan (major and secondary compounds: quartz, plagioclase feldspar, potassium feldspar, and mica (muscovite)) particles were weaker in both size categories.

4.2.2.3 Effects of Particle Shape

The shape of the particles, based on visual inspection, can be classified into five categories: (1) platy, (2) rectangular prismatic, (3), spherical, (4) triangular prismatic, or (5) other. A platy-shaped particle was classified as a particle with very thin to no edges and had 2-3 faces, as depicted in Figure 4-17a. A particle with a minimum of 8 edges and 6 faces was classified as a rectangular prismatic, as depicted in Figure 4-17b. A particle was considered spherical if it was rounded with 1 face, as shown in Figure 4-17c. A particle that had a minimum of 2 faces, each with 3 edges, was classified as triangular prismatic, as illustrated in Figure 4-17d. Particles classified as other were particles with descriptions that did not fit within or was a mix of two of the four previous mentioned shape categories. These descriptions included: curvy, rounded, seed-shaped, cylindrical prism, or no shape mentioned. Figure 4-17e and 4-17f depicts an irregular shaped particle and a triangular prismatic shaped with a rounded edge, respectively.



(a) (b) (c)

(d) (e) (f)

Figure 4-17. Classification based on visual inspection for (a) platy shaped, (b) rectangular prismatic shaped, (c) spherical shaped, (d) triangular prismatic shaped, and (e) (f) other shaped particles.

The effects of particle shape on tensile strength were examined based on particles retained between sieve #10 (2 mm) and #20 (0.84 mm) and by sieve #10 (2 mm), particle d_L, and mineralogy. Platy, rectangular prismatic, spherical, triangular prismatic, and other shaped particles were represented as circles, right-sided triangles, left-sided triangles, diamonds, and triangles, respectively. Red/pink (major and secondary compounds: quartz, potassium feldspar, and plagioclase feldspar), black/brown (major and secondary compounds: quartz, mica (biotite), tridymite, plagioclase feldspar, potassium feldspar, and calcite), white/tan (major and secondary compounds: quartz, plagioclase feldspar, potassium feldspar, and mica (muscovite)) and clear/translucent (major and secondary compounds: quartz and plagioclase feldspar) particles were denoted as red, blue, green, and black data points, respectively. It was predicted that spherical shaped particles will fracture at lower tensile strengths (Cavaretta et al 2010; Todisco et al 2016).

Figure 4-18a and 4-19a show the distribution of platy shaped particles retained between sieve #10 (2 mm) and #20 (0.84 mm) and by sieve #10 (2 mm), respectively. Table 4-10 compiles the frequency, d_L, and tensile strengths for both distributions subdivided into colored subgroups; values that changed due to outliers are denoted within parenthesis. The distributions for Figure 4-18a and 4-19a were left skewed with an average tensile strength of 34.50 and 23.17 MPa, respectively, and an average d_L of 1.86 and 1.02 mm, respectively. From Figure 4-18a, the distribution had 2 outliers at a tensile strength of 204.97 and 262.11 MPa, which were particles Black/Brown 25-21_C and Clear 25-38_J, respectively, shown in Figure 4-14a.1 and 4-16a.1, respectively, in Appendix I. Referring to Figure 4-19a, the red/pink, white/tan, and clear/translucent particles had a negative correlation between d_L and tensile strength while the black/brown particles had no correlation between d_L and tensile strength. From Figure 4-18a, the

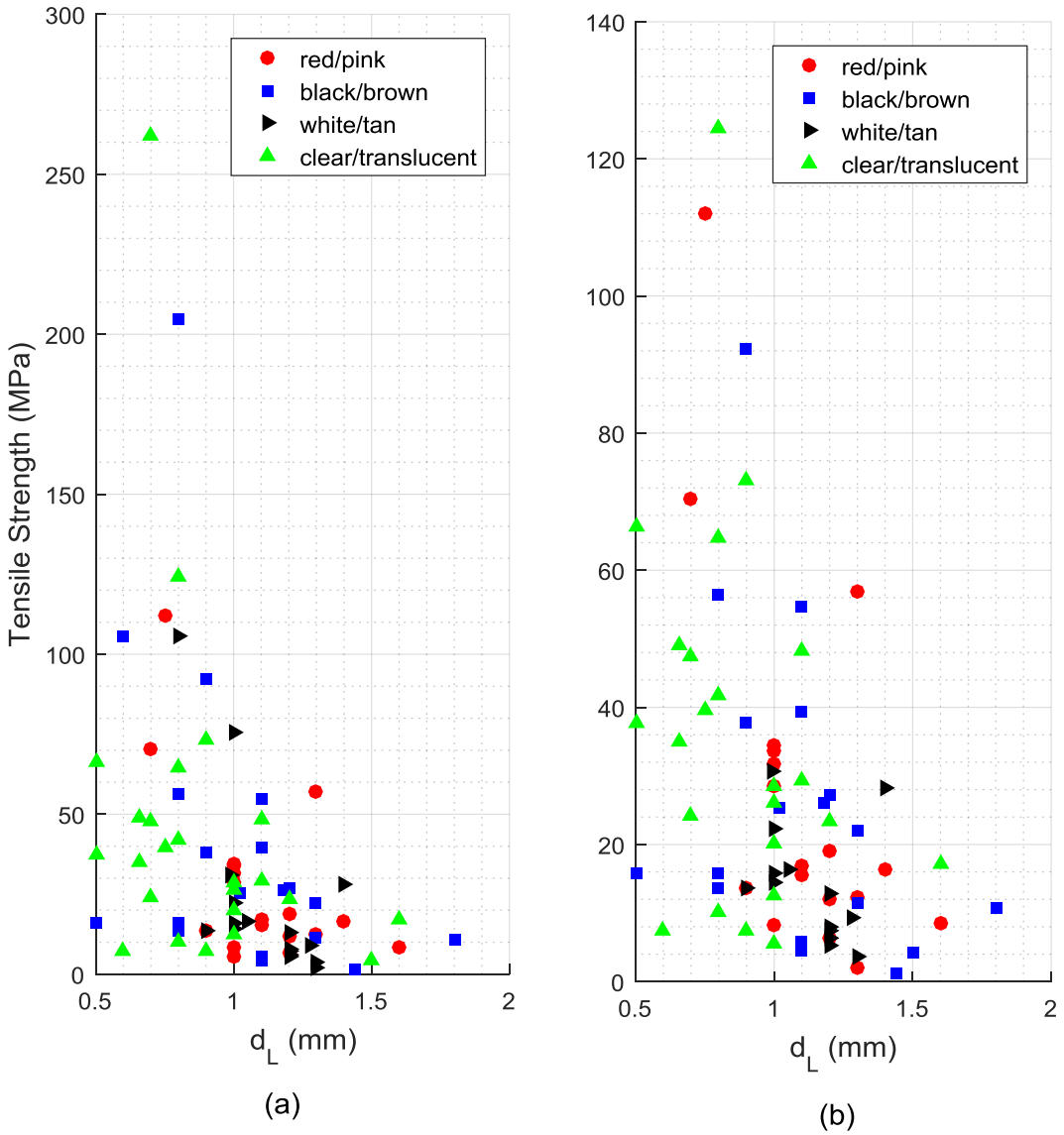


Figure 4-18. Platy shaped red/pink (major and secondary compounds: quartz, potassium feldspar, and plagioclase feldspar), black/brown (major and secondary compounds: quartz, mica (biotite), tridymite, plagioclase feldspar, potassium feldspar, and calcite), white/tan (major and secondary compounds: quartz, plagioclase feldspar, potassium feldspar, and mica (muscovite)) and clear/translucent (major and secondary compounds: quartz and plagioclase feldspar) particles retained between sieve #10 (2 mm) and #20 (0.84 mm) (a) with outliers (b) without outliers.

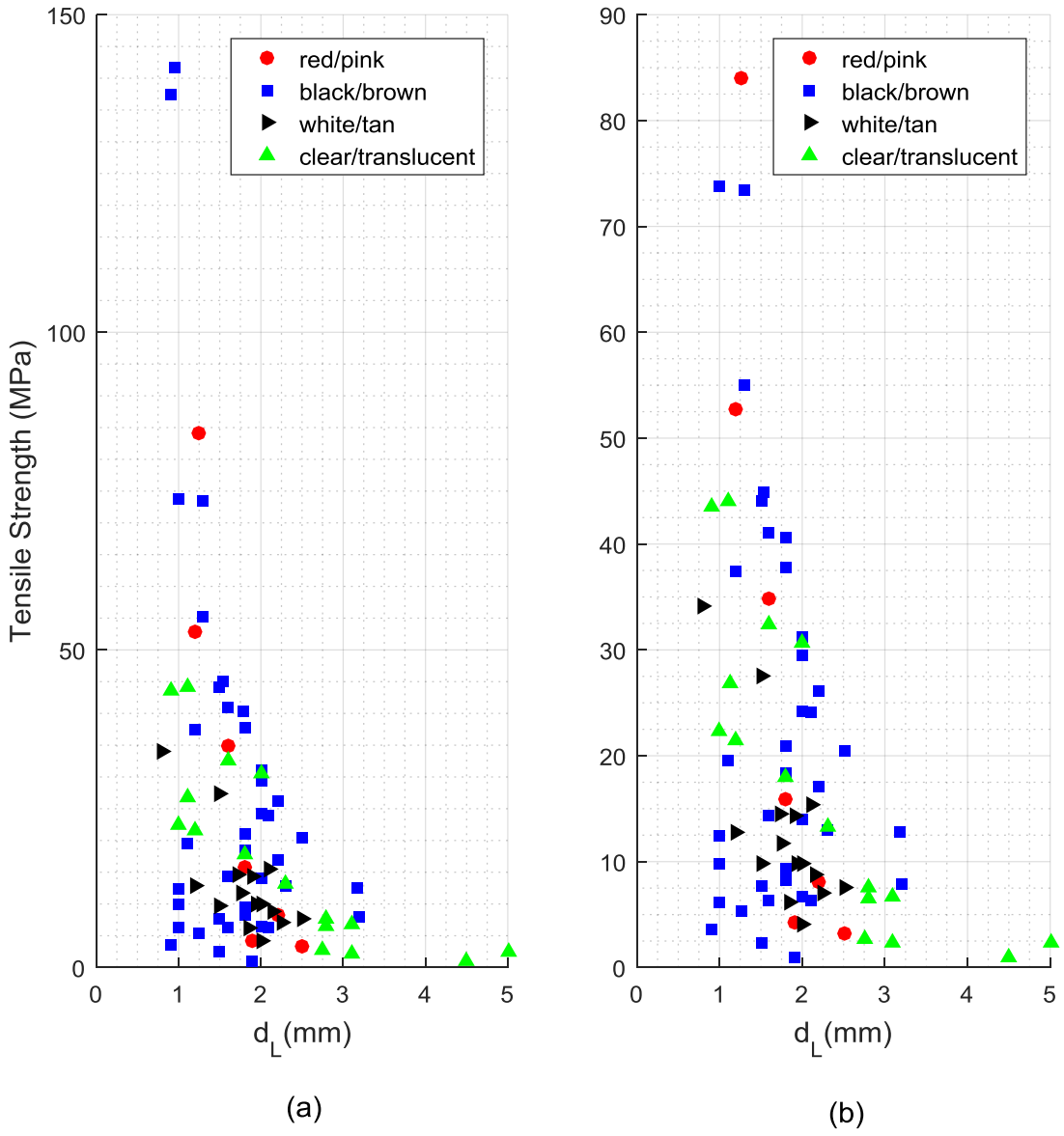


Figure 4-19. Platy shaped red/pink (major and secondary compounds: quartz, potassium feldspar, and plagioclase feldspar), black/brown (major and secondary compounds: quartz, mica (biotite), tridymite, plagioclase feldspar, potassium feldspar, and calcite), white/tan (major and secondary compounds: quartz, plagioclase feldspar, potassium feldspar, and mica (muscovite)) and clear/translucent (major and secondary compounds: quartz and plagioclase feldspar) particles retained by sieve #10 (2 mm) (a) with outliers (b) without outliers.

distribution had 2 outliers at a tensile strength of 204.97 and 262.11 MPa, which were particles Black/Brown 25-21_C and Clear 25-38_J, respectively, shown in Figure 4-14a.1 and 4-16a.1, respectively, in Appendix I. Referring to Figure 4-19a, the red/pink, white/tan, and clear/translucent particles had a negative correlation between d_L and tensile strength while the black/brown particles had no correlation between d_L and tensile strength. Two outlying particles with relatively high tensile strengths were present; one was particle Black/Brown 25-36_J with a tensile strength of 137.43 MPa, shown in Figure 4-14b.1 in Appendix I, and the other was particle Black/Brown 25-33_C with a tensile strength of 141.62 MPa, shown in Figure 4-14b.2 in Appendix I. Figures 4-18b and 4-19b display the left skewed distribution for particles retained between sieve #10 (2 mm) and #20 (0.84 mm) and by sieve #10 (2 mm), respectively, with the exclusion of the outliers; the d_L increased and the tensile strength decreased for both distributions. Regardless of the outliers, the particles that had larger d_L fractured at lower tensile strengths and the particles that had smaller d_L fractures at higher tensile strengths.

Table 4-10 compiles the number of particles, average d_L, and average tensile strengths for particles retained between sieve #10 (2 mm) and #20 (0.84 mm) and by sieve #10 (2 mm) subdivided into colored subgroups; values that changed due to the outliers are denoted within parentheses. For particles retained between sieve #10 (2 mm) and #20 (0.84 mm), the clear/translucent particles had smaller d_L and fractured at higher tensile strengths, with or without the inclusion of the outlier, while the white/tan particles had larger d_L and fractured at lower tensile strengths. There were more platy shaped black/brown and clear/translucent particles than platy shaped red/pink and white/tan particles. For particles retained by sieve #10 (2 mm), the black/brown particles, with and without the inclusion of the outliers, had smaller d_L while the clear/translucent particles had larger d_L, on average. The clear/translucent particles

Table 4-10. Number of particles, average d_L, and average tensile strengths for platy shaped particles retained between sieve #10 (2 mm) and #20 (0.84 mm) and by sieve #10 (2 mm) subdivided into colored subgroups.

Colored Subgroup	**Retained between sieve #10 (2 mm) and #20 (0.84 mm)**			**Retained by sieve #10 (2 mm)**		
	Number of Particles	**Average d_L (mm)**	**Average Tensile Strength (MPa)**	**Number of Particles**	**Average d_L (mm)**	**Average Tensile Strength (MPa)**
Red/Pink *(major and secondary compounds: quartz, potassium feldspar, and plagioclase feldspar)*	18	1.10	27.88	7 (6)	1.78 (1.86)	29.02 (19.84)
Black/Brown *(major and secondary compounds: quartz, mica (biotite), tridymite, plagioclase feldspar, potassium feldspar, and calcite)*	24 (20)	1.04 (1.10)	37.16 (23.70)	39 (37)	1.70 (1.74)	28.34 (22.33)

Table 4-10 Continued

Colored Subgroup	Retained between sieve #10 (2 mm) and #20 (0.84 mm)			Retained by sieve #10 (2 mm)		
	Number of Particles	**Average d_L (mm)**	**Average Tensile Strength (MPa)**	**Number of Particles**	**Average d_L (mm)**	**Average Tensile Strength (MPa)**
White/Tan *(major and secondary compounds: quartz, plagioclase feldspar, potassium feldspar, and mica (muscovite))*	17 (14)	1.12 (1.14)	22.20 (13.86)	15	1.81	12.91
Clear/Translucent *(major and secondary compounds: quartz and plagioclase feldspar)*	24 (23)	0.89 (0.87)	51.49 (36.50)	16	2.32	17.61

retained between sieve #10 (2 mm) and #20 (0.84 mm) and the red/pink particles retained by sieve #10 (2 mm) fractured at higher tensile strengths while the white/tan particles fractured at lower tensile strengths, on average. Thirty-nine platy shaped particles were black/brown particles while there only seven platy shaped were red/pink particles.

Figures 4-20 and 4-21 depict the average d_L and tensile strength within one standard deviation, without the inclusion of outliers, for platy shaped particles retained between sieve #10 (2 mm) and #20 (0.84 mm) and by sieve #10 (2 mm), respectively. The circle data points, square data points, right sided triangle data points, and triangle data points represent the red/pink (major and secondary compounds: quartz, potassium feldspar, and plagioclase feldspar), black/brown (major and secondary compounds: quartz, mica (biotite), tridymite, plagioclase feldspar, potassium feldspar, and calcite), white/tan (major and secondary compounds: quartz, plagioclase feldspar, potassium feldspar, and mica (muscovite)) and clear/translucent (major and secondary compounds: quartz and plagioclase feldspar) particles; the unfilled data points represent the particles retained between sieve #10 (2 mm) and #20 (0.84 mm) and the filled data points represent the particles retained by sieve #10 (2mm).

As depicted in Figure 4-20, the d_L range for the platy shaped particles retained by sieve #10 (2 mm) was larger compared to particles retained between sieve #10 (2 mm) and #20 (0.84 mm). The d_L range of the platy shaped white/tan particles in both size categories was relatively small, which indicated little variation in d_L. The d_L range of the platy shaped black/brown particles retained by sieve #10 (2 mm) was relatively large compared to the smaller d_L range of the particles retained between sieve #10 (2 mm) and #20 (0.84 mm). The platy shaped white/tan particle retained by sieve #10 (2 mm) had the lowest average tensile strength while the platy clear/translucent particle retained between sieve #10 (2 mm) and #20 (0.84 mm) had the highest

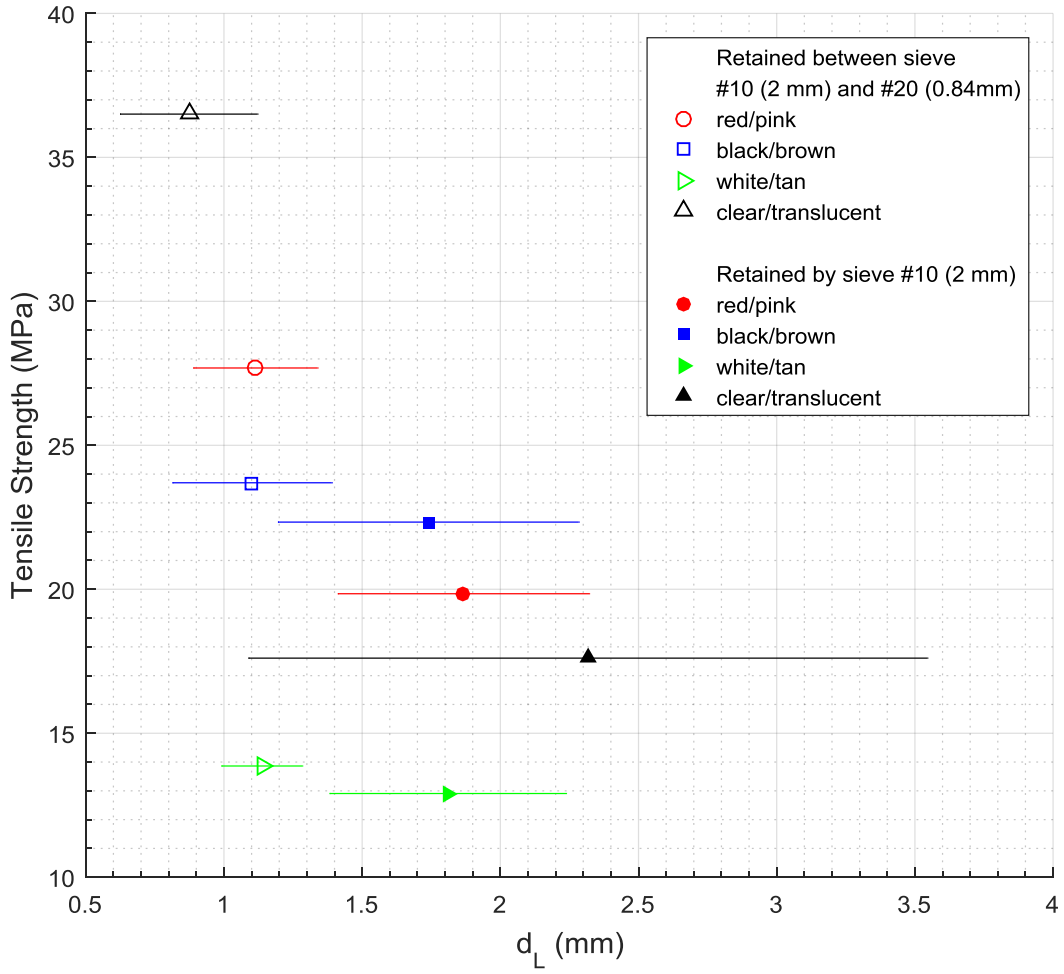


Figure 4-20. Average d_L within one standard deviation, without outliers, for platy shaped red/pink (major and secondary compounds: quartz, potassium feldspar, and plagioclase feldspar), black/brown (major and secondary compounds: quartz, mica (biotite), tridymite, plagioclase feldspar, potassium feldspar, and calcite), white/tan (major and secondary compounds: quartz, plagioclase feldspar, potassium feldspar, and mica (muscovite)) and clear/translucent (major and secondary compounds: quartz and plagioclase feldspar) particles retained between sieve #10 (2 mm) and #20 (0.84 mm) and by sieve #10 (2 mm)

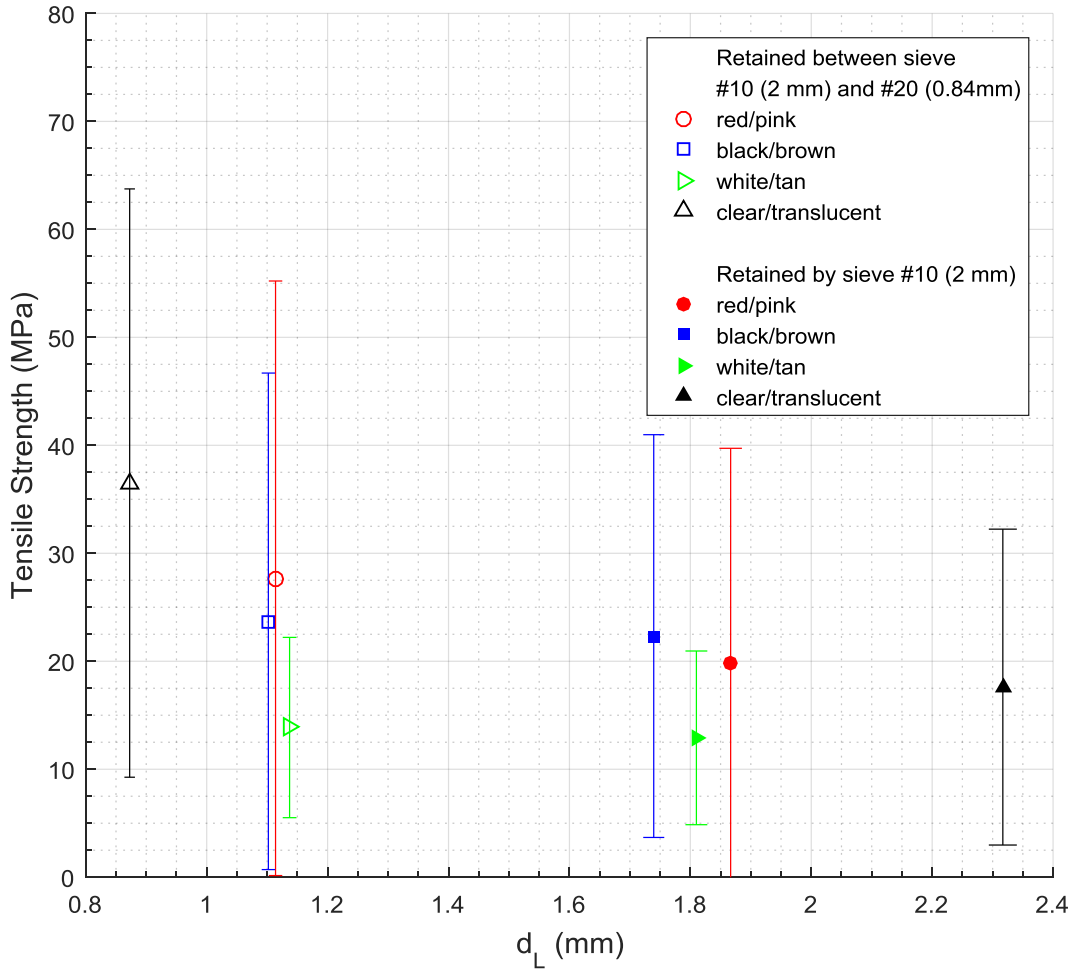


Figure 4-21. Average tensile strength within one standard deviation, without outliers, for platy shaped red/pink (major and secondary compounds: quartz, potassium feldspar, and plagioclase feldspar), black/brown (major and secondary compounds: quartz, mica (biotite), tridymite, plagioclase feldspar, potassium feldspar, and calcite), white/tan (major and secondary compounds: quartz, plagioclase feldspar, potassium feldspar, and mica (muscovite)) and clear/translucent (major and secondary compounds: quartz and plagioclase feldspar) particles retained between sieve #10 (2 mm) and #20 (0.84 mm) and by sieve #10 (2 mm)

average tensile strength.

As shown in Figure 4-21, platy shaped particles retained between sieve #10 (2 mm) and #20 (0.84 mm) had relatively similar tensile strength ranges while the tensile strengths ranges of the platy shaped particles retained by sieve #10 (2 mm) varied greatly. The platy shaped red/pink particles had the largest tensile strength range while the platy shaped white tan particles had the smallest tensile strength range. Particles retained by sieve #10 (2 mm) had larger average d_L compared to particles retained between sieve #10 (2 mm) and #20 (0.84 mm). The platy shaped black/brown particles retained by sieve #10 (2 mm) had the largest average d_L while particles retained between sieve #10 (2 mm) and #20 (0.84 mm) had the smallest average d_L. The platy shaped red/pink, clear/translucent, and white/tan particles retained by sieve #10 (2 mm) had larger average d_L while particles retained between sieve #10 (2 mm) and #20 (0.84 mm) had the smaller average d_L.

Figures 4-22a and 4-23a displays the distributions for the rectangular prismatic shaped particles retained between sieve #10 (2 mm) and #20 (0.84 mm) and by sieve #10 (2 mm), respectively. Figures 4-22a and 4-23a had a left skewed distribution with a negative correlation between tensile strength and d_L in which particles that had smaller d_L generally fractured at higher tensile strengths while particles that had larger d_L fractured at lower tensile strengths. The majority of particle in Figure 4-22a fractured at a tensile strength less than 40 MPa; the average tensile strength was 29.77 MPa and average d_L was 1.21 mm; Figure 4-23a had an average $d_{L\ of}$ 2.32 mm and an average tensile strength of 13.95 MPa.

Referring to the distribution in Figure 4-22a, there were 3 outliers with tensile strengths of 126.07, 127.73, and 199.90 MPa. From Table A-1 in Appendix A, the particles associated with the tensile strength of 126.07 and 127.73 MPa were particles Red/Pink 25-22_C and

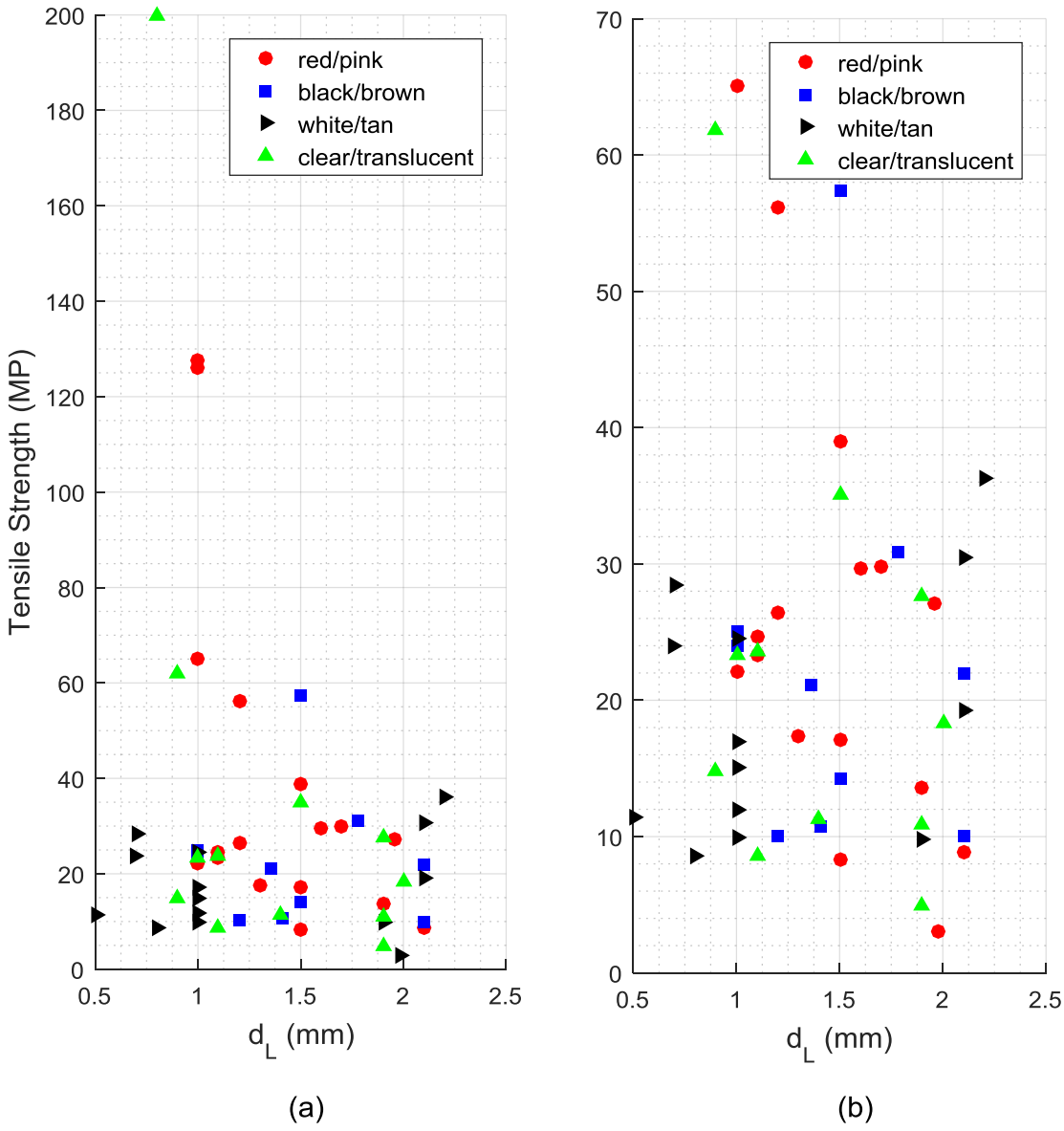


Figure 4-22. Rectangular prismatic shaped particles red/pink (major and secondary compounds: quartz, potassium feldspar, and plagioclase feldspar), black/brown (major and secondary compounds: quartz, mica (biotite), tridymite, plagioclase feldspar, potassium feldspar, and calcite), white/tan (major and secondary compounds: quartz, plagioclase feldspar, potassium feldspar, and mica (muscovite)) and clear/translucent (major and secondary compounds: quartz and plagioclase feldspar) retained between sieve #10 (2 mm) and #20 (0.84 mm) (a) with outliers (b) without outliers.

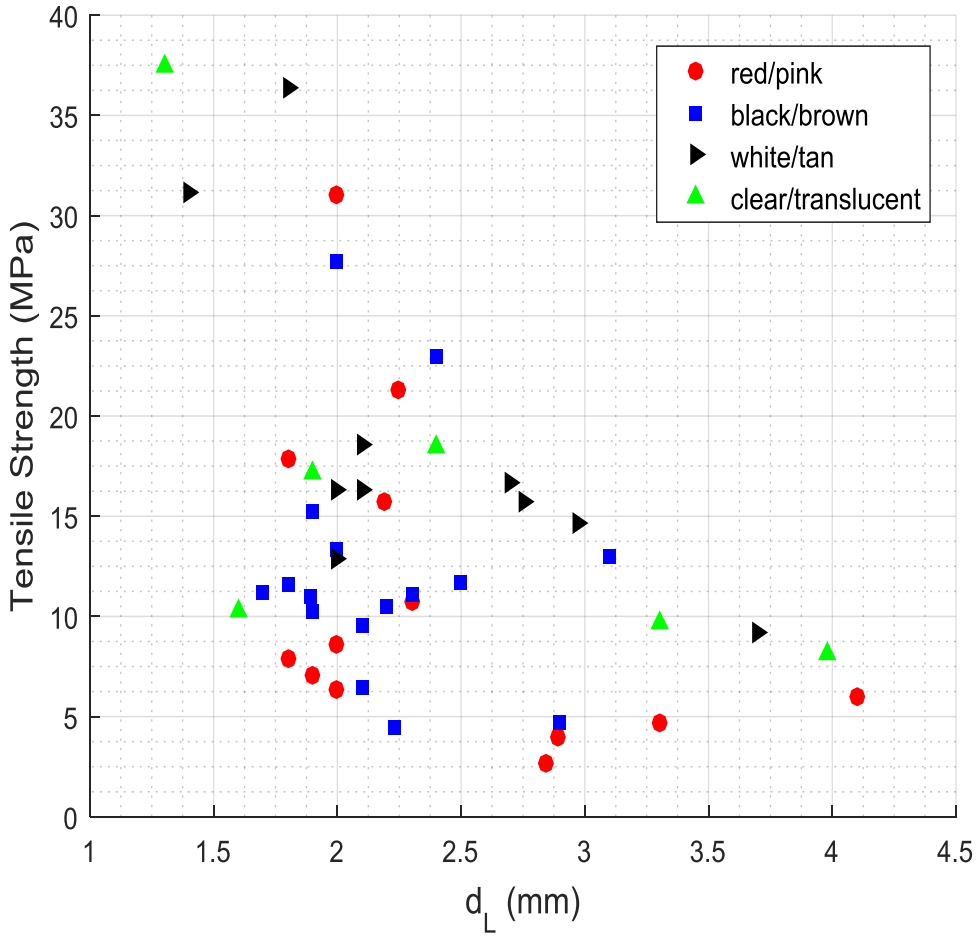


Figure 4-23. Rectangular prismatic shaped red/pink (major and secondary compounds: quartz, potassium feldspar, and plagioclase feldspar), black/brown (major and secondary compounds: quartz, mica (biotite), tridymite, plagioclase feldspar, potassium feldspar, and calcite), white/tan (major and secondary compounds: quartz, plagioclase feldspar, potassium feldspar, and mica (muscovite)) and clear/translucent (major and secondary compounds: quartz and plagioclase feldspar) particles retained by sieve #10 (2 mm).

Red/Pink 25-2_J, respectively; from Table 4 in Appendix D, the particle associated with the tensile strength of 199.90 MPa was Clear 25-42_J. Figures 4-22a.1 through 4-22a.3, in Appendix I, displays the curves generated from the uniaxial compression experiments for particles Red/Pink 25-22_C, Red/Pink 25-2_J, and Clear 25-42_J, respectively. Figure 4-22a.1 displays an exponential increase in load, with a constant load at approximately 113 N, until the particle plateaued and a visible fracture occurred. Though the graph does not display sudden drops that can imply particle fracturing occurred, cracking sounds were constantly heard as the particle sustained load, which can denote micro-fracturing occurring internally. Figure 4-22a.2 shows an exponential increase in load until approximately 20 MPa where a sudden decrease in load occurred, followed by a relatively linear increase in load until the particle plateaued and fractured. The sudden decrease in load was at the first peak could had been fracture, but due to load until a sudden and drastic decrease in load was observed at 127.47 N. Figure 4-22a.3 shows a relatively linear increase in load until approximately 43 N where a sudden decrease in load occurred, followed by a linear increase in load until the particle plateaued and fractured. It was recorded that the first peak was of an asperity fracture, but it could be possible that the particle experienced a major fracture that was not visible. Due to the difficulty in being able to perceive particle fracture with the current experimental set-up, the particle was assumed to have sustained an asperity fracture and therefore loading continued; therefore, the particle continued to sustain load until a visible fracture occurred. Figure 4-22b displays the rectangular prismatic shaped particles with the outliers excluded; the distribution was less left skewed with the average d_L increasing to 1.40 mm and average tensile strength decreasing to 22.48 MPa. Forty-six particles fractured prior to a tensile strength of 40 MPa but the correlation between tensile strength and d_L becomes almost non-existent.

Table 4-11 compiles the number of particles, average d_L, and average tensile strengths for the distributions for Figure 4-22a, 4-22b, and 4-23 based on colored subgroups; values that changed due to the outliers are denoted within parentheses. The black/brown particles retained between sieve #10 (2 mm) and #20 (0.84 mm) had larger d_L while black/ brown particles retained by sieve #10 (2 mm) had smaller d_L. The white/tan particles had smaller d_L; the clear/translucent and red/pink particles retained by sieve #10 (2 mm) had larger d_L. For particles retained between sieve #10 (2 mm) and #20 (0.84 mm), the red/pink particles fractured at higher tensile strengths, regardless of outliers, while the white/tan particles fractured at lower tensile strengths; the trend is reversed for particles retained by sieve #10 (2 mm). The majority of rectangular prismatic shaped particles are red/pink and white/tan particles retained between sieves #10 (2 mm) and #20 (0.84 mm) and black/brown particles retained by sieve #10 (2 mm); clear/translucent particles within both size categories had the least rectangular prismatic shaped particles.

Figures 4-24 and 4-25 depict the average d_L and tensile strength within one standard deviation, without the inclusion of outliers, for rectangular prismatic shaped particles retained between sieve #10 (2 mm) and #20 (0.84 mm) and by sieve #10 (2 mm), respectively. The circle data points, square data points, right sided triangle data points, and triangle data points represent the red/pink (major and secondary compounds: quartz, potassium feldspar, and plagioclase feldspar), black/brown (major and secondary compounds: quartz, mica (biotite), tridymite, plagioclase feldspar, potassium feldspar, and calcite), white/tan (major and secondary compounds: quartz, plagioclase feldspar, potassium feldspar, and mica (muscovite)) and clear/translucent (major and secondary compounds: quartz and plagioclase feldspar) particles;

Table 4-11. Number of particles, average d_L, and average tensile strengths for rectangular prismatic shaped particles retained between sieve #10 (2 mm) and #20 (0.84 mm) and by sieve #10 (2 mm) subdivided into colored subgroups.

Colored Subgroups	**Retained between sieve #10 (2 mm) and #20 (0.84 mm)**			**Retained by sieve #10 (2 mm)**		
	Number of Particles	**Average d_L (mm)**	**Average Tensile Strength (MPa)**	**Number of Particles**	**Average d_L (mm)**	**Average Tensile Strength (MPa)**
Red/Pink *(major and secondary compounds: quartz, potassium feldspar, and plagioclase feldspar)*	17 (15)	1.39 (1.44)	38.96 (27.38)	13	2.41	11.07
Black/Brown *(major and secondary compounds: quartz, mica (biotite), tridymite, plagioclase feldspar, potassium feldspar, and calcite)*	10	1.49	22.55	16	2.19	12.19

Table 4-11 Continued

Colored Subgroups	Retained between sieve #10 (2 mm) and #20 (0.84 mm)			Retained by sieve #10 (2 mm)		
	Number of Particles	**Average d_L (mm)**	**Average Tensile Strength (MPa)**	**Number of Particles**	**Average d_L (mm)**	**Average Tensile Strength (MPa)**
White/Tan *(major and secondary compounds: quartz, plagioclase feldspar, potassium feldspar, and mica (muscovite))*	14	1.28	17.82	10	2.36	18.79
Clear/Translucent *(major and secondary compounds: quartz and plagioclase feldspar)*	12 (11)	1.37 (1.42)	36.68 (21.84)	6	2.41	16.87

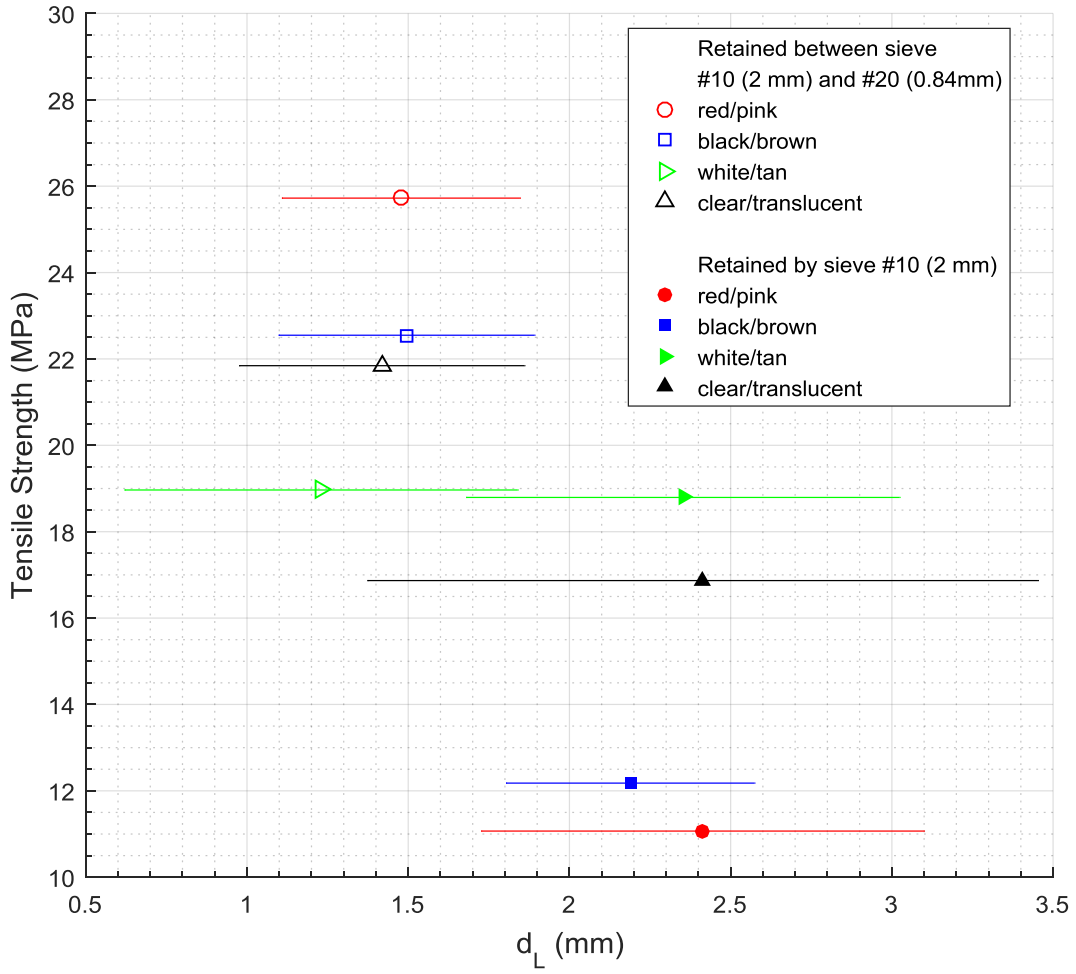


Figure 4-24. Average d_L within one standard deviation, without outliers, for rectangular prismatic shaped red/pink (major and secondary compounds: quartz, potassium feldspar, and plagioclase feldspar), black/brown (major and secondary compounds: quartz, mica (biotite), tridymite, plagioclase feldspar, potassium feldspar, and calcite), white/tan (major and secondary compounds: quartz, plagioclase feldspar, potassium feldspar, and mica (muscovite)) and clear/translucent (major and secondary compounds: quartz and plagioclase feldspar) particles retained between sieve #10 (2 mm) and #20 (0.84 mm) and by sieve #10 (2 mm)

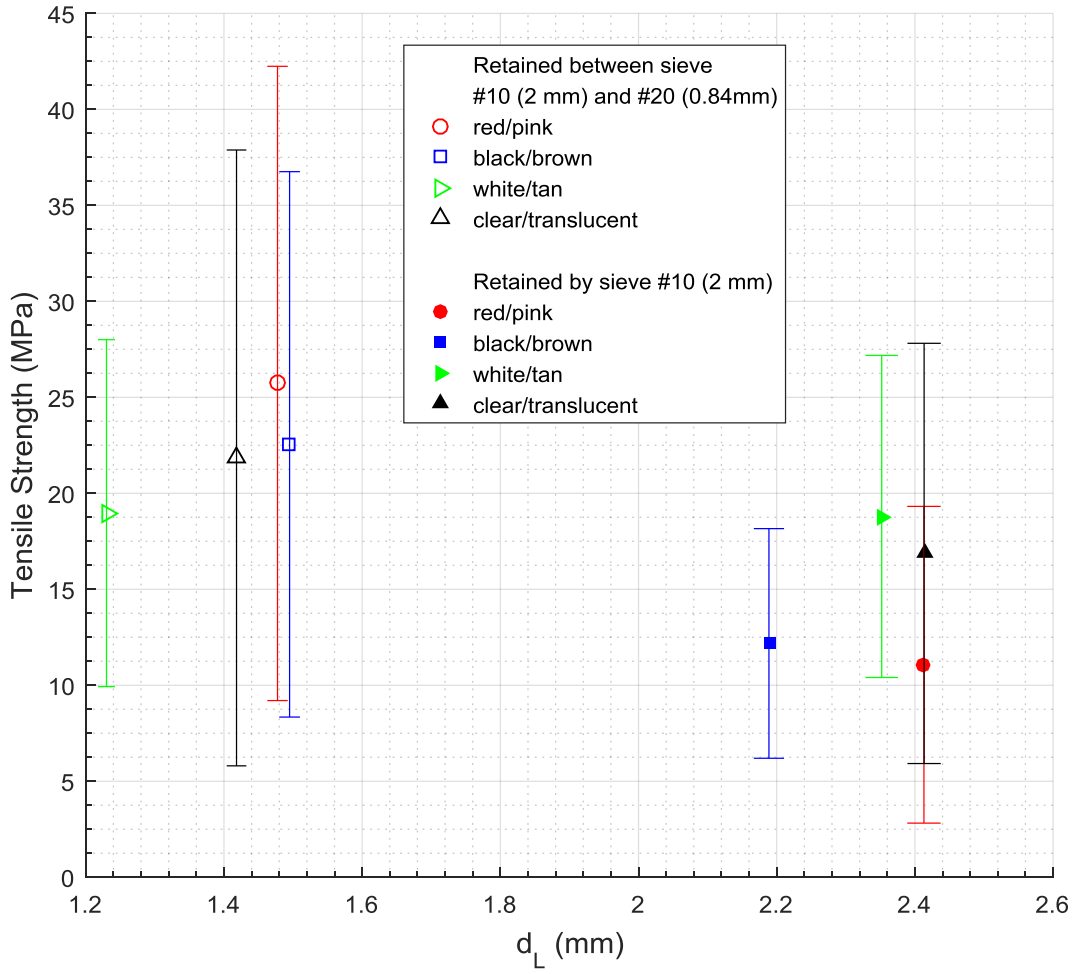


Figure 4-25. Average tensile strength within one standard deviation, without outliers, for rectangular prismatic shaped red/pink (major and secondary compounds: quartz, potassium feldspar, and plagioclase feldspar), black/brown (major and secondary compounds: quartz, mica (biotite), tridymite, plagioclase feldspar, potassium feldspar, and calcite), white/tan (major and secondary compounds: quartz, plagioclase feldspar, potassium feldspar, and mica (muscovite)) and clear/translucent (major and secondary compounds: quartz and plagioclase feldspar) particles retained between sieve #10 (2 mm) and #20 (0.84 mm) and by sieve #10 (2 mm)

the unfilled data points represent the particles retained between sieve #10 (2 mm) and #20 (0.84 mm) and the filled data points represent the particles retained by sieve #10 (2mm).

As shown in Figure 4-24, the d_L range for the rectangular prismatic shaped red/pink, black/brown, and clear/translucent particles retained between sieve #10 (2 mm) and #20 (0.84 mm) were relatively similar while the rectangular prismatic shaped white/tan particles retained between sieve #10 (2 mm) and #20 (0.84 mm) was larger, which indicated more variation in d_L for white/tan particles. The d_L range for the rectangular prismatic shaped white/tan retained between sieve #10 (2 mm) and #20 (0.84 mm) was relatively similar to the d_L range for the rectangular prismatic shaped white/tan retained by sieve #10 (2 mm). For particles retained by sieve #10 (2 mm), the clear/translucent particles had the largest d_L range while the black/brown particles had the smallest d_L range, which indicated more variation in d_L for the clear/translucent particles and less variation in d_L for the black/brown particles. The rectangular prismatic shaped red/pink particles retained between sieve #10 (2 mm) and #20 (0.84 mm) had the highest average tensile strength; the rectangular prismatic shaped red/pink particles retained by sieve #10 (2 mm) had the average tensile strength.

Referring to Figure 4-25, the tensile strength range for the rectangular prismatic shaped clear/translucent and red/pink particles retained between sieve #10 (2 mm) and #20 (0.84 mm) were similar and red/pink particles had the largest tensile strength range; the tensile strength range for the rectangular prismatic shaped white/tan retained between sieve #10 (2 mm) and #20 (0.84 mm) was the smallest. This indicated that there was more variation in tensile strength for the rectangular prismatic shaped red/pink particles and less variation in tensile strength for the rectangular prismatic shaped white/tan particles. The tensile strength range for the rectangular prismatic shaped clear/translucent retained by sieve #10 (2 mm) was the largest while the tensile

strength range for the rectangular prismatic shaped black/brown particles was the smallest. This indicated that the tensile strength for the rectangular prismatic shaped clear/translucent particles and less variation in tensile strength for the rectangular prismatic shaped black/brown particles.

Figures 4-26 and 4-27 show the distribution for the spherical particles retained between sieve #10 (2 mm) and #20 (0.84 mm) and by sieve #10 (2 mm), respectively. The distributions for Figures 4-26 and 4-27 were left skewed with an average d_L of 1.38 and 2.34 mm and an average tensile strength of 24.69 and 14.52 MPa for particles retained between sieve #10 (2 mm) and #20 (0.84 mm) and by sieve #10 (2 mm), respectively. It can be observed that particles that had larger d_L fractured at lower tensile strengths while particles that had smaller d_L fractured at higher tensile strengths. Table 4-12 compiles the displays the number of particles, average d_L, and tensile strengths for both distributions based on subgroups. Based on Table 4-12, the white/tan particles from both size categories had smaller d_L while the black/brown particles retained between sieve #10 (2 mm) and #20 (0.84 mm) and the red/pink particles retained by sieve #10 (2 mm) had larger d_L. Clear/translucent particles from both size categories fractured at higher tensile strengths while white/tan particles retained between sieve #10 (2 mm) and #20 (0.84 mm), that had smaller d_L, and red/pink particles retained by sieve #10 (2 mm), having larger d_L, fractured at lower tensile strengths. The distribution of spherical shaped particles was relatively constant across the four colored subgroups within both size categories.

Figures 4-28 and 4-29 depict the average d_L and tensile strength within one standard deviation, without the inclusion of outliers, for spherical shaped particles retained between sieve #10 (2 mm) and #20 (0.84 mm) and by sieve #10 (2 mm), respectively. The circle data points, square data points, right sided triangle data points, and triangle data points represent the red/pink (major and secondary compounds: quartz, potassium feldspar, and plagioclase feldspar),

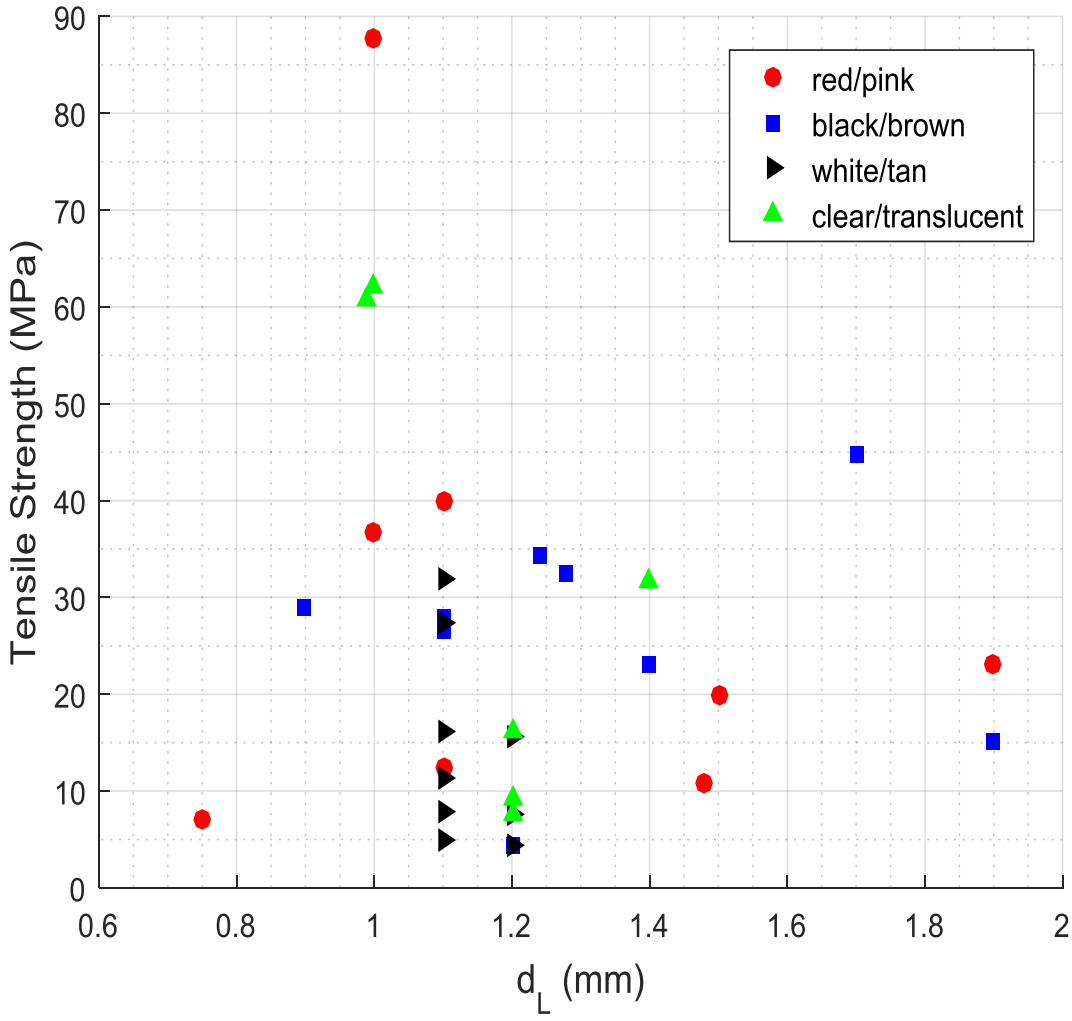


Figure 4-26. Spherical shaped red/pink (major and secondary compounds: quartz, potassium feldspar, and plagioclase feldspar), black/brown (major and secondary compounds: quartz, mica (biotite), tridymite, plagioclase feldspar, potassium feldspar, and calcite), white/tan (major and secondary compounds: quartz, plagioclase feldspar, potassium feldspar, and mica (muscovite)) and clear/translucent (major and secondary compounds: quartz and plagioclase feldspar) particles retained between sieve #10 (2 mm) and #20 (0.84 mm).

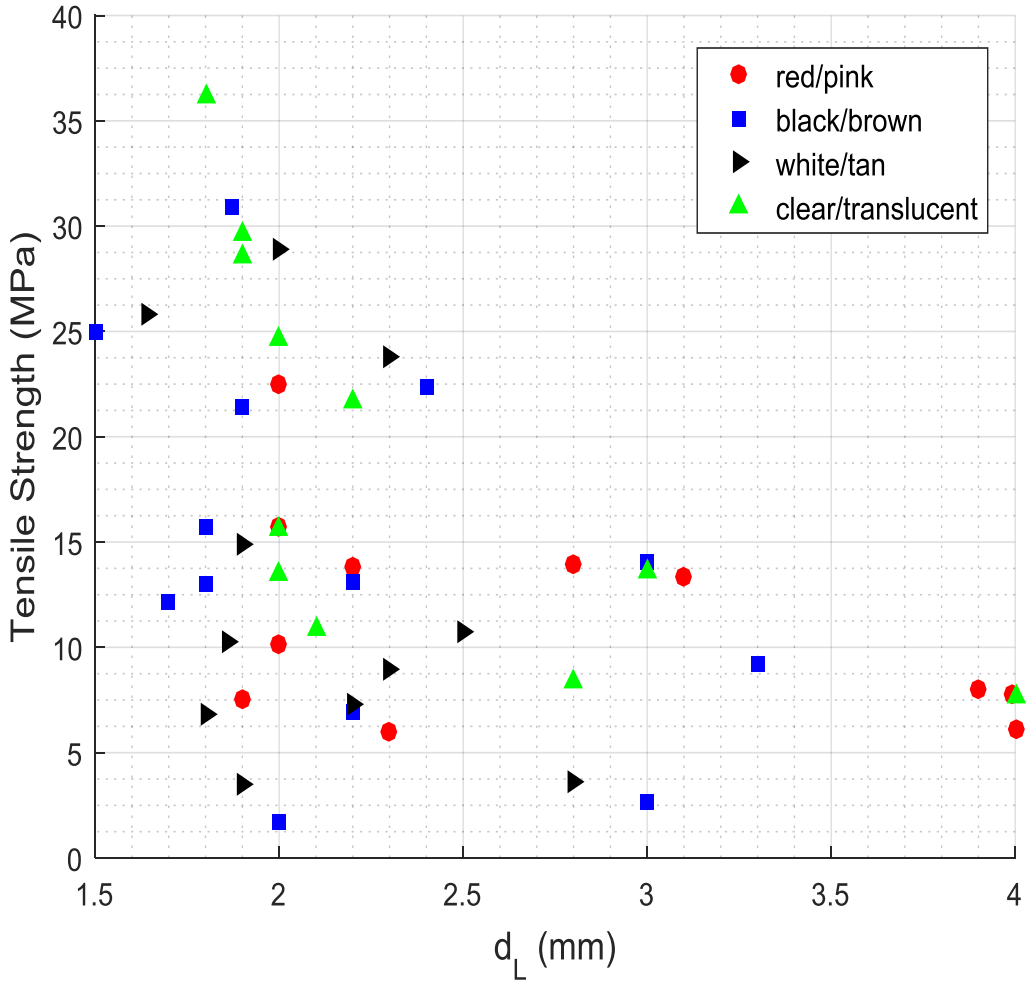


Figure 4-27. Spherical shaped red/pink (major and secondary compounds: quartz, potassium feldspar, and plagioclase feldspar), black/brown (major and secondary compounds: quartz, mica (biotite), tridymite, plagioclase feldspar, potassium feldspar, and calcite), white/tan (major and secondary compounds: quartz, plagioclase feldspar, potassium feldspar, and mica (muscovite)) and clear/translucent (major and secondary compounds: quartz and plagioclase feldspar) particles retained by sieve #10 (2 mm).

Table 4-12. Number of particles, average d_L, and average tensile strengths for spherical shaped particles retained between sieve #10 (2 mm) and #20 (0.84 mm) and by sieve #10 (2 mm) subdivided into colored subgroups.

Colored Subgroups	**Retained between sieve #10 (2 mm) and #20 (0.84 mm)**			**Retained by sieve #10 (2 mm)**		
	Number of Particles	**Average d_L (mm)**	**Average Tensile Strength (MPa)**	**Number of Particles**	**Average d_L (mm)**	**Average Tensile Strength (MPa)**
Red/Pink *(major and secondary compounds: quartz, potassium feldspar, and plagioclase feldspar)*	8	1.23	29.64	11	2.74	11.37
Black/Brown *(major and secondary compounds: quartz, mica (biotite), tridymite, plagioclase feldspar, potassium feldspar, and calcite)*	9	1.31	26.41	13	2.21	14.48

Table 4-12 Continued

Colored Subgroups	Retained between sieve #10 (2 mm) and #20 (0.84 mm)			Retained by sieve #10 (2 mm)		
	Number of Particles	**Average d_L (mm)**	**Average Tensile Strength (MPa)**	**Number of Particles**	**Average d_L (mm)**	**Average Tensile Strength (MPa)**
White/Tan *(major and secondary compounds: quartz, plagioclase feldspar, potassium feldspar, and mica (muscovite))*	9	1.13	14.14	11	2.11	13.15
Clear/Translucent *(major and secondary compounds: quartz and plagioclase feldspar)*	6	1.16	31.32	11	2.34	19.11

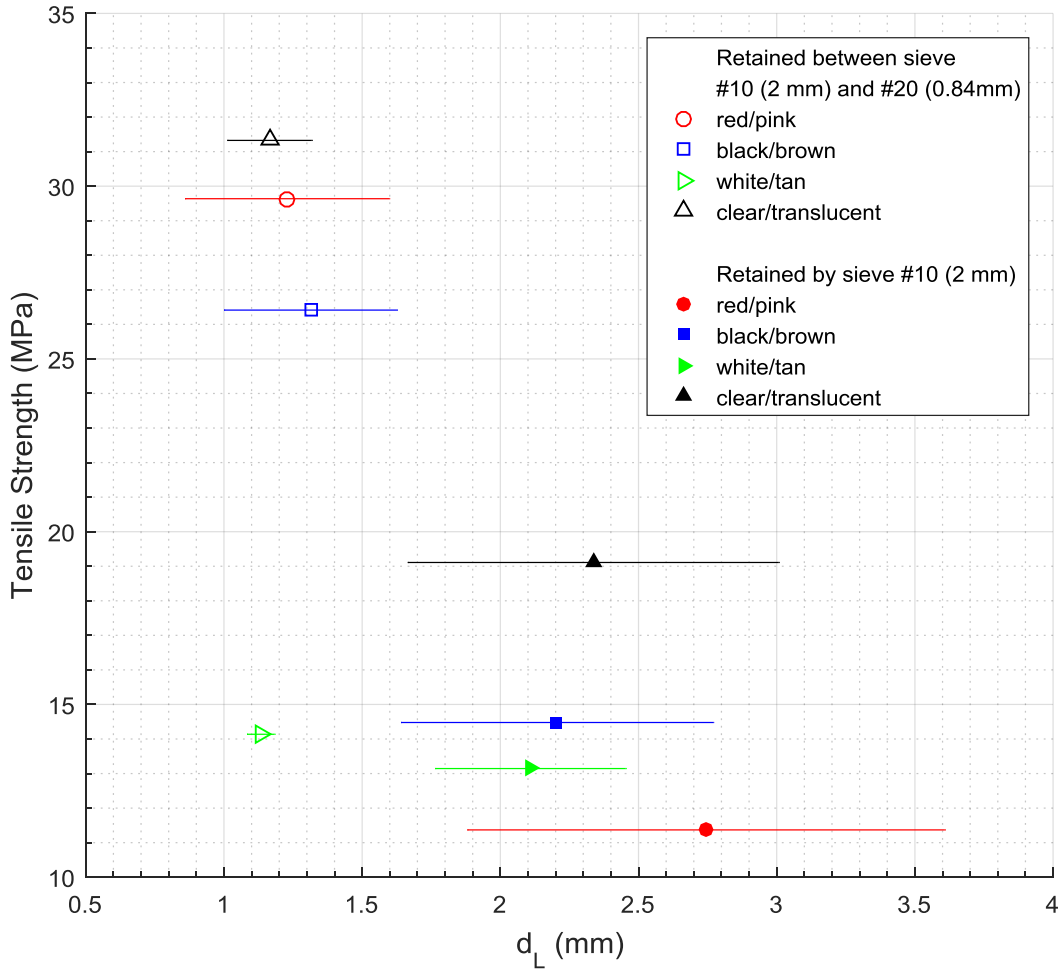


Figure 4-28. Average d_L within one standard deviation, without outliers, for spherical shaped red/pink (major and secondary compounds: quartz, potassium feldspar, and plagioclase feldspar), black/brown (major and secondary compounds: quartz, mica (biotite), tridymite, plagioclase feldspar, potassium feldspar, and calcite), white/tan (major and secondary compounds: quartz, plagioclase feldspar, potassium feldspar, and mica (muscovite)) and clear/translucent (major and secondary compounds: quartz and plagioclase feldspar) particles retained between sieve #10 (2 mm) and #20 (0.84 mm) and by sieve #10 (2 mm)

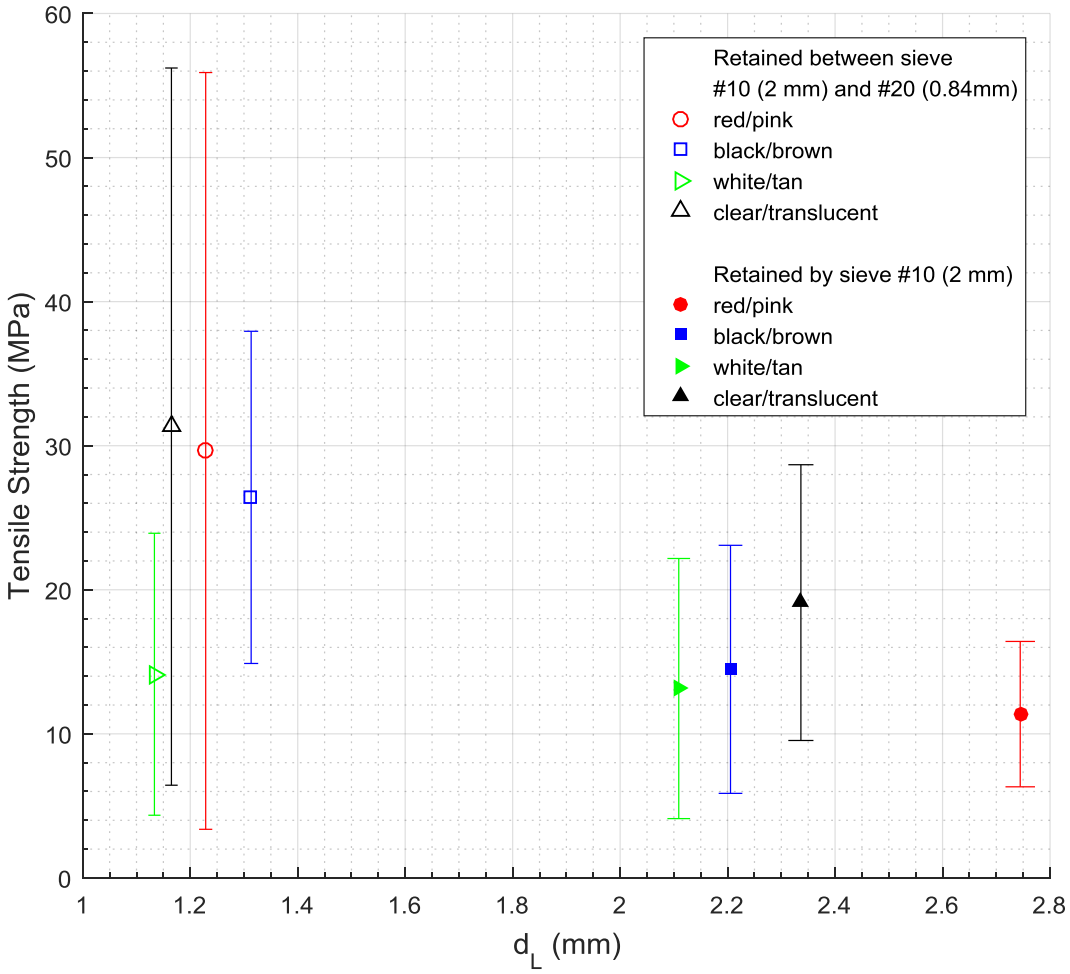


Figure 4-29. Average tensile strength within one standard deviation, without outliers, for spherical shaped red/pink (major and secondary compounds: quartz, potassium feldspar, and plagioclase feldspar), black/brown (major and secondary compounds: quartz, mica (biotite), tridymite, plagioclase feldspar, potassium feldspar, and calcite), white/tan (major and secondary compounds: quartz, plagioclase feldspar, potassium feldspar, and mica (muscovite)) and clear/translucent (major and secondary compounds: quartz and plagioclase feldspar) particles retained between sieve #10 (2 mm) and #20 (0.84 mm) and by sieve #10 (2 mm)

black/brown (major and secondary compounds: quartz, mica (biotite), tridymite, plagioclase feldspar, potassium feldspar, and calcite), white/tan (major and secondary compounds: quartz, plagioclase feldspar, potassium feldspar, and mica (muscovite)) and clear/translucent (major and secondary compounds: quartz and plagioclase feldspar) particles; the unfilled data points represent the particles retained between sieve #10 (2 mm) and #20 (0.84 mm) and the filled data points represent the particles retained by sieve #10 (2mm).

As shown in Figure 4-28, the d_L range for the spherical shaped red/pink particles retained between sieve #10 (2 mm) and #20 (0.84 mm) and by sieve #10 (2 mm) was the largest while the spherical shaped white/tan particles retained between sieve #10 (2 mm) and #20 (0.84 mm) and by sieve #10 (2 mm) was the smallest. This indicated that the d_L for the spherical shaped red/pink particles in both size categories varied the most while the d_L for the spherical shaped white/tan particles in both size categories varied the least. The spherical shaped clear/translucent particles retained between sieve #10 (2 mm) and #20 (0.84 mm) had the highest average tensile strength; the spherical shaped red/pink particles retained by sieve #10 (2 mm) had the lowest average tensile strength. Referring to Figure 4-29, the tensile strength range for the spherical shaped red/pink particles retained between sieve #10 (2 mm) and #20 (0.84 mm) was the largest while the spherical shaped white/tan particles had the smallest tensile strength range. This indicated more variation in the tensile strength range for the spherical shaped red/pink particles and less variation for the spherical shaped white/tan particles retained between sieve #10 (2 mm) and #20 (0.84 mm). The tensile strength range for the spherical shaped clear/translucent particles retained by sieve #10 (2 mm) was the largest; the spherical shaped red/pink particles had the smallest tensile strength range. This implied that the tensile strength range for the spherical shaped clear/translucent particles had more variation in tensile strength compared to the spherical

shaped red/pink particles that had less variation in tensile strength. The average d_L for spherical shaped clear/translucent particles retained between sieve #10 (2 mm) and #20 (0.84 mm) was largest; the average d_L for spherical shaped red/pink particles retained by sieve #10 (2 mm) was smallest.

Figures 4-30 and 4-31a displays the distribution for triangular prismatic shaped particles retained between sieve #10 (2 mm) and #20 (0.84 mm) and by sieve #10 (2 mm), respectively; both distributions were left skewed. The average d_L was 1.48 mm and the average tensile strength was 19.40 MPa for the distribution in Figure 4-30. Based on the distribution, particles with a smaller d_L fractured at higher tensile strengths and particles that had larger d_L fractured at lower tensile strengths. Referring to Figure 4-31a, the red/pink and white/tan particles fractured at tensile strengths less than 15 MPa while the black/brown and clear/translucent particle fractured at higher tensile strengths. The distribution had an average d_L of 1.48 mm, an average tensile strength of 19.40 MPa, and an outlier at 88.93 MPa. Based on Table F-1 in Appendix F, the particle associated with a tensile strength of 88.93 MPa was Black/Brown 25-9_J, shown in Figure 4-31a.1 in Appendix I. Figure 4-31a.1 displays an exponential increase in load with a plateau at approximately 126 N, where the particle experienced an explosive fractured at 127.64 N, in which only a few fine pieces were recovered. This implied that the particle was abnormally strong. Figure 4-31b displays the distribution of the triangular prismatic shaped particles retained by sieve #10 (2 mm) with the exclusion of the outlier. The distribution was shown to be left skewed with an average tensile strength of 12.35 MPa and an average d_L of 2.40mm. The distribution of the red/pink, white/tan, and clear/translucent remain constant while the distribution of the black/brown particles. The black/brown particles do not show a correlation between tensile strength and d_L.

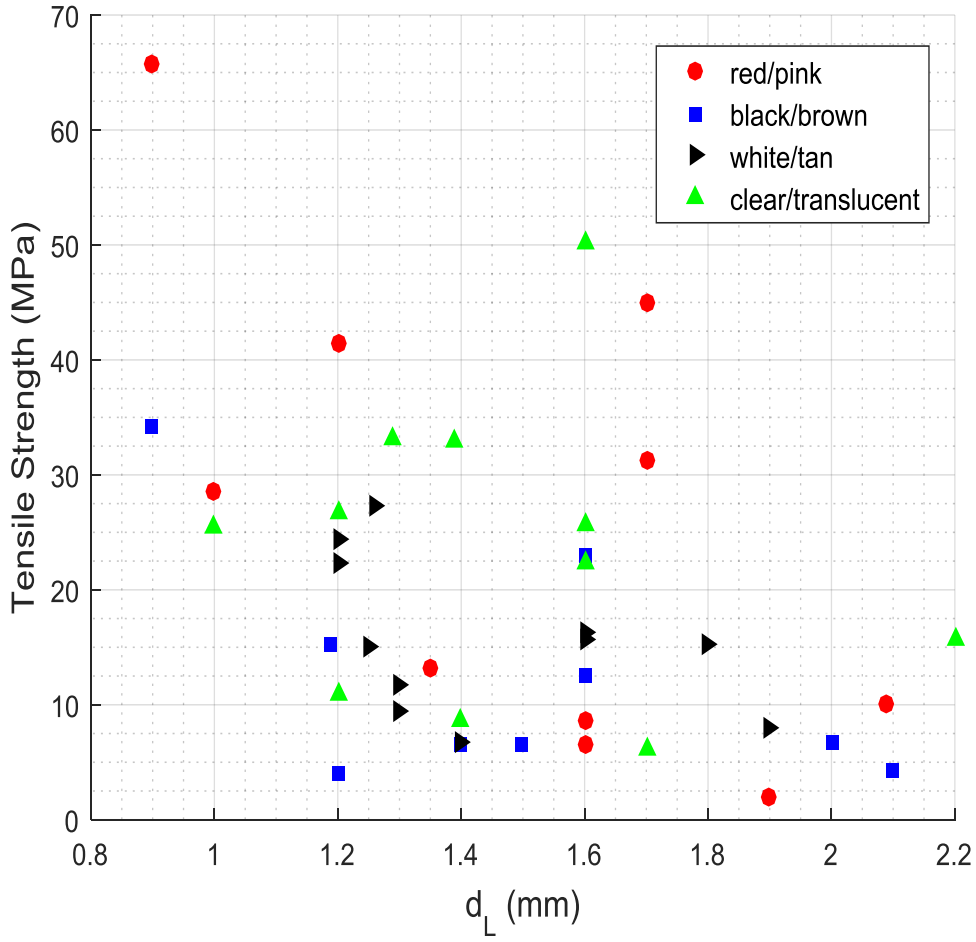


Figure 4-30. Triangular prismatic shaped red/pink (major and secondary compounds: quartz, potassium feldspar, and plagioclase feldspar), black/brown (major and secondary compounds: quartz, mica (biotite), tridymite, plagioclase feldspar, potassium feldspar, and calcite), white/tan (major and secondary compounds: quartz, plagioclase feldspar, potassium feldspar, and mica (muscovite)) and clear/translucent (major and secondary compounds: quartz and plagioclase feldspar) particles retained between sieve #10 (2 mm) and #20 (0.84 mm).

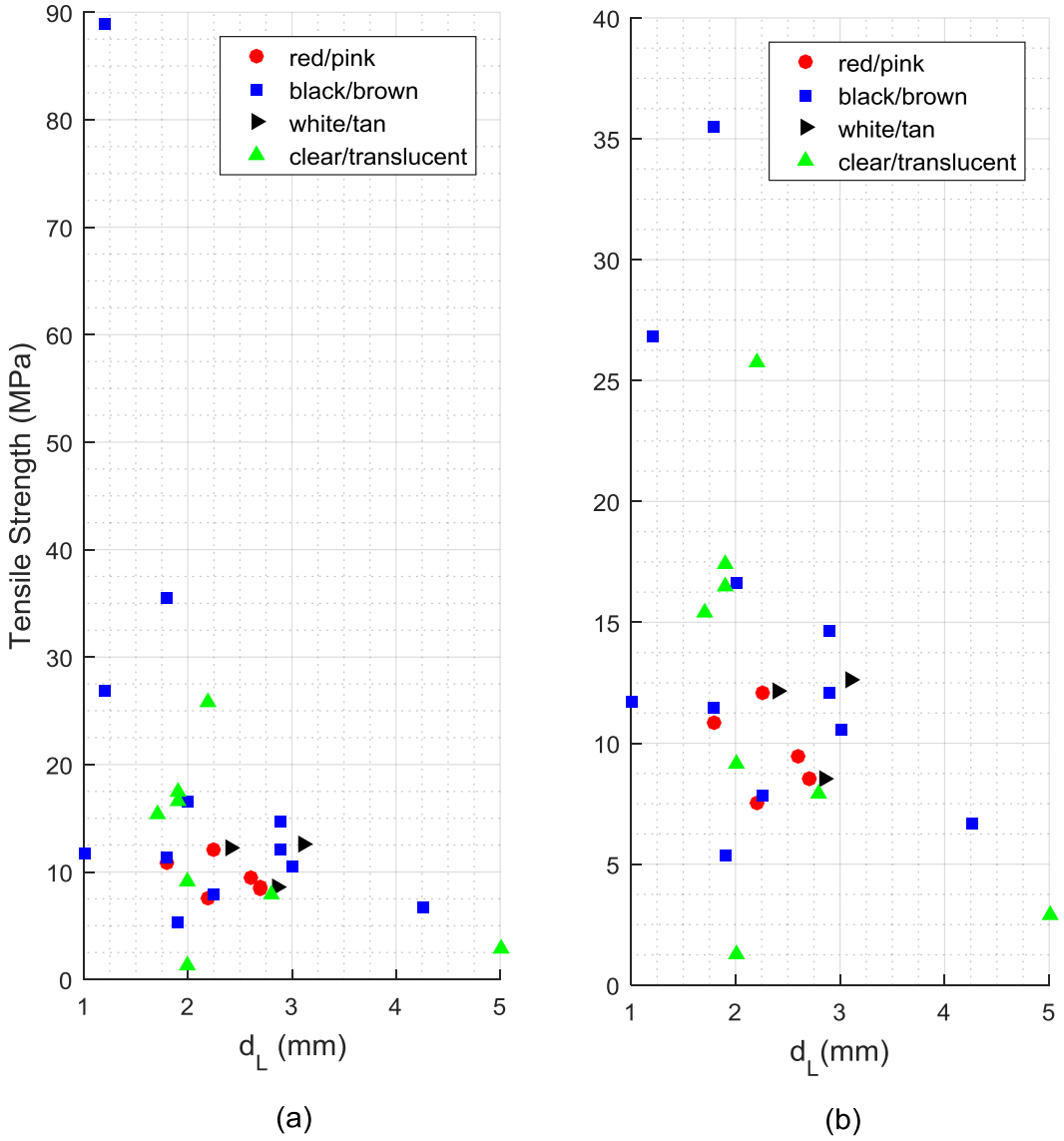


Figure 4-31. Triangular prismatic shaped red/pink (major and secondary compounds: quartz, potassium feldspar, and plagioclase feldspar), black/brown (major and secondary compounds: quartz, mica (biotite), tridymite, plagioclase feldspar, potassium feldspar, and calcite), white/tan (major and secondary compounds: quartz, plagioclase feldspar, potassium feldspar, and mica (muscovite)) and clear/translucent (major and secondary compounds: quartz and plagioclase feldspar) particles retained by sieve #10 (2 mm) (a) with outliers (b) without outliers.

Table 4-13 displays the number of particles, average d_L, and average tensile strengths for the triangular prismatic shaped particles based on colored subgroups for Figures 4-30, 4-31a, and 4-31b; values that were altered due to the removal of the outliers were presented in parentheses. Based on Table 4-13, particles retained between sieve #10 (2 mm) and #20 (0.84 mm) had relatively even distribution of triangular prismatic shaped particles while a majority of the black/brown particles and a small number of white/tan particles were triangular prismatic shaped. For particles retained between sieve #10 (2 mm) and #20 (0.84 mm), the red/pink particles had larger d_L while the white/tan particles had smaller d_L; the black/brown particles fractured lower tensile strengths and the clear/translucent particles fractured at higher tensile strengths. For particles retained by sieve #10 (2 mm), the black/brown particles had the smaller d_L and fractured at higher tensile strengths, regardless of the exclusion of the outlier; the red/pink particles fractured at lower tensile strengths while the white/tan particles had larger d_L.

Figures 4-32 and 4-33 depict the average d_L and tensile strength within one standard deviation, without the inclusion of outliers, for spherical shaped particles retained between sieve #10 (2 mm) and #20 (0.84 mm) and by sieve #10 (2 mm), respectively. The circle data points, square data points, right sided triangle data points, and triangle data points represent the red/pink (major and secondary compounds: quartz, potassium feldspar, and plagioclase feldspar), black/brown (major and secondary compounds: quartz, mica (biotite), tridymite, plagioclase feldspar, potassium feldspar, and calcite), white/tan (major and secondary compounds: quartz, plagioclase feldspar, potassium feldspar, and mica (muscovite)) and clear/translucent (major and secondary compounds: quartz and plagioclase feldspar) particles; the unfilled data points represent the particles retained between sieve #10 (2 mm) and #20 (0.84 mm) and the filled data points represent the particles retained by sieve #10 (2mm).

Table 4-13. Number of particles, average d_L, and average tensile strengths for triangular prismatic shaped particles retained between sieve #10 (2 mm) and #20 (0.84 mm) and by sieve #10 (2 mm) subdivided into colored subgroups.

Colored Subgroups	**Retained between sieve #10 (2 mm) and #20 (0.84 mm)**			**Retained by sieve #10 (2 mm)**		
	Number of Particles	**Average d_L (mm)**	**Average Tensile Strength (MPa)**	**Number of Particles**	**Average d_L (mm)**	**Average Tensile Strength (MPa)**
Red/Pink *(major and secondary compounds: quartz, potassium feldspar, and plagioclase feldspar)*	8	1.64	19.77	6	2.37	9.49
Black/Brown *(major and secondary compounds: quartz, mica (biotite), tridymite, plagioclase feldspar, potassium feldspar, and calcite)*	9	1.50	12.3	12 (11)	2.18 (2.27)	20.69 (14.48)

Table 4-13 Continued

Colored Subgroups	Retained between sieve #10 (2 mm) and #20 (0.84 mm)			Retained by sieve #10 (2 mm)		
	Number of Particles	**Average d_L (mm)**	**Average Tensile Strength (MPa)**	**Number of Particles**	**Average d_L (mm)**	**Average Tensile Strength (MPa)**
White/Tan *(major and secondary compounds: quartz, plagioclase feldspar, potassium feldspar, and mica (muscovite))*	11	1.44	15.65	3	2.78	11.10
Clear/Translucent *(major and secondary compounds: quartz and plagioclase feldspar)*	10	1.52	23.25	8	2.44	12.04

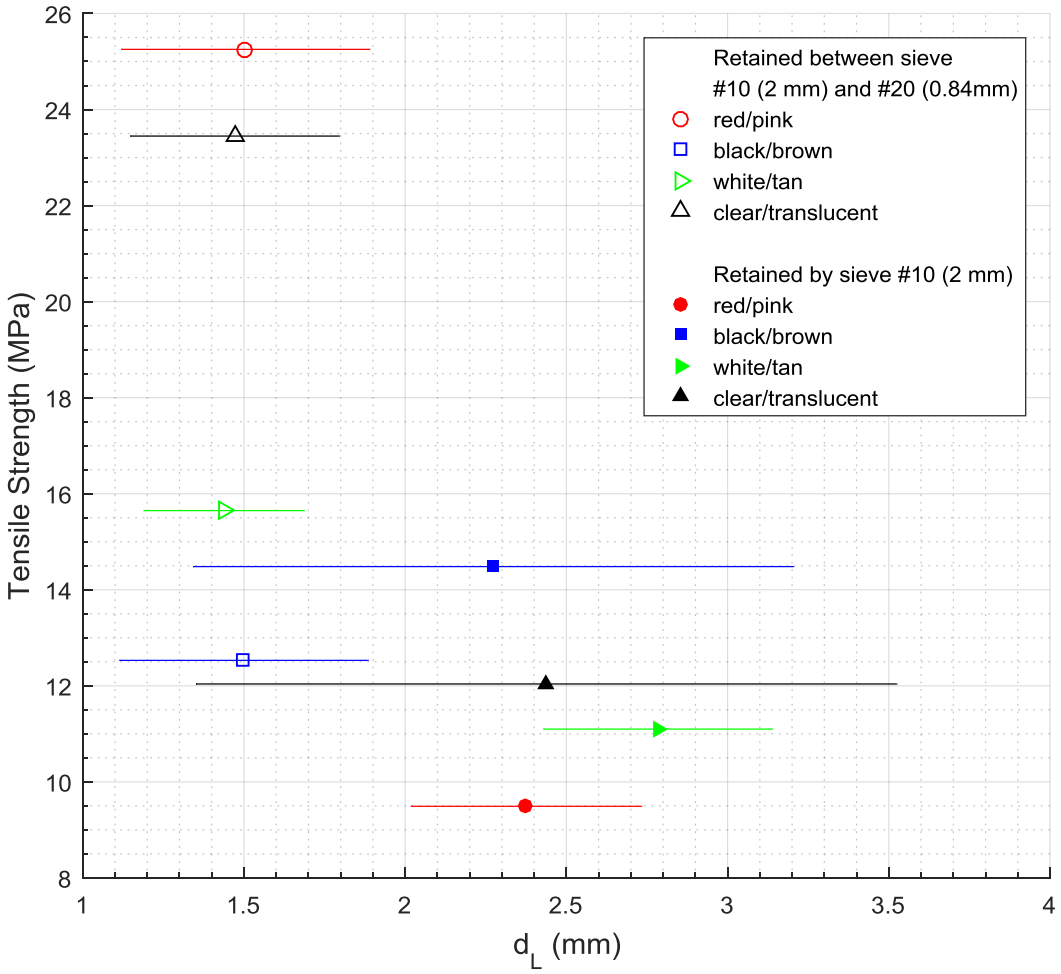


Figure 4-32. Average d_L within one standard deviation, without outliers, for triangular prismatic shaped red/pink (major and secondary compounds: quartz, potassium feldspar, and plagioclase feldspar), black/brown (major and secondary compounds: quartz, mica (biotite), tridymite, plagioclase feldspar, potassium feldspar, and calcite), white/tan (major and secondary compounds: quartz, plagioclase feldspar, potassium feldspar, and mica (muscovite)) and clear/translucent (major and secondary compounds: quartz and plagioclase feldspar) particles retained between sieve #10 (2 mm) and #20 (0.84 mm) and by sieve #10 (2 mm)

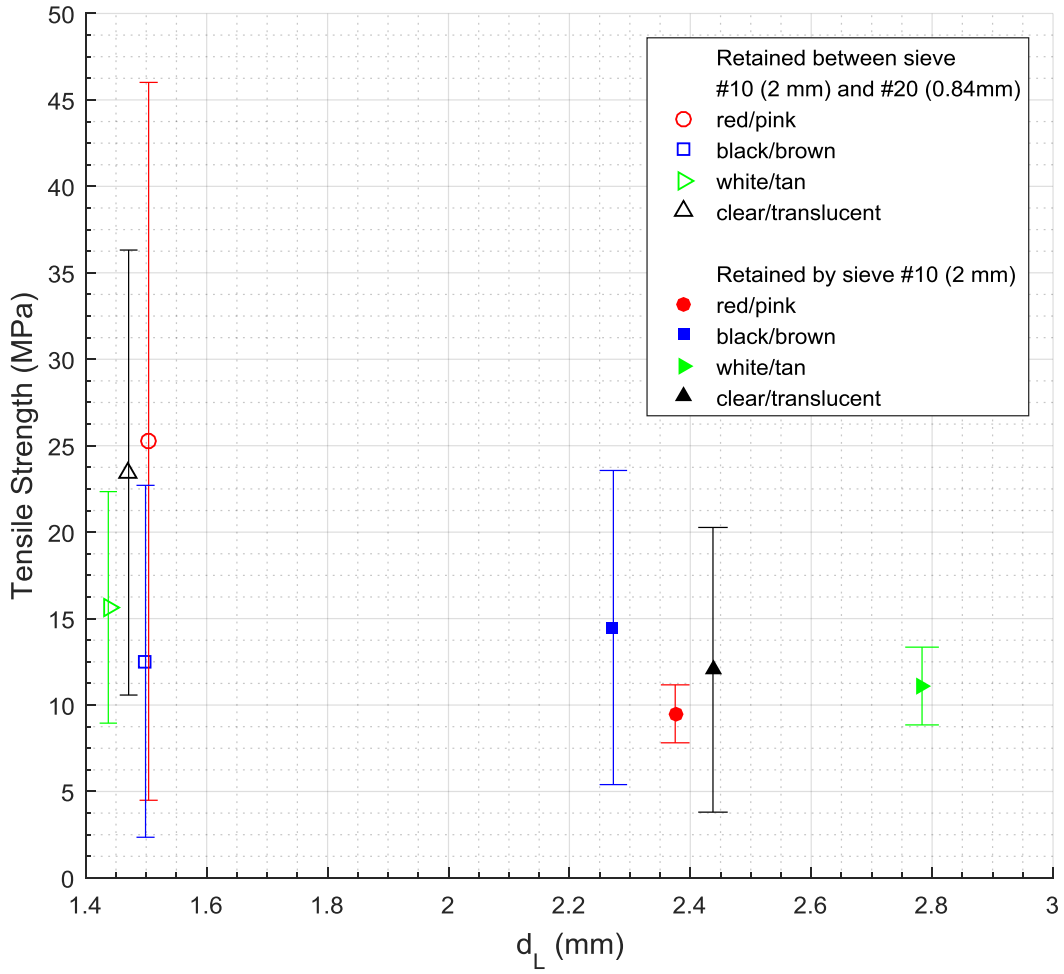


Figure 4-33. Average tensile strength within one standard deviation, without outliers, for triangular prismatic shaped red/pink (major and secondary compounds: quartz, potassium feldspar, and plagioclase feldspar), black/brown (major and secondary compounds: quartz, mica (biotite), tridymite, plagioclase feldspar, potassium feldspar, and calcite), white/tan (major and secondary compounds: quartz, plagioclase feldspar, potassium feldspar, and mica (muscovite)) and clear/translucent (major and secondary compounds: quartz and plagioclase feldspar) particles retained between sieve #10 (2 mm) and #20 (0.84 mm) and by sieve #10 (2 mm)

Referring to Figure 4-32, the d_L range for the triangular prismatic shaped particles retained between sieve #10 (2 mm) and #20 (0.84 mm), the red/pink and black/brown had the largest range while white/tan particles had the smallest range. This indicated that the triangular prismatic red/pink and black/brown particles had more variation in d_L while the triangular prismatic white/tan particles had the less variation in d_L. The d_L range for the triangular prismatic shaped particles retained by sieve #10 (2 mm) was largest for the clear/translucent particles and smallest for the white/tan and red/pink particles. This indicated that the triangular prismatic clear translucent particles had more variation in d_L while the triangular prismatic white/tan and red/pink particles had the less variation in d_L. The triangular prismatic shaped red/pink particle retained between sieve #10 (2 mm) and #20 (0.84 mm) had the highest average tensile strength; the triangular prismatic shaped red/pink particle retained by sieve #10 (2 mm) had the lowest average tensile strength.

As depicted in Figure 4-33, triangular prismatic shaped red/pink particles and white/tan particles retained between sieve #10 (2 mm) and #20 (0.84 mm) had the largest and smallest d_L range, respectively. The triangular prismatic black/brown and red/pink particles retained by sieve #10 (2 mm) had the largest and smallest d_L range, respectively. This indicated more variation in d_L for triangular prismatic shaped red/pink particles retained between sieve #10 (2 mm) and #20 (0.84 mm) and triangular prismatic shaped black/brown particles retained by sieve #10 (2 mm). There was less variation in d_L for triangular prismatic shaped white/tan particles retained between sieve #10 (2 mm) and #20 (0.84 mm) by sieve #10 (2 mm). The average d_L of triangular prismatic shaped particles retained between sieve #10 (2 mm) and #20 (0.84 mm) is relatively similar; the average d_L for triangular prismatic shaped white/tan particles was much higher compared to the red/pink, black/brown, and clear/translucent particles retained by sieve #10

(2 mm). The average d_L of triangular prismatic shaped white/tan particles was smallest for particles retained between sieve #10 (2 mm) and #20 (0.84 mm) and largest for particles retained by sieve #10 (2 mm).

Figures 4-34a and 4-35 shows the distributions for the other shaped particles retained between sieve #10 (2 mm) and #20 (0.84 mm) and by sieve #10 (2 mm), respectively. Particles retained between sieve #10 (2 mm) and #20 (0.84 mm), in Figure 4-34a, had an average tensile strength and d_L of 29.44 MPa and 1.37 mm; there was also an outlying particle, White/Tan_25-6_C, at a tensile strength of 83.26 MPa. Particles retained by sieve #10 (2 mm),in Figure 4-35, had an average tensile strength and d_L of 15.71 MPa and 2.10 mm. The distributions for Figures 4-34a, 4-34b, and 4-35 were left skewed; particles that had smaller d_L fractured at higher tensile strengths while particles that had larger d_L fractured at smaller tensile strengths. Table 4-14 summarizes the number of particles, average d_L, and average tensile strengths for the other shaped particles for both distributions subdivided into colored subgroups. Based on Table 4-14, the red/pink particles in both size categories had smaller d_L while the white/tan particles retained between sieve #10 (2 mm) and #20 (0.84 mm) and clear/translucent particles retained by sieve #10 (2 mm) had larger d_L. Black/brown particles in both size categories fractured at higher tensile strengths; clear/translucent particles retained between sieve #10 (2 mm) and #20 (0.84 mm) and white/tan particles retained by sieve #10 (2 mm) fractured at lower tensile strengths. From Figures 4-34a,4-34b and 4-35, the particles that had larger d_L fractured at lower tensile strengths.

Figures 4-36 and 4-37 depict the average d_L and tensile strength within one standard deviation for other shaped particles retained between sieve #10 (2 mm) and #20 (0.84 mm) and by sieve #10 (2 mm), respectively. The circle data points, square data points, right sided triangle

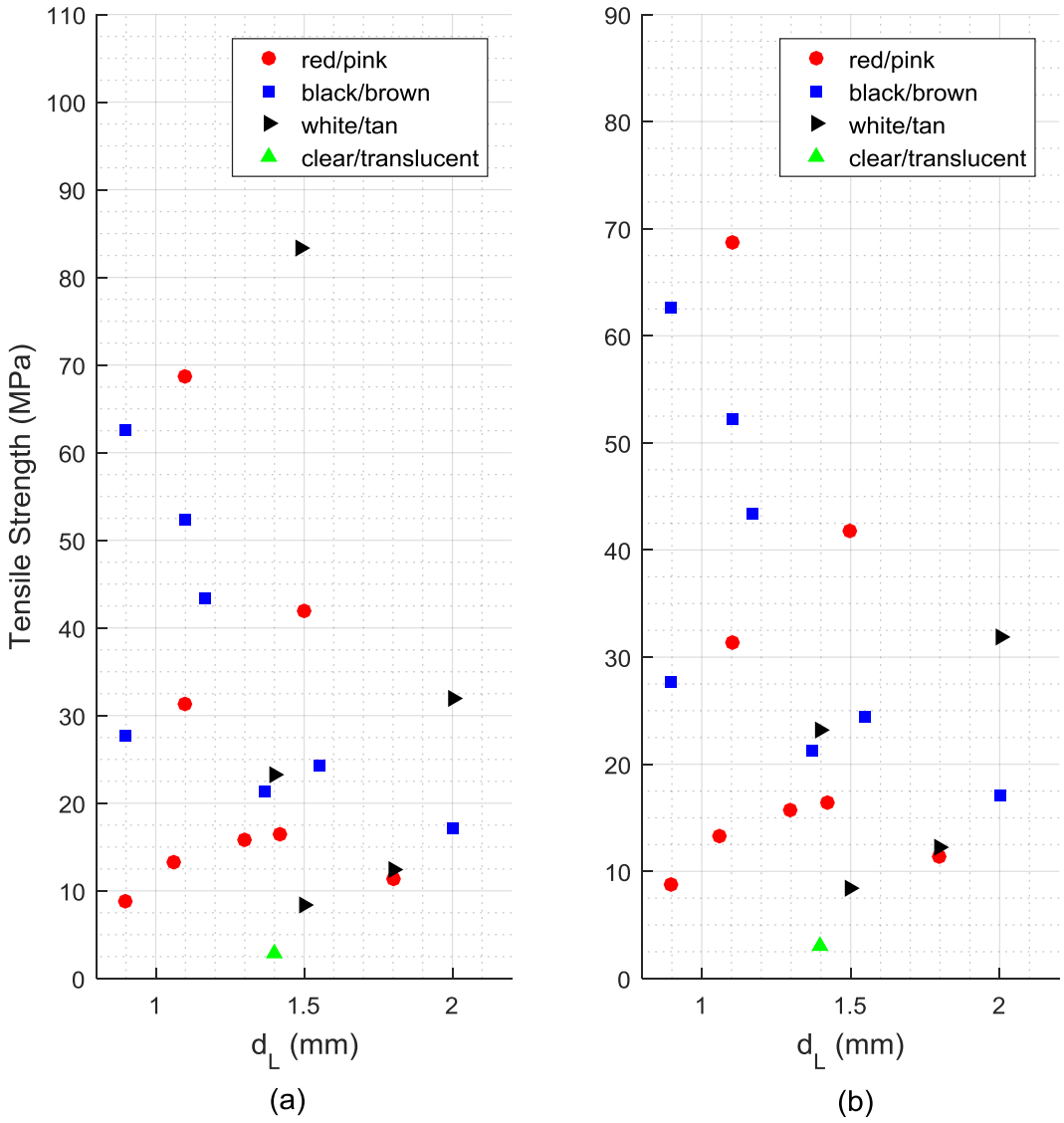


Figure 4-34. Other shaped red/pink (major and secondary compounds: quartz, potassium feldspar, and plagioclase feldspar), black/brown (major and secondary compounds: quartz, mica (biotite), tridymite, plagioclase feldspar, potassium feldspar, and calcite), white/tan (major and secondary compounds: quartz, plagioclase feldspar, potassium feldspar, and mica (muscovite)) and clear/translucent (major and secondary compounds: quartz and plagioclase feldspar) particles retained between sieve #10 (2 mm) and #20 (0.84 mm).

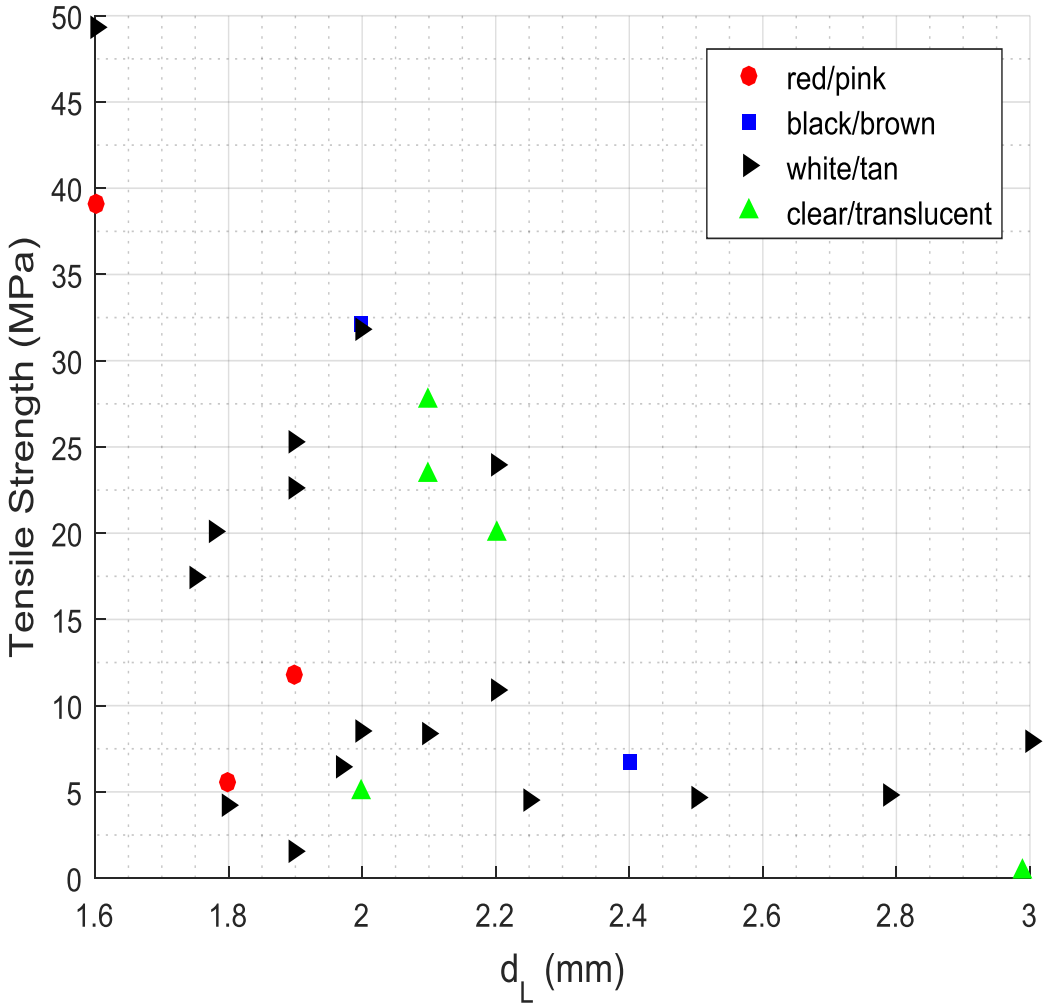


Figure 4-35. Other shaped red/pink (major and secondary compounds: quartz, potassium feldspar, and plagioclase feldspar), black/brown (major and secondary compounds: quartz, mica (biotite), tridymite, plagioclase feldspar, potassium feldspar, and calcite), white/tan (major and secondary compounds: quartz, plagioclase feldspar, potassium feldspar, and mica (muscovite)) and clear/translucent (major and secondary compounds: quartz and plagioclase feldspar) particles retained by sieve #10 (2 mm).

Table 4-14. Number of particles, average d_L, and average tensile strengths for other shaped particles retained between sieve #10 (2 mm) and #20 (0.84 mm) and by sieve #10 (2 mm) subdivided into colored subgroups.

Colored Subgroups	**Retained between sieve #10 (2 mm) and #20 (0.84 mm)**			**Retained by sieve #10 (2 mm)**		
	Number of Particles	**Average d_L (mm)**	**Average Tensile Strength (MPa)**	**Number of Particles**	**Average d_L (mm)**	**Average Tensile Strength (MPa)**
Red/Pink *(major and secondary compounds: quartz, potassium feldspar, and plagioclase feldspar)*	8	1.27	25.94	3	1.77	18.83
Black/Brown *(major and secondary compounds: quartz, mica (biotite), tridymite, plagioclase feldspar, potassium feldspar, and calcite)*	7	1.28	35.52	2	2.20	19.48

Table 4-14 Continued

Colored Subgroups	Retained between sieve #10 (2 mm) and #20 (0.84 mm)			Retained by sieve #10 (2 mm)		
	Number of Particles	**Average d_L (mm)**	**Average Tensile Strength (MPa)**	**Number of Particles**	**Average d_L (mm)**	**Average Tensile Strength (MPa)**
White/Tan *(major and secondary compounds: quartz, plagioclase feldspar, potassium feldspar, and mica (muscovite))*	5 (4)	1.64 (1.675)	31.80 (18.94)	17	2.10	14.85
Clear/Translucent *(major and secondary compounds: quartz and plagioclase feldspar)*	1	1.40	2.97	5	2.28	15.27

data points, and triangle data points represent the red/pink (major and secondary compounds: quartz, potassium feldspar, and plagioclase feldspar), black/brown (major and secondary compounds: quartz, mica (biotite), tridymite, plagioclase feldspar, potassium feldspar, and calcite), white/tan (major and secondary compounds: quartz, plagioclase feldspar, potassium feldspar, and mica (muscovite)) and clear/translucent (major and secondary compounds: quartz and plagioclase feldspar) particles; the unfilled data points represent the particles retained between sieve #10 (2 mm) and #20 (0.84 mm) and the filled data points represent the particles retained by sieve #10 (2mm).

As seen in Figure 4-36, the other shaped black/brown particles retained between sieve #10 (2 mm) and #20 (0.84 mm) had the largest d_L range while the other shaped particles retained between sieve #10 (2 mm) and #20 (0.84 mm) had the smallest d_L range. The other shaped clear/translucent particle retained between sieve #10 (2 mm) and #20 (0.84 mm) only contains 1 particle and therefore did not had a d_L range. The other shaped clear/translucent particles retained by sieve #10 (2 mm) had the largest d_L range and the red/pink particles had the smallest d_L range. The average tensile strength for the other shaped black/brown particles retained between sieve #10 (2 mm) and #20 (0.84 mm) was the highest and the other shaped clear/translucent retained between sieve #10 (2 mm) and #20 (0.84 mm) had the lowest average tensile strength.

As shown in Figure 4-37, the other shaped red/pink particles retained between sieve #10 (2 mm) and #20 (0.84 mm) had the largest tensile strength range while the other shaped white/tan particles had the smallest tensile strength range. The clear/translucent particle retained between sieve #10 (2 mm) and #20 (0.84 mm) was a lone particle and does not had a tensile strength range. The other shaped black/brown and red/pink particles retained by sieve #10.

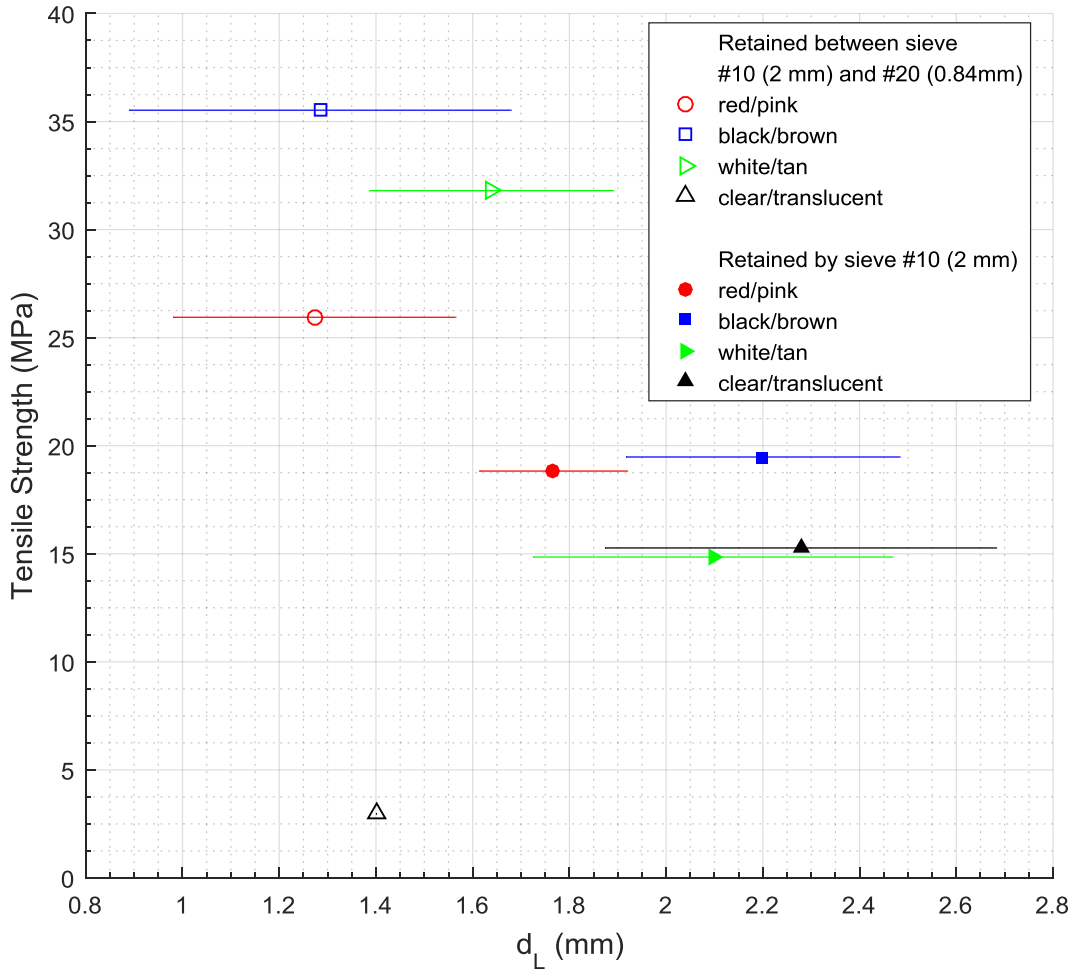


Figure 4-36. Average d_L within one standard deviation for other shaped red/pink (major and secondary compounds: quartz, potassium feldspar, and plagioclase feldspar), black/brown (major and secondary compounds: quartz, mica (biotite), tridymite, plagioclase feldspar, potassium feldspar, and calcite), white/tan (major and secondary compounds: quartz, plagioclase feldspar, potassium feldspar, and mica (muscovite)) and clear/translucent (major and secondary compounds: quartz and plagioclase feldspar) particles retained between sieve #10 (2 mm) and #20 (0.84 mm) and by sieve #10 (2 mm)

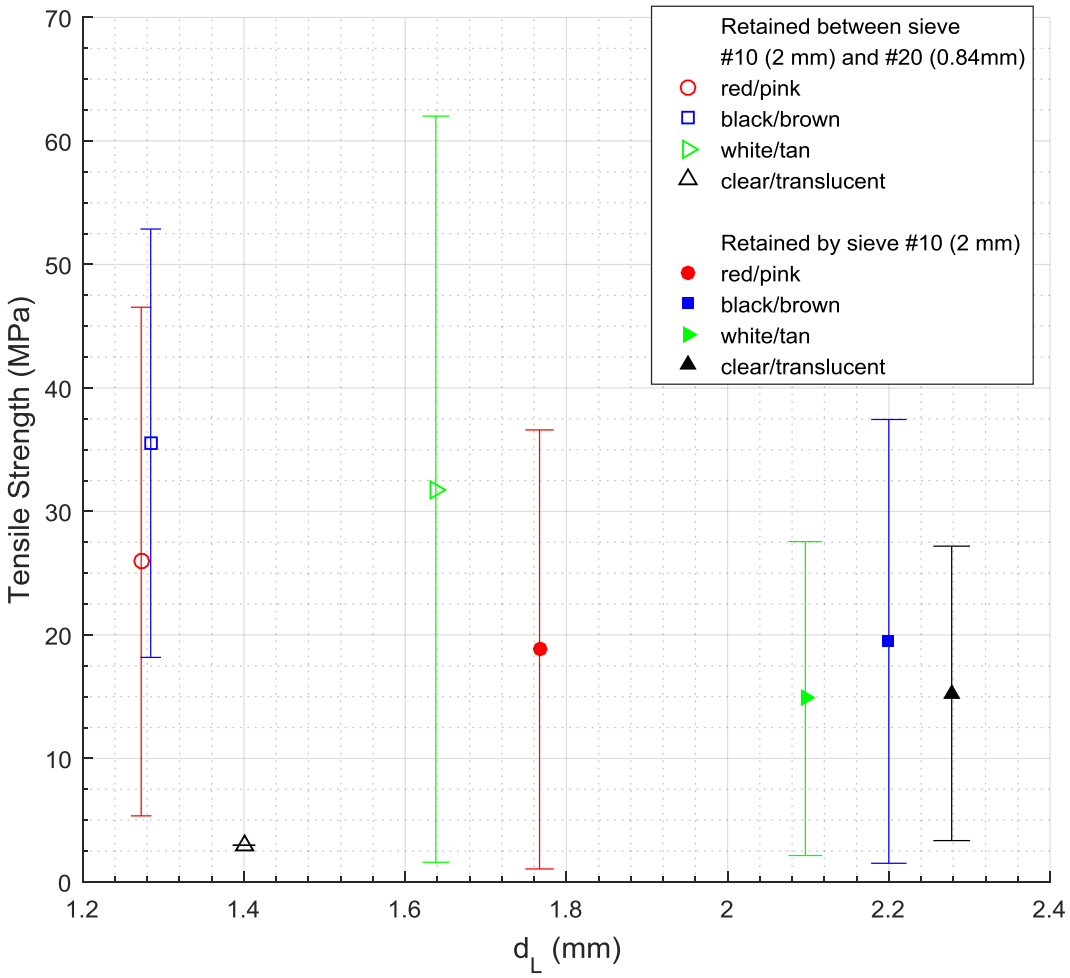


Figure 4-37. Average tensile strength within one standard deviation for other shaped red/pink (major and secondary compounds: quartz, potassium feldspar, and plagioclase feldspar), black/brown (major and secondary compounds: quartz, mica (biotite), tridymite, plagioclase feldspar, potassium feldspar, and calcite), white/tan (major and secondary compounds: quartz, plagioclase feldspar, potassium feldspar, and mica (muscovite)) and clear/translucent (major and secondary compounds: quartz and plagioclase feldspar) particles retained between sieve #10 (2 mm) and #20 (0.84 mm) and by sieve #10 (2 mm)

(2 mm) had the largest tensile strength range while the other shaped clear/translucent particles had the smallest tensile strength range. The other shaped red/pink particles retained between sieve #10 (2 mm) and #20 (0.84 mm) had the smallest average d_L; the other shaped clear/translucent particles retained by sieve #10 (2 mm) had the largest average d_L.

The distribution for the platy, other, rectangular prismatic, spherical, and triangular prismatic shaped particles retained between sieve #10 (2 mm) and #20 (0.84 mm) and by sieve (2 mm) and #20 (0.84 mm) and the platy, other, rectangular prismatic, and spherical shaped particles retained by sieve #10 (2 mm) showed that particles that had smaller d_L fractured at higher tensile strengths. The platy shaped particles in both size categories fractured at higher tensile strengths and smaller d_L, with and without the inclusions of the outliers. The rectangular prismatic shaped particles retained between sieve #10 (2 mm) and #20 (0.84 mm) experienced the greatest change in average d_L and tensile strength with the inclusion of outliers and particles retained by sieve #10 (2 mm) fractured at lower tensile strengths. With and without the inclusion of outliers, triangular prismatic shaped particles in both size categories generally had larger d_L and fractured at lower tensile strengths. Other shaped particles retained between sieve #10 (2 mm) and #20 (0.84 mm) fractured at higher tensile strengths without the inclusion of outliers.

For particle retained between sieve #10 (2 mm) and #20 (0.84 mm), clear/translucent (major and secondary compounds: quartz and plagioclase feldspar) particle fractured at higher tensile strengths shaped as platy, spherical, and triangular prismatic particles; the majority of the platy shaped clear/translucent particles had d_L less than 1.20 mm. White/tan (major and secondary compounds: quartz, plagioclase feldspar, potassium feldspar, and mica (muscovite)) particles fractured at lower tensile strengths shaped as platy, rectangular prismatic, and spherical particles and had larger d_L as platy shaped particles but had smaller d_L as rectangular prismatic,

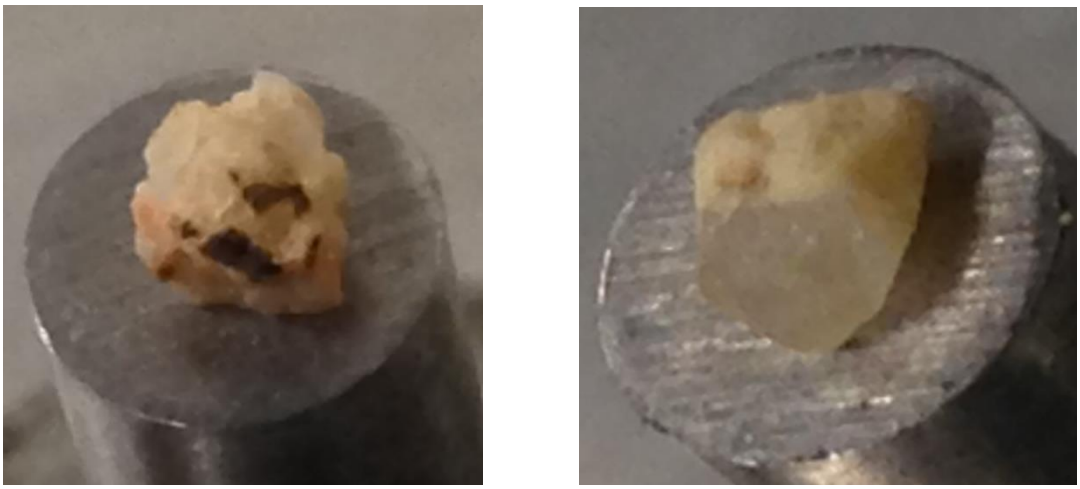
spherical, and triangular prismatic shaped particles. The spherical shaped white/tan particles generally had a d_L between the range of 1.10 and 1.20 mm. Black/brown (major and secondary compounds: quartz, mica (biotite), tridymite, plagioclase feldspar, potassium feldspar, and calcite) particles had larger d_L shaped as rectangular prismatic and spherical particles and fractured at lower tensile strengths shaped as triangular prismatic particles. Red/pink (major and secondary compounds: quartz, potassium feldspar, and plagioclase feldspar) particles fractured at higher tensile strengths shaped as rectangular prismatic particles and had larger d_L shaped as triangular prismatic particles. The distributions of spherical and triangular prismatic shaped particles are relatively constant between the four colored subgroups while the clear/translucent particles are predominantly platy shaped and the red/pink particles are predominantly rectangular prismatic shaped.

For particles retained by sieve #10 (2 mm), platy and rectangular prismatic shaped clear/translucent particles had larger d_L and spherical shaped clear/translucent particles fractured at higher tensile strengths. White/tan particles fractured at lower tensile strengths shaped as platy particles and higher tensile strengths shaped as rectangular prismatic particles. Triangular prismatic shaped white/tan particles had larger d_L while spherical shaped white/tan particles had smaller d_L. Black/brown particles had smaller d_L as platy, rectangular prismatic, and triangular prismatic shaped particles and fractured at high tensile strengths shaped as triangular prismatic particles. Red/pink particle with rectangular prismatic, spherical, and triangular prismatic shaped fractured at lower tensile strengths while red/pink particles with platy shaped particles fractured at higher tensile strengths; rectangular prismatic and spherical shaped red/pink particles had larger d_L.

Overall, the platy shaped particles retained between sieve #10 (2 mm) and #20 (0.84 mm) and by sieve #10 (2 mm) fractured at higher tensile strengths and smaller d_L, regardless of outliers. The triangular prismatic shaped particles retained between sieve #10 (2 mm) and #20 (0.84 mm) and by sieve #10 (2 mm), with the exclusion of outliers, fractured at lower tensile strengths and larger d_L. This implied that particles with smaller d_L will fracture at higher tensile strengths. White/tan platy shaped particles retained between sieve #10 (2 mm) and #20 (0.84 mm) and by sieve #10 (2 mm) fractured at lower tensile strengths; white/tan spherical shaped particles retained between sieve #10 (2 mm) and #20 (0.84 mm) and by sieve #10 (2 mm) had smaller d_L. Clear/translucent spherical shaped particles retained between sieve #10 (2 mm) and #20 (0.84 mm) and by sieve #10 (2 mm) fractured at higher tensile strengths.

4.2.2.4 Effects of Particle Morphology

Particle morphology can be defined based on sphericity and roundness. The determination of sphericity was not feasible based on visual inspection and therefore was not performed. The classification of roundness was performed based on visual inspection on particle angularity rather than a on a numerical classification of roundness; the particles were classified as either subangular or subrounded particles (Alshibli and Alsaleh, 2004). Therefore, the effects of particle morphology will focus on the influence of particle angularity on tensile strength. Subangular particles had a surface with many sharp points and subrounded particles had surfaces that had minimal few sharp points, as shown in Figures 4-38a and 4-38b, respectively. The effects of particle subangular on the tensile strength were examined based on particle size and morphology. It was hypothesized that subangular particles will fracture at lower tensile strengths due less contact points; a lower coordination number indicated that more stress will be concentrated at the contact points because less stress was redistributed onto the particles surface



(a) (b)

Figure 4-38. Particle classified as (a) subangular and (b) subrounded.

(Cavaretta et al. 2010; Todisco et al. 2016). It is acknowledged that coordination number contributes to the fracture behavior of sand particles but due to the limitations of the current experimental set-up, coordination number could not be obtained and therefore was not examined.

Figure 4-39 illustrate the distribution of particle angularity based on minerology, tensile strength, and d_L. Subangular and subrounded particles were denoted with red circular data points and blue triangular data points, respectively.

Figure 4-39a illustrates the distribution of angularity for 61 red/pink (major and secondary compounds: quartz, potassium feldspar, and plagioclase feldspar) particles retained between sieve #10 (2 mm) and #20 (0.84 mm). The distribution was left skewed with an average tensile strength of 30.51 MPa and an average d_L of 1.29 mm. The average tensile strength and d_L for 35 subangular particles was 26.78 MPa and 1.35 mm, respectively; the average tensile strength and d_L for 26 subrounded particles was 35.54 MPa and 1.20 mm, respectively. From the distribution, particles that had smaller d_L fractured at higher tensile strengths, regardless of particle angularity. The subangular and subrounded particles had relatively similar distributions

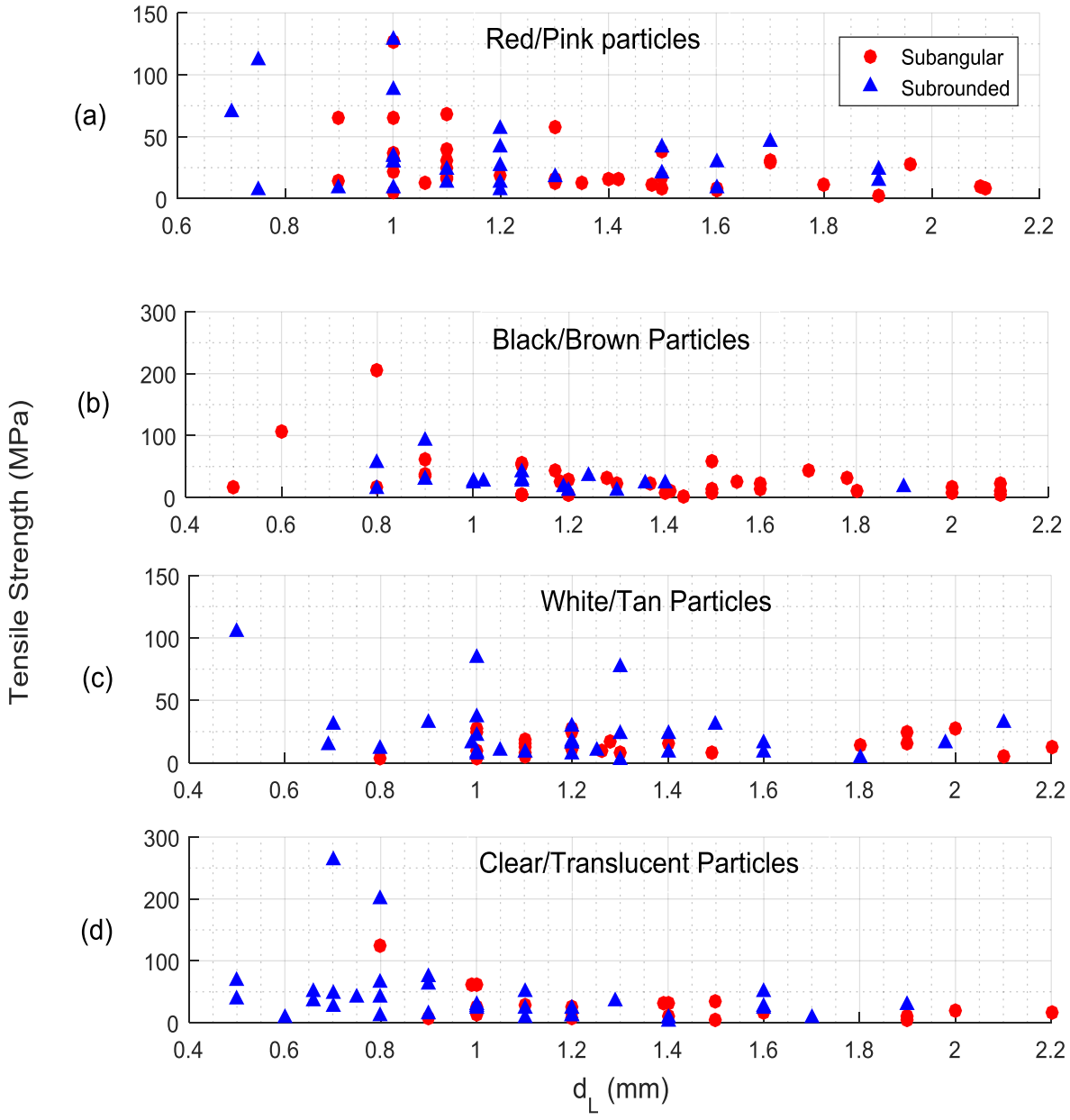


Figure 4-39. Angularity of particles retained between sieve #10 (2 mm) and #20 (0.84 mm) for particles in the (a) red/pink (major and secondary compounds: quartz, potassium feldspar, and plagioclase feldspar), (b) black/brown(major and secondary compounds: quartz, mica (biotite), tridymite, plagioclase feldspar, potassium feldspar, and calcite), (c) white/tan white/tan (major and secondary compounds: quartz, plagioclase feldspar, potassium feldspar, and (d) clear/translucent major and secondary compounds: quartz and plagioclase feldspar)subgroups.

tensile strength and d_L distributions.

Figure 4-39b displays the distribution of angularity for 56 black/brown (major and secondary compounds: quartz, mica (biotite), tridymite, plagioclase feldspar, potassium feldspar, and calcite) particles retained between sieve #10 (2 mm) and #20 (0.84 mm). The distribution was strongly left skewed with an average tensile strength of 28.66 MPa and an average d_L of 1.27 mm. The distribution contains 38 subangular particles with an average tensile strength of 26.04 MPa and an average d_L of 1.34 mm. The remaining 18 particles were subrounded and had an average tensile strength and d_L of 28.77 MPa and 1.12 mm, respectively. As seen in the distribution, there was an outlier at a tensile strength of 204.96 MPa, identified as Particle Black/Brown 25-21_C, shown in Figure 4-14a.1 in Appendix I. With the exclusion of outlier, the distribution the average tensile strength decreased to 25.45 MPa and the average d_L increased to 1.28 mm; the average tensile strength of the subangular particles decreased to 23.89 MPa and the average d_L increased to 1.3 6mm. The subrounded particles are unaffected by the outlier. Based on Figure 4-39b, with and without the outlier, the subangular particles fractured at lower tensile strengths and had larger d_L. Furthermore, regardless of angularity, particles that had larger d_L fractured at lower tensile strengths.

Figure 4-39c depicts the distribution for 56 white/tan (major and secondary compounds: quartz, plagioclase feldspar, potassium feldspar, and mica (muscovite)) particles retained between sieve #10 (2 mm) and #20 (0.84 mm) with an average tensile strength range of 19.38 MPa and an average d_L of 1.27 mm. The distribution was left skewed due to the three outliers at tensile strengths of 75.86, 83.26, and 105.43 MPa, identified as particle White/Tan 25-15_J, White/Tan 25-6_C, and White/Tan 25-17_J, respectively; the uniaxial compression curves for the three outliers were displayed in Figures 4-15a.3, 4-15a.4, and 4-15a.1 in Appendix I. Because

all outlying particles were subrounded particles, the average tensile strength and d_L of the subangular particles were maintained at 14.35 MPa and 1.34 mm, respectively while the average tensile strength of the subrounded particles decreased from 23.74 to 16.58 MPa and the average d_L and increased from 1.21 to 1.24 mm. The distribution of the particles, without the outliers, would be more normally distributed with a tensile strength range from 2.10 to 36.23 MPa, an average of 15.49 MPa, and d_L range from 0.60 to 2.20 mm, with an average of 1.29 mm. With and without the inclusion of outliers, the subrounded particles fractured at higher tensile strengths compared to the subangular particles while the distribution of loading platen size for the two types of particles was relatively similar.

Figure 4-39d displays the distribution for 54 clear/translucent (major and secondary compounds: quartz and plagioclase feldspar) particles retained between sieve #10 (2 mm) and #20 (0.84 mm). The distribution was left skewed with an average tensile strength of 36.84 MPa and an average d_L was 1.15 mm. There are 21 subangular particles with an average tensile strength of 27.42 MPa and an average d_L of 1.34 mm; there were 31 subrounded particles with an average tensile strength of 42.83 MPa and an average d_L of 1.03 mm. The distribution contains 3 outlying particles with a tensile strength of 124.48, 199.90, and 262.11 MPa, identified as particles Clear 25-26_C, Clear 25-42_J, and Clear 25-38_J. In Appendix I, Figures 4-16a.1, 4-22a.3, and 4-39d.1 shows the uniaxial compression curves for particles Clear 25-38_J, Clear 25-42_J, and Clear 25-26_C, respectively. Referring to Figure 4-39a.1, the curve for the Clear 25-26_C particle increased exponential until a sudden decrease in load occurred at approximately 23 N, followed by a linear increase in load until the particle fractured at 79.67 N. It was noted that the particle had possibly fractured at the first peak, but due to the difficulty in ability to perceive particle fracture with the current experimental set-up, the particle continued to sustain load until

a visible fracture occurred at 79.67 N. With the exclusion of the outliers, the average tensile strength decreased to 24.51 MPa while the average d_L increased to 1.17 mm. The average tensile strength of the subangular and subrounded particles decreased to 22.7 and 30.69 MPa, respectively; the average d_L of the subangular and subrounded particles increased to 1.37 and 1.05 mm, respectively. Based on the distribution, the subangular particles had larger d_L compared to subrounded particles; the subrounded particles fractured at higher tensile strengths compared to the subangular particles, regardless of outliers.

Table 4-15 summarizes the number of particles and average d_L and tensile strengths for particles retained between sieve #10 (2 mm) and #20 (0.84 mm) based on the distribution in Figure 4-39. The subangular particles had larger d_L compared to the subrounded particles and lower tensile strengths, regardless of outliers. The d_L of the subangular particles in the red/pink, brown/black, white/tan, and clear/translucent subgroups averaged approximately 1.34 mm. For the subrounded particles, the red/pink and white/tan particles had larger and similar d_L; the clear/translucent particles had smaller d_L. The tensile strengths of subangular red/pink, black/brown, and clear/translucent particles are higher and similar while the tensile strengths of the white/tan particles are lower. For the subrounded particles, the tensile strengths of the clear/translucent particles were higher while the tensile strengths of the white/tan particles were smaller, on average. Furthermore, red/pink and black/brown particles had more subangular particles while white/tan particle had a relatively even distribution of both types of particles and clear/translucent particles had more subrounded particles. The black/brown particles had approximately 2xs more subrounded particles than subangular particles.

Table 4-15. Summary of particles angularity for particles retained between sieve #10 (2 mm) and #20 (0.84 mm) based on colored subgroups

Colored Subgroups	**Subangular Particles**			**Subrounded Particles**		
	Number of Particles	***d_L (mm)***	***Average Tensile Strength (MPa)***	***Number of Particles***	***d_L (mm)***	***Average Tensile Strength (MPa)***
Red/Pink *(major and secondary compounds: quartz, potassium feldspar, and plagioclase feldspar)*	35	1.35	26.78	26	1.20	35.54
Black/Brown *(major and secondary compounds: quartz, mica (biotite), tridymite, plagioclase feldspar, potassium feldspar, and calcite)*	38 (37)	1.34 (1.36)	26.04 (23.89)	18	1.10	28.77
White/Tan *(major and secondary compounds: quartz, plagioclase feldspar, potassium feldspar, and mica (muscovite))*	26	1.34	14.35	30 (27)	1.21 (1.24)	23.74 (16.58)

Table 4-15 Continued

Colored Subgroups	Subangular Particles			Subrounded Particles		
	Number of Particles	***d_L (mm)***	***Average Tensile Strength (MPa)***	***Number of Particles***	***d_L (mm)***	***Average Tensile Strength (MPa)***
Clear/Translucent *(major and secondary compounds: quartz and plagioclase feldspar)*	21 (20)	1.34 (1.37)	27.42 (22.57)	33 (31)	1.03 (1.05)	42.83 (30.69)

Figure 4-40 and 4-41 display the average d_L and tensile strength, without outliers, for subangular and subrounded particles retained between sieve #10 (2 mm) and #20 (0.84 mm) based on mineralogy and size. The circle data points, square data points, right sided triangle data points, and triangle data points represent the rthe red/pink (major and secondary compounds: quartz, potassium feldspar, and plagioclase feldspar), black/brown (major and secondary compounds: quartz, mica (biotite), tridymite, plagioclase feldspar, potassium feldspar, and calcite), white/tan (major and secondary compounds: quartz, plagioclase feldspar, potassium feldspar, and mica (muscovite)) and clear/translucent (major and secondary compounds: quartz and plagioclase feldspar) particles, respectively; the unfilled data points represent the subangular particles and the filled data points represent the subrounded particles. As shown in Figure 4-40, the d_L range for the subrounded red/pink, white/tan, and clear/translucent particles are relatively similar while the subrounded black/brown particles had the smallest d_L range. This trend is also observed for the subangular particles. This implied that the subangular and subrounded black/brown particles had little variation in d_L. The average d_L for the subangular black/brown particles was the smallest; the average d_L for the subangular clear/translucent particles was the largest. The average tensile strength for the subrounded red/pink particles was the highest; the average tensile strength for the subangular white/tan particle was the lowest. As depicted in Figure 4-41, the tensile strengths range for the subangular and subrounded red/pink particles were the largest while the tensile strength range for the subangular and subrounded white/tan particles were the smallest. The average tensile strengths for the subrounded and subangular red/pink particles were the highest while the average tensile strengths for the subrounded and subangular white/tan particles were the lowest. This implies that the subrounded and subangular red/pink particles were the strongest particles with the most variation in tensile strengths while

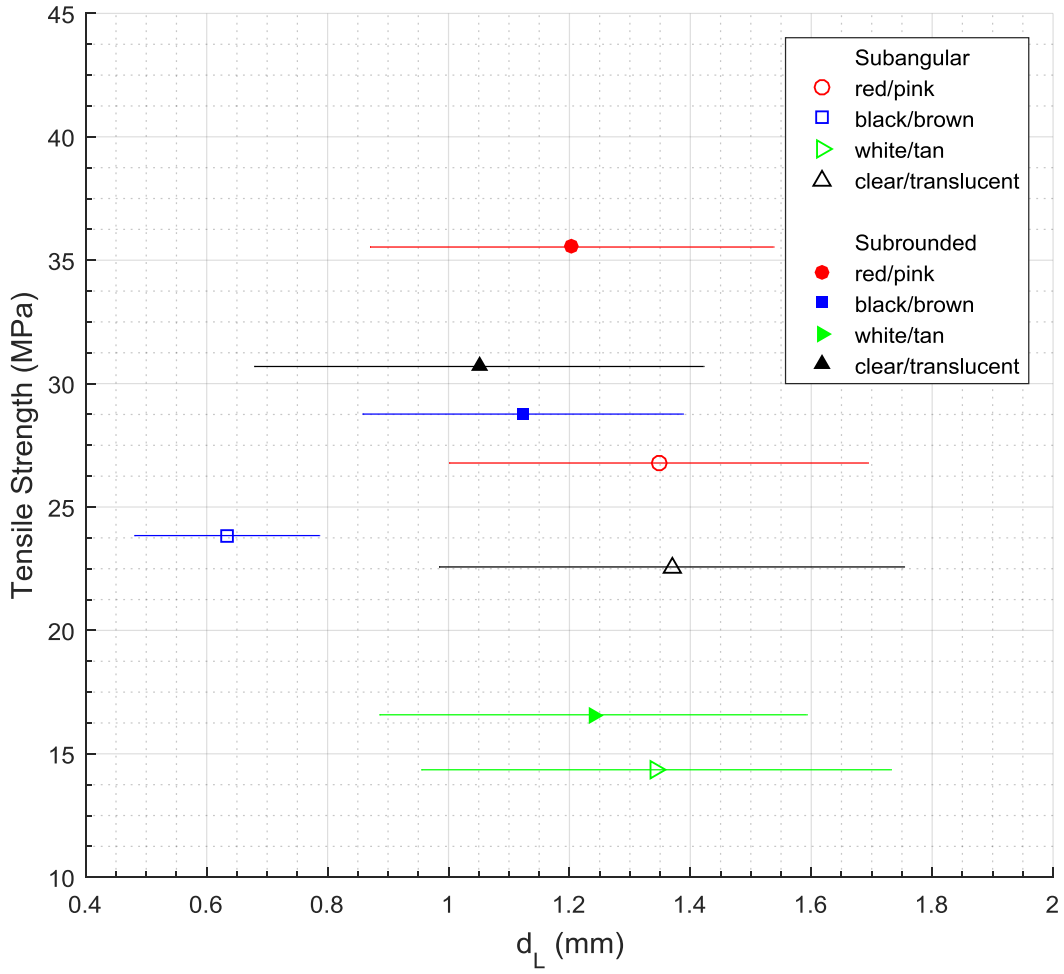


Figure 4-40. Average d_L within one standard deviation for subangular and subrounded particles, without outliers, retained between sieve #10 (2 mm) and #20 (0.84 mm) based on the red/pink (major and secondary compounds: quartz, potassium feldspar, and plagioclase feldspar), black/brown (major and secondary compounds: quartz, mica (biotite), tridymite, plagioclase feldspar, potassium feldspar, and calcite), white/tan (major and secondary compounds: quartz, plagioclase feldspar, potassium feldspar, and mica (muscovite)) and clear/translucent (major and secondary compounds: quartz and plagioclase feldspar) subgroups

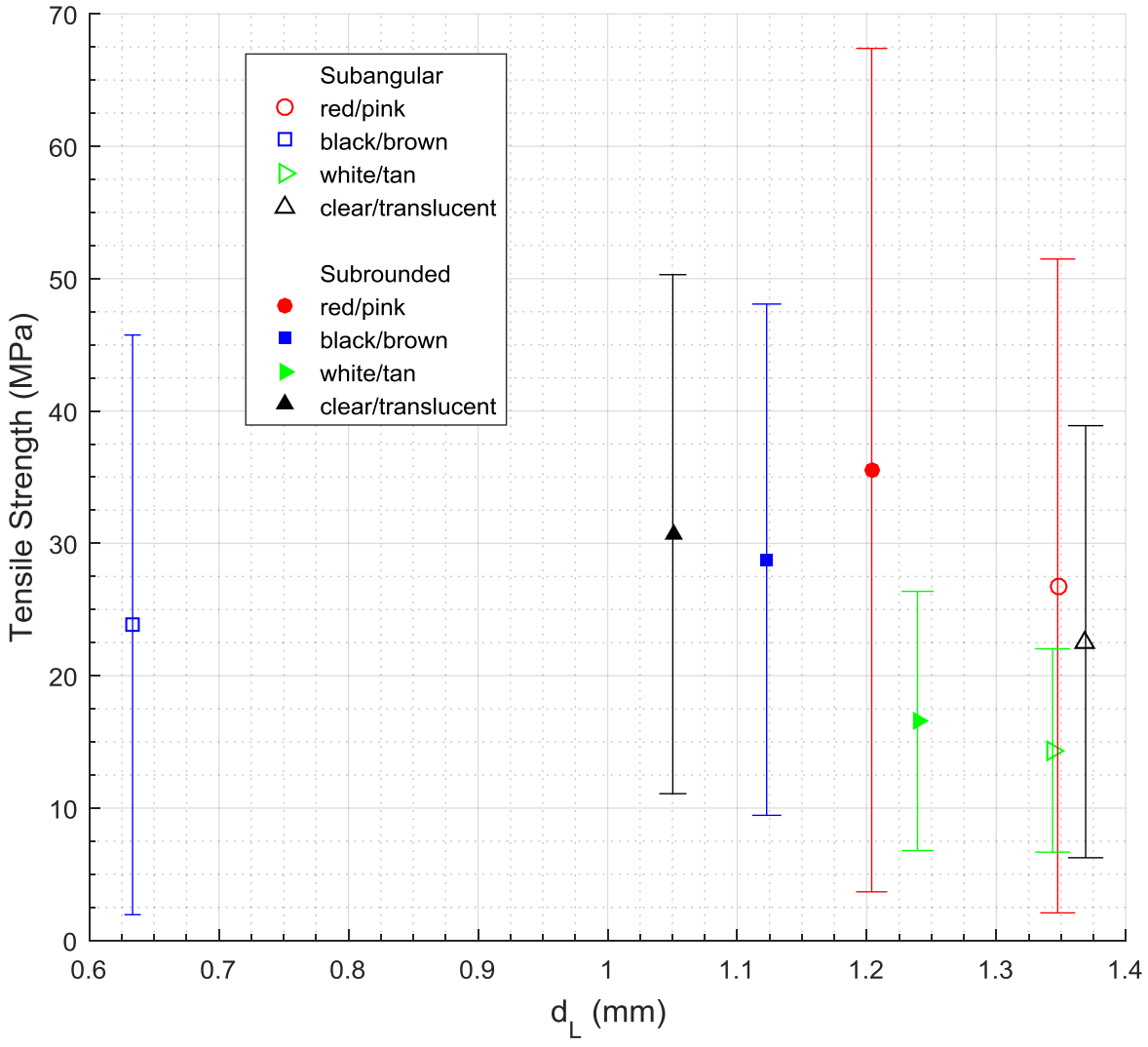


Figure 4-41. Average tensile strength within one standard deviation for subangular and subrounded particles, without outliers, retained between sieve #10 (2 mm) and #20 (0.84 mm) based on the red/pink (major and secondary compounds: quartz, potassium feldspar, and plagioclase feldspar), black/brown (major and secondary compounds: quartz, mica (biotite), tridymite, plagioclase feldspar, potassium feldspar, and calcite), white/tan (major and secondary compounds: quartz, plagioclase feldspar, potassium feldspar, and mica (muscovite)) and clear/translucent (major and secondary compounds: quartz and plagioclase feldspar) subgroups

the subrounded and subangular white/tan particles were the weakest with the least variation in tensile strengths.

Figure 4-42 illustrate the distribution of particle angularity based on minerology, tensile strength, and d_L. Subangular and subrounded particles were denoted with red circular data points and blue triangular data points, respectively.

Figure 4-42a illustrates the distribution of angularity for 40 red/pink (major and secondary compounds: quartz, potassium feldspar, and plagioclase feldspar) particles retained between by #10. The distribution was left skewed with an average tensile strength and d_L of 14.64 MPa and 2.34 mm, respectively. The average tensile strength and d_L for the 11 subangular particles was 8.95 MPa and 2.29 mm, respectively. The average tensile strength and dL for the 29 subangular particles was 16.80 MPa and 2.36 mm, respectively. There was also an outlier at a tensile strength of 84.05 MPa, identified as particle Red/Pink 25-11_J, shown in Figure 4-13b.1 shown in Appendix I. The removal of the outlier decreased the average tensile strength of the distribution to 12.86 MPa and increased the average d_L to 2.37 mm. The average tensile strength and d_L of the subangular particles were not affected while the average tensile strength of the subrounded particles decreased to 14.39 MPa and increased to 2.40 mm. Based on the distribution, and regardless of the outlier, the subrounded particles fractured at higher tensile strengths and larger d_L; particles that had smaller d_L fractured at higher tensile strengths while the particles that had larger d_L fractured at lower tensile strengths.

Figure 4-42b depicts the distribution for 82 black/brown (major and secondary compounds: quartz, mica (biotite), tridymite, plagioclase feldspar, potassium feldspar, and calcite) particles, 26 subangular particles and 56 subrounded particles, retained by sieve #10

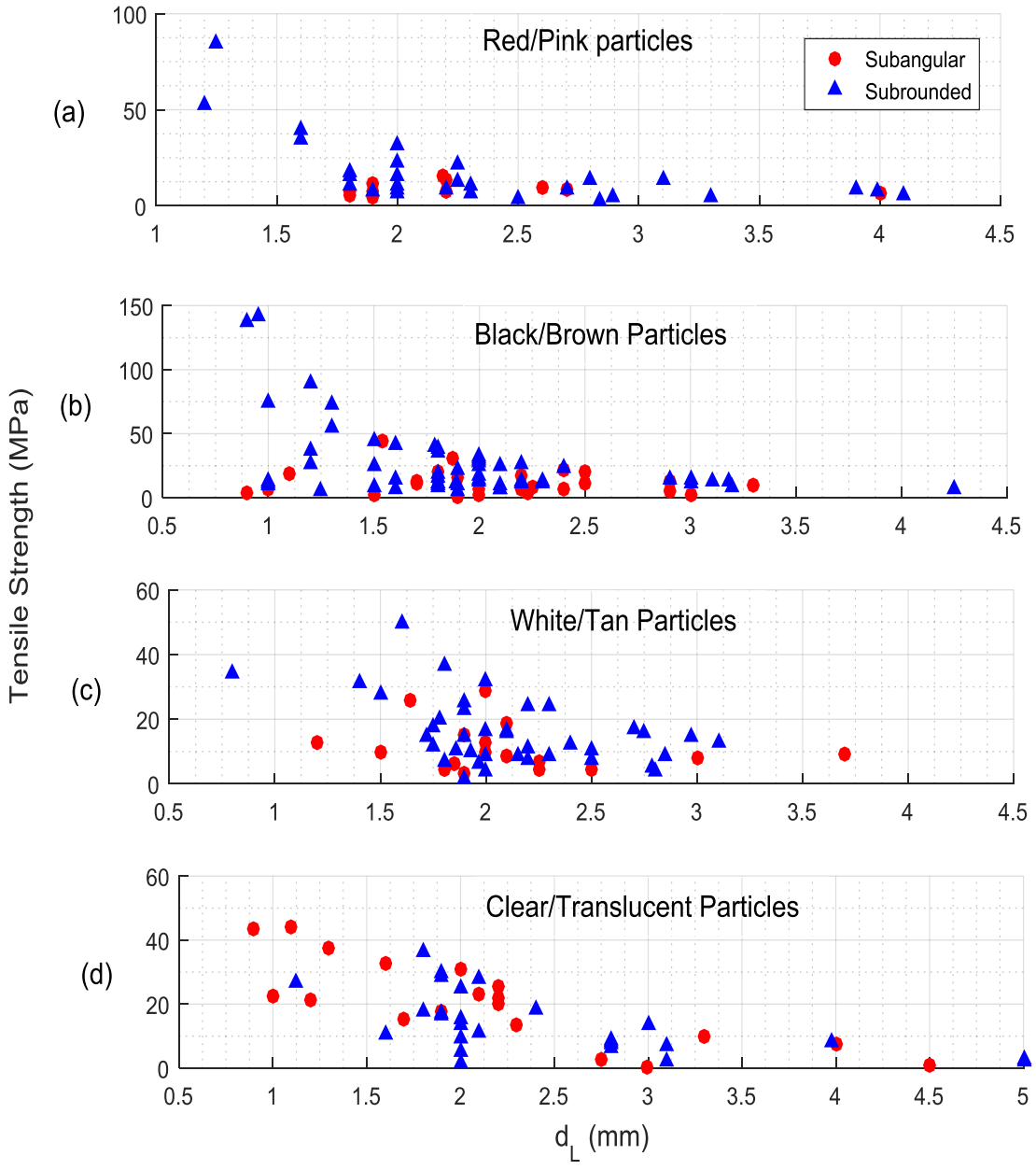


Figure 4-42. Angularity of particles retained by sieve #10 (2 mm) for particles in the (a) red/pink (major and secondary compounds: quartz, potassium feldspar, and plagioclase feldspar), (b) black/brown (major and secondary compounds: quartz, mica (biotite), tridymite, plagioclase feldspar, potassium feldspar, and calcite), (c) white/tan (major and secondary compounds: quartz, plagioclase feldspar, potassium feldspar, and mica (muscovite)) and (d) clear/translucent (major and secondary compounds: quartz and plagioclase feldspar) subgroups

(2 mm). The distribution had an average tensile strength of 21.65 MPa; the subangular and subrounded particles had an average tensile strength of 12.14 and 26.07 MPa, respectively. The average d_L was 1.96 mm; the subangular and subrounded particles had an average d_L of 2.06 and 1.91 MPa, respectively. The distribution was left skewed with a right sided tail and contains 2 outliers, the first at a tensile strength of 137.43 MPa, identified as Black/Brown 25-36_J, and the second at a tensile strength of 141.62 MPa, identified as Black/Brown 25-33_C, shown in Figures 4-14b.1 and 4-14b.2, respectively, in Appendix I. The exclusion of these outliers from the distribution decreased the tensile strength to 18.71 MPa and increased the average d_L to 1.98 mm. The average tensile strength of the subangular particles was not affected while the average tensile strength of the subrounded particles decreased to 21.87 MPa; the average d_L of the subangular particles was not affected while the average d_L of the subrounded particles increased to 1.95 mm. Based on the distribution, with and without the inclusion of outliers, the subangular particles fractured at lower tensile strengths while the subrounded particles fractured at higher tensile strengths; the distribution of d_L was relatively even amongst subangular and subrounded particles. Particle that had smaller d_L fractured at higher tensile strengths.

Figure 4-42c displays the distribution for 56 white/tan (major and secondary compounds: quartz, plagioclase feldspar, potassium feldspar, and mica (muscovite)) particles in which 17 were subangular and 39 were subrounded. The distribution had an average tensile strength of 14.50 MPa; the subangular and subrounded particles had an average tensile strength of 11.13 and 15.96 MPa, respectively. The d_L average was 2.10 mm; the subangular and subrounded particles had an average d_L of 2.10 and 2.11 MPa, respectively. The distribution had one outlier at a tensile strength of 49.39 MPa, identified as White/Tan 25-3_C, shown in Figure 4-15b.1 in Appendix I. The exclusion of the outlying particle decreased the average tensile strength for the

distribution and subrounded particles to 13.86 and 15.08 MPa, respectively; the average d_L for the distribution and subrounded particles increased to 2.11 and 2.12 mm, respectively; the subangular particles were not affected. Based on the left skewed distribution, with and without the outlier, the subrounded particles fractured at higher tensile strengths; the distribution of loading platen size was relatively constant between the subangular and subrounded particles.

Figure 4-42d shows the distribution 46 clear/translucent (major and secondary compounds: quartz and plagioclase feldspar) particles containing 19 subangular and 27 subrounded particles. The distribution was slightly left skewed with an average tensile strength of 16.65 MPa and an average d_L of 2.35 mm. The subangular particles had an average tensile strength and d_L of 20.54 MPa and 2.17 mm while the subrounded particles had an average tensile strength and d_L of 13.91 MPa and 2.48 mm. Based on the distribution, there was an overall negative correlation between size and tensile strength, in which particles that had larger d_L fractured at lower tensile strengths while particles with a smaller d_L fractured at higher tensile strengths, regardless of angularity. The subangular particles fractured at higher tensile strengths compared to subrounded particles; the distribution of d_L was similar between the subangular and subrounded particles.

Table 4-16 summarizes the number of particles and the average d_L and tensile strengths for particles retained by sieve #10 (2 mm) based on the distributions in Figure 4-42. Particles that had smaller d_L fractured at higher tensile strengths, regardless of angularity. The number of subrounded particles in all subgroups was generally higher compared to subangular particles; red/pink, black/brown and white/tan particles had 3xs, 2xs, and 2xs more subrounded particle compared to subangular particles, respectively. Subangular particles in the black/brown subgroup

Table 4-16. Summary of particles angularity for particles retained by sieve #10 (2 mm) based on colored subgroups

Colored Subgroups	**Subangular Particles**			**Subrounded Particles**		
	Number of Particles	***d_L (mm)***	***Average Tensile Strength (MPa)***	***Number of Particles***	***d_L (mm)***	***Average Tensile Strength (MPa)***
Red/Pink *(major and secondary compounds: quartz, potassium feldspar, and plagioclase feldspar)*	11	2.29	8.95	29 (28)	2.36 (2.40)	16.80 (14.39)
Black/Brown *(major and secondary compounds: quartz, mica (biotite), tridymite, plagioclase feldspar, potassium feldspar, and calcite)*	26	2.06	12.14	56 (54)	1.91 (1.95)	26.07 (21.87)
White/Tan *(major and secondary compounds: quartz, plagioclase feldspar, potassium feldspar, and mica (muscovite))*	17	2.10	11.13	39 (38)	2.11 (2.12)	15.96 (15.08)

Table 4-16 Continued

Colored Subgroups	**Subangular Particles**			**Subrounded Particles**		
	Number of Particles	***d_L (mm)***	***Average Tensile Strength (MPa)***	***Number of Particles***	***d_L (mm)***	***Average Tensile Strength (MPa)***
Clear/Translucent *(major and secondary compounds: quartz and plagioclase feldspar)*	19	2.17	20.54	27	2.48	13.91

had larger d_L while subrounded particles in the red/pink and clear/translucent subgroups had larger d_L; particles in the white/tan subgroup had relatively equivalent d_L. Subangular clear/translucent particles had higher tensile strengths while subrounded red/pink, brown/black, and white/tan particles had higher tensile strengths; the tensile strengths of the subrounded red/pink and brown/black are approximately double the tensile strengths of the subangular particles.

Figure 4-43 and 4-44 display the average d_L and tensile strength, without outliers, for subangular and subrounded particles retained by sieve #10 (2 mm) based on mineralogy and size. The circle data points, square data points, right sided triangle data points, and triangle data points represent the red/pink (major and secondary compounds: quartz, potassium feldspar, and plagioclase feldspar), black/brown (major and secondary compounds: quartz, mica (biotite), tridymite, plagioclase feldspar, potassium feldspar, and calcite), white/tan (major and secondary compounds: quartz, plagioclase feldspar, potassium feldspar, and mica (muscovite)) and clear/translucent (major and secondary compounds: quartz and plagioclase feldspar) particles, respectively; the unfilled data points represent the subangular particles and the filled data points represent the subrounded particles.

As illustrated in Figure 4-43, the d_L range of the subangular and subrounded clear/translucent particles was the largest while the d_L range of the subangular and subrounded white/tan particles was the smallest. This indicated greater variation in d_L for the subangular and subrounded clear/translucent particles and less variation in d_L for the subangular and subrounded white/tan particles. The subrounded black/brown particles had the highest average tensile strength while the subangular red/pink particles had the lowest average tensile strength. Referring to Figure 4-44, the tensile strength range for the subrounded black/brown particles was

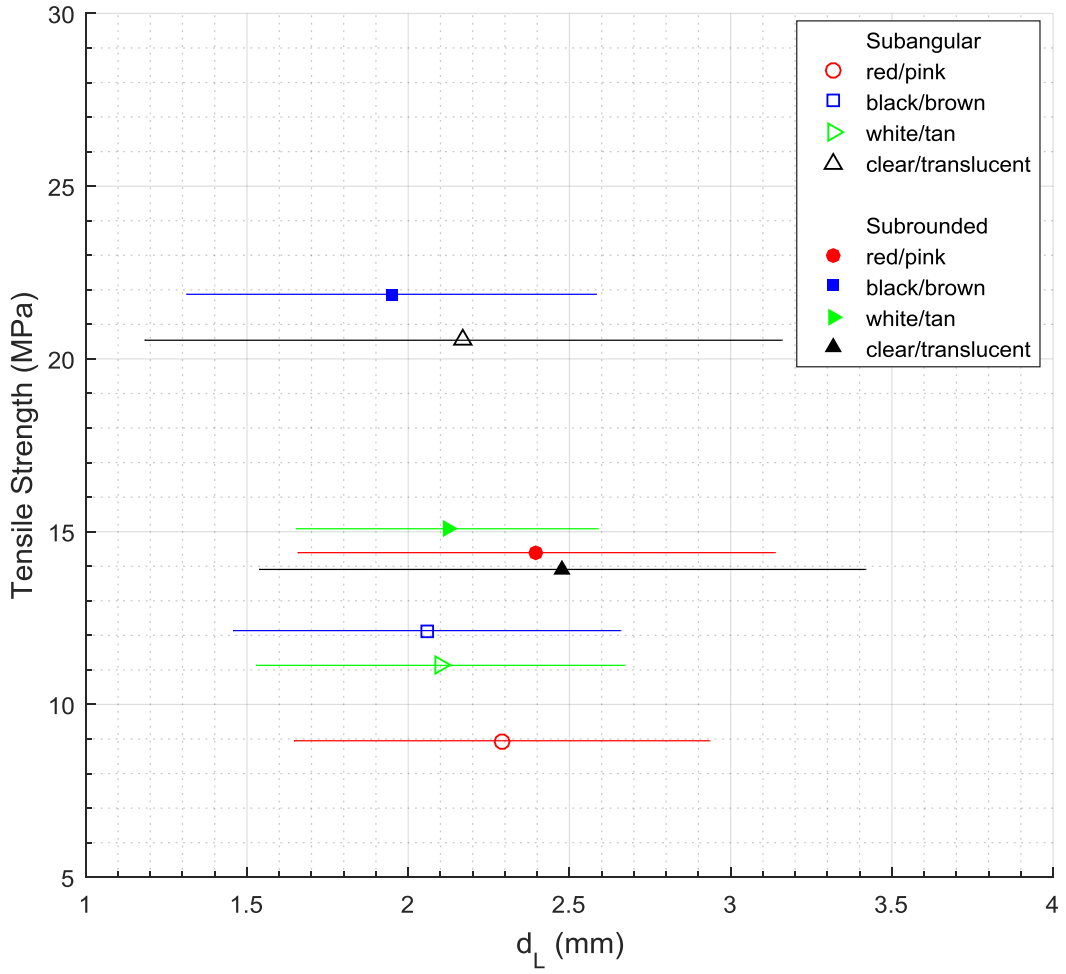


Figure 4-43. Average d_L within one standard deviation for subangular and subrounded particles, without outliers, retained by sieve #10 (2 mm) based on the red/pink (major and secondary compounds: quartz, potassium feldspar, and plagioclase feldspar), black/brown (major and secondary compounds: quartz, mica (biotite), tridymite, plagioclase feldspar, potassium feldspar, and calcite), white/tan (major and secondary compounds: quartz, plagioclase feldspar, potassium feldspar, and mica (muscovite)) and clear/translucent (major and secondary compounds: quartz and plagioclase feldspar) subgroups

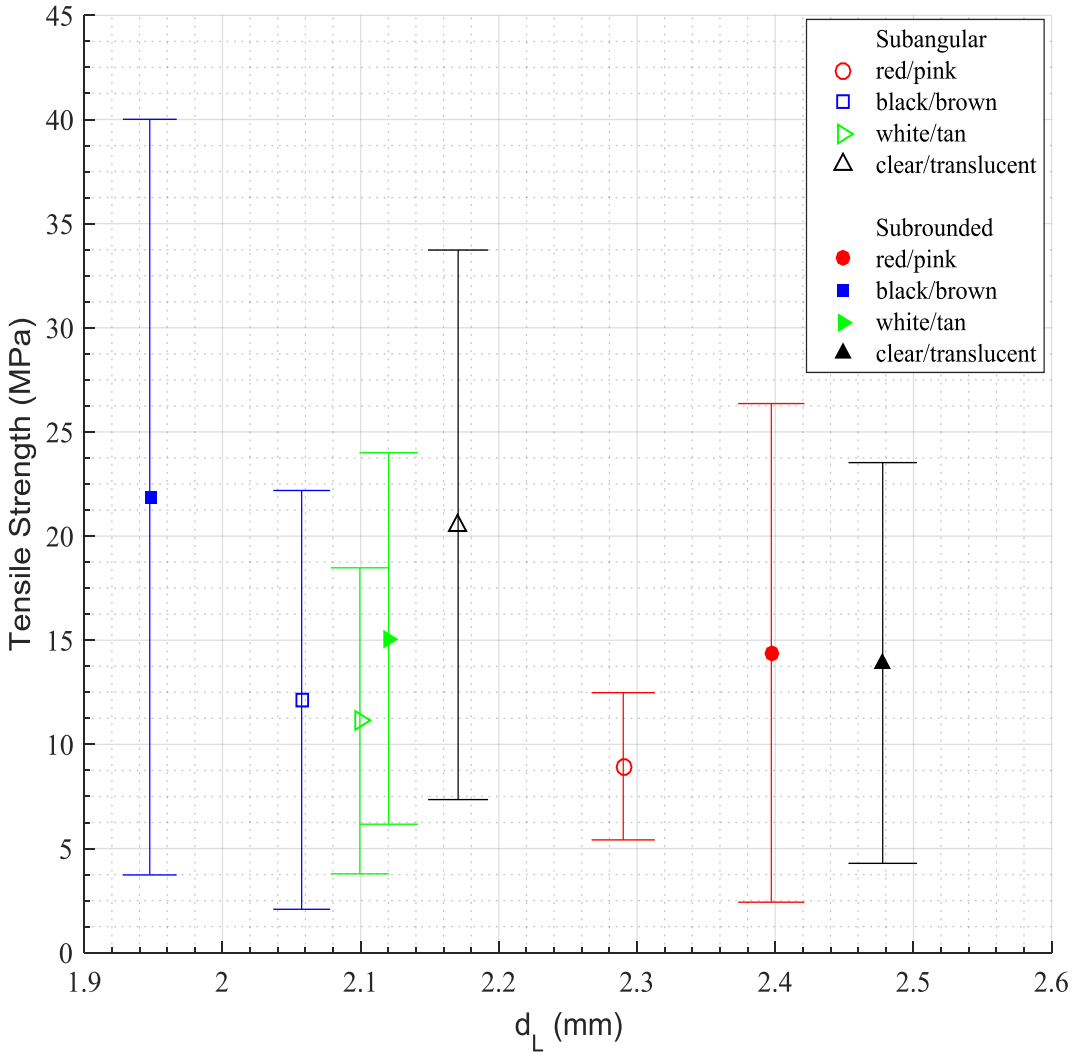


Figure 4-44. Average tensile strength within one standard deviation for subangular and subrounded particles, without outliers, retained by sieve #10 (2 mm) based on the red/pink (major and secondary compounds: quartz, potassium feldspar, and plagioclase feldspar), black/brown (major and secondary compounds: quartz, mica (biotite), tridymite, plagioclase feldspar, potassium feldspar, and calcite), white/tan (major and secondary compounds: quartz, plagioclase feldspar, potassium feldspar, and mica (muscovite)) and clear/translucent (major and secondary compounds: quartz and plagioclase feldspar) subgroups

the largest, which indicated more variation in tensile strengths. The subrounded white/tan particles had the smallest tensile strength range, which indicated little variation in tensile strength. The subangular clear/translucent particles had the largest tensile strength range, which implied more variation in tensile strengths, while the subangular red/pink particles had the smallest tensile strength range, which implied less variation in tensile strengths. The subrounded black/brown particles had the highest average tensile strength and lowest average d_L. The subangular red/pink particles had the lowest average tensile strength and the subrounded clear/translucent particles had the highest average d_L.

Overall, the effects of particle angularity on d_L and tensile strength was more prominent for particles retained between sieve #10 (2 mm) and #20 (0.84 mm) compared to particles retained by sieve #10 (2 mm). Subangular red/pink and white/tan particle fractured at lower tensile strengths in both size categories; particles retained between sieve #10 (2 mm) and #20 (0.84 mm) had smaller d_L while particles retained by sieve #10 (2 mm) had larger d_L. In both size categories, subangular black/brown particles fractured at lower tensile strengths while subrounded black/brown particles had smaller d_L. Subangular clear/translucent particles retained between sieve #10 (2 mm) and #20 (0.84 mm) had smaller d_L and fractures at higher tensile strengths; the opposite was true for clear/translucent particles retained by sieve #10 (2 mm). The number of subangular particles generally varied based on subgroups and particle size categories; black/brown particles in both size categories had approximately 2xs more subrounded particles compared to subangular particles.

4.2.2.5 Effects of Particle Surface Texture

The surface texture of the particle was classified as rough or smooth through visual inspection. A particle was classified as rough if, to the naked eye, the surface was coarse and

covered with many crests and valleys, as depicted in Figure 4-45. A particle was classified as smooth if, to the naked eye, the surface was leveled and does not contain or contain very meniscal crests or troughs, as shown in Figure 4-46. A particle that contained both types of surfaces or is not classified as others. It is predicted that particles with smooth surfaces will fracture at lower tensile strengths due to the ability to sustain larger loads as a result of lower stress concentrations on the surface (Wang and Coop 2016).

Analysis on surface texture will be performed predominantly on surfaces classified as rough or smooth because surfaces classified as other contains unclassified surfaces and therefore was not an accurate representation of the relationship between surface texture and tensile strength. The effects of particle surface texture on the tensile strength were examined based on particle size and morphology. The surface texture of particles retained between sieve #10 (2 mm)

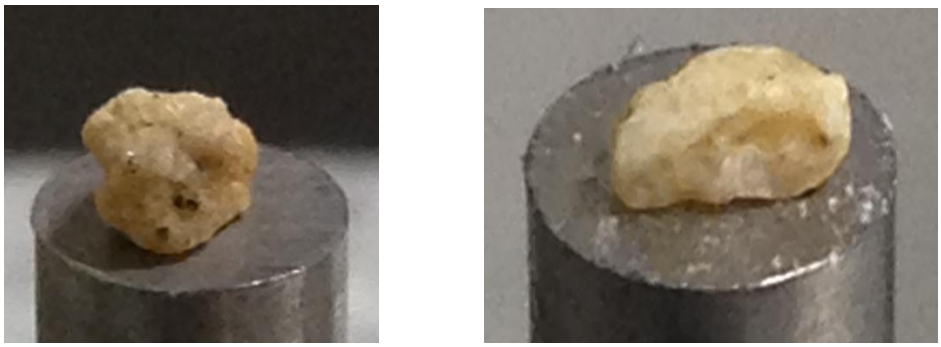


Figure 4-45. Particles classified as rough.



Figure 4-46. Particles classified as smooth.

and #20 (0.84 mm) and by sieve #10 (2 mm), based on the red/pink, black/brown, white/tan, and clear/translucent subgroups are shown in Figures 4-47 and 4-48, respectively. The red circle data points represent the rough particles, the blue square data points represent the smooth particles, and the black diamond data points represent the other particles. Other particles will not be discussed in detail due to the lack of classification for them.

Figure 4-47a displays the surface texture distribution for red/pink (major and secondary compounds: quartz, potassium feldspar, and plagioclase feldspar) particles retained between sieve #10 (2 mm) and #20 (0.84 mm). No correlation exists between surface texture and tensile strength as the data was distributed randomly but particles that had larger d_L fractured at lower tensile strength while smaller particles fractured at higher tensile strength, regardless of surface texture. The distribution contains 61 particles with an average d_L of 1.29 mm and average tensile strength of 30.51 MPa; there were 22 particles with a rough surface texture, 29 particles with a smooth surface texture, and 10 particles with an other type of surface texture. The average d_L for particles with a rough, smooth, and other surface texture were 1.28, 1.24, and 1.41mm, respectively; the average tensile strengths for the particle with a rough, smooth, and other surface texture were 29.17, 32.13, and 28.77 MPa, respectively. Based on the average d_L and tensile strength of the distribution, the particles with a rough surface texture are, on average, larger while the particles with a smooth surface texture, on average, fractured at higher tensile strengths.

Figure 4-47b illustrates the distribution of surface texture for the black/brown (major and secondary compounds: quartz, mica (biotite), tridymite, plagioclase feldspar, potassium feldspar, and calcite) particles retained retained between sieve #10 (2 mm) and #20 (0.84 mm). A majority of rough particles had a larger d_L compared to smooth particles while a majority of smooth

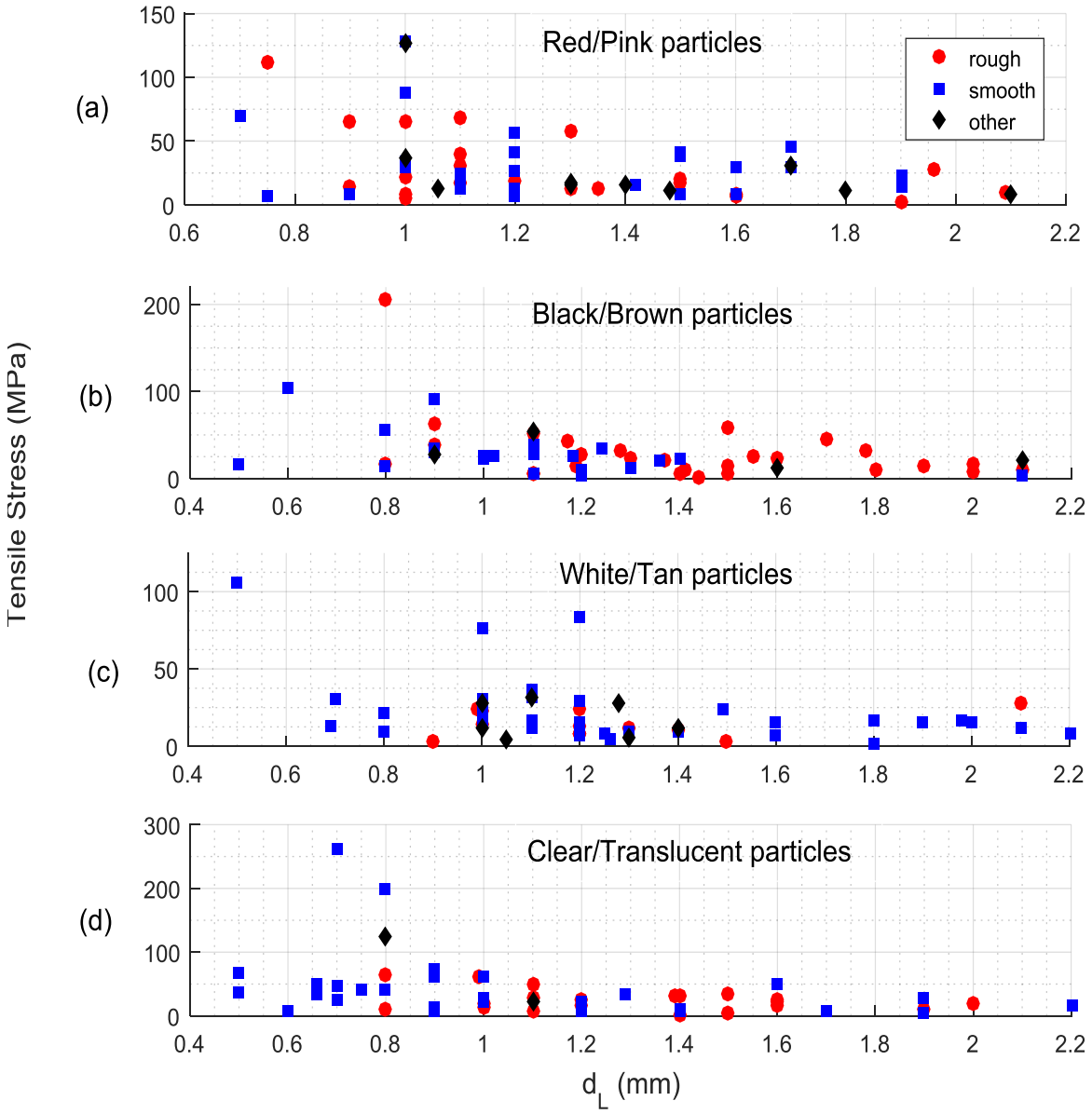


Figure 4-47. Surface texture of particles retained between sieve #10 (2 mm) and #20 (0.84 mm) for particles in the (a) red/pink (major and secondary compounds: quartz, potassium feldspar, and plagioclase feldspar), (b) black/brown (major and secondary compounds: quartz, mica (biotite), tridymite, plagioclase feldspar, potassium feldspar, and calcite), (c) white/tan (major and secondary compounds: quartz, plagioclase feldspar, potassium feldspar, and mica (muscovite)) and (d) clear/translucent (major and secondary compounds: quartz and plagioclase feldspar) subgroups.

particles fractured at higher tensile strengths compared to rough particles; this was expected because particles that had larger d_L fractured at lower tensile strengths, as indicated by Figure 4-47b. The distribution has 56 particles with an average diameter of 1.27 mm and average tensile strength of 28.66 MPa. There are 28 rough particles with an average d_L and tensile strength of 1.41 mm and 29.40 MPa, respectively, 24 smooth particles with an average d_L and tensile strength of 1.09 mm and 27.69 MPa, respectively, and 4 other particles with an average d_L and tensile strength of 1.42 mm and 29.28 MPa, respectively. The rough particles fractured at a higher tensile strength than expected due to a particle with a tensile strength of 204.97 MPa, identified as particle Black/Brown 25-21_C, shown in Figure 4-14a.1 in Appendix I. With the exclusion of the outlier, the average d_L increased to 1.28 mm and the average tensile strength decreased to 25.63 MPa for distribution; the average d_L increased to 1.43 mm and average tensile strength decreased to 22.90 MPa for rough particles; smooth and other particles were not affected. The rough particles generally had larger d_L compared to the smooth particles. With the outlier, the average tensile strength of the rough particles was higher compared to the smooth particles; without the outlier, the average tensile strength of the smooth particles was higher.

Figure 4-47c displays the distribution for the white/tan (major and secondary compounds: quartz, plagioclase feldspar, potassium feldspar, and mica (muscovite)) particles retained between sieve #10 (2 mm) and #20 (0.84 mm). The smooth particles predominantly had larger d_L and fractured at higher tensile strengths compared to the rough particles; particles that had larger d_L fractured at lower tensile strengths. The distribution showed that, with the exclusion of the 3 particles with the highest tensile strength, the white/tan particles predominantly fractured at a tensile strength below 50MPa. The distribution contains 56 particles with an average d_L of 1.27 mm and average tensile strength of 19.38 MPa. Within the distribution were 13 rough particles

with an average d_L of 1.24mm and average tensile strength of 13.70 MPa, 36 smooth particles with an average d_L of 1.30mm and average tensile strength of 21.87, and 7 other particles with an average d_L of 1.16mm and tensile strength of 17.12 MPa. The smooth particles had a higher average tensile strength due to the three outlying particles with a tensile strength of 75.86, 83.26, and 105.43 MPa, identified as White/tan 25-15_J, White/Tan 25-6_C, and White/Tan 25-17_J, respectively, shown in Figure 4-15a.3, 21a.4, and 21a.1 in Appendix I, respectively; the remaining 53 particles (both rough and smooth) had tensile strengths less than 50 MPa. Based on the average d_L and tensile strength of the distribution, rough particles generally had smaller d_L compared to the smooth particles; smooth particles generally fractured at higher tensile strengths compared to the rough particles. This implied that the white/tan particles had a high probability of containing smooth particles with various d_L sizes, causing the tensile strength to vary greatly, but will generally fracture at low tensile strengths.

Figure 4-47d illustrates the distribution for the clear/translucent (major and secondary compounds: quartz and plagioclase feldspar) particles retained between sieve #10 (2 mm) and #20 (0.84 mm). The distribution contained 51 particles that fractured prior to a tensile strength of 100 MPa, with the exception of the 3 particles with tensile strengths of 124.48, 199.90, and 262.11 MPa, identified as Clear 25-26_C, Clear 25-42_J, and Clear 25-38_C, respectively, shown in Figures 4-39d.1, 4-22a.3, and 4-16a.1 in Appendix I, respectively; more particles with a smooth surface texture had smaller d_L compared to particles with a rough or other surface texture. Particles with smooth surface textures fractured at higher tensile strengths. The distribution had a total of 54 particles with an average d_L of 1.15 mm and average tensile strength of 36.84 MPa; there were 20 rough particles, 32 smooth particles, and 2 other particles. The average d_L for the rough, smooth, and other particles are 1.31, 1.07, and 1.95 mm,

respectively. The average tensile strengths for the rough, smooth, and other particles are 24.95, 41.95, and 74.02 MPa, respectively. The smooth particles had a higher average tensile strength than the rough particles due to the 2 outlying smooth particles. With the exclusion of these two particles, the average d_L and tensile strength for the smooth particle would be 1.09 mm and 29.35 MPa, respectively. With or without the outlier and based on the average d_L and tensile strength of the distribution, the smoother particles are smaller and stronger compared to the rougher particles.

Table 4-17 summarizes the number of particles and the average d_L and tensile strength for the distributions in Figure 4-47. The red/pink, white/tan, and clear/translucent particles contained predominantly smooth particles while black/brown particles contained predominantly rough particles; white/tan particles had 2xs more smooth particles than rough particles. Rough red/pink, black/brown, and clear/translucent particles had larger d_L; smooth white/tan particles had larger d_L. Rough black/brown particles had larger d_L while rough clear/translucent particles had smaller d_L. Smooth white/tan had larger d_L while black/brown and clear/translucent (without outliers) had the smaller d_L. With the exclusion of outliers, smooth particles in all subgroups fractured at higher tensile strengths, in which smooth white/tan and clear/translucent particles had tensile strengths approximately 2xs higher than rough white/tan and clear/translucent particles. Rough red/pink particles fractured at higher tensile strengths while and smooth clear/translucent particles fractured at higher tensile strengths. Rough and smooth white/tan particles fractured at lower tensile strengths. Based on the distributions, the clear/translucent particles fractured at higher tensile strengths while the white/tan particles fractured at lower tensile strengths, on average; the red/pink, black/brown, and white/tan particles had

Table 4-17. Summary of particles surface texture properties for particles retained between sieve #10 (2 mm) and #20 (0.84 mm)

Colored Subgroups	**Rough Particles**			**Smooth Particles**		
	Number of Particles	***d_L (mm)***	***Average Tensile Strength (MPa)***	***Number of Particles***	***d_L (mm)***	***Average Tensile Strength (MPa)***
Red/Pink *(major and secondary compounds: quartz, potassium feldspar, and plagioclase feldspar)*	22	1.28	29.17	29	1.24	32.13
Black/Brown *(major and secondary compounds: quartz, mica (biotite), tridymite, plagioclase feldspar, potassium feldspar, and calcite)*	28 (27)	1.41 (1.43)	29.40 (22.90)	24	1.09	27.69
White/Tan *(major and secondary compounds: quartz, plagioclase feldspar, potassium feldspar, and mica (muscovite))*	13	1.24	13.70	36 (33)	1.30 (1.34)	21.87 (15.85)

Table 4-17 Continued

Colored Subgroups	Rough Particles			Smooth Particles		
	Number of Particles	***d_L (mm)***	***Average Tensile Strength (MPa)***	***Number of Particles***	***d_L (mm)***	***Average Tensile Strength (MPa)***
Clear/Translucent *(major and secondary compounds: quartz and plagioclase feldspar)*	20	1.31	24.95	32 (30)	1.07 (1.09)	41.95 (29.35)

approximately similar average d_L while the clear/translucent particles had the smallest average d_L.

Figure 4-48 and 4-49 display the average d_L and tensile strength, without outliers, for rough and smooth particles retained between sieve #10 (2 mm) and sieve #20 (0.84 mm) based on mineralogy and size. The circle data points, square data points, right sided triangle data points, and triangle data points represent the red/pink (major and secondary compounds: quartz, potassium feldspar, and plagioclase feldspar), black/brown (major and secondary compounds: quartz, mica (biotite), tridymite, plagioclase feldspar, potassium feldspar, and calcite), white/tan (major and secondary compounds: quartz, plagioclase feldspar, potassium feldspar, and mica (muscovite)) and clear/translucent (major and secondary compounds: quartz, mica, pyroxene, ferrihydrite, potassium feldspar, and plagioclase feldspar) particles, respectively; the unfilled data points represent the rough particles and the filled data points represent the smooth particles.

As illustrated in Figure 4-48, the smooth clear/translucent and white/tan particles had the largest d_L range while the smooth black/brown particles had the smallest d_L range. The rough red/pink particles had the largest d_L range; the rough white/tan particles had the smallest d_L range. This indicated more variation in d_L for smooth clear/translucent and rough red/pink particles and less variation in d_L for smooth black/brown and rough white/tan particles. The smooth red/pink, black/brown, and clear/translucent particles had smaller average d_L compared to the rough red/pink, black/brown, and clear/translucent particles. Contrastingly, the smooth white/tan particles had larger average d_L compared to the rough white/tan particles. The rough black/brown particles had the largest average d_L; the smooth black/brown and clear/translucent particles had the smallest average d_L. The smooth red/pink particles had the highest average tensile strength and the rough white/tan particles had the lowest average tensile strength. The

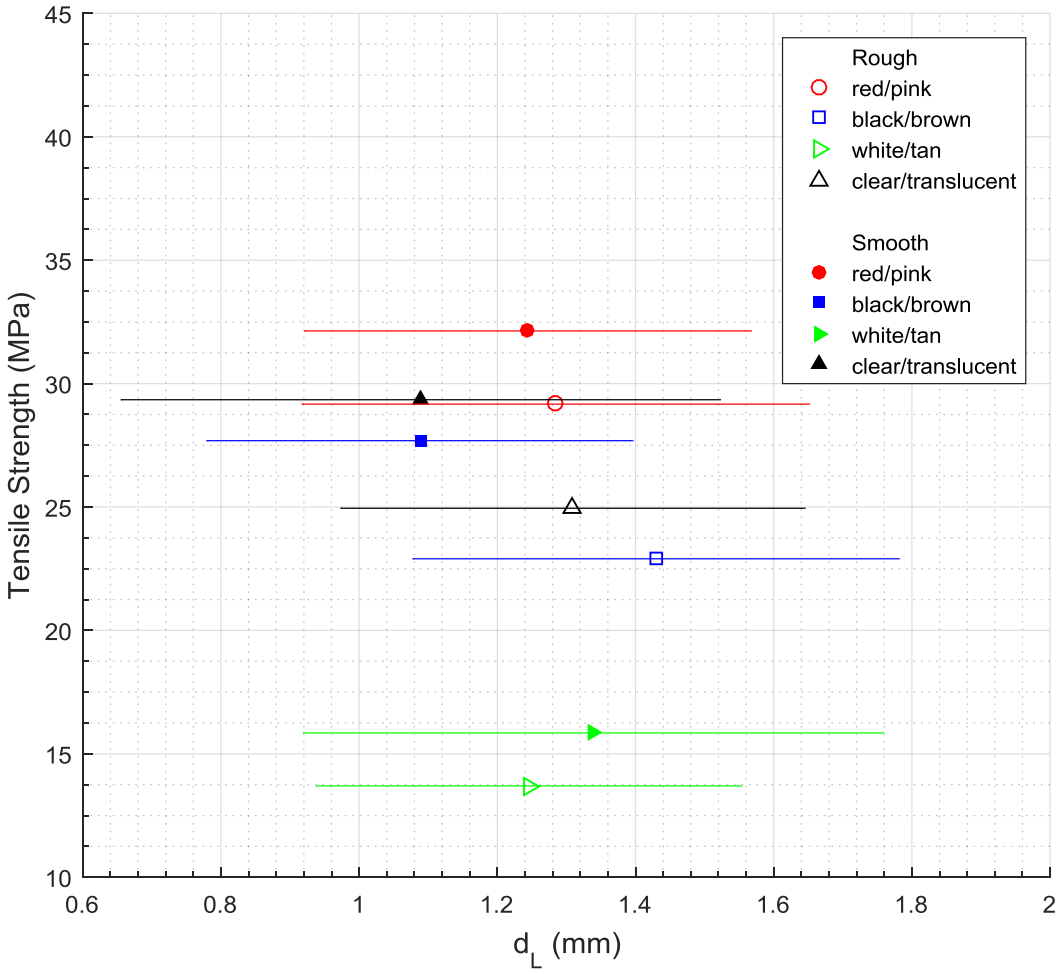


Figure 4-48. Average d_L within one standard deviation for rough and smooth particles, without outliers, retained between sieve #10 (2 mm) and #20 (0.84 mm) based on the red/pink (major and secondary compounds: quartz, potassium feldspar, and plagioclase feldspar), black/brown (major and secondary compounds: quartz, mica (biotite), tridymite, plagioclase feldspar, potassium feldspar, and calcite), white/tan (major and secondary compounds: quartz, plagioclase feldspar, potassium feldspar, and mica (muscovite)) and clear/translucent (major and secondary compounds: quartz and plagioclase feldspar) subgroups

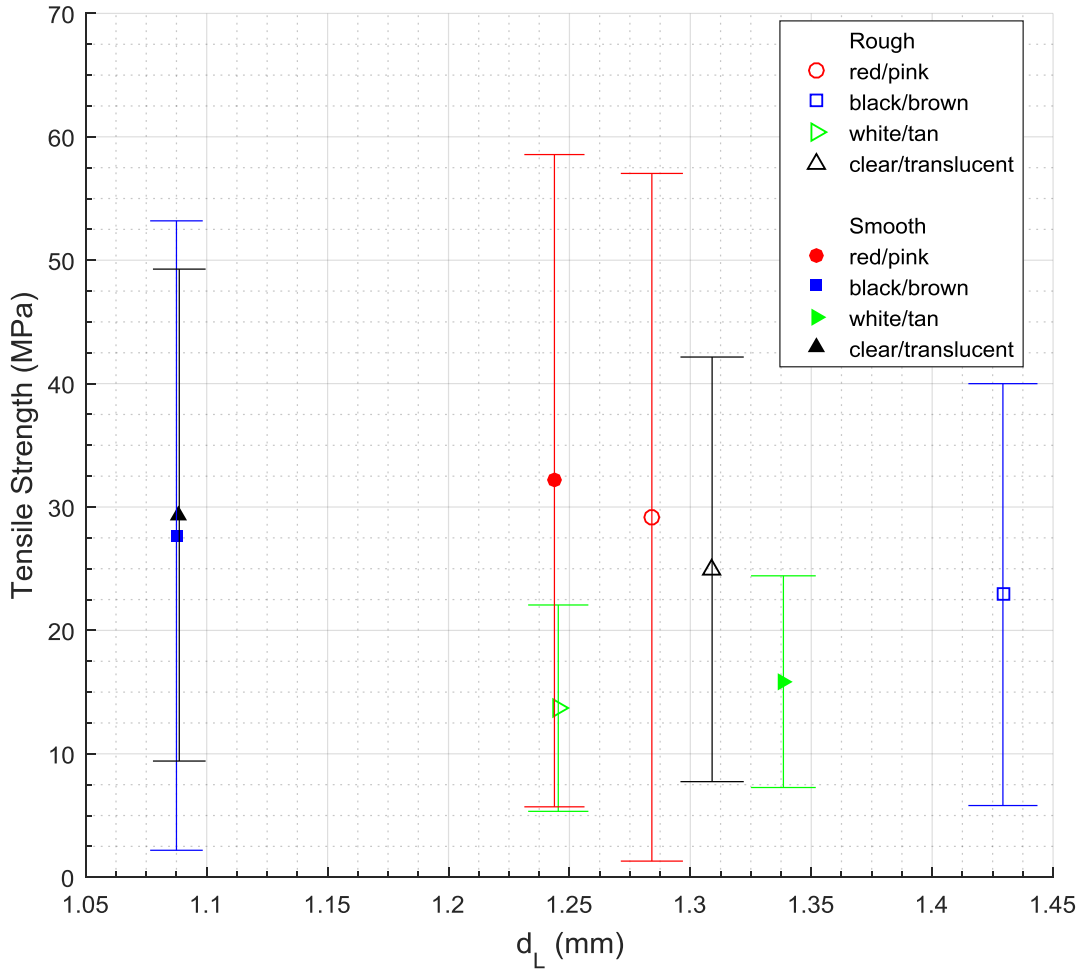


Figure 4-49. Average tensile strength within one standard deviation for rough and smooth particles, without outliers, retained between sieve #10 (2 mm) and #20 (0.84 mm) based on the red/pink (major and secondary compounds: quartz, potassium feldspar, and plagioclase feldspar), black/brown (major and secondary compounds: quartz, mica (biotite), tridymite, plagioclase feldspar, potassium feldspar, and calcite), white/tan (major and secondary compounds: quartz, plagioclase feldspar, potassium feldspar, and mica (muscovite)) and clear/translucent (major and secondary compounds: quartz and plagioclase feldspar) subgroups

rough and smooth white/tan particles had lower average tensile strengths. Referring to Figure 4-49, rough and smooth red/pink particles had the largest tensile strength range and the rough and smooth white/tan particles had the smallest tensile strength range; this implied that tensile strength of the rough and smooth red/pink particles contains more variation while the tensile strength of the rough and smooth white/tan particles contain less variation. The average tensile strength of the smooth red/pink particles was the highest, which indicated that it was the strongest; the average tensile strength of the rough white/tan particles was the lowest, which indicated that it was the weakest. The average d_L of the rough black/brown particles was the largest; the average d_L of the smooth black/brown and clear/translucent particles were the smallest.

Figure 4-50a illustrates the distribution of surface texture for red/pink (major and secondary compounds: quartz, potassium feldspar, and plagioclase feldspar) particles retained by sieve #10 (2 mm). Particles that had smaller d_L fractured at higher tensile strengths compared strength of 14.63 MPa. It contains of 17 rough particles with an average d_L of 2.32 mm and average tensile strength of 10.32 MPa, 23 smooth particles with an average d_L of 2.35 mm to particles that had larger $d_{L;}$ the d_L of the smooth particles varied greatly compared to the rough particles. The distribution contained 40 particles with average d_L of 2.34 mm and average tensile strength of 17.83 MPa, and 0 other particles. The smooth particles had a much higher tensile strength due to an outlier with a stress of 84.05 MPa, identified as particle Red/Pink 25-11_J, shown in Figure 4-13b.1 in Appendix I. With the exclusion of the outlier, the average d_L for the distribution and smooth particles increased to 2.37 and 2.4 0mm, respectively; the average tensile strength for the distribution and smooth particles decreased to 12.86 and 14.82 MPa,

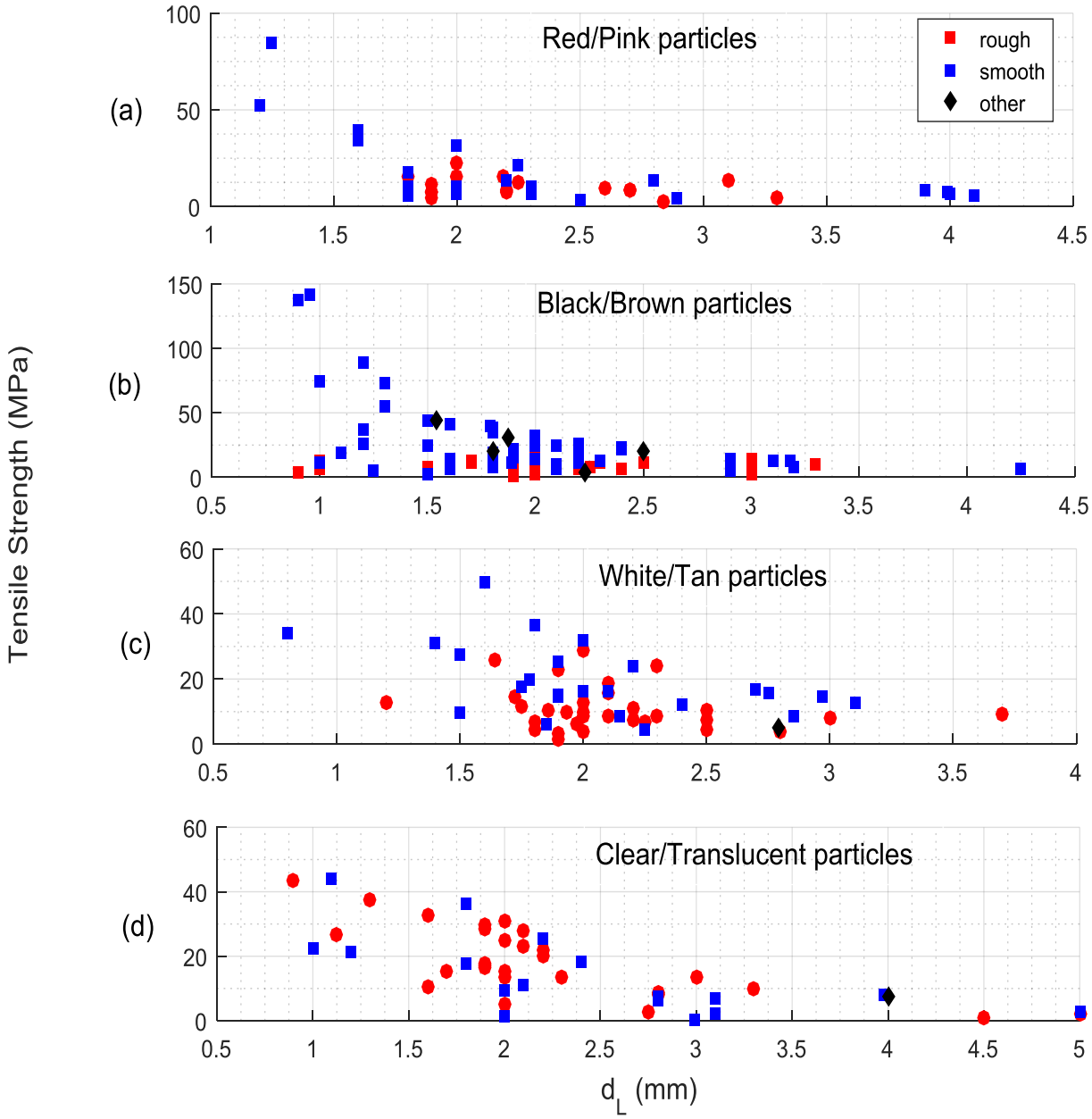


Figure 4-50. Surface texture of particles retained by sieve #10 (2 mm) for particles in the (a) red/pink (major and secondary compounds: quartz, potassium feldspar, and plagioclase feldspar), (b) black/brown (major and secondary compounds: quartz, mica (biotite), tridymite, plagioclase feldspar, potassium feldspar, and calcite), (c) white/tan (major and secondary compounds: quartz, plagioclase feldspar, potassium feldspar, and mica (muscovite)) and (d) clear/translucent (major and secondary compounds: quartz and plagioclase feldspar) subgroups.

respectively. Based on the distribution, and regardless of the outlier, the rough particles were generally smaller and fractured at lower tensile strengths; the smooth particles were generally larger and fractured at higher tensile strengths. This implied that red/pink particles had a high probability of containing smooth particles with varying sizes and tensile strengths.

Figure 4-50b displays the distribution for the black/brown (major and secondary compounds: quartz, mica (biotite), tridymite, plagioclase feldspar, potassium feldspar, and calcite) particles retained by sieve #10 (2 mm). The distribution contained 82 particles with an average d_L of 1.96 mm and average tensile strength of 21.65 MPa with a majority rough particle fracturing at lower tensile strengths compared to smooth particles. Within the distribution were 27 rough particles with an average d_L of 2.04 mm and average tensile strength of 9.13 MPa, 50 smooth particles with an average d_L of 1.91 mm and average tensile strength of 28.15 MPa, and 5 other particles with an average d_L of 1.99 mm and average tensile strength of 24.33 MPa. The smooth particles had an average tensile strength 3xs greater than the rough particles was due to two particles with a tensile strength of 137.43 and 141.62 MPa, identified as particle Black/Brown 25-36_J and Black/Brown 25-33_C, respectively, shown in Figures 4-14b.1 and 4-14b.2 in Appendix I, respectively. The removal of these particles increased the average d_L of the distribution and smooth particles to 1.98 and 1.95mm, respectively; the average tensile strength decreased to 18.71 and 23.51 MPa, respectively. Regardless of the outliers, the rough particles, on average, had a larger d_L and fractured at lower tensile strengths when compared to the smooth particles. The black/brown particles had a higher probability of containing smooth particles than rough particles.

Figure 4-50c illustrates the distribution of the white/tan (major and secondary compounds: quartz, plagioclase feldspar, potassium feldspar, and mica (muscovite)) particles

retained by sieve #10 (2 mm). The distribution contains 56 particles with an average d_L and tensile strength of 2.10 mm and 14.50 MPa. The smooth particles fractured at higher tensile strengths compared to the rough particles and the distribution of particle sizes for smooth and rough particle is approximately the same. The distribution contained 31 rough particles with an average d_L and tensile strength of 2.13 mm and 10.92 MPa, respectively, 24 smooth particles with an average d_L and tensile strength of 2.05 mm and 19.53 MPa, respectively, and 1 other particle with a d_L and tensile strength of 2.79 mm and 4.81 MPa, respectively. The rough particles generally had a larger d_L compared to the smooth particles and the smooth particles fractured at higher tensile strengths compared to the rough particles, on average.

Figure 4-50d illustrates the distribution of the clear/translucent (major and secondary compounds: quartz and plagioclase feldspar) particles retained by sieve #10 (2 mm). As shown in the distribution, the tensile strengths of rough and smooth particles are relatively similar. The distribution contained 46 particles, in which 28 are rough, 17 are smooth, and 1 had an other surface texture, and has an average d_L of 2.35 mm and tensile strength of 16.65 MPa. The rough particles had an average d_L and tensile strength of 2.24 mm and 18.43 MPa, respectively; the smooth particles had an average d_L and tensile strength of 2.43 mm and 14.24 MPa, respectively, while the clear particle has a d_L and tensile strength of 4.00 mm and 7.67 MPa, respectively. Based on the distribution, the smooth particles generally had larger d_L and fractured at smaller tensile strengths when compared to the rough particles.

Table 4-18 summarizes the number of particles and the average d_L and tensile strengths for the distributions in Figure 4-50. Particles with higher tensile strengths had smaller d_L. The black/brown particles fractured at higher tensile strengths and had smaller d_L while the red/pink particles fractured at lower tensile strengths and had larger d_L, regardless of outliers. The rough

Table 4-18. Summary of particles surface texture properties for particles retained by sieve #10 (2 mm)

Colored Subgroups	**Rough Particles**			**Smooth Particles**		
	Number of Particles	***d_L (mm)***	***Average Tensile Strength (MPa)***	***Number of Particles***	***d_L (mm)***	***Average Tensile Strength (MPa)***
Red/Pink *(major and secondary compounds: quartz, potassium feldspar, and plagioclase feldspar)*	17	2.32	10.32	23 (22)	2.35 (2.40)	17.83 (14.82)
Black/Brown *(major and secondary compounds: quartz, mica (biotite), tridymite, plagioclase feldspar, potassium feldspar, and calcite)*	27	2.04	9.13	50 (48)	1.91 (1.95)	28.15 (23.51)
White/Tan *(major and secondary compounds: quartz, plagioclase feldspar, potassium feldspar, and mica (muscovite))*	31	2.13	10.92	24 (23)	2.05 (2.07)	19.53 (18.23)

Table 4-18 Continued

Colored Subgroups	Rough Particles			Smooth Particles		
	Number of Particles	***d_L (mm)***	***Average Tensile Strength (MPa)***	***Number of Particles***	***d_L (mm)***	***Average Tensile Strength (MPa)***
Clear/Translucent *(major and secondary compounds: quartz and plagioclase feldspar)*	28	2.24	18.43	17	2.43	14.24

red/pink particles had larger d_L while the rough black/brown particles had smaller d_L. Smooth clear/translucent particles had larger d_L while smooth black/brown particles had smaller d_L. Rough clear/translucent particle fractured at higher tensile strengths while rough black/brown particle fractured at lower tensile strengths. Smooth black/brown particle fractured at higher tensile strengths while smooth clear/translucent particle fractured at lower tensile strengths.

Figure 4-51 and 4-52 display the average d_L and tensile strength, without outliers, for rough and smooth particles retained by sieve #10 (2 mm) based on mineralogy and size. The circle data points, square data points, right sided triangle data points, and triangle data points represent the red/pink (major and secondary compounds: quartz, potassium feldspar, and plagioclase feldspar), black/brown (major and secondary compounds: quartz, mica (biotite), tridymite, plagioclase feldspar, potassium feldspar, and calcite), white/tan (major and secondary compounds: quartz, plagioclase feldspar, potassium feldspar, and mica (muscovite)), and clear/translucent (major and secondary compounds: quartz and plagioclase feldspar) particles; the unfilled data points represent the rough particles and the filled data points represent the smooth particles.

As illustrated in Figure 4-51, the rough and smooth clear/translucent particles had the largest d_L range while the rough and smooth white/tan particles had the smallest d_L range. This indicates more variation in d_L for rough and smooth clear/translucent and less variation in d_L for smooth and rough white/tan particles. The smooth black/brown particles had the smallest average d_L while the smooth clear/translucent particles had the largest average d_L. The rough white/tan, black/brown, and red/pink particles had smaller average tensile strengths, with the rough black/brown particles having the lowest average tensile strength, implying that it was the weakest. Contrastingly, the smooth black/brown particles had the highest average tensile

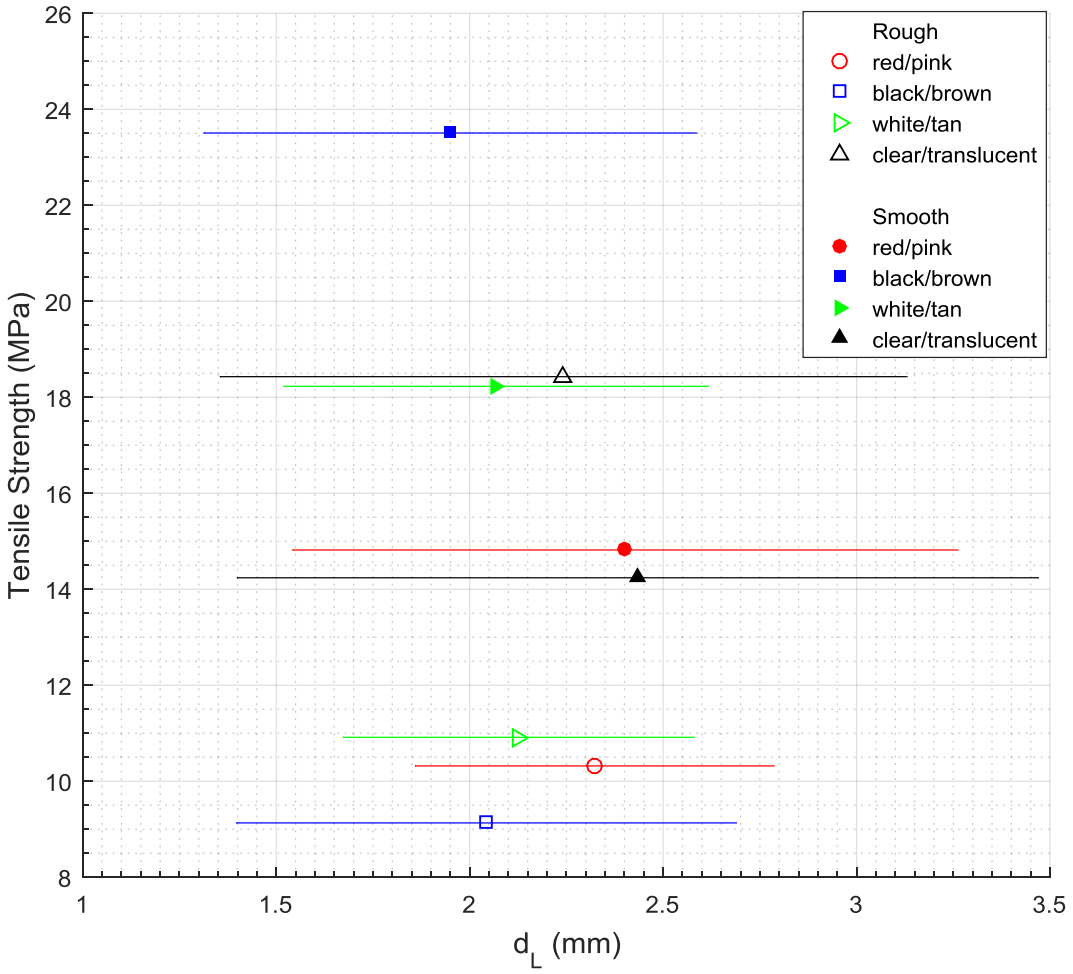


Figure 4-51. Average d_L within one standard deviation for rough and smooth particles, without outliers, retained by sieve #10 (2 mm) based on the red/pink (major and secondary compounds: quartz, potassium feldspar, and plagioclase feldspar) particles, black/brown (major and secondary compounds: quartz, mica (biotite), tridymite, plagioclase feldspar, potassium feldspar, and calcite) particles, white/tan (major and secondary compounds: quartz, plagioclase feldspar, potassium feldspar, and mica (muscovite)) particles, and clear/translucent (major and secondary compounds: quartz and plagioclase feldspar) particles subgroups

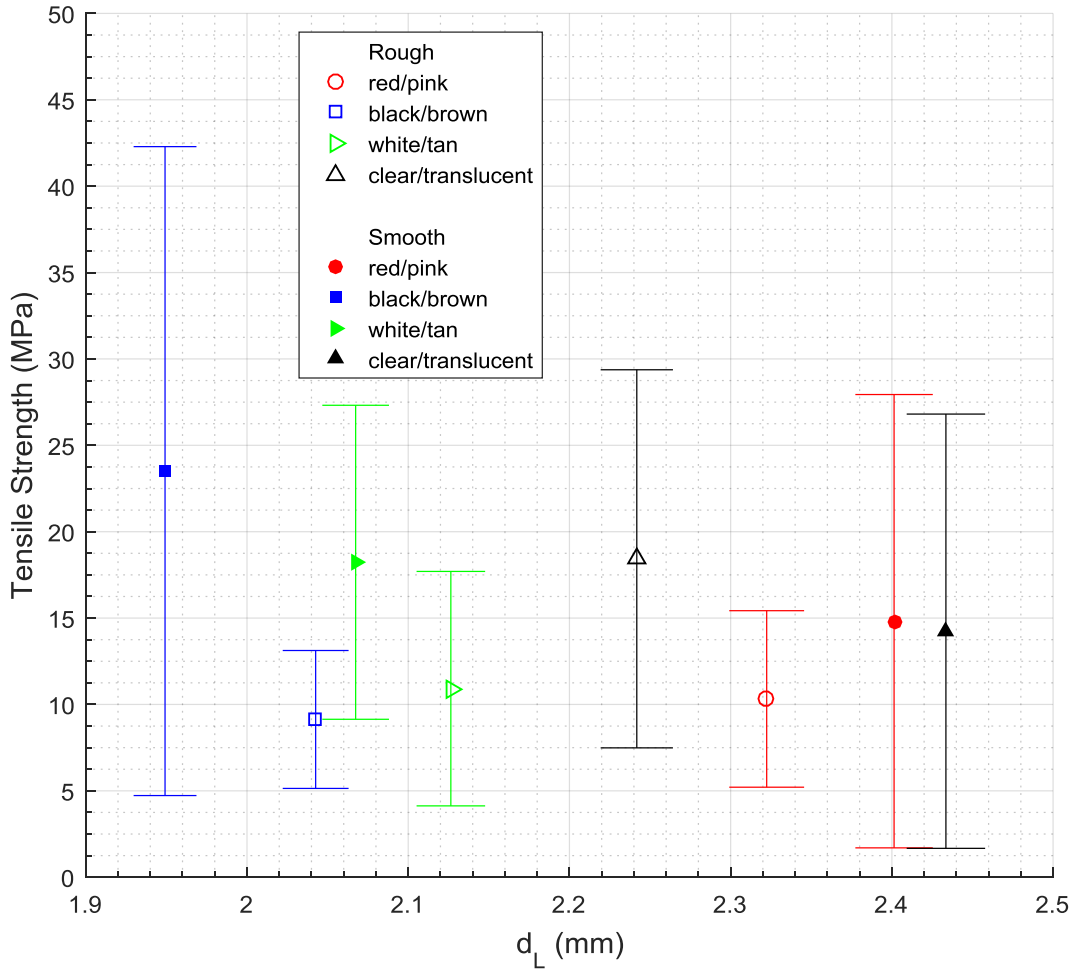


Figure 4-52. Average tensile strength within one standard deviation for rough and smooth particles, without outliers, retained by sieve #10 (2 mm) based on the red/pink (major and secondary compounds: quartz, potassium feldspar, and plagioclase feldspar) particles, black/brown (major and secondary compounds: quartz, mica (biotite), tridymite, plagioclase feldspar, potassium feldspar, and calcite) particles, white/tan (major and secondary compounds: quartz, plagioclase feldspar, potassium feldspar, and mica (muscovite)) particles, and clear/translucent (major and secondary compounds: quartz and plagioclase feldspar) particles subgroups.

strength, implying that it was the strongest. Based on Figure 4-52, smooth black/brown particles and rough clear/translucent particles had the largest tensile strength range; smooth white/tan and rough black/brown particles had the smallest tensile strength range. This implied that tensile strength of the rough clear/translucent and smooth black/brown particles contains more variation while the tensile strength of the rough black/brown and smooth white/tan particles contains less variation. The average tensile strength of the smooth black/brown particles was the highest, which indicated that it was the strongest; the average tensile strength of the rough black/brown particles was the lowest, which indicated that it was the weakest. The average d_L of the smooth clear/translucent particles is the largest; the average d_L of the smooth black/brown particles is the smallest.

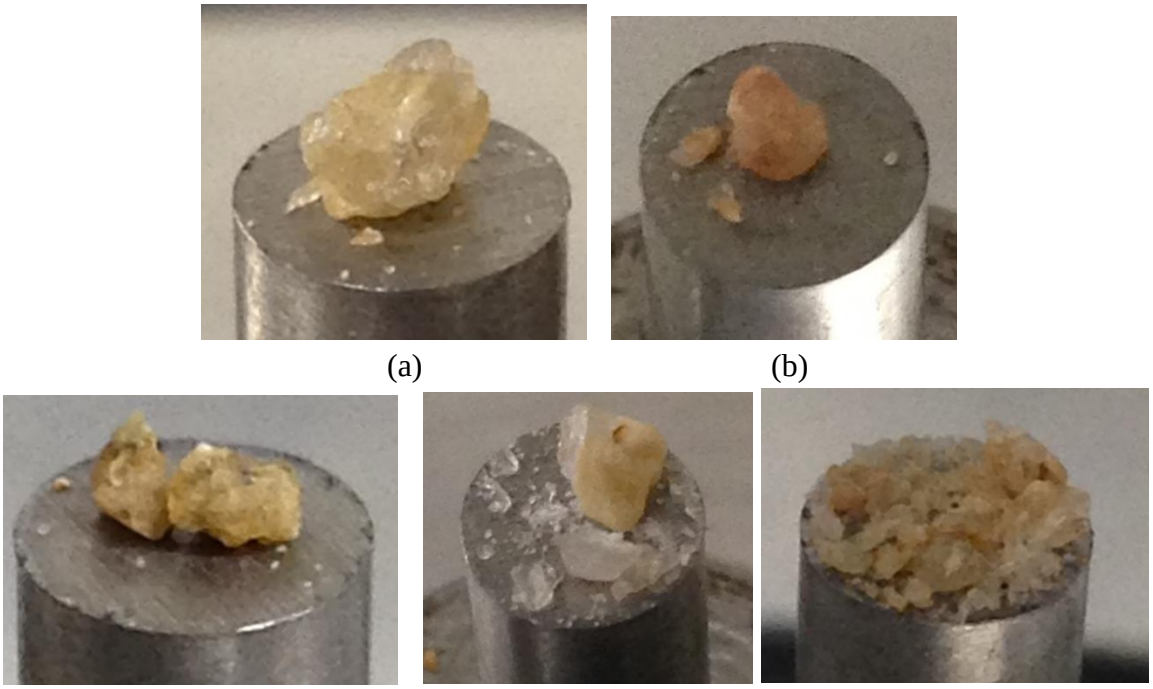
Overall, smooth red/pink (major and secondary compounds: quartz, potassium feldspar, and plagioclase feldspar), black/brown (major and secondary compounds: quartz, mica (biotite), tridymite, plagioclase feldspar, potassium feldspar, and calcite), and white/tan (major and secondary compounds: quartz, plagioclase feldspar, potassium feldspar, and mica (muscovite)) particles retained between sieve #10 (2 mm) and #20 (0.84 mm) and by sieve #10 (2 mm) fractured at higher tensile strengths compared to the rough particles. Contrastingly, the smooth clear/translucent (major and secondary compounds: quartz and plagioclase feldspar) particles retained between sieve #10 (2 mm) and #20 (0.84 mm), and by sieve #10 (2 mm) fractured at a lower tensile strength compared to the rough particles. The rough red/pink particles and clear/translucent particles retained by sieve #10 (2 mm) particles generally had smaller d_L compared to the particle retained between sieve #10 (2 mm) and #20 (0.84 mm). The rough black/brown particles in both size categories generally had a larger d_L. The rough white/tan

particles retained between sieve #10 (2 mm) and #20 (0.84 mm) generally had a smaller d_L in comparison to the particles retained by sieve #10 (2 mm).

4.2.2.6 Particle Fracture Mode

The fracture modes, based on Nakata et al. (2001) and other literature, were summarized by Parab et al., (2014) and adopted as: (a) Mode 1, small abrasion failure or fracture with large piece remaining with a tiny piece or asperities, (b) Mode 2, multiple abrasion failure or fracture of large piece with small or tiny piece with or without asperities, (c) Mode 3, major fracture into at least 2 pieces, (d) Mode 4, fracture of sub-particles into smaller pieces, and (e) Mode 5, pulverization of particle into many small pieces. Images of fracture Modes 1 through 5 are shown in Figures 4-53. Particle that did not post particle descriptions were categorized as fracture Mode 0 and particles that exhibited fracture modes between two categories were categorize as Mode 2.5, a particle that displayed fractures from Mode 2 and 3, or Mode 3.5, a particle that displayed fractures from Mode 3 and 4. Prediction of how particles will fracture was dependent on the particle mineralogy and morphology as it affects the hardness and coordination number of the particles, influencing the fracture pattern. It was predicted that the majority of particles in both size groups and colored subgroups will exhibit a Mode 3 or 4 fractures as the particles are loaded until initial fracture is observed.

Figure 4-54 illustrates the tensile strength distribution, based on fracture modes, for red/pink (major and secondary compounds: quartz, potassium feldspar, and plagioclase feldspar) particles retained between sieve #10 (2 mm) and #20 (0.84 mm) and by sieve #10 (2 mm), respectively. The number of particles and average tensile strengths, based on fracture modes, for red/pink particles retained by between sieve #10 (2 mm) and #20 (0.84 mm) and by sieve #10 (2 mm) are shown in Table 4-19. Particles retained between sieve #10 (2 mm) and #20 (0.84 mm)



(a) (b)

(c) (d) (e)

Figure 4-53. Particle classification based on fracture (a) Mode 1, (b) Mode 2, (c) Mode 3, (d) Mode 4, and (e) Mode 5.

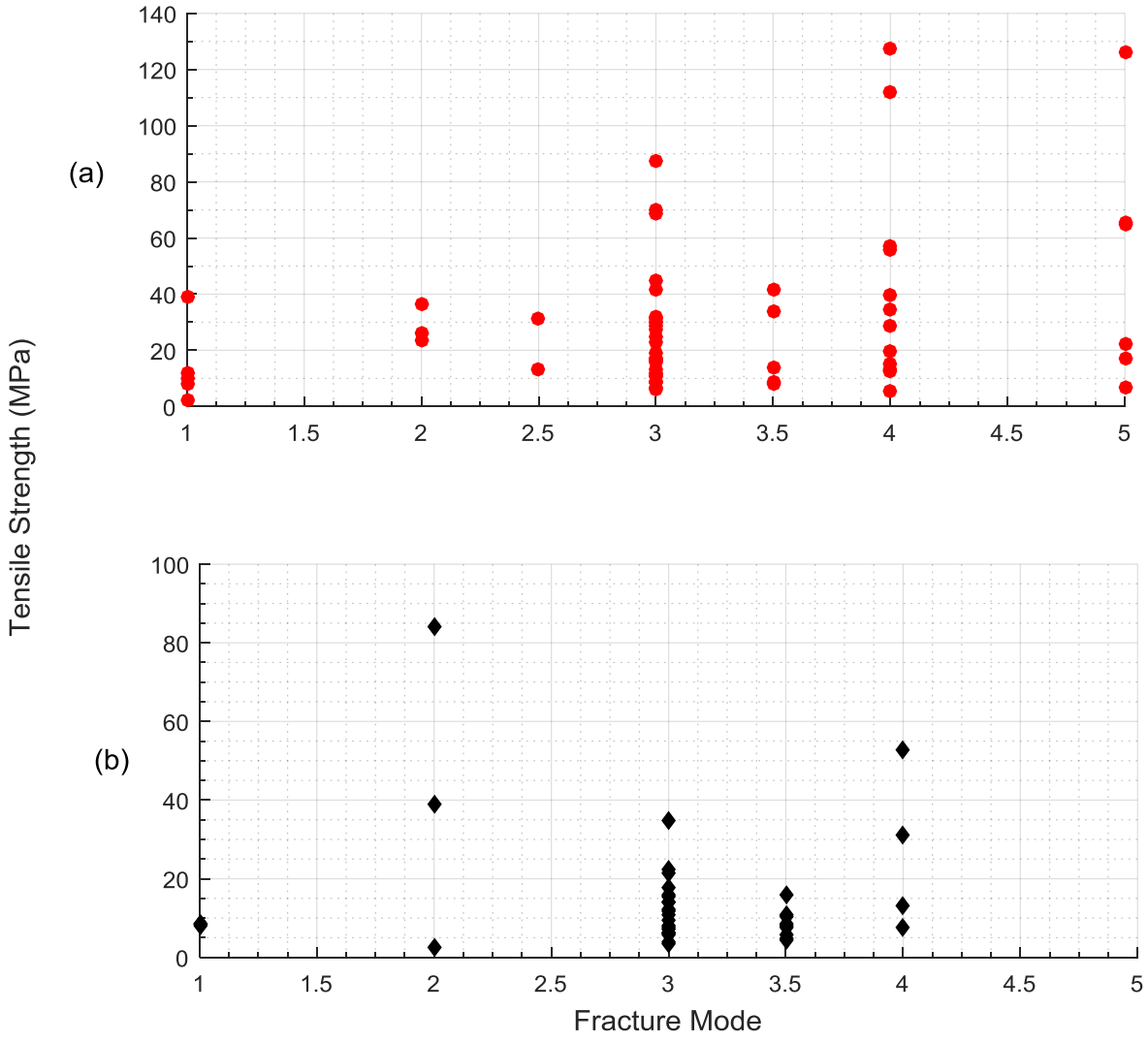


Figure 4-54. Fracture mode vs. tensile strengths for red/pink (major and secondary compounds: quartz, potassium feldspar, and plagioclase feldspar) particles retained (a) between sieve #10 (2 mm) and #20 (0.84 mm) and (b) by sieve #10 (2 mm)

Table 4-19. Number of particles and average tensile strengths based on fracture modes for red/pink (major and secondary compounds: quartz, potassium feldspar, and plagioclase feldspar) particles retained between sieve #10 (2 mm) and #20 (0.84 mm) and by sieve #10 (2 mm)

Fracture mode	**Retained between sieve #10 (2 mm) and #20 (0.84 mm)**		**Retained by sieve #10 (2 mm)**	
	Number of Particles	*Average Tensile Strength (MPa)*	*Number of Particles*	*Average Tensile Strength (MPa)*
1	5	14.32	3	8.33
2	3	28.83	3	41.91 (20.84)
2.5	2	22.36	0	0
3	28	26.01	21	12.10
3.5	5	21.11	9	8.41
4	12	43.47 (28.20)	4	26.25
5	6	50.52 (35.42)	0	0

fractured at various Modes in which Modes 3 through 4 occurred at higher tensile strengths compared to fractures that occurred at Modes 1 through 2.5. Based on the distribution in Figure 4-54a, there were three outlying particles at a tensile strength of 111.99, 126.07, and 127.73 MPa, identified as particle Red/Pink 25-5_J, Red/Pink 25-22_C, and Red/Pink 25-2_J, with a fracture mode of 4, 5, and 4, respectively. The exclusion of these particles decreased the tensile strength of fracture Mode 5, as shown in Table 4-19. Particles retained by sieve #10 (2 mm) predominantly experienced fractures between Modes 3 to 5. Based on Figure 4-54b, the outlier had a tensile strength of 84.05 MPa, identified as Red/Pink 25-11_J, with a fracture Mode of 2. The exclusion of this outlying particle decreased the tensile strength of Mode 2from 41.91 to 20.84 MPa. Mode 3 and 4 fractures occur at both low and higher tensile strengths for particles in both size categories and all fracture Modes for particles in both size categories occurred at low tensile strengths. From Table 4-19, particles retained between sieve #10 (2 mm) and #20 (0.84 mm) fractured at lower tensile strengths at Mode 1 and at higher tensile strengths at Mode 5, regardless of outliers. Twenty-eight particles experienced a Mode 3 with at an average tensile strength of 26.01 MPa. Particles retained by sieve #10 (2 mm) fractured at lower tensile strengths at Mode 1 and at higher tensile strengths at Mode 2; Mode 4 type fractures occurred at higher tensile strengths with the exclusion of the outlier. Twenty-one particles experienced a Mode 3 fracture with an average tensile strength of 12.10 MPa; no particles experienced a Mode 2.5 or 5 fracture. The majority of particles retained between sieve #10 (2 mm) and #20 (0.84 mm) and by sieve #10 (2 mm) fractured as Mode 3.

Figure 4-55 depicts the average tensile strength, without outliers, of the fracture modes within one standard deviation for the red/pink (major and secondary compounds: quartz, potassium feldspar, and plagioclase feldspar) particles retained between sieve #10 (2 mm) and

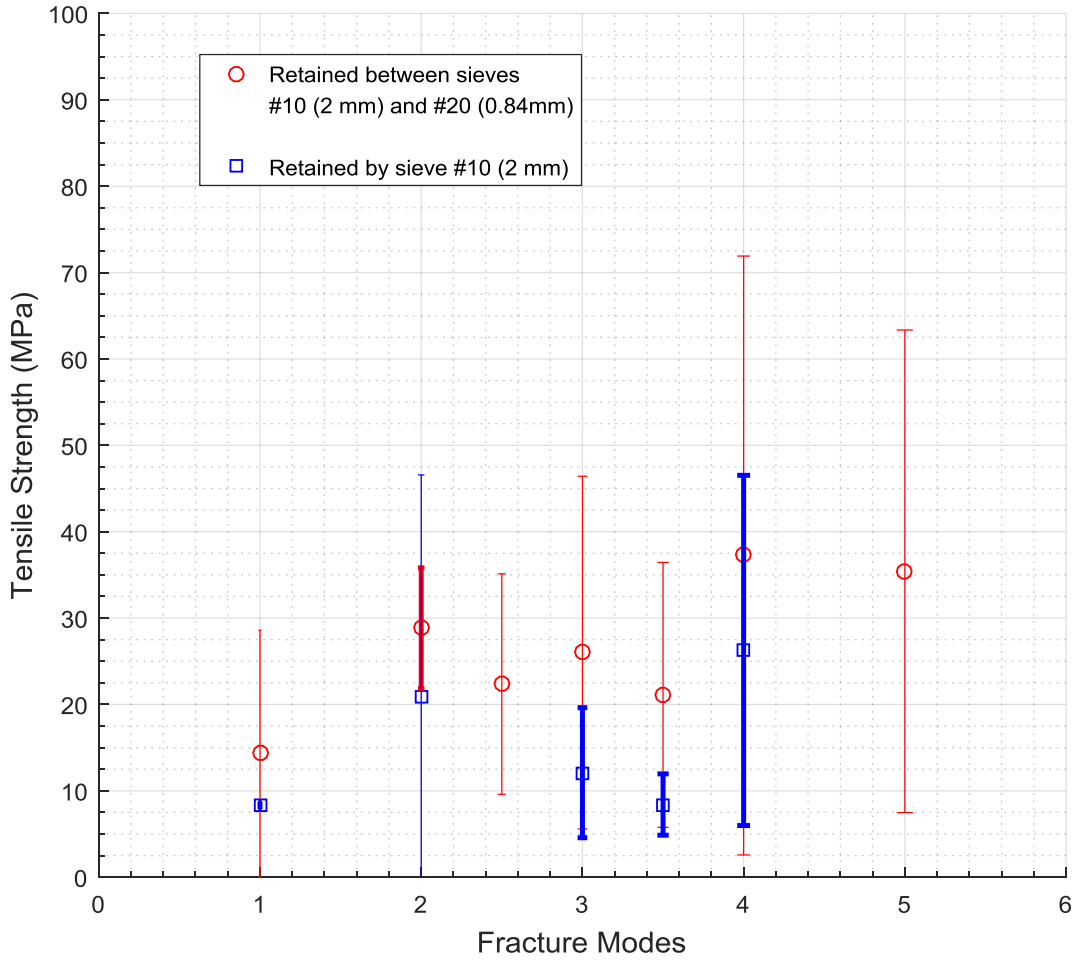


Figure 4-55. Average tensile strengths, without outliers, of the fracture modes within one standard deviation for the red/pink (major and secondary compounds: quartz, mica (biotite), tridymite, plagioclase feldspar, potassium feldspar, and calcite) particles retained between sieve #10 (2 mm) and #20 (0.84 mm) and by sieve #10 (2 mm).

#20 (0.84 mm), depicted with red circle data points, and by sieve #10 (2 mm), represented with blue square data points. The size category containing the smaller tensile strength range is shown with thicker error bar lines to distinguish it from the larger tensile strength range in the same fracture mode. For particles retained between sieve #10 (2 mm) and #20 (0.84 mm), Mode 4 contains the largest tensile strength range while Mode 2 contains the smallest tensile strength range. The average tensile strength for particles that exhibited a Mode 4 fracture was highest and lowest for particles that exhibited a Mode 1 fracture. For particles retained by sieve #10 (2 mm), Mode 2 contains the largest tensile strength range while Mode 3.5 contains the smallest tensile strength range. Mode 1 was not considered as it was composed of 1 particle and did not contain a tensile strength range. The average tensile strength for particles that exhibited a Mode 4 fracture was highest and lowest for particles that exhibited a Mode 1 fracture. This indicated greater variation in tensile strengths for Mode 4 and Mode 2 fracture of red/pink particles retained between sieve #10 (2 mm) and #20 (0.84 mm) and by sieve #10 (2 mm), respectively. There was less variation in tensile strengths for Mode 2 and Mode 3.2 fracture of red/pink particles retained between sieve #10 (2 mm) and #20 (0.84 mm) and by sieve #10 (2 mm), respectively. Particles that exhibited a Mode 4 fracture will generally fractured at higher tensile strengths; particles that exhibited a Mode 1 generally fractured at lower tensile strengths.

Figure 4-56 depicts the tensile strength distribution, based on fracture modes, black/brown (major and secondary compounds: quartz, mica (biotite), tridymite, plagioclase feldspar, potassium feldspar, and calcite) particles retained between sieve #10 (2 mm) and #20 0.84 mm) and by sieve #10 (2 mm), respectively. The number of particles and average tensile strengths, based on fracture modes, for black/brown particles retained by between sieve #10 (2 mm) and #20 (0.84 mm) and by sieve #10 (2 mm) are shown in Table 4-20. Particles retained by

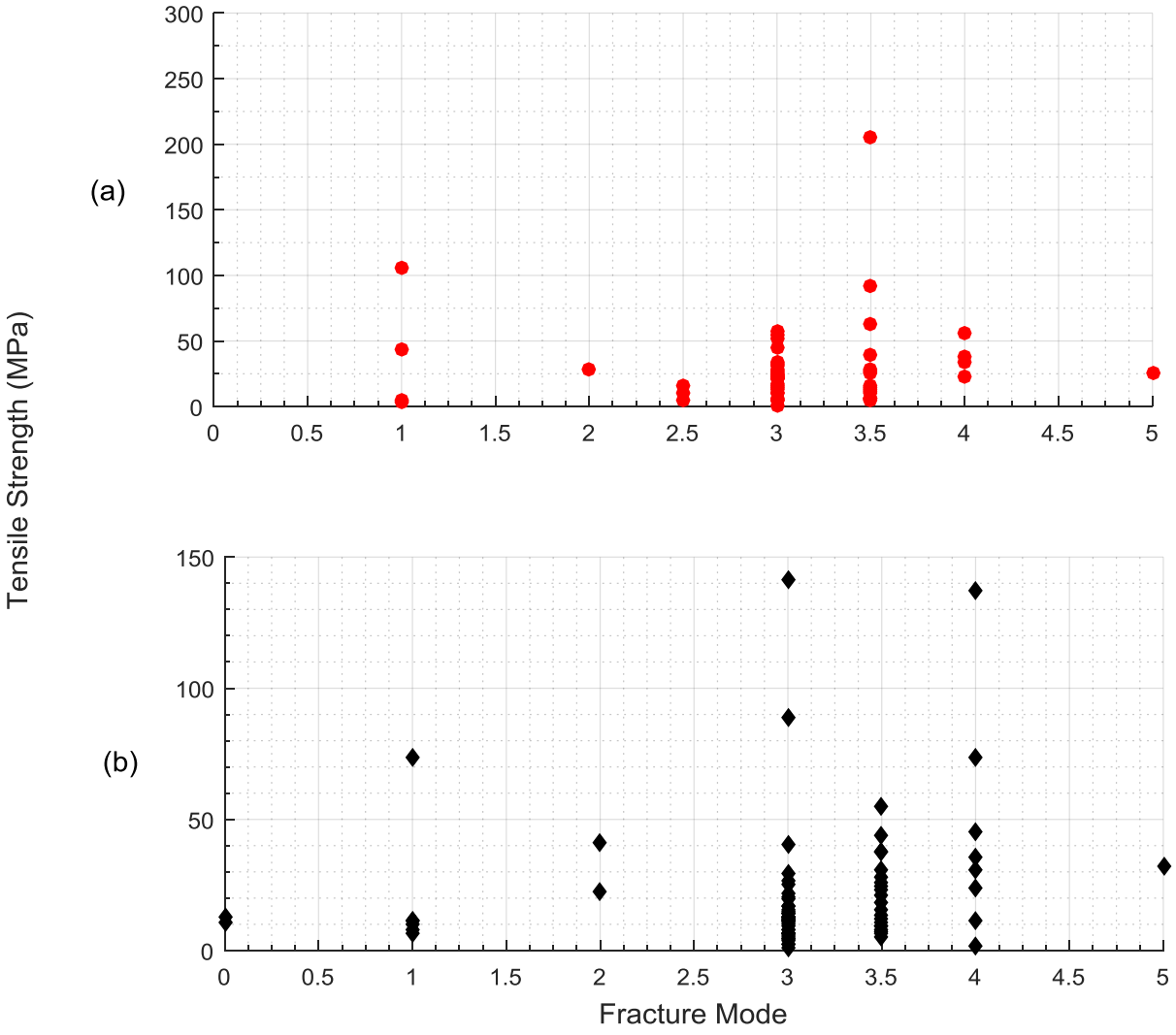


Figure 4-56. Fracture mode vs. tensile strengths for black/brown (major and secondary compounds: quartz, mica (biotite), tridymite, plagioclase feldspar, potassium feldspar, and calcite) particles retained (a) between sieve #10 (2 mm) and #20 (0.84 mm) and (b) by sieve #10 (2 mm)

Table 4-20. Number of particles and average tensile strengths based on fracture modes for black/brown (major and secondary compounds: quartz, mica (biotite), tridymite, plagioclase feldspar, potassium feldspar, and calcite) particles retained between sieve #10 (2 mm) and #20 (0.84 mm) and by sieve #10 (2 mm)

Fracture mode	**Retained between sieve #10 (2 mm) and #20 (0.84 mm)**		**Retained by sieve #10 (2 mm)**	
	Number of Particles	*Average Tensile Strength (MPa)*	*Number of Particles*	*Average Tensile Strength (MPa)*
0	0	0	2	11.78
1	4	39.46	6	20.14
2	1	28.93	2	31.68
2.5	3	10.19	0	0
3	27	23.84	42(41)	17.47 (14.45)
3.5	16(15)	35.54 (24.24)	21	21.07
4	4	37.86	8(7)	44.93 (31.71)
5	5	25.08	1	32.18

both size categories fractured at various Modes and fractures at low tensile strengths occurred at various modes. Based on Figure 4-56a, an outlying particle with a tensile strength of 204.96 MPa, identified as Black/Brown 25-21_C, experienced a Mode 3.5 fracture. The exclusion of this particle decreased the average tensile strength of Mode 3.5, as shown in Table 4-20. Based on Figure 4-56b, outlying particles with tensile strengths at 137.43 and 141.62 MPa, identified as Black/Brown 25-36_J and Black/Brown 25-33_C, had a fracture mode of 4 and 3, respectively. The exclusion of these outlying particles decreased the tensile strength of Mode 3 and 4, as shown in Table C-15. From Table 4-20, particles retained between sieve #10 (2 mm) and #20 (0.84 mm) fractured at lower tensile strengths at Mode 2.5 and at higher tensile strengths at Mode 1. Twenty-seven particles experienced a Mode 3 with an average tensile strength of 23.81 MPa. Particles retained by sieve #10 (2 mm) fractured at lower tensile strengths at Mode 1 and at higher tensile strengths at Mode 4; Mode 5 type fractures occurred at higher stresses with the exclusion of the outlier. Forty-two particles experienced a Mode 3 with at an average tensile strength of 17.47 MPa. There were two particles with no fracture modes due to lack of post-fracture description; no particles experienced a Mode 2.5 fracture. The majority of particles retained between sieve #10 (2 mm) and #20 (0.84 mm) and by sieve #10 (2 mm) fractured as Mode 3; there is 1 particle in each size category that had a Mode 5 fracture at similar tensile strengths.

Figure 4-57 depicts the average tensile strengths, without outliers, of the fracture modes within one standard deviation for the black/brown (major and secondary compounds: quartz, mica (biotite), tridymite, plagioclase feldspar, potassium feldspar, and calcite) particles retained between sieve #10 (2 mm) and #20 (0.84 mm), depicted with red circle data points, and by sieve #10 (2 mm), represented with blue square data points. The size category containing the smaller

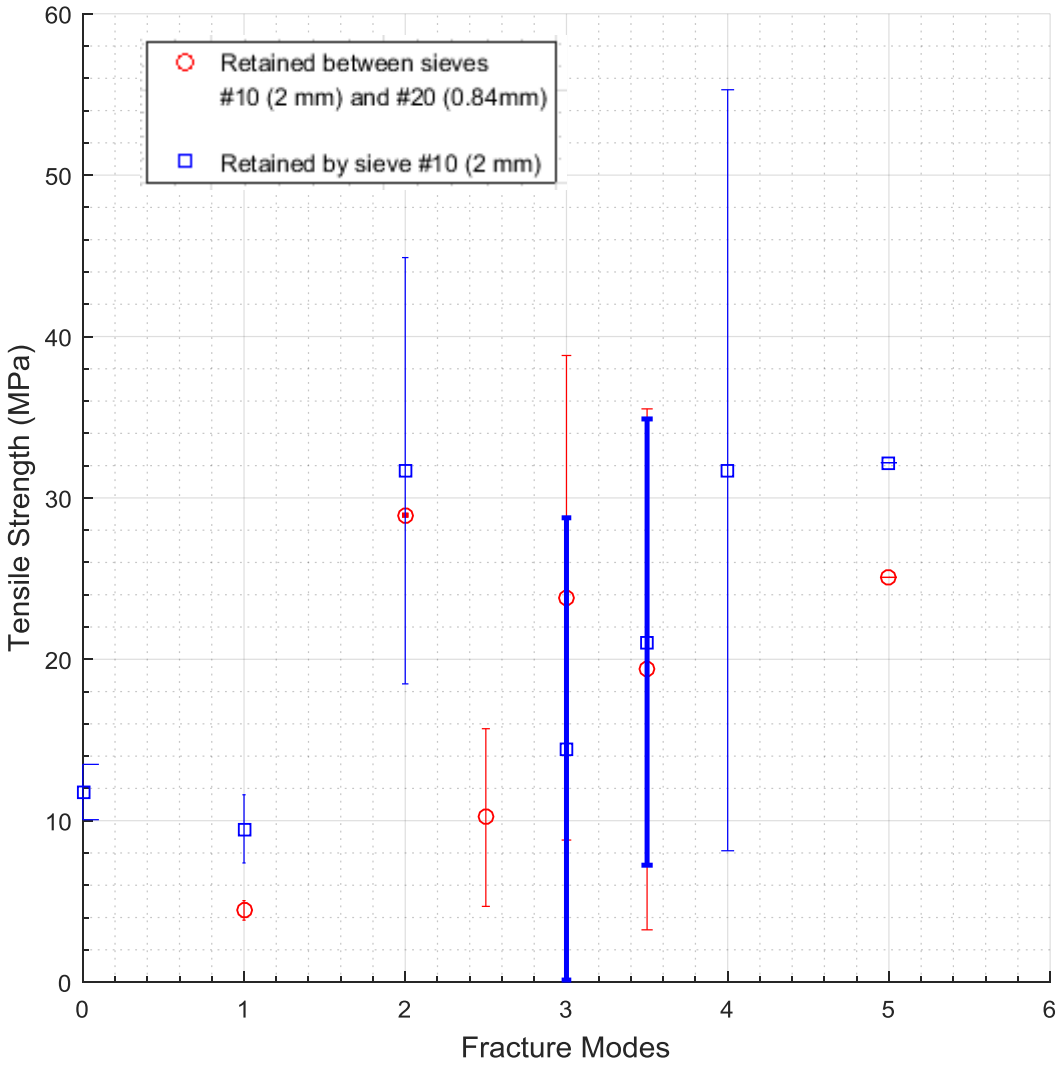


Figure 4-57. Average tensile strengths, without outliers, of the fracture modes within one standard deviation for the black/brown (major and secondary compounds: quartz, mica (biotite), tridymite, plagioclase feldspar, potassium feldspar, and calcite) particles retained between sieve #10 (2 mm) and #20 (0.84 mm) and by sieve #10 (2 mm).

tensile strength range was shown with thicker error bar lines to distinguish it from the larger tensile strength range in the same fracture mode. For particles retained between sieve #10 (2 mm) and #20 (0.84 mm), Mode 3.5 contained the largest tensile strength range and Mode 1 contains the smallest tensile strength range. Mode 5 was not considered as having the smallest tensile strength as it was composed of 1 particle. This indicated more variation in tensile strength for Mode 3.5 and less variation in tensile strength for Mode 1. For particles retained by sieve #10 (2 mm), the tensile strength range of Mode 4 was the largest and smallest for Mode 1. Mode 5 and 0 were not considered as having the smallest tensile strength as it was composed of 1 particle and particles did not fracture, respectively. This implied there were more variations in tensile strength for Mode 4 and less variation in tensile strength for Mode 1. The particle retained between sieve #10 (2 mm) and #20 (0.84 mm) that exhibited a Mode 2 and the particle retained by sieve #10 (2mm) that exhibited a Mode 5 fractured at higher average tensile strengths; particles that exhibit a Mode 1 for both size categories generally fractured at lower tensile strengths.

Figure 4-58 depicts the tensile strength distribution, based on fracture modes, white/tan (major and secondary compounds: quartz, plagioclase feldspar, potassium feldspar, and mica (muscovite)) particles retained between sieve #10 (2 mm) and #20 (0.84 mm) and by sieve #10 (2 mm), respectively. The number of particles and average tensile strengths, based on fracture modes, for white/tan particles retained by between sieve #10 (2 mm) and #20 (0.84 mm) and by sieve #10 (2 mm) are shown in Table 4-21. Particles retained between sieve #10 (2 mm) and #20 (0.84 mm) fractured at various modes and the fracture modes occurred at various tensile strengths. Based on Figure 4-58a, three outliers, identified as White/Tan 25-15_J, White/Tan 25-

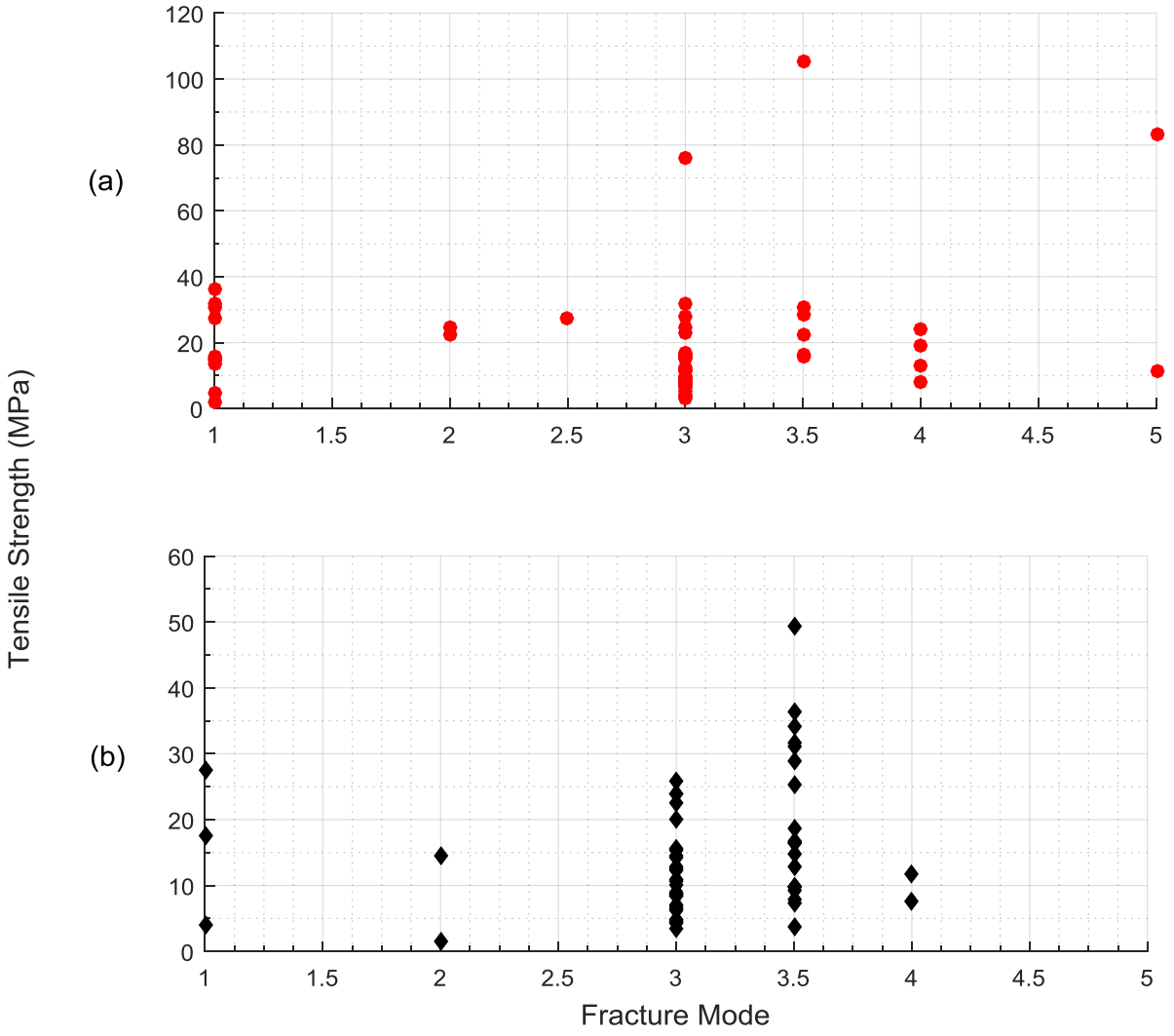


Figure 4-58. Fracture mode vs. tensile strengths for white/tan (major and secondary compounds: quartz, plagioclase feldspar, potassium feldspar, and mica (muscovite)) particles retained (a) between sieve #10 (2 mm) and #20 (0.84 mm) and (b) by sieve #10 (2 mm)

6_C, and White/Tan 25-17_J, experienced Mode 3, 5, and 3.5 fractures, respectively. The exclusion of these particles decreased the tensile strength of Mode 3, 3.5, and 5, as shown in Table 4-21. Furthermore, the fracture modes occurred at various stresses. Particles retained by sieve #10 (2 mm) fractured predominantly at Modes 3, 3.5, and 4, in which Mode 3.5 fractures occurred at higher tensile strengths. All fracture Modes for both size categories occurred at low tensile strengths. From Table 4-21, particles retained between sieve #10 (2 mm) and #20 (0.84 mm) fractured at lower tensile strengths at Mode 1 and at higher tensile strengths at Mode 5; Mode 4 type fractures occurred at higher stresses and Mode 5 type fractures occurred at lower stresses with the exclusion of the outliers. Twenty-one particles fractured as Mode 3 with an average tensile strength of 24.26 MPa. Particles retained by sieve #10 (2 mm) fractured at lower tensile strengths at Mode 1 and at higher tensile strengths at Mode 2. Twenty-eight particles fractured as Mode 3 with at an average tensile strength of 15.11 MPa; no particles experienced a Mode 2.5 or 5 fracture. The majority of particles retained between sieve #10 (2 mm) and #20 (0.84 mm) and by sieve #10 (2 mm) fractured as Mode 3.

Figure 4-59 depicts the average tensile strengths, without outliers, of the fracture modes within one standard deviation for the white/tan (major and secondary compounds: quartz, plagioclase feldspar, potassium feldspar, and mica (muscovite)) particles retained between sieve #10 (2 mm) and #20 (0.84 mm), depicted with red circle data points, and by sieve #10 (2 mm), represented with blue square data points. The size category containing the smaller tensile strength range was shown with thicker error bar lines to distinguish it from the larger tensile strength range in the same fracture mode. For particles retained between sieve #10 (2 mm) and #20 (0.84 mm), the tensile strength range of Mode 3 was largest and smallest for Mode 2. The particle that exhibited a Mode 2.5 fractured at the highest average tensile strength; the particle

Table 4-21. Number of particles and average tensile strengths based on fracture modes for white/tan (major and secondary compounds: quartz, plagioclase feldspar, potassium feldspar, and mica (muscovite)) particles retained between sieve #10 (2 mm) and #20 (0.84 mm) and by sieve #10 (2 mm)

Fracture mode	**Retained between sieve #10 (2 mm) and #20 (0.84 mm)**		**Retained by sieve #10 (2 mm)**	
	Number of Particles	*Average Tensile Strength (MPa)*	*Number of Particles*	*Average Tensile Strength (MPa)*
1	8	14.44	2	3.12
2	6	37.99	4	27.95
2.5	1	23.45	0	0
3	21(20)	24.26 (12.21)	28	15.11
3.5	6(5)	48.34 (22.66)	8	15.98
4	8	38.86	4	24.21
5	4(3)	128.03 (11.45)	0	0

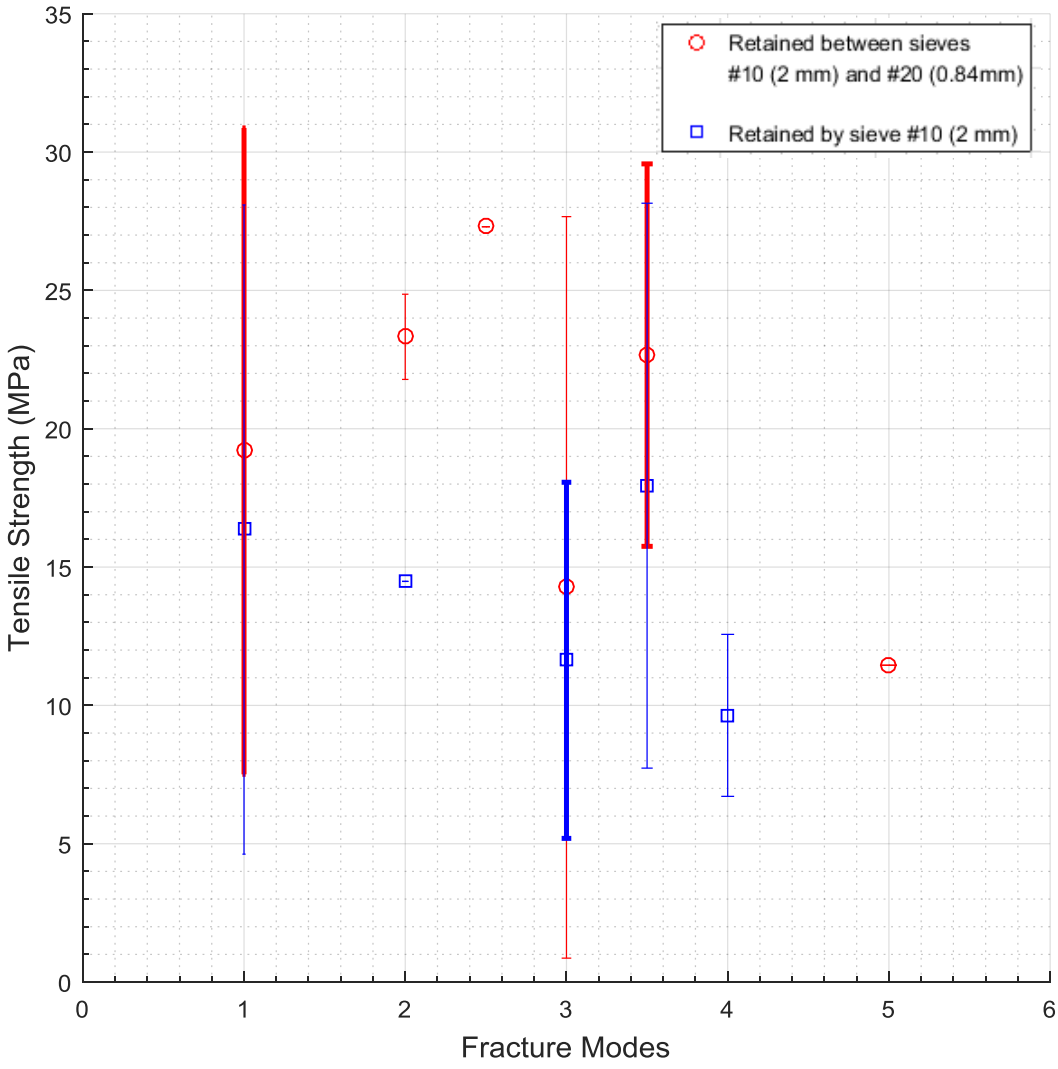


Figure 4-59. Average tensile strengths, without outliers, of the fracture modes within one standard deviation for the white/tan (major and secondary compounds: quartz, plagioclase feldspar, potassium feldspar, and mica (muscovite)) particles retained between sieve #10 (2 mm) and #20 (0.84 mm) and by sieve #10 (2 mm).

that exhibited a Mode 5 fractured at the lowest average tensile strength. For particles retained by sieve #10 (2 mm), Mode 1 has the largest tensile strength range and Mode 4 had the smallest tensile strength range. Particles that exhibit a Mode 3.5 generally fractured at higher tensile strengths; particles that exhibit a Mode 4 generally fractured at lower tensile strengths Modes 2.5 and 5, for particles retained between sieve #10 (2 mm) and #20 (0.84 mm), and Mode 2, for particles retained by sieve #10 (2 mm), were not considered as having the smallest tensile strength range as it as composed of 1 particle. The large tensile strength range of Mode 3, for particles retained between sieve #10 (2 mm) and #20 (0.84 mm), and Mode 1, for particles retained by sieve #10 (2 mm), indicated more variation in tensile strength; The small tensile strength range of Mode 2, for particles retained between sieve #10 (2 mm) and #20 (0.84 mm), and Mode 4, for particles retained by sieve #10 (2 mm), indicated less variation in tensile strength.

Figure 4-60 shows the tensile strength distribution, based on fracture modes, clear/translucent (major and secondary compounds: quartz and plagioclase feldspar) particles retained between sieve #10 (2 mm) and #20 (0.84 mm) and by sieve #10 (2 mm), respectively. The number of particles and average tensile strengths, based on fracture modes, for clear/translucent particles retained by between sieve #10 (2 mm) and #20 (0.84 mm) and by sieve #10 (2 mm) are shown in Table 4-22. Particles retained between sieve #10 (2 mm) and #20 (0.84 mm) fractured at various modes; three outliers, identified as Clear/Translucent 25-26_C, Clear/Translucent 25-42_J, and Clear/Translucent 25-38_J, experienced Mode 3.5, 5, and 5 fractures, respectively. With the exclusion of the outliers, tensile strengths at Mode 3.5 and 5 decreased, as shown in Table 4-22. Particles retained by sieve #10 (2 mm) fractured

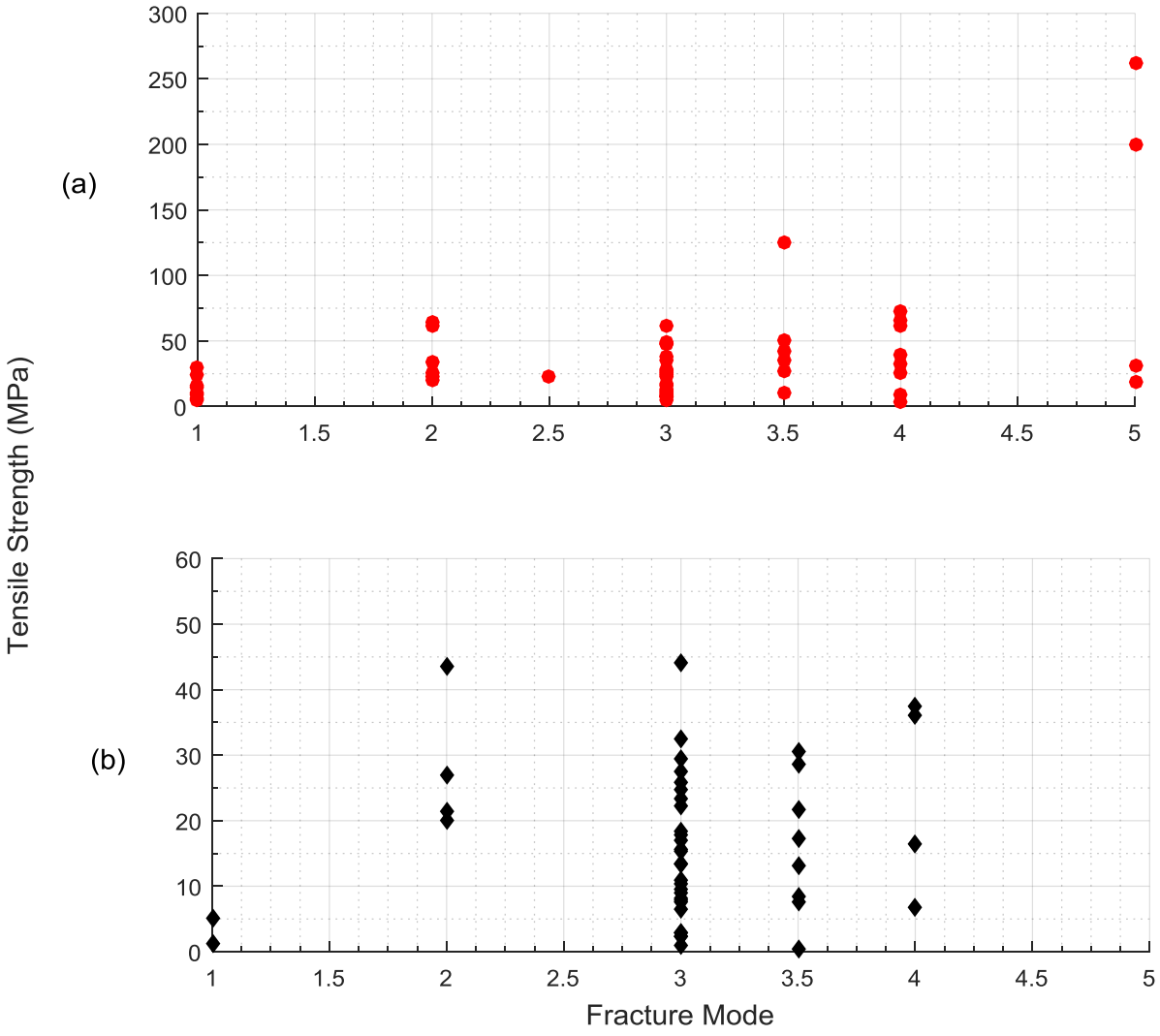


Figure 4-60. Fracture mode vs. tensile strengths for clear/translucent (major and secondary compounds: quartz and plagioclase feldspar) particles retained (a) between sieve #10 (2 mm) and #20 (0.84 mm) and (b) by sieve #10 (2 mm)

Table 4-22. Number of particles and average tensile strengths based on fracture modes for clear/translucent (major and secondary compounds: quartz and plagioclase feldspar) particles retained between sieve #10 (2 mm) and #20 (0.84 mm) and by sieve #10 (2 mm)

Fracture mode	**Retained between sieve #10 (2 mm) and #20 (0.84 mm)**		**Retained by sieve #10 (2 mm)**	
	Number of Particles	*Average Tensile Strength (MPa)*	*Number of Particles*	*Average Tensile Strength (MPa)*
1	10	19.19	3	16.36
2	2	23.32	2	7.99
2.5	1	27.30	0	0
3	31	14.27	29	11.63
3.5	6	36.46	20	19.51
4	4	15.97	2	9.64
5	2	47.36	0	0

predominantly at Modes 3 through 4 at various stresses. All fracture Modes for both size categories occurred at low tensile strengths. From Table 4-22, particles retained between sieve #10 (2 mm) and #20 (0.84 mm) fractured at lower tensile strengths at Mode 3 and at higher tensile strengths at Mode 5; Mode 3.5 type fractures would occur at higher stress with the exclusion of the outliers. Thirty-one particles fractured as Mode 3 with an average tensile strength of 14.27 MPa. Particles retained by sieve #10 (2 mm) fractured at lower tensile strengths at Mode 3.5 and at higher tensile strengths at Mode 2. Twenty-nine particles fractured as Mode 3 with at an average tensile strength of 11.63 MPa; no particles experienced a Mode 2.5 or 5 fracture. The majority of particles retained between sieve #10 (2 mm) and #20 (0.84 mm) and by sieve #10 (2 mm) fractured as Mode 3.

Figure 4-61 depicts the average tensile strengths, without outliers, of the fracture modes within one standard deviation for the clear/translucent (major and secondary compounds: quartz and plagioclase feldspar) particles retained between sieve #10 (2 mm) and #20 (0.84 mm), depicted with red circle data points, and by sieve #10 (2 mm), represented with blue square data points. The size category containing the smaller tensile strength range was shown with thicker error bar lines to distinguish it from the larger tensile strength range in the same fracture mode. For particles retained between sieve #10 (2 mm) and #20 (0.84 mm), the tensile strength range for Mode 2 is the largest and smallest for Mode 5; Mode 2.5 is not considered to be the smallest as it is composed of 1 particle. For particles retained by sieve #10 (2 mm), the tensile strength range of Mode 4 is the largest and smallest for Mode 1. This indicated that Mode 2, for particles retained between sieve #10 (2 mm) and #20 (0.84 mm), and Mode 4, for particles retained by sieve #10 (2 mm) had more variation in tensile strength. Mode 5, for particles retained between sieve #10 (2 mm) and #20 (0.84 mm), and Mode 1, for particles retained by sieve #10 (2mm) had

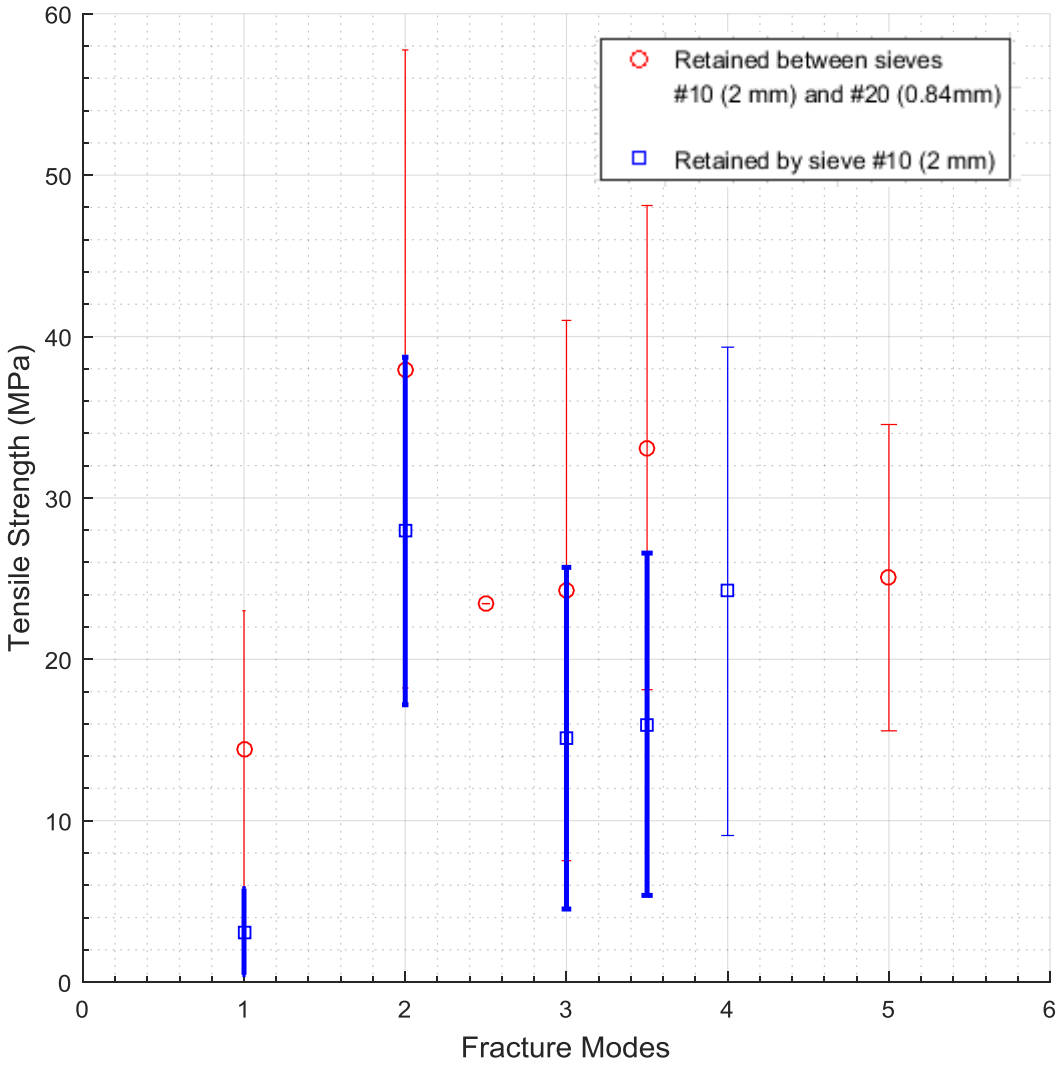


Figure 4-61. Average tensile strengths, without outliers, of the fracture modes within one standard deviation for the clear/translucent (major and secondary compounds: quartz and plagioclase feldspar) particles retained between sieve #10 (2 mm) and #20 (0.84 mm) and by sieve #10 (2 mm).

the least variation in tensile strength. Mode 2 in both size categories had the highest average tensile strengths and Mode 1 in both size categories had the lowest average tensile strengths.

Overall, the red/pink (major and secondary compounds: quartz, potassium feldspar, and plagioclase feldspar), black/brown (major and secondary compounds: quartz, mica (biotite), tridymite, plagioclase feldspar, potassium feldspar, and calcite), white/tan (major and secondary compounds: quartz, plagioclase feldspar, potassium feldspar, and mica (muscovite)) and clear/translucent (major and secondary compounds: quartz and plagioclase feldspar) particles retained between sieve #10 (2 mm) and #20 (0.84 mm) and by sieve #10 (2 mm) predominantly experienced a Mode 3 fracture. Furthermore, all particles at lower tensile strengths experienced various fracture modes while particle at higher tensile strengths experienced a smaller range of fracture modes; this range varies based on particle morphology and size. For particles retained between sieve #10 (2 mm) and #20 (0.84 mm), red/pink, white/tan, and clear/translucent particles experienced higher tensile strengths at Mode 5 fractures while the brown/black particles experienced higher tensile strengths at Mode 1 fractures, with the inclusion of the outliers; without the inclusions of the outliers, the particles experienced higher tensile strengths at various modes. Regardless of outliers, these particles experienced lower tensile strengths at various modes. Particle retained by sieve #10 (2 mm) experienced higher tensile strengths at various modes, regardless of outliers, and lower tensile strengths at Mode 1 fractures, with the exclusion of clear/translucent particles that experienced lower tensile strengths at Mode 2 fractures. Regardless of outliers, the black/brown particles had higher. Furthermore, there was no correlation between particle mineralogy, tensile strength, and fracture mode for particles retained between sieve #10 (2 mm) and #20 (0.84 mm). For particles retained by sieve #10 (2 mm), the black/brown particles were observed to maintain high tensile strengths in all fracture modes, with

the exclusion of Mode 2.5 and 3. Therefore, it is predicted that black/brown particles will fracture at high tensile strengths regardless of which fracture mode is experienced.

4.3 SYNCHROTRON MICRO-TOMOGRAPHY (SMT) IMAGING

Synchrotron micro-tomography imaging is a non-destructive method used to obtain 3-D x-ray images during single particle compression to provide d_L, fracture mode, and internal structure of 14 mason sand particles. Particle d_L and internal structures were obtained from the pre-loading 3-D images; particle fracture modes were obtained from 3-D fracture images. Tensile strengths of the particles were calculated from the facture load and d_L. Particle label, color, size (retained between sieve #10 (2 mm) and #20 (0.84 mm) and by sieve #10 (2 mm)), d_L (mm), peak load (N), fracture load (N), tensile strength (MPa), fracture mode, and internal structure mode are listed in Table J-1 in Appendix J.

The sample contained 4 red/pink (major and secondary compounds: quartz, potassium feldspar, and plagioclase feldspar) particles, 3 black/brown (major and secondary compounds: quartz, mica (biotite), tridymite, plagioclase feldspar, potassium feldspar, and calcite) particles, 4 white/tan (major and secondary compounds: quartz, plagioclase feldspar, potassium feldspar, and mica (muscovite)) particles, and 3 clear/translucent (major and secondary compounds: quartz and plagioclase feldspar) particles. Two red/pink, 1 black/brown, 2 white/tan, and 2 clear/translucent particles were retained between sieve #10 (2 mm) and #20 (0.84 mm); 2 red/pink, 2 black/brown, 2 white/tan, and 1 clear/translucent particles were retained by sieve #10 (2 mm). The outliers will not be removed from the analysis because the sample contains only 1 to 2 particles in each colored subgroup and size category.

Based on previous research, it was predicted that the Weibull model was be an excellent model to determine the characteristic tensile strength (σ_{0f}) of the sample; from the uniaxial

experiments, it was hypothesized that σ_{0f} will be higher than σ_{63} obtained from the tensile histogram. The fracture modes exhibited by the particles will depend on the mineralogy and morphology of the particle. From results of the uniaxial compression experiments, it was predicted that particles in both size categories will predominantly exhibit a Mode 3 fracture and black/brown (major and secondary compounds: quartz, mica (biotite), tridymite, plagioclase feldspar, potassium feldspar, and calcite) particles will fracture at the highest tensile strengths in all fracture Modes. Particles with more internal flaws will fracture at lower tensile strengths due to the decrease in mineral hardness (Lade at al. 1996; Todisco et al. 2016).

4.3.1 Weibull Model and Tensile Strength

Weibull statistical analysis was performed to examine the distribution of tensile strength and to determine the characteristic tensile strength of the 14 mason sand particle that SMT imaging is performed on; Figure 4-62 displays the Weibull statistical model for these particles. As shown in Figure 4-62, the values for R^2, Weibull modulus (m_f), and characteristic tensile strength (σ_{0f}) are 0.81, 0.682, and 20.93 MPa. The R^2 value of 0.81 was relatively high and indicates that the Weibull model was a good statistical indicator of particle distribution based on tensile strength. The m_f value was relatively low, implying high variations in particle strength, and therefore, no correlation between particle size and tensile strength. The σ_{0f} of 20.93 MPa indicates the tensile stress in which 37% of particles will survive. This implied that approximately 63% of the particles will had already fractured at a tensile strength of 20.93 MPa and 37% of the particles can still sustain further tensile strength until fracturing stage.

A tensile strengths histogram of the 14 mason sand particles was created to examine the distribution of tensile strength, as shown in Figure 4-63. The 63rd percentile strength, mean, and standard deviation tensile strength was examined. The distribution was strongly left skewed in

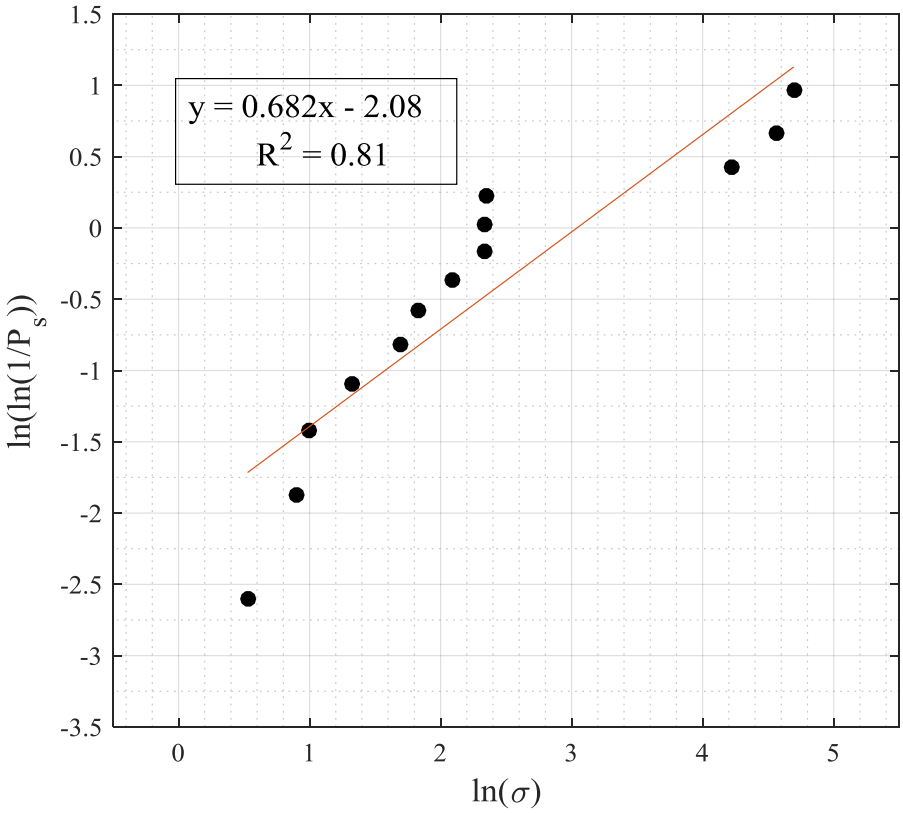


Figure 4-62. Weibull distribution of characteristic tensile strength for mason sand particles retained between sieve #10 (2 mm) and #20 (0.84 mm) and by sieve #10 (2 mm)

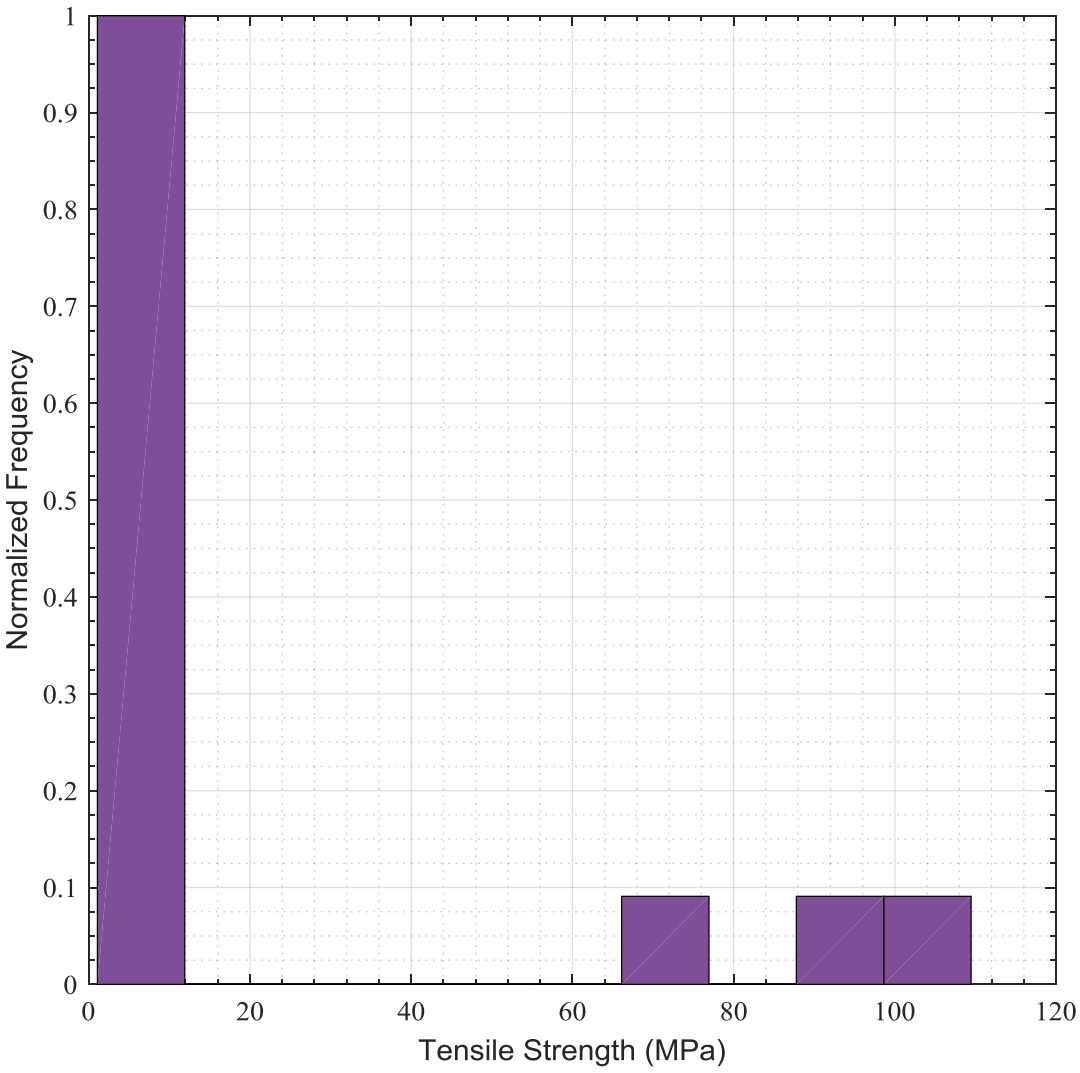


Figure 4-63. Tensile histogram for mason sand particles retained between sieve #10 (2 mm) and #20 (0.84 mm) and by sieve #10 (2 mm)

which 11 particles had a tensile strength between 1.00 to 10.50 MPa and 3 particles had a tensile strength greater than 10.5 MPa. The 63rd percentile strength is 10.37 MPa; this implied that 63% of particles will fracture prior to a tensile strength of 10.37 MPa; compared to the σ_{0f} of 20.93 MPa, the σ_{63} was approximately half. The reason may be due to the small sample size causing a large variation in tensile strength between the 14 particles. The mean and standard deviation tensile strengths of the distribution were 23.98 and 37.39 MPa. The mean tensile strength indicates that approximately 50% of particles fractured at a tensile strength of 23.98 MPa. Overall, the Weibull model was a good indicator of the tensile stress of sand particles but the characteristic tensile stress value obtained will be greater than the actual value at which 63% of particles fracture.

4.3.2 Fracture Mode

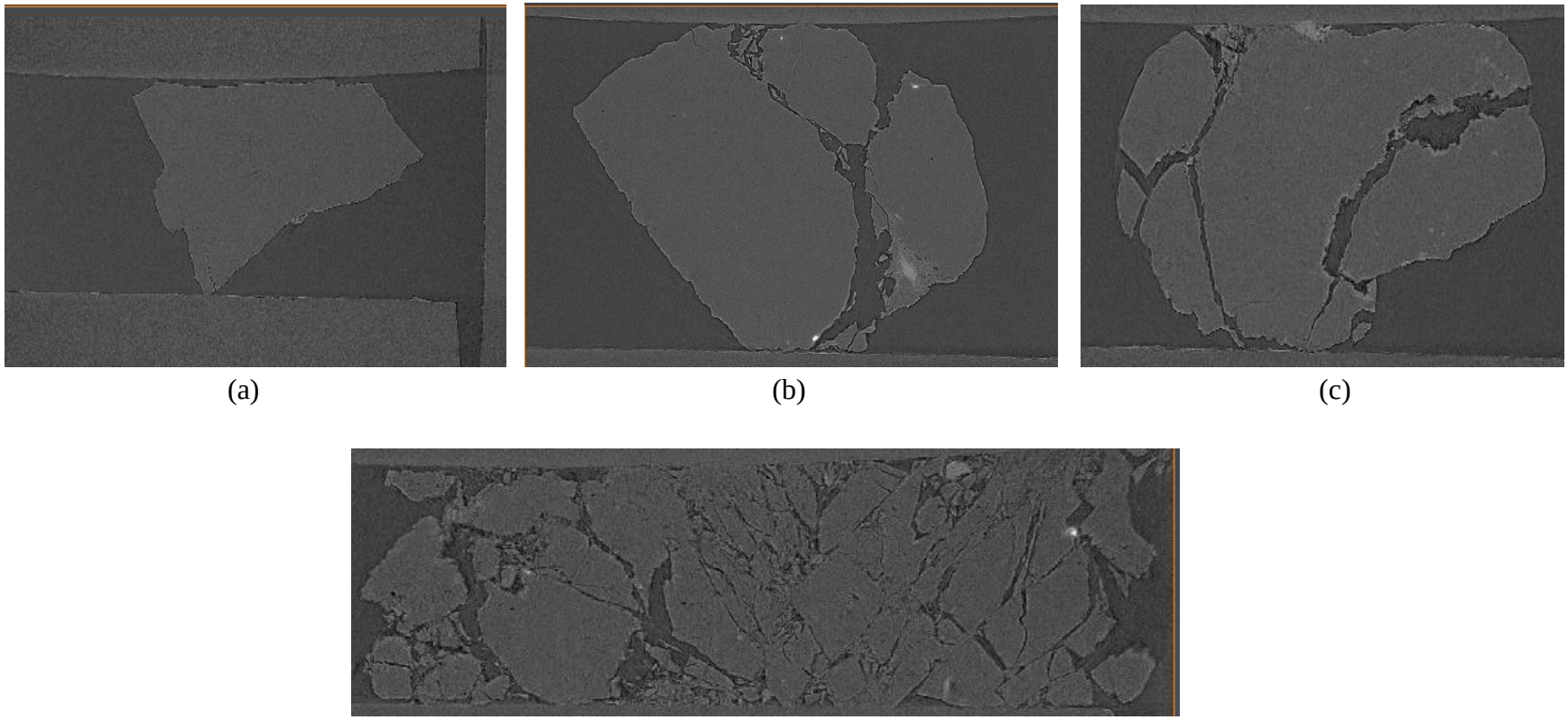
The fracture modes are classified, based on Nakate at al. (2001) and other literature and summarized by Parab et al. (2014), as (a) Mode 1, small abrasion failure or fracture with large piece remaining with a tiny piece or asperities, (b) Mode 2, multiple abrasion failure or fracture of large piece with small or tiny piece with or without asperities, (c) Mode 3, major fracture into at least 2 pieces, (d) Mode 4, fracture of sub-particles into smaller pieces, and (e) Mode 5, pulverization of particle into many small pieces. Particle that did not post particle descriptions were categorized as fracture Mode 0 and particles that exhibited fracture modes between two categories were categorize as Mode 3.5, a particle that displayed fractures from Mode 3 and 4. The particles in this sample experienced fracture Modes 1, 3, 3.5, and 4; 3-D x-ray images of these fracture modes are shown in Figure 4-64.

Prediction of how particles will fracture was dependent on the particle mineralogy and morphology as it affects the hardness and coordination number of the particles, influencing the

fracture pattern. It was predicted that the majority of particles in both size groups and colored subgroups will exhibit a Mode 3 or 4 fractures as the particles are loaded until initial fracture is observed. Furthermore, the black/brown (major and secondary compounds: quartz, mica (biotite), tridymite, plagioclase feldspar, potassium feldspar, and calcite) particles is expected to fracture at higher tensile strengths compared to other colored particles.

Figure 4-65 displays the fracture modes for the 14 mason sand particles. The circle data points, square data points, right sided triangle data points, and triangle data points represent the red/pink (major and secondary compounds: quartz, potassium feldspar, and plagioclase feldspar), black/brown (major and secondary compounds: quartz, mica (biotite), tridymite, plagioclase feldspar, potassium feldspar, and calcite), white/tan (major and secondary compounds: quartz, plagioclase feldspar, potassium feldspar, and mica (muscovite)) and clear/translucent (major and secondary compounds: quartz and plagioclase feldspar) particles; the unfilled data points represent the particles retained between sieve #10 (2 mm) and #20 (0.84 mm) and the filled data points represent the particles retained by sieve #10 (2mm).

As shown in Figure 4-65, particles retained between sieve #10 (2 mm) and #20 (0.84 mm) predominantly exhibited a Mode 3 fracture; particles retained by sieve #10 (2mm) predominantly fractured at Mode 4. For particles retained between sieve #10 (2 mm) and #20 (0.84 mm), a red/pink particle fractured at the lowest tensile strength and a white/tan particle fractured at the highest tensile strength. For particles retained by sieve #10 (2 mm), a black/brown particle fracture at the lowest and highest tensile strength. A red/pink particle retained between sieve #10 (2 mm) and #20 (0.84 mm) fractured at the lowest tensile strength and a black/brown particle retained by sieve #10 (2 mm) fractured at the highest tensile strength; a white/tan particle retained by sieve #10 (2 mm) did not fracture. As predicted, particles



(a) (b) (c)

(d)

Figure 4-64. Particle classification based on fracture (a) Mode 1, (b) Mode 3, (c) Mode 3.5, and (d) Mode 4.

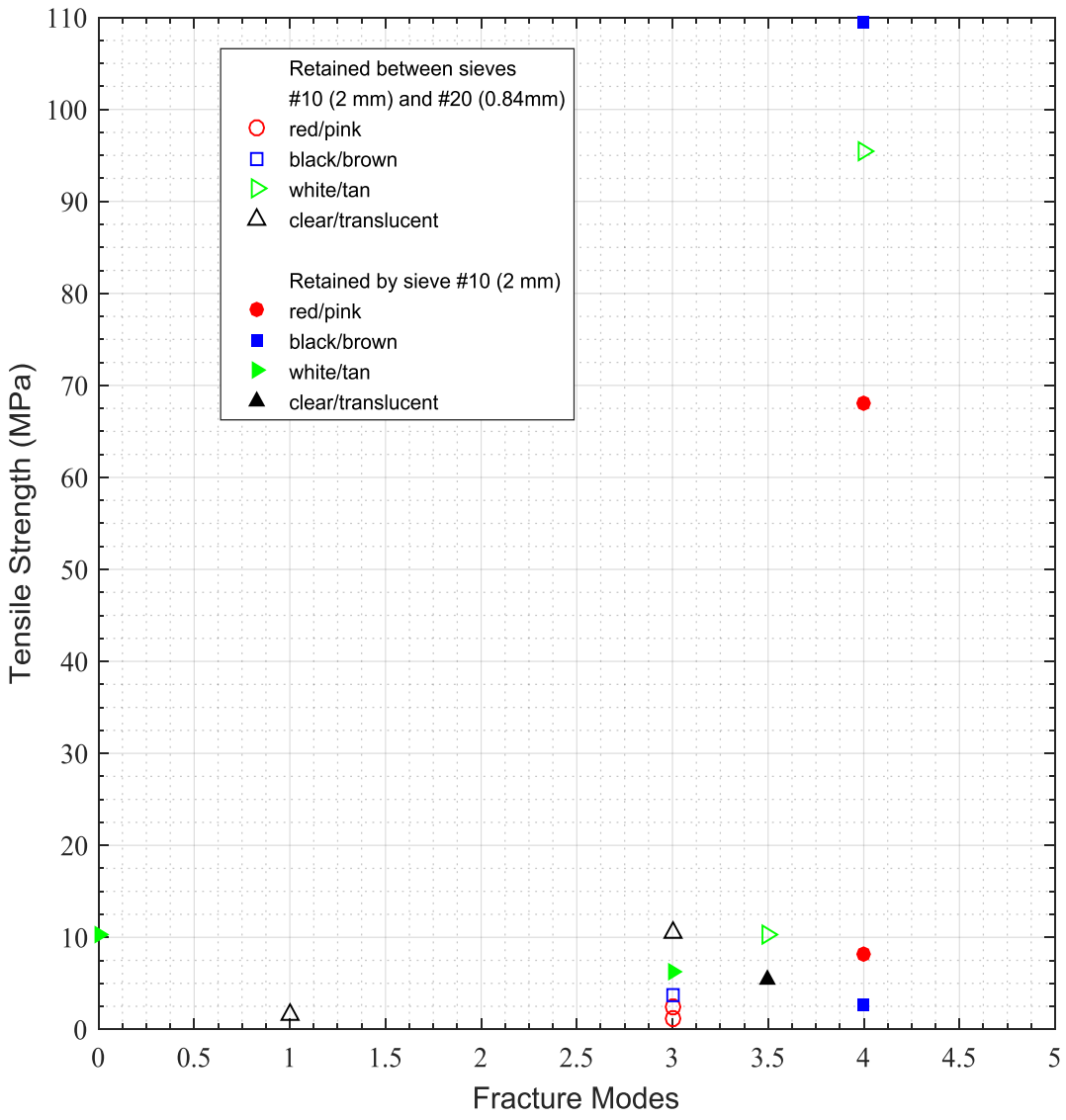


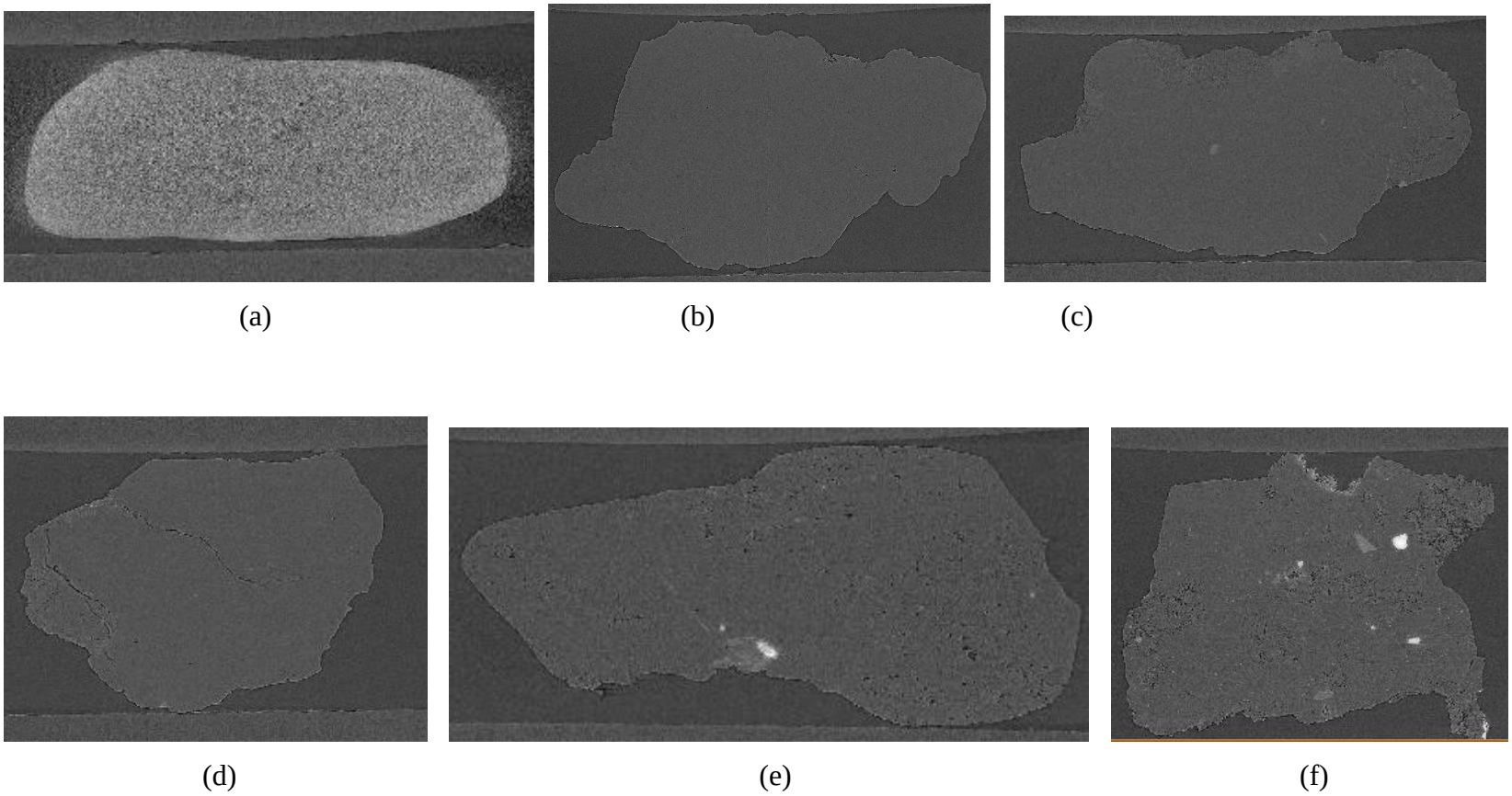
Figure 4-65. Fracture mode vs. tensile strengths for red/pink (major and secondary compounds: quartz, potassium feldspar, and plagioclase feldspar), black/brown (major and secondary compounds: quartz, mica (biotite), tridymite, plagioclase feldspar, potassium feldspar, and calcite), white/tan (major and secondary compounds: quartz, plagioclase feldspar, potassium feldspar, and mica (muscovite)) and clear/translucent (major and secondary compounds: quartz and plagioclase feldspar) particles retained between sieve #10 (2 mm) and #20 (0.84 mm) and by sieve #10 (2 mm)

retained between sieve #10 (2 mm) and #20 (0.84 mm) predominantly exhibited a Mode 3 fracture and particles retained by sieve #10 (2 mm) predominantly exhibited a Mode 4 fracture,coinciding with fracture pattern results from the uniaxial compression experiments performed Furthermore, though the black/brown (major and secondary compounds: quartz, mica (biotite), tridymite, plagioclase feldspar, potassium feldspar, and calcite) particles did had fracture at the highest tensile strength in all Modes, the black/brown particle retained by sieve #10 (2 mm) exhibiting a fracture Mode 4 fractured at the highest tensile strength.

4.3.3 Internal Structure

Internal structures of particles were classified based on an internal structure rating system from 1 through 6, adopted from Druckrey (2016). A particle with solid internal structure containing little to no internal flaws was denoted with an internal structure rating of 1. A particle with very few small internal flaws was denoted with an internal structure rating of 2. An internal structure rating of 3 implied that the particle had small flaws scattered throughout; a rating of 4 suggested that the particle had various flaws and a few micro-cracks scattered throughout. A rating of 5 indicated a particle with an abundant of flaws and micro-cracks; a rating of 6 denoted a particle that was internally strewn with flaws and microcracks; 3-D x-ray images of these fracture modes are shown in Figure 4-66. It was predicted that particles with a higher internal structure rating will fracture at lower tensile strengths due to decrease in mineral hardness as a result of increasing internal structural flaws (Lade at al. 1996; Todisco et al. 2016).

Figure 4-67 shows the internal structure ratings (referred to as rating) for the 14 mason sand particles. The circle data points, square data points, right sided triangle data points, and triangle data points represent the red/pink (major and secondary compounds: quartz, potassium feldspar, and plagioclase feldspar), black/brown (major and secondary compounds: quartz, mica



(a) (b) (c)

(d) (e) (f)

Figure 4-66. Particle classifications based on internal structure (a) rating 1, (b) rating 2, (c) rating 3 (d) rating 4, (e) rating 5, and (f) Mode 6.

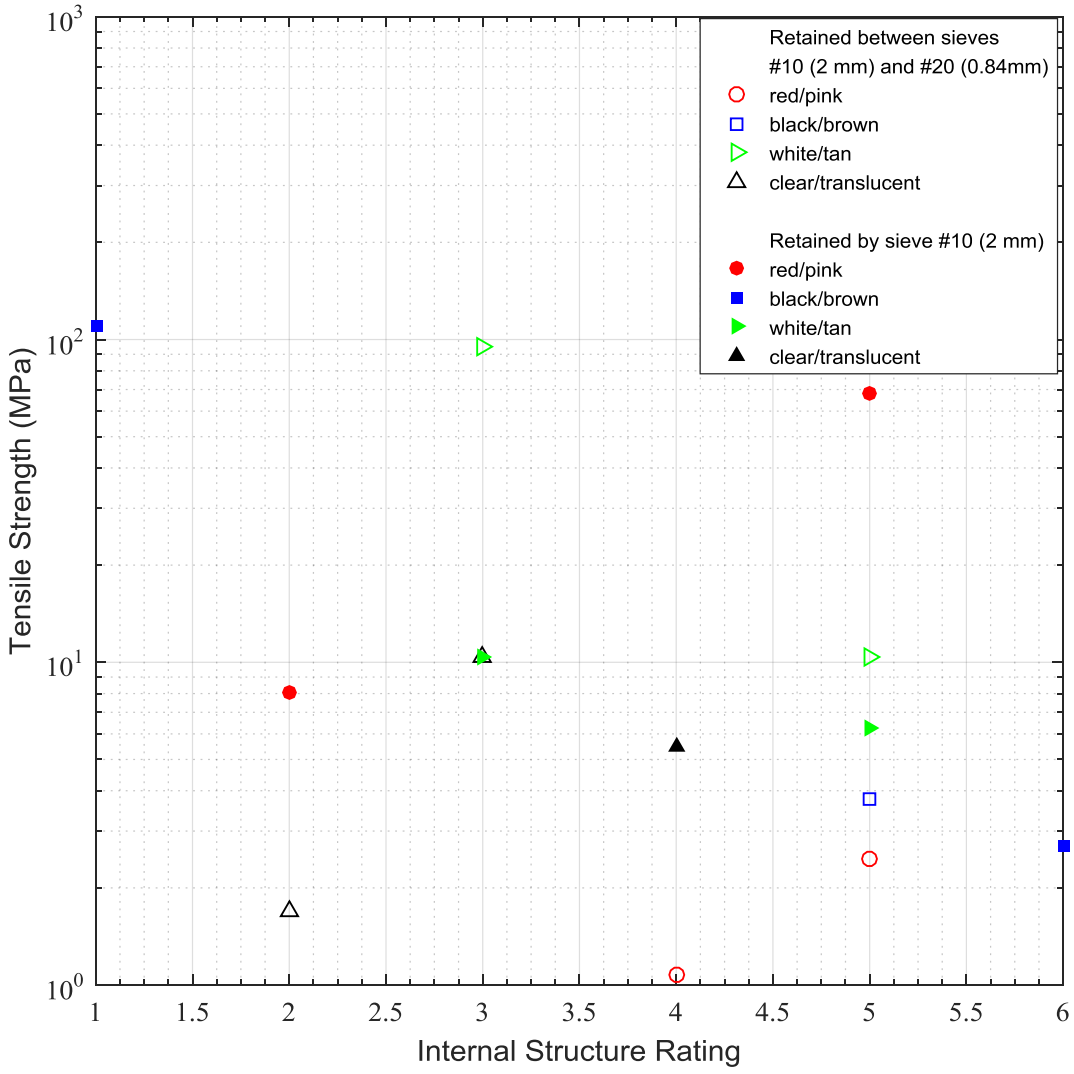


Figure 4-67. Internal structure rating vs. tensile strengths for red/pink (major and secondary compounds: quartz, potassium feldspar, and plagioclase feldspar), black/brown (major and secondary compounds: quartz, mica (biotite), tridymite, plagioclase feldspar, potassium feldspar, and calcite), white/tan (major and secondary compounds: quartz, plagioclase feldspar, potassium feldspar, and mica (muscovite)) and clear/translucent (major and secondary compounds: quartz and plagioclase feldspar) particles retained between sieve #10 (2 mm) and #20 (0.84 mm) and by sieve #10 (2 mm)

(biotite), tridymite, plagioclase feldspar, potassium feldspar, and calcite), white/tan (major and secondary compounds: quartz, plagioclase feldspar, potassium feldspar, and mica (muscovite))and clear/translucent (major and secondary compounds: quartz and plagioclase feldspar) particles; the unfilled data points represent the particles retained between sieve #10 (2 mm) and #20 (0.84 mm) and the filled data points represent the particles retained by sieve #10 (2mm).

As seen in Figure 4-67, particles retained between sieve #10 (2 mm) and #20 (0.84 mm) and by sieve #10 (2 mm) had various ratings. A black/brown particle retained by sieve #10 (2 mm) had the lowest and highest rating. A red/pink particle retained between sieve #10 (2 mm) and #20 (0.84 mm), with a rating of 4, fractured at the lowest tensile strength while a black/brown particle, with a rating of 1, fractured at the highest tensile strength. A black/brown and red/pink particle retained by sieve #10 (2 mm) and a white/tan particle retained between sieve #10 (2 mm) and #20 (0.84 mm) had high tensile strengths; the black/brown and red/pink particle retained by sieve #10 (2 mm) had the highest and lowest tensile strength. As the tensile strengths of the particles decreased, the internal structural ratings increased. For the red/pink particles retained between sieve #10 (2 mm) and #20 (0.84 mm) and by sieve #10 (2 mm) and the clear/translucent particles retained between sieve #10 (2 mm) and #20 (0.84 mm), the internal structure ratings increased as the tensile strengths increased. For the white/tan particles retained between sieve #10 (2 mm) and #20 (0.84 mm) and by sieve #10 (2 mm) and the black/brown particles retained by sieve #10 (2 mm), the internal structure ratings decreased as the tensile strengths increased. The trend for the black/brown particles retained between sieve #10 (2 mm) and #20 (0.84 mm) and the clear/translucent particles retained by sieve #10 (2 mm) cannot be assessed as there is only 1 particle in these subgroups and size category. Based on Figure 4-67,

the internal structure rating increased as the tensile strength decreased for white/tan and black/brown particles and for particles having high tensile strengths. This indicated that the hypothesis that internal structure ratings increased as tensile strengths decreased is true with the exception of the red/pink particles in both size categories and clear translucent particles retained between sieve #10 (2 mm) and #20 (0.84 mm).

CHAPTER FIVE: CONCLUSIONS AND RECOMMENDATIONS

5.1 CONCLUSION

This thesis examined the Weibull distribution model and investigated the influence of particle size, mineralogy, shape, angularity, surface texture, and fracture mode on tensile strength using uniaxial compression and the influence of internal structure and fracture mode using synchrotron micro-tomography. Particle mineralogy classifications and fracture modes were adopted from Druckrey (2016) and Parab et al., (2014). Uniaxial compression experiments were conducted on particles based on four colored subgroups (red/pink (major and secondary compounds: quartz, potassium feldspar, and plagioclase feldspar), black/brown (major and secondary compounds: quartz, mica (biotite), tridymite, plagioclase feldspar, potassium feldspar, and calcite), white/tan (major and secondary compounds: quartz, plagioclase feldspar, potassium feldspar, and mica (muscovite)) and clear/translucent (major and secondary compounds: quartz and plagioclase feldspar)) and two size categories (particles retained between sieve #10 (2 mm) and #20 (0.84 mm) and by sieve #10 (2 mm)). Through experimental work, the following conclusions were drawn:

- Weibull statistical distribution was a good model to for determining the characteristic tensile strength of unconfined uniaxial compressed sand particles, with a tendency to overestimate the tensile strength at which 63% of particles will fracture. The Weibull model can be used to determine how similar the tensile strengths of the particles are based on the clusters formed within the distribution.

- Particles with larger d_L generally fractured at lower tensile strengths; particles retained between sieve #10 (2 mm) and #20 (0.84 mm) fractured at higher tensile strengths.

- Clear/translucent particles retained between sieve #10 (2 mm) and #20 (0.84 mm) fractured at higher tensile strengths while white/tan particles, within the same size category, fractured at lower tensile strengths. For particles retained by sieve #10 (2 mm), black/brown particles fractured at higher tensile strengths while white/tan particle fractured at lower tensile strengths. Furthermore, the distribution of tensile stress for particles retained between sieve #10 (2 mm) and #20 (0.84 mm) is wider, which indicated greater variation in tensile strengths within smaller particles.

- Platy shaped particles had smaller d_L and fractured at higher tensile strengths, with the exclusion of white/tan platy shaped particles fracturing at lower tensile strengths; triangular prismatic shaped particles had larger d_L and fractured at lower tensile strengths. Clear/translucent spherical shaped particles fractured at higher tensile strengths while tan/white spherical shaped particles had smaller d_L.

- Subrounded particles fractured at higher tensile strengths, with the exclusion of clear/translucent particles retained by sieve #10 (2 mm). For particles retained between sieve #10 (2 mm) and #20 (0.84 mm), subrounded particles generally had smaller d_L; for particles retained by sieve #10 (2 mm), subrounded particles generally had larger d_L, with the exception of the black/brown particles. With the exclusion of red/pink and black/brown particles, all other colored subgroups within the two size categories had predominantly subrounded particles.

- Smooth particles generally fractured at higher tensile strengths compared to rough particles, with the exception of clear/translucent particles retained by sieve #10 (2 mm) and black/brown particles retained between sieve #10 (2 mm) and #20 (0.84 mm) with

outliers. The d_L of smooth particles were generally smaller compared to rough particles, with the exception of white/tan particles retained between sieve #10 (2 mm) and #20 (0.84 mm) and red/pink and clear/translucent particles retained by sieve #10 (2 mm).

- All particles exhibited a Mode 3 fracture. For particles retained between sieve #10 (2 mm) and #20 (0.84 mm), red/pink, white/tan, and clear/translucent particles that fractured at higher tensile strengths exhibited a Mode 5 fracture while brown/black particles, with outliers, that fractured at higher tensile strengths exhibited a Mode 1 fracture; black/brown particles without outliers exhibited various fracture modes at high tensile strengths. For particles retained by sieve #10 (2 mm), all particles exhibited various fracture modes at high tensile stress and Mode 1 fracture at low tensile strengths, with the exception of clear/translucent particles exhibiting a Mode 2 fracture at low tensile strengths. Black/brown particles retained by sieve #10 (2 mm) fracture at high tensile strengths within all 5 fracture modes.

- Particles will predominantly exhibit a Mode 3 or 4 fractures under uniaxial compression, regardless of particle size and mineralogy.

- Particles with higher internal structure ratings are likely to fracture at lower tensile strengths.

This study examined various factors that influenced the tensile stress of single sand particles under uniaxial compression. The understanding of these factors and their influence on tensile strength can aid in the comprehension of sand particle fractures in bulk material.

5.2 RECOMMENDATIONS

Experimental work and visual inspections provided information to classify the particle size, mineralogy, shape, angularity, surface texture, and fracture mode and its influence on tensile strength; particle minerology and fracture mode were adopted from Druckrey (2016) and Parab et al., (2014). This thesis builds on previous research regarding particle fracture and tensile strength examined based on Weibull statistical model, DEM, high-speed microscope camera, and 3D imaging by investigation the influence of particle size, mineralogy, shape, angularity, surface texture, and fracture mode on tensile stress. Thus, the results lead to the following recommendations for future research:

- Utilize a microscopic camera to measure the d_L to 0.001mm for better accuracy.
- Examine the correlation between particle displacement and tensile strength
- Perform 1-D compression of a sand cluster to examine the influence of these factors, as well as chain reactions, within the cluster.
- Investigate the influence of internal structure, morphology, and triangular prismatic loading, of a larger sand sample, on particle fracture by utilizing a non-destructive technique

REFERENCES

Al Mahbub, A. and Haque, A. (2016). "X-ray computed tomography imaging of the microstructure of sand particles subjected to high pressure one-dimensional compression." *Materials*, 9 (890), doi:10.3390/ma9110890.

Alshibli, K.A., and Alsaleh, M.I. (2004). "Characterizing surface roughness and shape of sands using digital microscopy." *Journal of Computing in Civil Engineering*, 36-45

Alshibli, K.A., Druckrey, A.M., Al-Raoush, R.I., Weiskittel, T., and Lavrik, N.V. (2014). "Quantifying morphology of sands using 3D imaging." *Journal of Materials in Civil Engineering*, 10.1061/(ASCE)MT.1943-5533.0001246

Blasi, A., Brajkovic, A., de Pol Blasi, C., Foord, E.E., Martin, R.F., and Zanazzi, P.F. (1984). "Structure refinement and genetic aspects of a microcline overgrowth on amazonite from Pikes Peak batholith Colorado, U.S.A.". *Bulletin de Mineralogie*, 107, 411-422.

Blasi, A., de Pol Blasi, C., and Zanazzi, P.F. (1987). "A re-examination of the Pellotsalo microcline: Mineralogical implications and genetic considerations". *Canadian Mineralogist*, 25, 527-537.

Carraro, A. and Salviulo, G. (1998). "Pressure and temperature estimates from crystal chemical studies of pyroxenes in spinel lherzolite xenoliths from the Predazzo igneous complex, Dolomites region, North Italy". *Neues Jahrbuch fuer Mineralogie*, Monatshefte, 529-544.

Cavarretta, I. and O'Sullivan, C. (2012). "The mechanics of rigid irregular particles subject to uniaxial compression." *Géotechnique*, 62(8), 681-692.

Cavarretta, I., Coop, M., and O'Sullivan, C. (2010). "The influence of particle characteristics on the behavior of coarse grained soils." *Géotechnique*, 60(6), 413-423.

Cil, M.B. and Alshibli, K.A. (2012).”3D assessment fracture of sand particles using discrete element method.” *Géotechnique Letters*, 2, 161-166.

Cil, M.B. and Alshibli, K.A. (2014).”3-D evolution of sand fracture under 1d compression.” *Géotechnique*, 64(5), 351-364.

Druckrey, A.M. and Alshibli, K.A. (2015). “3D finite element modeling of sand particle fracture based on in situ x-ray synchrotron imaging.” *International Journal for Numerical and Analytical Methods in Geomechanics*. DOI:10.1002/nag.2396.

Druckrey, A.M., Alshibli, K.A., Al-Raoush, R.I. (2016). “3D characterization of sand particle-to-particle contact and morphology.” *Computers and Geotechnics*, 74, 26-35.

Druckrey, A. (2016). “3D Multi-Scale Behavior of Granular Materials using Experimental and Numerical Techniques.” Ph.D dissertation, University of Tennessee, Knoxville.

Eberl (2003). “User’s guide to RockJock – A program for determining quantitative mineralogy from powder x-ray diffraction data.” U.S. Geological Survey, Boulder, CO.

Elbouaanani, L.K., Malaman, B., and Gerardin, R. (1999). “Synthesis, crystal structure, and magnetic properties of Fe P3 Si O11: first example of iron(III) silicophosphate”. *Journal of Solid State Chemistry*, 147, 565-572.

Finney, J.J. (1962). “The crystal structure of carminite and authigenic maximum microcline”. *Thesis*, University of Wisconsin, 1-111

Ghose, S., McMullan, R.K., and Weber, H.P. (1993). “Studies of the P1- I1- transition in anorthite, Ca Al2 Si2 O8, and the crystal structure of the body-centered phase at 514 K”. *Zeitschrift fuer Kristallographie*, 204, 215-237.

Hagerty, M.M., Hite, D.R., Ulrich, C.R., and Hagerty, D.J. (1993). "One-dimensional high pressure compression of granular media." *Journal of Geotechnical Engineering*, 199, 1-18.

Hardin, B.O. (1985). "Crushing of soil particles." *Journal of Geotechnical Engineering,* ASCE, 111(10), 1177-1192.

Harremoes, P. (1959). "Compressibility of ground sand at high pressure," MS thesis, Massachusetts Institute of Technology, Cambridge, Mass., 18.

HighScore Plus Version 4.0 [Computer software]. (2014). Almelo, The Netherlands: PANalytical B.V.

Hybler, J., Petricek, V., Fabry, J., and Durovic, S. (2002). "Refinement of the crystal structure of cronstedtite - 2H". *Clays and Clay Minerals*. 50(5), 601-613.

Jackson, W.W. and West, J. (1931). "The crystal structure of muscovite - K Al3 Si3 O10 (O H)2". *Zeitschrift fuer Kristallographie*, 76, 211-227.

Jaeger, J.C. (1967). "Failure of rocks under tensile conditions." *International Journal of Rock Mechanics and Mining Sciences & Geomechanics Abstract*, **4** (2),219-227.

Janeczek, J. and Sachanbinski, M. (1992). "Babingtonite, Y-Al-rich titanite, and zoned epidote from the Strzegom pegmatites, Poland". *Euopean Journal of Mineralogy*, 4, 307-319.

Konnert, J.H. and Appleman, D.E. (1978). "The crystal structure of low tridymite". *Acta Crystallographica B*, 34, 391-403.

Lade, P.V., Yamamuro, J.A., and Bopp, P.A. (1996). "Significance of particle crushing in granular materials." *Journal of Geotechnical Engineering,* 122(4), 309-316.

Lee, K.L. and Farhoomand, I. (1967). "Compressibility and crushing of granular soils in anisotropic triaxial compression." *Canadian Geotechnical Journal,* 4(1), 68-86.

Marsal, R.J. (1967). "Large scale testing of rockfill materials." *Journal of the Soil Mechanics and Foundations Division,* ASCE, 93(2), 27-43.

McDowell, G.R. (2002). "On the yielding and plastic compression of sand." *Soils and Foundations,* 41(1), 139-145.

McDowell, G.R. and Amon, A. (2000). "The application of Weibull statistics to the fracture of soil particles." *Soils and Foundations*, 40(5), 133-141.

McDowell, G.R. and Bolton, M.D. (1998). "On the micromechanics of crushable aggregates." *Géotechnique,* 48(5), 667-679.

McDowell, G.R., Bolton, M.D., and Robertson, D. (1996). "The fractal crushing of granular material." *Journal of Mechanics and Physics of Solids*, 44(12), 2079-2102.

McDowell, G.R. and Harireche, O. (2002). "Discrete element modelling of soil particle fracture." *Géotechnique,* 52(2), 131-135.

Mesri, G. and Vardhanabhuti, B. (2009). "Compression of granular material." *Canadian Geotechnical Journal,* 46, 369-392.

Miura, N. and Yamanouchi, T. (1975). "Effect of water on the behavior of a quartz-rich sand under high stresses." *Soils and Foundations*, 15(4), 23-34.

"Mohs Hardness Scale. " 2005. <http://geology.com/minerals/mohs-hardness-scale.shtml> (May 1, 2017)

"Mohs Scale of Mineral Hardness." 1998. < http://www.amfed.org/t_mohs.htm > (May 1, 2017)

Nakata, Y., Hyde, A.F.L., Hyodo, M., and Murata, H. (1999). "A probabilistic approach to sand particle crushing in the triaxial test." *Géotechnique*, 49(5), 567-583.

Nakata, Y., Hyodo, M., Hyde, A.F.L., Kato, Y., and Murata, H. (2001). "Microscopic particle crushing of sand subjected to high pressure one-dimensional compression." *Soils and Foundations*, 41(1), 69-82.

Nikitin, A.N.; Markova, G.V. Balagurov, A.M. Vasin, R.N. and Alekseeva, O.V. (2007). "Investigation of the structure and properties of quartz in the alpha - beta transition range by neutron diffraction and mechanical spectroscopy". *Kristallografiya*, 52(3) p450-457.

Oda, M. (1977). "Co-ordination number and its relation to shear strength of granular material." *Soils and Foundations*, 17(2), 29-42.

Oldecop, L.A. and Alonso, E.E. (2001). "A model for rockfill compressibility." *Géotechnique*, 51(2), 127-139.

Oldecop, L.A. and Alonso, E.E. (2003). "Suction effects on rockfill compressibility." *Géotechnique*, 53(2), 289-292.

Organova, N.I., Marsii, I.M., Rozhdestvenskaya, I.V., Ivanova, T.I., Zakharov, N.D., Nasdekin, V.V., and Borisovskii, S.B.(1999). "Structures of the K- and Na-components of two-phase feldspar from Primor'e". *Kristallografiya*, 44(5), 829-834.

Orowan, E. (1955). “Energy criteria of fracture.” *Welding Research Supplement*, 9, 157-160.

Parab, N.D., Claus, B., Hudspeth, M.C., Black, J.T., Mondal, A., Sun, J., Fezzaa, K., Xiao, X., Luo, S.N., and Chen, W. (2014). “Experimental assessment of fracture of individual sand particles at different loading rates.” *International Journal of Impact Engineering*, 68, 8-14.

Redhammer G.J. and Roth G. (2002). “Single-crystal structure refinements and crystal chemistry of synthetic trioctahedral micas K M3 (Al(3+), Si(3+))4 O10 (O H)2 ,where M = Ni(2+), Mg(2+), Co(2+), Fe(2+) or Al(3+).” *American Mineralogist*, 87, 1464-1476.

Ribbe, P.H., Megaw, H.D., Taylor, W.H., Ferguson, R.B., and Traill, R.J. (1969). “The albite structures”. *Acta Crystallographica B*, 25, 1503-1518.

Rojas, A. and Camblor, M.A. (2012). “A pure silica chiral polymorph with helical pores”. *Angewandte Chemi, International Edition*, 51(16), 3854-3856.

Rothbauer, R. (1971). “Untersuchung eines 2M1-Muskovits mit Neutronenstrahlen”. *Neues Jahrbuch fuer Mineralogie*, Monatshefte, 143-154.

Rutherford, M.J. (1973). “The phase relations of aluminous iron biotites in the system KAISi3 O8--KA1SiO4--A1203--Fe--O—H.” *Journal of Petrology*, 14(1), 159--180.

Scambos, T.A., Smyth, J.R., and McCormick, T.C. (1987). “Crystal-structure refinement of high sanidine from the upper mantle”. *American Mineralogist*, 72, 973-978.

Schulz, H. and Tscherry, V. (1972). “Structural relations between the low- and high-temperature forms of beta-eucryptite (Li Al Si O4) and low and high quartz. I” *Acta Crystallographica., Sec. B: Struct. Crystallogr. Cryst*, 28, 2168-2173.

Sleight, A.W.and Prewitt, C.T. (1970). "Preparation of Cu Nb O3 and Cu Ta O3 at high pressure". *Materials Research Bulletin*, 5, 207-212.

Takane, K. (1932). "Crystal structure of bronzite from chichi-jiama in the bonin islands". *Proceedings of the Japan Academy*, 8, 308-311.

Tavares, L.M. (2007). "Chapter 1 Breakage of Single Particle: Quasi-Static." *Handbook of Powder Technology*, 12, pp. 3-68.

Terzaghi, K. and Peck, R.B. (1948). *Soil mechanics in engineering practice*, 1st ed., John Wiley & Sons, Inc., New York, N.Y., 61.

Todisco, M.C., Wang, W., Coop, M.R., and Senetakis, K. (2016). "Multiple contact compression tests on sand particles."

Wang, P. and Arson, C. (2016). "Discrete element modeling of shielding and size effects during single particle crushing." *Computers and Geotechnics*, 78, 227-236.

Wang, W. and Coop, M.R. (2016). "An investigation of breakage behavior of single sand particles using a high-speed microscope camera." *Géotechnique*, http://dx.doi.org/10.1680/jgeot.15.P.247

Zhao, B., Wang, J., Coop, M.R., Viggiani, G., and Jiang, M. (2015). "An investigation of single sand particle fracture using X-ray micro-tomography." *Géotechnique*, 65(8), 625-641.

APPENDICES

APPENDIX A

Table A-1. The label (C or J), particle number, peak load (N), compressive displacement (mm), d_L (mm), tensile strength (MPa), fracture mode, and particle description prior to and post fracture for red/pink (major and secondary compounds: quartz, potassium feldspar, and plagioclase feldspar) particles retained between sieve #10 (2 mm) and #20 (0.84 mm)

Label	**Particle number**	**Peak Load (N)**	**Displacement of DVRT (mm)**	**d_L (mm)**	**Tensile Strength (MPa)**	**Pre-break description**	**Post break description**
C	25-1	14.853	0.041	1.055	13.336	Angular, few brown spots	Fractured into 1 large piece, 1 small piece, and 1 tiny piece
J	25-1	38.055	0.053	1.200	26.427	Rectangular prismatic, brownish pink, smooth	Fractured into 1 large piece and a few smaller pieces with asperities
J	25-10	20.520	0.052	1.099	16.987	platy, pinkish brown, angular, rough	Fractured into 1 large piece and 1 small piece with some asperities
J	25-11	59.544	0.060	1.200	41.350	Triangular prismatic, red w/tan spotting, smooth	Fractured into 1 large piece, 3 small pieces, and 1 tiny piece with some asperities

Table A-1 Continued

Label	Particle number	Peak Load (N)	Displacement of DVRT (mm)	d_L (mm)	Tensile Strength (MPa)	Pre-break description	Post break description
J	25-12	104.615	0.124	1.964	27.112	Rectangular prismatic, red w/pink spotting, angular, rough	Fractured into at least 1 small piece, 1 tiny piece, and some asperities
C	25-13	27.448	0.071	1.200	19.061	Platy, angular, rough, light orange-red.	Fractured in 3 pieces with some dust
J	25-13	96.371	0.118	1.300	57.024	platy, pink w/grey spotting, rough, angular	Fractured into 2 medium pieces, 3 small pieces, 3 tiny pieces, and many asperities
C	25-14	34.376	0.060	1.000	34.376	Platy, light pink, smooth	Fractured into at least 5 pieces
J	25-14	130.235	0.088	1.700	45.064	Triangular prismatic, light pink, smooth	Fractured into at least 1 large piece

Table A-1 Continued

Label	Particle number	Peak Load (N)	Displacement of DVRT (mm)	d_L (mm)	Tensile Strength (MPa)	Pre-break description	Post break description
C	25-15	87.664	0.074	1.000	87.664	Spherical, smooth, shiny, light pink/white	Fractured into 3 pieces with some dust
J	25-15	87.598	0.091	1.500	38.932	rectangular prismatic, red, angular, smooth	Fractured into 1 large piece and 1 thin small piece with some asperities
J	25-16	8.162	0.079	1.000	8.162	platy, tan and grey spotting, rough	Fractured into 1 large piece, 3 medium pieces, 2 small pieces, and 1 tiny piece with some asperities
C	25-16	14.858	0.046	1.100	12.289	Spherical, smooth, bright red with brown spots	Fractured into multiple pieces

Table A-1 Continued

Label	Particle number	Peak Load (N)	Displacement of DVRT (mm)	d_L (mm)	Tensile Strength (MPa)	Pre-break description	Post break description
C	25-17	22.128	0.023	1.000	22.128	Rectangular prismatic, rough, angular, light pink with white spots.	Pulverized at fracture
C	25-18	38.903	0.074	2.100	8.822	Rectangular prismatic, light red with clear spots throughout, shiny, angular	Fractured into 1 large piece, 1 medium piece, and 1 small piece with asperities
C	25-19	34.442	0.063	0.700	70.290	Platy, shiny, smooth, bright red-orange	Fractured into 2 small pieces and a tiny piece with little asperities
J	25-19	33.198	0.067	1.423	16.385	Two smooth sides that form a corner and on angular side, tannish pink	Fractured into 1 large piece, 1 medium piece, and 1 small piece with some asperities

Table A-1 Continued

Label	Particle number	Peak Load (N)	Displacement of DVRT (mm)	d_L (mm)	Tensile Strength (MPa)	Pre-break description	Post break description
J	25-2	127.735	0.061	1.000	127.735	Rectangular prismatic, pink w/ white spotting, smooth, a few shiny spots	Fractured into many small pieces with asperities
C	25-2	26.589	0.063	1.300	15.733	Angular, Has curved surface on one side and platy on other side, pinkish, one dark spot	Fractured into 3 medium pieces with little asperities
C	25-20	94.196	0.071	1.500	41.865	Spherical with a rectangular prismatic edge, smooth, light red	Fractured into at least 1 medium piece and 1 small piece with some asperities

Table A-1 Continued

Label	Particle number	Peak Load (N)	Displacement of DVRT (mm)	d_L (mm)	Tensile Strength (MPa)	Pre-break description	Post break description
J	25-20	49.113	0.077	1.900	13.605	rectangular prismatic, pink w/white spotting, smooth	Fractured into 1 large piece, 3 small pieces, and 3 tiny pieces with many asperities
C	25-21	65.062	0.072	1.000	65.062	Rectangular prismatic, red to light pink, rough, angular	Pulverized at fracture
J	25-21	82.652	0.099	1.895	23.007	spherical, dark red w/ black spotting, smooth	Fractured into 1 large piece and 1 medium piece
C	25-22	126.071	0.127	1.000	126.071	Rectangular prismatic, shiny, red-brown, angular	Pulverized at fracture

Table A-1 Continued

Label	Particle number	Peak Load (N)	Displacement of DVRT (mm)	d_L (mm)	Tensile Strength (MPa)	Pre-break description	Post break description
C	25-23	90.208	0.105	1.700	31.214	Triangular prismatic , white with red-brown marbling, shiny, angular	Fractured into at least 1 large piece and 1 medium piece with some asperities
C	25-24	21.935	0.037	1.600	8.568	Platy, white to light pink with brown spots, angular, rough	Fractured into 1 large piece and 1 small piece
C	25-25	9.186	0.022	1.200	6.379	Platy, red-orange, smooth, shiny	Fractured into 1 large piece and 1 small piece
C	25-26	5.518	0.013	1.000	5.518	Platy, rough, angular, bright red-orange	Fractured into 3 medium pieces, 3 small pieces, and 2 tiny pieces with little asperities

Table A-1 Continued

Label	Particle number	Peak Load (N)	Displacement of DVRT (mm)	d_L (mm)	Tensile Strength (MPa)	Pre-break description	Post break description
C	25-27	44.267	0.078	2.089	10.140	Triangular prismatic , light pink with white and brown throughout, angular, rough	Fractured into 1 large piece and some asperities
C	25-28	20.564	0.026	1.300	12.168	Platy, angular, rough, red with white throughout.	Fractured into 1 large particle and 1 tiny particle with some asperities
C	25-29	38.495	0.058	1.500	17.109	Rectangular prismatic, pink with clear spots, angular, rough, shiny	Pulverized at fracture
J	25-3	28.560	0.042	1.000	28.560	Triangular prismatic, brownish pink, smooth	Fractured into at least 4 small pieces

Table A-1 Continued

Label	Particle number	Peak Load (N)	Displacement of DVRT (mm)	d_L (mm)	Tensile Strength (MPa)	Pre-break description	Post break description
C	25-3	36.843	0.091	1.800	11.371	Angular, Shiny with smooth surface on one side, and rough on other, white with one pink streak	Fractured into 1 large piece and 1 small piece
C	25-31	17.513	0.036	1.200	12.162	Platy, pink and white, smooth	Fractured into 1 medium piece, 1 small piece, and 1 tiny piece
C	25-32	18.692	0.032	1.500	8.307	Rectangular prismatic, clear with red lines, angular, shiny, smooth	Didn't fracture; only asperities broke off
C	25-33	29.849	0.062	1.099	24.696	Rectangular prismatic, shiny, dark red, smooth, angular	Fractured into 2 pieces, only able to recover one

Table A-1 Continued

Label	Particle number	Peak Load (N)	Displacement of DVRT (mm)	d_L (mm)	Tensile Strength (MPa)	Pre-break description	Post break description
C	25-34	3.932	0.123	0.750	6.990	Light orange, spherical, smooth, shiny	Pulverized at fracture
C	25-35	83.082	0.152	1.100	68.663	Light pink, rough, angular, shiny, clear spots	Exploded at fracture, no pieces recovered
C	25-37	33.605	0.052	1.000	33.605	Platy, clear with red-brown marbling, shiny, smooth	Fractured into 1 medium piece, 1 small piece, and 2 tiny pieces
C	25-38	7.336	0.021	1.900	2.032	Triangular prismatic , red with brown lines, angular, rough	Fractured into 1 large piece with some asperities
C	25-39	44.553	0.041	1.500	19.802	Spherical, light pink with brown spots, rough	Fractured into 1 medium piece, 2 small pieces, and 1 tiny piece

Table A-1 Continued

Label	Particle number	Peak Load (N)	Displacement of DVRT (mm)	d_L (mm)	Tensile Strength (MPa)	Pre-break description	Post break description
C	25-4	37.967	0.106	1.100	31.377	Angular, Shiny, rough, creamy with one dark side	Fractured into 1 large piece, 1 small piece, and 2 tiny pieces with some asperities
J	25-4	85.990	0.088	1.697	29.845	Rectangular prismatic, pinkish tan, angular, smooth	Fractured into 3 pieces
C	25-40	10.970	0.019	0.900	13.544	Platy, dark red, angular, rough	Fractured into 1 medium piece and 1 small piece with some asperities
C	25-41	53.288	0.050	0.900	65.787	Triangular prismatic , orange, rough, angular, few brown spots	Pulverized at fracture

Table A-1 Continued

Label	Particle number	Peak Load (N)	Displacement of DVRT (mm)	d_L (mm)	Tensile Strength (MPa)	Pre-break description	Post break description
C	25-42	80.758	0.063	1.200	56.082	Rectangular prismatic, smooth, shiny, light pink-orange	Fractured into at least 1 tiny piece
C	25-43	23.967	0.101	1.353	13.087	Triangular prismatic , red-orange with brown spots, angular, shiny, rough	Fractured into 1 medium piece, 2 small pieces, and 2 tiny pieces with asperities
C	25-44	18.680	0.038	1.100	15.438	Platy, pink-white, smooth, angular	Fractured into 1 medium piece and 2 small pieces with asperities
C	25-45	31.799	0.072	1.400	16.224	Platy, angular, clear with pink marbling, shiny	Fractured into 2 medium pieces

Table A-1 Continued

Label	Particle number	Peak Load (N)	Displacement of DVRT (mm)	d_L (mm)	Tensile Strength (MPa)	Pre-break description	Post break description
C	25-46	23.736	0.055	1.479	10.845	Spherical, light pink with brown lines, angular	Fractured into 2 medium pieces
C	25-47	16.896	0.046	1.600	6.600	Triangular prismatic , light pink with white lines, angular, rough, shiny	Fractured into 1 large piece and 1 small piece
C	25-48	31.711	0.053	1.000	31.711	Platy, smooth, red with white, angular	Fractured into 2 small pieces
J	25-5	63.069	0.184	0.750	111.986	Platy, Brownish pink, rough	Fractured into two pieces, some is pulverized

Table A-1 Continued

Label	Particle number	Peak Load (N)	Displacement of DVRT (mm)	d_L (mm)	Tensile Strength (MPa)	Pre-break description	Post break description
C	25-5	29.409	0.041	1.300	17.402	Rectangular prismatic, two flat surfaces, white and brown streaks	Fractured into 3 evenly sized medium piece with little asperities
C	25-50	7.137	0.029	0.900	8.812	Platy, rectangular prismatic, red, smooth, shiny	Fractured into 1 medium piece and 2 small pieces with asperities
J	25-6	28.582	0.036	1.000	28.562	Platy, Pink w/red spotting, smooth	Fractured into 2 pieces
C	25-7	28.252	0.056	1.100	23.349	Parallogram-like, smooth, pinkish	Fractured into 1 large piece and 2 small pieces with some asperities

Table A-1 Continued

Label	Particle number	Peak Load (N)	Displacement of DVRT (mm)	d_L (mm)	Tensile Strength (MPa)	Pre-break description	Post break description
J	25-7	76.022	0.102	1.600	29.696	Rectangular prismatic, pink w/grey and black spotting, smooth	Fractured into at least 3 medium size pieces with little asperities
J	25-8	48.100	0.091	1.099	39.800	Spherical, angular, rough, brownish pink	Fractured into at least 3 small pieces with some little asperities
C	25-8	22.249	0.037	1.600	8.691	Triangular prismatic, one smooth, shiny, and flat surface, white with 2 red spots	Fractured into 1 large and 1 medium piece
J	25-9	36.700	0.036	1.000	36.700	Spherical, deep red, angular	Fractured into 1 large piece and 1 tiny piece with some asperities

APPENDIX B

Table B-1. The label (C or J), particle number, peak load (N), compressive displacement (mm), d_L (mm), tensile strength (MPa), fracture mode, and particle description prior to and post fracture for black/brown (major and secondary compounds: quartz, mica (biotite), tridymite, plagioclase feldspar, potassium feldspar, and calcite) particles retained between sieve #10 (2 mm) and #20 (0.84 mm)

Label	**Particle number**	**Peak Load (N)**	**Displacement of DVRT (mm)**	**d_L (mm)**	**Tensile Strength (MPa)**	**Pre-break description**	**Post break description**
C	25-1	45.346	0.045	1.399	23.161	Spherical, smooth, light brown	Fractured into a least 2 pieces with some asperities
C	25-10	37.394	0.034	1.300	22.127	Platy, dark brown and light brown, rough, angular	Fractured into 2 pieces with few asperities
J	25-10	32.063	0.024	1.099	26.547	Spherical, black, smooth	Fractured into four pieces
J	25-11	19.297	0.023	1.297	11.471	platy, black, smooth	Fractured into three large pieces and on small pieces

Table B-1 Continued

Label	Particle number	Peak Load (N)	Displacement of DVRT (mm)	d_L (mm)	Tensile Strength (MPa)	Pre-break description	Post break description
C	25-12	27.481	0.053	0.898	34.096	Triangular prismatic , dark brown, angular, shiny, smooth	Fractured into 5 small pieces with little asperities
J	25-12	52.517	0.129	1.237	34.327	Spherical w/platy bottom, lt. gray, smooth	Fractured into three pieces
J	25-13	14.407	0.044	1.197	10.055	Rectangular prismatic, dark gray, smooth	Fractured into three pieces with some asperities
C	25-14	18.383	0.033	2.100	4.169	Triangular prismatic , light grey with clear spots, shiny, sooth, angular	Fractured into 1 large piece and 2 small pieces with many asperities
J	25-14	24.975	0.023	0.998	25.075	Rectangular prismatic, gray w/ white spotting, smooth	pulverized

Table B-1 Continued

Label	Particle number	Peak Load (N)	Displacement of DVRT (mm)	d_L (mm)	Tensile Strength (MPa)	Pre-break description	Post break description
J	25-15	5.750	0.077	1.197	4.013	Triangular prismatic, black top w/gray bottom, angular, smooth	Remained mostly intact w asperities created
C	25-15	129.266	0.110	1.700	44.747	Spherical, light brown with clear, shiny, angular, rough	Fractured into at least 1 small piece
C	25-16	22.464	0.045	0.899	27.783	One side rounded and two straight sides, pointy edge, platy, smooth on top and bottom, rounded and short straight side smooth, long straight side rough, dark brown	Fractured into 1 large piece, 1 medium piece, 1 small piece

Table B-1 Continued

Label	Particle number	Peak Load (N)	Displacement of DVRT (mm)	d_L (mm)	Tensile Strength (MPa)	Pre-break description	Post break description
C	25-17	44.113	0.084	2.100	10.003	Rectangular prismatic, dark grey with red spots, angular, rough	Fractured into 1 large piece, 1 small piece, and 1 tiny piece
C	25-18	2.522	0.023	1.439	1.219	Platy, black and white, angular, rough	Fractured into 2 pieces with few asperities; 1 piece slightly larger than the other
C	25-19	34.266	0.046	1.800	10.578	Platy, black brown and white, angular, rough	Split into 4 pieces, 1 medium and 3 small pieces of approximately the same size
C	25-2	96.828	0.071	2.099	21.968	Rectangular prismatic, light brown with clear throughout, angular, shiny	Fractured into a least 2 pieces; fractured between the division of light brown and clear area

Table B-1 Continued

Label	Particle number	Peak Load (N)	Displacement of DVRT (mm)	d_L (mm)	Tensile Strength (MPa)	Pre-break description	Post break description
C	25-20	3.932	0.011	0.499	15.793	Platy, dark brown, angular, smooth	Fractured into 1 large piece, 1 small piece, and 1 tiny piece
C	25-21	131.028	0.083	0.800	204.965	Platy, dark gray, rough, angular, shiny	Fractured into 1 large piece and 2 small pieces with some asperities
C	25-22	26.787	0.042	1.999	6.707	Triangular prismatic , black and white, rough, angular	Fractured into 1 large piece and 3 smaller pieces
C	25-23	54.290	0.141	1.899	15.047	Spherical, light red brown, rough, shiny	Fractured into a least 1 medium size piece with asperities
C	25-24	30.455	0.040	0.899	37.688	Platy, brown with black spots, rough, angular	Fractured into 4 small pieces with little asperities

Table B-1 Continued

Label	Particle number	Peak Load (N)	Displacement of DVRT (mm)	d_L (mm)	Tensile Strength (MPa)	Pre-break description	Post break description
C	25-25	6.884	0.024	1.099	5.701	Platy, light brown with black marbling, angular, smooth	Fractured into 2 pieces with little asperities
C	25-26	32.080	0.076	1.499	14.273	Rectangular prismatic, light brown with dark brown spots, angular, rough	Fractured into 1 large piece and 3 small pieces with some asperities
C	25-27	62.683	0.075	1.095	52.246	Prism-like but platy, dark brown, rough, angular, a few white spots	Fractured into 1 large piece and one small piece with little asperities

Table B-1 Continued

Label	Particle number	Peak Load (N)	Displacement of DVRT (mm)	d_L (mm)	Tensile Strength (MPa)	Pre-break description	Post break description
C	25-28	50.424	0.079	0.897	62.618	Rectangular prismatic like with slightly rounded surfaces, dark gray, rough, small white spots, angular	Fractured into 1 large piece and 2 small pieces with many asperities
C	25-29	5.441	0.039	1.098	4.513	Platy, black with dark brown, rough, angular	Fractured into 1 large piece and 1 small piece with some asperities
C	25-3	58.465	0.070	1.599	22.859	Triangular prismatic , black, rough, angular	Fractured into many small pieces;
C	25-30	23.428	0.023	0.900	28.930	Spherical, dark grey with clear, smooth, shiny	Fractured into at least 1 large piece

Table B-1 Continued

Label	Particle number	Peak Load (N)	Displacement of DVRT (mm)	d_L (mm)	Tensile Strength (MPa)	Pre-break description	Post break description
C	25-32	8.779	0.025	0.800	13.715	Platy, black and dark brown, smooth, shiny	Fractured into 1 large piece and 1 small piece
C	25-33	38.011	0.061	0.600	105.586	Platy, light and dark brown, smooth, shiny, angular	Fractured into 1 large piece and 1 tiny piece with little asperities
C	25-34	58.316	0.077	1.547	24.371	Light gray with white spots and patches, rough, angular, cylindrical prism-like	Fractured into 1 large piece and 1 small piece; some asperities
C	25-35	58.982	0.085	1.166	43.362	Angular, black with clear, shiny, rough	Fractured into 1 large piece and 1 tiny piece with many asperities

Table B-1 Continued

Label	Particle number	Peak Load (N)	Displacement of DVRT (mm)	d_L (mm)	Tensile Strength (MPa)	Pre-break description	Post break description
C	25-36	32.184	0.051	1.599	12.584	Triangular prismatic , light brown with grey lines and spots, angular	Fractured into 1 large piece, 1 small piece, and 2 tiny pieces
C	25-37	66.230	0.090	1.100	54.781	Platy, angular, grey with brown spots, shiny	Fractured into at least 1 small piece
C	25-38	10.155	0.037	0.798	15.940	Platy, dark brown, angular, rough	Fractured into 1 large piece, 1 medium piece, 1 small piece, and 1 tiny piece
C	25-39	5.865	0.029	1.098	4.869	Platy, dark brown black, angular, rough	Fractured into 1 large piece and 1 tiny piece

Table B-1 Continued

Label	Particle number	Peak Load (N)	Displacement of DVRT (mm)	d_L (mm)	Tensile Strength (MPa)	Pre-break description	Post break description
C	25-4	74.705	0.038	0.899	92.354	Platy, one side dark reddish brown, other side dark brown, smooth	Fractured into two large pieces and many small pieces with asperities
C	25-40	14.660	0.032	1.498	6.531	Triangular prismatic , brown with black spots, rough, angular	Fractured into 2 medium piece, 1 small piece, and 1 tiny piece with some asperities
C	25-41	5.761	0.061	1.097	4.788	Platy, red brown, angular, smooth	Fractured into 1 large piece, 1 small piece, and 2 tiny pieces with little asperities
C	25-42	21.357	0.387	1.410	10.744	Rectangular prismatic prism, light grey with black lines, angular, rough	Fractured into 1 large piece and 1 small piece with some asperities

Table B-1 Continued

Label	Particle number	Peak Load (N)	Displacement of DVRT (mm)	d_L (mm)	Tensile Strength (MPa)	Pre-break description	Post break description
C	25-43	53.123	0.056	1.279	32.475	Light gray, angular, spherical, rough, has black spot	Fractured into 1 large piece and 1 small piece with little asperities
C	25-44	47.626	0.080	1.099	39.397	Platy, light brown, smooth	Fractured into 1 large piece and 1 medium piece with many tiny pieces and asperities
C	25-45	36.623	0.062	1.182	26.203	Platy, dark brown with light brown spots, angular, smooth	Fractured into 1 large piece and 2 small pieces with little asperities
C	25-46	36.083	0.065	0.800	56.380	Platy, dark brown, smooth	Fractured into many small pieces

Table B-1 Continued

Label	Particle number	Peak Load (N)	Displacement of DVRT (mm)	d_L (mm)	Tensile Strength (MPa)	Pre-break description	Post break description
C	25-47	12.678	0.117	1.399	6.478	Triangular prismatic , light red brown, angular, rough	Fractured into 1 large piece and 3 small pieces with some asperities
C	25-48	39.674	0.057	1.366	21.258	Gray with tan patches and dark gray lines, angular, rough, seed-shaped	Fractured into at least 1 medium piece with little asperities
C	25-49	39.311	0.055	1.365	21.106	Rectangular prismatic, light brown, smooth, shiny	Fractured into at least 1 large piece and 1 small piece
C	25-5	68.135	0.064	2.000	17.034	Angular, light brown to grey, rough, shiny	Fractured into two approximately equal size pieces; no asperities

Table B-1 Continued

Label	Particle number	Peak Load (N)	Displacement of DVRT (mm)	d_L (mm)	Tensile Strength (MPa)	Pre-break description	Post break description
C	25-50	25.994	0.051	1.016	25.185	Platy, black, smooth	Fractured into 1 medium piece and 1 small piece with some asperities
J	25-6	23.863	0.042	0.998	23.959	rectangular prismatic, dark gray, smooth	Fractured into three pieces
C	25-6	129.029	0.077	1.499	57.397	Rectangular prismatic, dark brown with light brown and clear, angular, rough	light brown portion fractured off as asperities; fractured into approximately 4 pieces with a few asperities
C	25-7	98.128	0.122	1.782	30.913	Rectangular prismatic, dark grey, light brown spots, angular, rough	Fractured into small asperity with at least two pieces

Table B-1 Continued

Label	Particle number	Peak Load (N)	Displacement of DVRT (mm)	d_L (mm)	Tensile Strength (MPa)	Pre-break description	Post break description
J	25-8	6.504	0.005	1.199	4.524	Spherical, black w/ white, angular, smooth	Fractured into three pieces, with some asperities
C	25-8	38.622	0.040	1.195	27.040	Platy, very light brown, angular, rough, shiny	Fractured into two pieces, one small and one large, with some asperities
J	25-9	21.566	0.064	1.186	15.332	triangular prismatic, gray w/white spotting, rough	Fractured into two uniform pieces
C	25-9	33.770	0.059	1.099	27.969	Spherical, smooth, black with white spots	Fractured into 2 pieces with few asperities

APPENDIX C

Table C-1. The label (C or J), particle number, peak load (N), Compressive displacement (mm), d_L (mm), tensile strength (MPa), fracture mode, and particle description prior to and post fracture for white/tan (major and secondary compounds: quartz, plagioclase feldspar, potassium feldspar, and mica (muscovite)) particles retained between sieve #10 (2 mm) and #20 (0.84 mm)

Label	**Particle number**	**Peak Load (N)**	**Displacement of DVRT (mm)**	**d_L (mm)**	**Tensile Strength (MPa)**	**Pre-break description**	**Post break description**
J	25-1	19.556	0.005	1.099	16.191	Spherical, chalky white, smooth	One triangular prismatic piece recovered
C	25-1	12.061	0.094	1.248	7.741	Spherical, white with brown dots, smooth	Fractured into 1 medium piece and 1 small piece
J	25-10	56.636	0.037	1.898	15.717	Triangular prismatic, chalky white, smooth	Only one piece recovered
C	25-11	18.350	0.057	1.199	12.757	Platy, cream white with grey, rough, angular	Fractured into 4 pieces with asperities
J	25-11	18.108	0.006	1.400	9.243	Platy, grayish white, smooth	Fractured into two large pieces and one small piece

Table C-1 Continued

Label	Particle number	Peak Load (N)	Displacement of DVRT (mm)	d_L (mm)	Tensile Strength (MPa)	Pre-break description	Post break description
J	25-12	6.377	0.015	0.685	13.579	Platy, cloudy, smooth	Remained largely intact with one small piece fractured off
C	25-12	23.141	0.007	0.999	23.186	Platy rectangular prismatic, white, smooth	Fractured into 2 large pieces
J	25-13	38.617	0.013	1.100	31.938	Spherical, cloudy white, smooth	Fractured into at least 1 large piece
C	25-14	12.039	0.005	1.199	8.369	Platy triangular prismatic, clear cream with red, rough	Fractured into at least 2 larger pieces with asperities
J	25-14	13.361	0.010	1.298	7.927	platy, translucent white, smooth	Fractured into one large piece and one small piece
J	25-15	75.735	0.021	0.999	75.856	Platy, white w/ tan spot, smooth	Fractured into four uniform pieces

Table C-1 Continued

Label	Particle number	Peak Load (N)	Displacement of DVRT (mm)	d_L (mm)	Tensile Strength (MPa)	Pre-break description	Post break description
C	25-15	60.739	0.102	2.000	15.185	Triangular prismatic , white with brown and red spots, smooth	Fractured into 3 large pieces with asperities
C	25-16	11.367	0.034	1.200	7.898	Spherical angular, white with grey spots, rough	Fractured into 3 small pieces with asperities
J	25-17	26.126	0.034	0.498	105.430	Platy, pink spotting, smooth	Two larger pieces and two tiny pieces remain
C	25-17	14.429	0.032	1.000	14.429	Platy, white, angular, rough	Fractured into at least 1 large piece and asperities
C	25-18	10.701	0.023	1.200	7.431	Platy, angular, white with black spots, rough	Fractured into 2 large pieces and 1 small piece

Table C-1 Continued

Label	Particle number	Peak Load (N)	Displacement of DVRT (mm)	d_L (mm)	Tensile Strength (MPa)	Pre-break description	Post break description
J	25-18	124.012	0.046	2.099	28.142	Platy, white w/various spotting, angular, rough	Fractured into two roughly same sized pieces
J	25-19	43.727	0.019	1.099	36.230	Rectangular prismatic, milky w/black spot, smooth	Fractured into at least 1 large piece
C	25-2	54.378	0.023	2.100	12.332	Angular, white with brown lines, smooth	Fractured into 2 medium pieces with little asperities
J	25-20	22.271	0.027	0.999	22.305	Platy, tan, rough	Fractured into one large piece, two medium pieces, and a small piece
C	25-20	30.493	0.020	0.999	30.525	Rectangular prismatic, clear white with pink, smooth	Fractured into 1 large piece and asperities

Table C-1 Continued

Label	Particle number	Peak Load (N)	Displacement of DVRT (mm)	d_L (mm)	Tensile Strength (MPa)	Pre-break description	Post break description
C	25-22	7.005	0.052	1.265	4.379	Spherical, bright white with grey spots, smooth	Fractured into 3 medium pieces
C	25-23	15.800	0.086	1.298	9.373	Triangular prismatic , cream white pink, smooth	Fractured into 2 pieces
C	25-25	20.123	0.011	1.300	11.907	Rectangular prismatic, cream white with red, rough, angular	Fractured into at least 1 large piece and 1 small piece
C	25-26	19.110	0.012	0.995	19.287	Rectangular prismatic, milky, smooth, angular	Fractured into multiple small-tiny pieces
C	25-27	19.451	0.010	1.400	9.924	Rectangular prismatic, white with red spotting, rough, angular	Fractured into at least 2 larger pieces with asperities

Table C-1 Continued

Label	Particle number	Peak Load (N)	Displacement of DVRT (mm)	d_L (mm)	Tensile Strength (MPa)	Pre-break description	Post break description
C	25-28	21.704	0.052	1.199	15.091	triangular prismatic, heavy brown spotting, smooth, angular	Fractured into 1 large piece and asperities
C	25-29	2.434	0.002	0.900	3.005	Rectangular prismatic, tannish white, jagged	Fractured into 1 large piece and 1 small piece
C	25-3	54.246	0.093	1.487	24.545	Rectangular prismatic, angular, cream with pink, smooth	Fractured into at least 3 small pieces with some asperities
C	25-30	9.021	0.013	1.199	6.274	Platy, white, smooth	Fractured into 2 large pieces
C	25-31	44.928	0.016	1.283	27.301	Triangular prismatic , White with brown spotting, angular	Fractured into 1 large piece, 1small piece and 1 tiny piece

Table C-1 Continued

Label	Particle number	Peak Load (N)	Displacement of DVRT (mm)	d_L (mm)	Tensile Strength (MPa)	Pre-break description	Post break description
C	25-32	27.217	0.012	0.998	27.325	Spherical, milky white, angular	Fractured into at least 1 large piece
C	25-34	11.356	0.180	0.996	11.452	Spherical, powder white, smooth	Particle pulverized at fracture
J	25-34	13.746	0.006	1.100	11.362	Rectangular prismatic, powder white w/tan spotting, smooth	Fractured into one large piece and one smaller piece
J	25-36	12.287	0.012	1.200	8.537	Rectangular prismatic, heavy dark spotting, smooth	Fractured into two uniform pieces
C	25-37	19.920	0.018	1.099	16.478	Platy, powder white, smooth	Fractured into 2 near equal size pieces

Table C-1 Continued

Label	Particle number	Peak Load (N)	Displacement of DVRT (mm)	d_L (mm)	Tensile Strength (MPa)	Pre-break description	Post break description
J	25-37	55.034	0.018	1.799	16.997	Rectangular prismatic, milky w/pinkish tint, angular, smooth	Fractured into one large piece and one smaller piece
C	25-38	5.298	0.031	1.050	4.809	Spherical, tannish white, angular	Fractured into 1 large piece and asperities
C	25-4	63.972	0.255	1.982	16.284	Triangular prismatic , white with black lines, smooth, angular	Fractured into 1 large piece and 2 small pieces with some asperities
C	25-40	15.828	0.008	0.998	15.881	Platy, pink spotting, smooth	No visible fracture
C	25-41	17.408	0.037	1.599	6.809	Triangular prismatic , tannish white with brown spotting, smooth	Fractured into 2 large pieces and asperities

Table C-1 Continued

Label	Particle number	Peak Load (N)	Displacement of DVRT (mm)	d_L (mm)	Tensile Strength (MPa)	Pre-break description	Post break description
C	25-43	22.943	0.049	1.398	11.736	triangular prismatic , milky white, angular	Fractured into two near equal size pieces
C	25-44	40.996	0.035	1.200	28.491	Rectangular prismatic, tan spotting, smooth	Fractured into 1 large piece and 2 small pieces
C	25-45	6.807	0.012	1.800	2.101	Platy, grey spotting, smooth	Fractured into at least 1 large piece
C	25-46	8.988	0.035	1.300	5.322	Platy, tannish, angular	Fractured into 2 larger pieces and asperities
C	25-47	14.176	0.060	0.798	22.234	Triangular prismatic, powder white, smooth	Fractured into 1 large piece and multiple tiny pieces
C	25-5	23.857	0.015	0.989	24.411	Triangular prismatic, clear white, angular, rough	Fractured into 1 large piece and multiple asperities

Table C-1 Continued

Label	Particle number	Peak Load (N)	Displacement of DVRT (mm)	d_L (mm)	Tensile Strength (MPa)	Pre-break description	Post break description
J	25-5	38.319	0.065	1.597	15.028	Rectangular prismatic, tan with gray spotting, smooth	Fractured into three pieces
C	25-50	38.562	0.124	1.100	31.869		Fractured into 1 large piece and 1 small piece
C	25-6	119.694	0.067	1.199	83.261	Platy rectangular prismatic, white with red lines, smooth	Particle pulverized at fracture
J	25-7	14.991	0.011	0.699	30.725	Platy, tan, smooth	One larger piece with several small pieces
C	25-7	55.843	0.058	1.898	15.500	Spherical angular, white with light grey, smooth	Fractured into 3 large pieces and 2 small pieces
C	25-8	34.431	0.041	1.199	23.935	Rectangular prismatic, bright white, angular, rough, shiny	Fracture into at least 5 small pieces

Table C-1 Continued

Label	Particle number	Peak Load (N)	Displacement of DVRT (mm)	d_L (mm)	Tensile Strength (MPa)	Pre-break description	Post break description
J	25-8	8.041	0.018	1.498	3.586	Platy, white, angular, rough	Fractured into two large pieces and several small fragments
C	25-9	6.229	0.035	0.798	9.788	Rectangular prismatic, cream white with black spot, smooth, angular	Fractured into at least 3 small pieces
J	25-9	38.661	0.012	2.200	7.990	Triangular prismatic, white w/gray spotting, angular smooth	Fractured into two uniform pieces with some asperities

APPENDIX D

Table D-1. The label (C or J), particle number, peak load (N), compressive displacement (mm), particle d_L (mm), tensile strength (MPa), fracture mode, and particle description prior to and post fracture clear/translucent (major and secondary compounds: quartz and plagioclase feldspar) particles retained between sieve #10 (2 mm) and #20 (0.84 mm)

Label	**Particle number**	**Peak Load (N)**	**Displacement of DVRT (mm)**	**d_L (mm)**	**Tensile Strength (MPa)**	**Pre-break description**	**Post break description**
J	25-10	16.670	0.016	1.398	8.533	Triangular prismatic, brown and black spotting, smooth	
C	25-12	18.020	0.023	1.900	4.992	Rectangular prismatic, cloudy white, smooth, angular, shiny	Fractured into at least 1 large piece with some asperities
C	25-13	76.236	0.132	2.200	15.751	Triangular prismatic , clear with red-brown lines, angular, smooth	Fractured into 1 large piece and 1 tiny piece

Table D-1 Continued

Label	Particle number	Peak Load (N)	Displacement of DVRT (mm)	d_L (mm)	Tensile Strength (MPa)	Pre-break description	Post break description
J	25-13	22.172	0.012	0.749	39.575	Platy, grayish white, smooth	Fractured into 1 medium piece, 3 small pieces, and 5 tiny pieces with some asperities
C	25-14	13.416	0.072	1.200	9.316	Spherical, clear, smooth, shiny	Fractured into 1 large piece and 1 tiny piece
C	25-15	22.073	0.029	1.400	11.262	Rectangular prismatic, clear-yellow with black spot, smooth, angular	Fractured into 2 medium pieces
J	25-15	15.211	0.051	0.659	35.068	Platy, clear, smooth	Fractured into 2 medium pieces and 3 tiny pieces

Table D-1 Continued

Label	Particle number	Peak Load (N)	Displacement of DVRT (mm)	d_L (mm)	Tensile Strength (MPa)	Pre-break description	Post break description
C	25-16	99.626	0.122	1.900	27.597	Rectangular prismatic, cloudy clear with red-orange lines, smooth	Fractured into 2 medium pieces and 1 small piece with some asperities
C	25-19	9.527	0.024	1.500	4.234	Platy, cloudy clear, rough, angular	Fracture into 2 medium piece with some asperities
J	25-2	62.055	0.040	0.999	62.154	Spherical, clear, angular, smooth	Fractured into a least 1 medium piece
C	25-20	17.788	0.026	1.700	6.155	Triangular prismatic , clear pink with brown, smooth, shiny	Fractured into 1 large piece and 1 tiny piece
C	25-21	15.850	0.044	1.200	11.007	Triangular prismatic , clear with brown, smooth, shiny	Fractured into 1 large piece

Table D-1 Continued

Label	Particle number	Peak Load (N)	Displacement of DVRT (mm)	d_L (mm)	Tensile Strength (MPa)	Pre-break description	Post break description
C	25-22	5.827	0.043	1.400	2.973	Platy-rectangle, clear, rough, shiny	Fractured into 1 medium piece and 2 small pieces
J	25-22	58.189	0.025	1.098	48.248	Platy, translucent, rough	Fractured into at least 1 medium and 1 small piece with few asperities
J	25-23	11.995	0.006	0.899	14.827	Rectangular prismatic, clear, smooth	Fractured into at least 1 large piece
C	25-23	62.265	0.073	1.400	31.768	Spherical, cloudy white, rough, angular	Pulverized
J	25-24	25.344	0.017	0.998	25.425	Triangular prismatic, clear w/tan spotting, smooth	Fractured into 1 large piece and 1 small piece, some asperities

Table D-1 Continued

Label	Particle number	Peak Load (N)	Displacement of DVRT (mm)	d_L (mm)	Tensile Strength (MPa)	Pre-break description	Post break description
C	25-24	128.594	0.156	1.600	50.232	Triangular prismatic , cloudy white with brown lines, smooth, shiny	Fracture into 3 medium and 1 tiny piece with some asperities
C	25-25	44.124	0.046	1.600	17.236	Platy, clear with white spot, rough, angular	Fractured into 2 medium pieces
J	25-25	16.456	0.022	0.498	66.274	Platy, milky, smooth	Fractured into at least 1 small piece with some asperities
J	25-26	78.790	0.016	1.498	35.093	Rectangular prismatic, milky, angular, rough	Fractured into 2 medium pieces and 1 small piece with little asperities

Table D-1 Continued

Label	Particle number	Peak Load (N)	Displacement of DVRT (mm)	d_L (mm)	Tensile Strength (MPa)	Pre-break description	Post break description
C	25-26	79.667	0.105	0.800	124.480	Platy, cloudy white, angular	Fractured into 3 medium piece and 1 small pieces with asperities
J	25-28	2.699	0.003	0.600	7.497	platy, half clear/half milky, smooth	Fractured into 1 large piece and 1 small piece
C	25-29	39.101	0.012	1.900	10.831	Rectangular prismatic, Clear with White spots, angular, rough	Fractured into at least 2 medium pieces and a small piece
J	25-29	49.973	0.018	0.899	61.887	rectangular prismatic, clear, smooth	Fractured into at least 1 small piece with some asperities
C	25-30	5.970	0.003	0.900	7.370	platy, cloudy white, angular, smooth	Fractured into 2 medium pieces

Table D-1 Continued

Label	Particle number	Peak Load (N)	Displacement of DVRT (mm)	d_L (mm)	Tensile Strength (MPa)	Pre-break description	Post break description
C	25-31	28.500	0.014	1.100	23.554	Rectangular prismatic, clear, shiny	Fractured into at least 1 small piece
J	25-32	6.432	0.003	0.798	10.109	platy, clear, rough	Fractured into 1 large piece and 1 small piece
C	25-34	26.115	0.026	1.000	26.115	Platy, white, smooth, angular	Fractured into 1 medium and 1 tiny piece
J	25-35	9.263	0.008	0.496	37.637	Platy, clear, smooth	Fractured into at least 2 small pieces
C	25-37	33.770	0.014	1.200	23.452	Platy, Cloudy with assorted spotting, smooth	Fractured into 1 large piece, I small piece, and 1 tiny piece

Table D-1 Continued

Label	Particle number	Peak Load (N)	Displacement of DVRT (mm)	d_L (mm)	Tensile Strength (MPa)	Pre-break description	Post break description
J	25-38	128.032	0.082	0.699	262.113	Platy, clear w/black lines and spotting, smooth	Pulverization
J	25-39	57.319	0.058	1.599	22.427	Triangular prismatic, milky, rough	Fractured into a large piece and a small piece
C	25-39	59.181	0.018	0.900	73.062	Platy, milky, smooth	Fractured into 2 medium pieces, 1 small, piece, and 2 tiny pieces with some asperities
J	25-4	28.505	0.018	0.999	28.551	Platy, milky, smooth	Fractured into 1 large piece and 1 small piece
J	25-40	11.014	0.005	1.199	7.668	Spherical, milky, angular, smooth	Fractured into at least 1 large piece and 1 small piece

Table D-1 Continued

Label	Particle number	Peak Load (N)	Displacement of DVRT (mm)	d_L (mm)	Tensile Strength (MPa)	Pre-break description	Post break description
C	25-41	35.555	0.036	1.100	29.384	Platy, clear with white spotting, angular, rough	Fractured into at least 1 large piece with some asperities
J	25-41	41.348	0.017	0.799	64.833	platy, clear, rough, shiny	Fractured into 1 large piece with many small and tiny pieces and little asperities
C	25-42	23.296	0.054	0.700	47.542	Platy, cloudy, smooth	Fractured into 2 medium particles with 1 small particle and some asperities
J	25-42	127.487	0.068	0.799	199.897	rectangular prismatic, milky, smooth	Pulverization

Table D-1 Continued

Label	Particle number	Peak Load (N)	Displacement of DVRT (mm)	d_L (mm)	Tensile Strength (MPa)	Pre-break description	Post break description
J	25-43	65.822	0.021	1.599	25.753	Triangular prismatic, clear, rough	Fractured into at least a small piece with some asperities
C	25-44	23.362	0.036	1.000	23.362	Rectangular prismatic, Clear with Yellow tint, smooth	Fractured into at least 1 large piece and tiny piece with some asperities
J	25-44	38.242	0.016	1.199	26.606	Triangular prismatic, cloudy, angular, rough	Fractured into 1 large piece and 1 small piece
J	25-45	63.895	0.220	1.395	32.843	Triangular prismatic, milky, angular, rough	Fractured into at least 1 small piece with some asperities
C	25-46	23.285	0.029	1.200	16.170	Spherical, cloudy white, rough, angular	Fractured into a medium piece and a small piece

Table D-1 Continued

Label	Particle number	Peak Load (N)	Displacement of DVRT (mm)	d_L (mm)	Tensile Strength (MPa)	Pre-break description	Post break description
J	25-46	59.313	0.107	0.987	60.873	Spherical, clear, angular, rough, shiny	Fractured into at least some asperities
J	25-47	11.642	0.031	0.695	24.081	Platy, clear, smooth	Fractured into at least 1 large piece
C	25-47	26.787	0.038	0.800	41.855	Platy, milky, smooth	Fractured into 2 medium pieces and a small piece
C	25-48	20.256	0.008	1.000	20.256	Platy, rough, angular, shiny	Fractured into at least 2 pieces, only one larger piece recovered
C	25-49	10.321	0.054	1.100	8.529	rectangular prismatic, cloudy, rough	Fractured into at least 1 medium piece, 1 small piece, and 1 tiny piece

Table D-1 Continued

Label	Particle number	Peak Load (N)	Displacement of DVRT (mm)	d_L (mm)	Tensile Strength (MPa)	Pre-break description	Post break description
J	25-49	21.203	0.036	0.658	48.962	Platy, clear w/brown spotting, smooth	Fractured into 2 medium pieces with some asperities
J	25-5	55.134	0.021	1.289	33.188	Triangular prismatic, cloudy, smooth	Fractured into at least 1 large piece
C	25-50	12.479	0.008	1.000	12.479	Platy, cloudy, angular, rough	Fractured into 1 large and 1 small piece
J	25-7	73.224	0.089	1.998	18.346	Rectangular prismatic, cloudy, angular, rough	Most likely pulverized

APPENDIX E

Table E-1. The label (C or J), particle number, peak load (N), Compressive displacement (mm), d_L (mm), tensile strength (MPa), fracture mode, and particle description prior to and post fracture for red/pink (major and secondary compounds: quartz, potassium feldspar, and plagioclase feldspar) particles retained by sieve #10 (2 mm)

Label	**Particle number**	**Peak Load (N)**	**Displacement of DVRT (mm)**	**d_L (mm)**	**Tensile Strength (MPa)**	**Pre-break description**	**Post break description**
C	25-1	98.414	0.030	4.000	6.151	Spherical, red-brown with cream, smooth, angular	Fractured into 1 large piece and 1 medium piece
C	25-10	62.408	0.045	2.700	8.561	Triangular prismatic , bright red with brown spots, rough, angular	Fractured into at least 1 large piece
J	25-10	34.993	0.027	1.799	10.811	Triangular prismatic , dark pink with gray spotting, smooth	Two similarly sized (small) pieces remain
C	25-11	33.638	0.042	2.893	4.020	Rectangular prismatic, pink with grey lines, smooth	Fractured into 2 large pieces
J	25-11	130.290	0.058	1.245	84.053	Platy, dark pink with light pink edges, smooth	Fractured into one large piece and several tiny pieces

Table E-1 Continued

Label	Particle number	Peak Load (N)	Displacement of DVRT (mm)	d_L (mm)	Tensile Strength (MPa)	Pre-break description	Post break description
J	25-12	75.901	0.006	1.199	52.762	platy, light pink smooth	Fractured into several tiny (but similarly sized) pieces
C	25-13	27.085	0.015	1.899	7.509	Spherical, red-brown, rough, angular	Fractured into 1 large piece and 2 smaller pieces
J	25-14	109.175	0.020	2.803	13.899	Spherical, pink with gray spotting, smooth	Fractured into three equally sized (small) pieces
C	25-16	51.404	0.023	1.800	15.866	Platy, red-brown with clear, rough	Fractured into 3 near equal size pieces
C	25-17	88.975	0.028	1.600	34.756	Platy, red-orange, smooth	Fractured into 2 large pieces and 1 small piece
C	25-18	39.399	0.011	2.200	8.140	Platy, light red with black spot, rough	Fractured into 3 larger pieces and asperities

Table E-1 Continued

Label	Particle number	Peak Load (N)	Displacement of DVRT (mm)	d_L (mm)	Tensile Strength (MPa)	Pre-break description	Post break description
C	25-19	34.332	0.014	2.000	8.583	Rectangular prismatic, bright red-orange with white, smooth, shiny	Fractured into at least 1 large piece and asperities
J	25-2	75.752	0.099	2.192	15.764	Rectangular prismatic, light pink, angular, rough	Fractured into one medium piece and several small pieces
C	25-21	122.745	0.122	3.900	8.069	Spherical, dull red-orange with white, smooth	Fractured into 4 large pieces and asperities
C	25-22	21.258	0.008	2.841	2.633	Rectangular prismatic, red-brown with white, rough	Fractured into 1 large piece and two tiny pieces
C	25-23	15.541	0.005	1.900	4.305	Platy, light pink, rough, angular	Fractured into 1 large piece, 3 small pieces, and asperities

Table E-1 Continued

Label	Particle number	Peak Load (N)	Displacement of DVRT (mm)	d_L (mm)	Tensile Strength (MPa)	Pre-break description	Post break description
C	25-24	56.978	0.012	2.300	10.771	Rectangular prismatic, light pink and white, smooth, shiny	Fractured into 2 large pieces and 2 small pieces
C	25-26	90.065	0.007	2.000	22.513	Spherical, dull light pink with cream, rough	Fractured into at least 3 small pieces
C	25-27	61.064	0.005	2.250	12.062	Triangular prismatic , light orange-red with cream, rough, shiny	Fractured into 3 large pieces
C	25-28	128.197	0.013	3.100	13.340	Spherical, light pink with brown spots, rough	Fractured into 5 large pieces and multiple tiny pieces
C	25-29	61.934	0.006	2.700	8.498	Triangular prismatic , pink with white and black spots, rough	Fractured into 2 large pieces, and 3 small pieces

Table E-1 Continued

Label	Particle number	Peak Load (N)	Displacement of DVRT (mm)	d_L (mm)	Tensile Strength (MPa)	Pre-break description	Post break description
J	25-3	57.815	0.031	1.800	17.844	Rectangular prismatic, pink with gray spotting, smooth	Clean fracture with approximately symmetric pieces
C	25-31	64.159	0.004	2.600	9.489	Triangular prismatic , pink-orange with grey marbling, rough, angular	Fractured into 3 near equal size pieces
C	25-33	42.483	0.017	1.896	11.817	Angular, dark red-brown with grey and cream, rough, platy but curvy	Fractured into 3 large pieces
C	25-37	50.496	0.009	3.300	4.637	Rectangular prismatic, pink with white and black, rough	Fractured into 3 large pieces, 3 small pieces, and asperities

Table E-1 Continued

Label	Particle number	Peak Load (N)	Displacement of DVRT (mm)	d_L (mm)	Tensile Strength (MPa)	Pre-break description	Post break description
C	25-38	25.609	0.002	1.900	7.095	Rectangular prismatic, light red-brown with white, rough	Fractured into 2 large pieces
C	25-39	20.272	0.001	2.500	3.244	Platy, white pink and black marbling, smooth	Fractured into 2 large pieces
C	25-41	40.709	0.002	1.998	10.200	Spherical, light pink, smooth, shiny	Fractured into 1 large piece, 1 medium piece, and 1 small piece
C	25-44	67.056	0.005	2.200	13.855	Spherical, light red with creamy clear, smooth, angular	Fractured into 2 large pieces and asperities
C	25-45	107.363	0.006	2.245	21.299	Rectangular prismatic, light pink, smooth	Fractured into 2 large pieces, 1 medium piece and asperities

Table E-1 Continued

Label	Particle number	Peak Load (N)	Displacement of DVRT (mm)	d_L (mm)	Tensile Strength (MPa)	Pre-break description	Post break description
C	25-46	36.458	0.018	2.201	7.529	Triangular prismatic , bright red, angular, rough, shiny	Fractured into 2 large pieces
C	25-47	31.964	0.007	2.300	6.041	Spherical, light pink and white, smooth	Fractured into 2 near equal large pieces
J	25-5	100.144	0.014	4.098	5.963	Rectangular prismatic, Tannish pink, smooth	Fractured into one large, two medium, and one small piece. One asperity
C	25-50	25.388	0.006	1.800	7.836	Rectangular prismatic, orange-red with white, angular, smooth	Fractured into 1 large piece and 1 tiny piece
J	25-6	124.326	0.459	2.000	31.097	Rectangular prismatic, brownish red, smooth	Fractured into a variety of small-sized pieces

Table E-1 Continued

Label	Particle number	Peak Load (N)	Displacement of DVRT (mm)	d_L (mm)	Tensile Strength (MPa)	Pre-break description	Post break description
C	25-7	18.229	0.029	1.800	5.626	Angular, light red-brown with black lines, smooth	Fractured into 1 large piece and 2 smaller pieces
J	25-7	124.695	0.210	3.994	7.818	Spherical, light pink, smooth	Fractured into a variety of sizes
C	25-8	25.388	0.018	2.000	6.349	Rectangular prismatic, Pink with clear and black, smooth	Fractured into two near equal size pieces
J	25-8	62.760	0.298	2.001	15.668	Spherical, red with gray spotting, rough	Three tiny particles recovered
C	25-9	99.934	0.075	1.600	39.037	Platy rectangle, red with brown lines, smooth	Fractured into 1 large piece and multiple smaller pieces

APPENDIX F

Table F-1. The label (C or J), particle number, peak load (N), Compressive displacement (mm), d_L (mm), tensile strength (MPa), fracture mode, and particle description prior to and post fracture for black/brown (major and secondary compounds: quartz, mica (biotite), tridymite, plagioclase feldspar, potassium feldspar, and calcite) particles retained by sieve #10 (2 mm)

Label	**Particle number**	**Peak Load (N)**	**Displacement of DVRT (mm)**	**d_L (mm)**	**Tensile Strength (MPa)**	**Pre-break description**	**Post break description**
C	25-1	36.662	0.081	1.600	14.321	Platy, black-brown with white spots, smooth	Fractured into 2 pieces with asperities
J	25-1	38.672	0.009	1.200	26.851	Triangular prismatic, brown, smooth	Clean fracture. Two pieces, no asperities
C	25-10	63.333	0.021	2.200	13.085	Spherical, grey with white spots, rough, shiny	Fractured into at least 1 large piece and 1 medium piece
J	25-10	53.717	0.018	1.199	37.366	Platy, Black, Smooth	Fractured into one medium and three tiny pieces. Some fine remnants

Table F-1 Continued

Label	Particle number	Peak Load (N)	Displacement of DVRT (mm)	d_L (mm)	Tensile Strength (MPa)	Pre-break description	Post break description
C	25-11	19.418	0.009	1.900	5.379	Triangular prismatic , brown with black lines and white spots, rough	Fractured into 2 medium pieces and asperities
J	25-11	68.262	0.042	2.300	12.903	Platy, Grayish Brown, Smooth	Clean fracture. Some asperity
C	25-12	5.419	0.026	1.500	2.408	Platy, grey with red spots, smooth, angular	Fractured into 2 medium pieces
C	25-13	23.560	0.018	1.100	19.471	Platy, light grey, smooth, angular	Fractured into 1 large piece and 1 medium piece
J	25-14	11.675	0.009	1.000	11.675	Triangular prismatic, black, smooth	fractured into at least 1 large piece
J	25-15	105.959	0.037	2.100	24.027	Platy, Brown, smooth	Variety of sizes recovered

Table F-1 Continued

Label	Particle number	Peak Load (N)	Displacement of DVRT (mm)	d_L (mm)	Tensile Strength (MPa)	Pre-break description	Post break description
C	25-15	128.715	0.148	2.000	32.184	Platy triangle, light brown with black lines, smooth	essentially obliterated
C	25-16	53.431	0.024	2.000	13.358	Rectangular prismatic, grey with white, rough, shiny	Fractured into 2 large pieces, 1 small piece, and asperities
J	25-16	55.116	0.019	1.899	15.277	rectangular prismatic, gray w/white spotting, angular, smooth	Fractured into two medium pieces and two tiny pieces
J	25-17	16.136	0.031	1.599	6.314	Platy, Black w/brown spotting, smooth	two medium pieces, one small
C	25-17	111.048	0.022	2.000	27.762	Rectangular prismatic, light grey with cream lines, smooth	Fractured into 1 large piece, 1 medium piece, and at least 2 tiny pieces

Table F-1 Continued

Label	Particle number	Peak Load (N)	Displacement of DVRT (mm)	d_L (mm)	Tensile Strength (MPa)	Pre-break description	Post break description
J	25-18	8.178	0.017	1.250	5.234	Platy, Dark. Brown w/tan spotting, smooth, edges curvy	Fractured into two large pieces one small piece. Some fine material.
C	25-18	42.240	0.027	1.800	13.037	Spherical, black and white marble, rough, angular	fractured into at least 1 medium piece
J	25-19	23.835	0.118	2.997	2.654	Spherical, Lt. Brown w/black spotting, angular, rough	two large pieces recovered.
J	25-2	97.236	0.013	2.000	24.309	Platy, Black, Smooth	Two large pieces. Several small pieces
C	25-2	117.596	0.048	2.000	29.395	Platy, dark brown, smooth, shiny	Fractured into at least 2 medium pieces

Table F-1 Continued

Label	Particle number	Peak Load (N)	Displacement of DVRT (mm)	d_L (mm)	Tensile Strength (MPa)	Pre-break description	Post break description
J	25-20	32.316	0.028	1.699	11.197	rectangular prismatic, gray w/tan spotting, angular, rough	Several small pieces with some fine material
C	25-20	66.450	0.026	1.999	16.634	Triangular prismatic , grey and white spots, rough	Fractured into at least 1 large piece and 1 small piece
J	25-21	94.812	0.317	2.996	10.564	Triangular prismatic, Lt. Gray w/tan spotting, rough	
C	25-21	82.619	0.046	2.200	17.070	Platy, light grey with red-brown, smooth, angular	Fractured into 3 large pieces and asperities
C	25-22	132.030	0.096	2.400	22.922	Rectangular prismatic, light grey with white spots, smooth	Fractured into 2 large pieces, 4 small pieces, and asperities

Table F-1 Continued

Label	Particle number	Peak Load (N)	Displacement of DVRT (mm)	d_L (mm)	Tensile Strength (MPa)	Pre-break description	Post break description
J	25-23	6.201	0.005	1.000	6.201	Platy, Lt. Gray, angular, rough, curvy edges	Fractured into two similarly sized pieces
J	25-24	93.039	0.011	1.300	55.070	Platy, Dark. Brown, Smooth	Fractured into one medium and three tiny pieces. Some fine remnants
C	25-25	2.930	0.007	0.900	3.617	Platy, grey with black spots, rough, angular	Fractured into 1 large piece and 1 small piece
C	25-26	26.424	0.027	2.000	6.606	Platy, black with white, rough, angular, slightly curvy	Fractured into 3 medium pieces and asperities
J	25-26	30.207	0.035	1.799	9.335	Platy, Gray w/tan spots, rough	Fractured into one large piece and one small

Table F-1 Continued

Label	Particle number	Peak Load (N)	Displacement of DVRT (mm)	d_L (mm)	Tensile Strength (MPa)	Pre-break description	Post break description
C	25-27	17.370	0.045	1.500	7.720	Platy, light grey with white, rough, curvy	Fractured into 1 large piece and 1 medium piece
J	25-27	50.931	0.015	1.800	15.721	Spherical, Gray w/pink spots, smooth	Fractured into one large piece and one small
C	25-28	58.586	0.029	2.300	11.075	Rectangular prismatic, light grey with black spots, rough, shiny	didn't fracture
J	25-28	127.603	0.067	2.498	20.449	Platy, Gray w/tan spots, angular	Clean, approximately symmetric, fracture
J	25-29	108.647	0.066	1.875	30.914	Spherical, Dark. Brown, Angular	fracture into a variety of sizes

Table F-1 Continued

Label	Particle number	Peak Load (N)	Displacement of DVRT (mm)	d_L (mm)	Tensile Strength (MPa)	Pre-break description	Post break description
C	25-3	39.112	0.014	2.900	4.651	Rectangular prismatic, black with orange spots, angular, smooth	Fractured into 1 large piece and 1 small piece
J	25-30	26.589	0.022	1.800	8.211	Platy, Brown w/Reddish tint, smooth	Fractured into one large and one tiny piece. Some fine material
C	25-30	12.424	0.017	1.000	12.424	Platy, light grey with white spots, rough, curvy	Fractured into 1 large piece and 1 small pieces
J	25-31	122.525	0.037	1.799	37.842	Platy, Dark. Gray, Smooth	Fractured into two medium pieces and two tiny pieces
J	25-33	28.384	0.034	2.099	6.444	Rectangular prismatic, Brown w/ pink section, smooth	one large pieces w/ several small asperities

Table F-1 Continued

Label	Particle number	Peak Load (N)	Displacement of DVRT (mm)	d_L (mm)	Tensile Strength (MPa)	Pre-break description	Post break description
C	25-33	127.812	0.150	0.950	141.620	Platy, dark grey, smooth, shiny	Fractured into 2 large pieces and asperities
J	25-34	22.062	0.110	2.233	4.424	Rectangular prismatic, Brown, angular	Fractured into two medium pieces and two tiny pieces
C	25-34	42.229	0.056	2.100	9.576	Rectangular prismatic, black and white marble, smooth, shiny	Fractured into at least 2 medium pieces and 1 tiny piece
C	25-35	37.179	0.095	1.900	10.299	Rectangular prismatic, light brown, rough	Fractured into at least 1 large piece
J	25-35	67.651	0.106	1.800	20.880	Platy, Lt. Brown w/Gray spotting, Angular	Fractured into two medium pieces and two tiny pieces

Table F-1 Continued

Label	Particle number	Peak Load (N)	Displacement of DVRT (mm)	d_L (mm)	Tensile Strength (MPa)	Pre-break description	Post break description
J	25-36	110.816	0.108	0.898	137.429	Platy, Reddish Brown, Smooth	two tiny pieces and fine material recovered
C	25-37	56.130	0.021	1.500	24.946	Spherical, black and white, smooth	Fractured into 3 small pieces and asperities
J	25-37	73.521	0.040	0.999	73.686	Platy, Black, Smooth	six roughly equal tiny pieces and some fine material recovered
C	25-38	101.575	0.143	2.900	12.078	Triangular prismatic , grey with brown, rough, angular, shiny	Fractured into 2 large pieces
J	25-38	123.670	0.084	1.299	73.347	Platy, Lt. Gray, smooth	one large piece w/ one tiny piece sheared off side of large piece

Table F-1 Continued

Label	Particle number	Peak Load (N)	Displacement of DVRT (mm)	d_L (mm)	Tensile Strength (MPa)	Pre-break description	Post break description
C	25-39	27.784	0.004	2.100	6.300	Platy, grey with white spots, smooth	Fractured into 1 large piece, 1 medium piece and asperities
J	25-39	107.143	0.144	1.543	44.996	Platy, Dark. Gray with Brown Spotting, angular	several tiny pieces recovered
J	25-4	124.397	0.037	2.000	31.102	Platy, Brown, Smooth	Three large pieces, one tiny piece
J	25-40	121.269	0.021	4.250	6.714	Triangular prismatic, Lt. Gray, Smooth	One large, medium, and small piece recovered
C	25-40	73.422	0.053	2.500	11.748	Rectangular prismatic, light brown-red, rough, angular	Fractured into 1 large piece, 1 small piece, and asperities
J	25-41	81.110	0.058	3.200	7.923	Platy, Black/tan, smooth	Fractured into two large pieces and two small pieces

Table F-1 Continued

Label	Particle number	Peak Load (N)	Displacement of DVRT (mm)	d_L (mm)	Tensile Strength (MPa)	Pre-break description	Post break description
J	25-42	56.119	0.051	1.999	14.042	Platy, Brown, smooth	Fractured into three roughly equal-sized, small particles
C	25-42	126.887	0.053	3.000	14.099	Spherical, light brown with black lines, rough	Fractured into at least 1 large piece
C	25-43	99.896	0.049	3.300	9.173	Spherical, light brown with grey spots, rough, angular	Fractured into 2 large pieces, 2 medium pieces and 1 small piece
J	25-43	126.545	0.059	2.200	26.150	Platy, Brown, smooth	Clean fracture into one large, one small, and one tiny piece
C	25-44	37.647	0.020	1.800	11.621	Rectangular prismatic, dark grey-brown, smooth, shiny	Fractured into 1 large piece and 1 small piece
J	25-44	124.805	0.036	3.100	12.988	Rectangular prismatic, Gray with tan spotting, smooth	

Table F-1 Continued

Label	Particle number	Peak Load (N)	Displacement of DVRT (mm)	d_L (mm)	Tensile Strength (MPa)	Pre-break description	Post break description
C	25-45	39.602	0.046	2.250	7.821	Triangular prismatic , dark grey with white, rough, angular	fractured into at least 1 medium piece
J	25-45	114.550	0.092	1.796	35.501	Triangular prismatic, Black, Smooth	Fractured into one small, and several tiny pieces
J	25-46	77.410	0.027	1.900	21.450	Spherical, Brown, Smooth	Fractured into three equal sized pieces
C	25-46	128.704	0.057	2.400	22.344	Spherical, black, smooth, angular	Fractured into 1 large piece and multiple small and tiny pieces
C	25-47	37.053	0.026	1.800	11.436	Triangular prismatic , black with brown spots, smooth	fractured into at least 1 large piece with some asperities

Table F-1 Continued

Label	Particle number	Peak Load (N)	Displacement of DVRT (mm)	d_L (mm)	Tensile Strength (MPa)	Pre-break description	Post break description
J	25-47	123.230	0.024	2.900	14.655	Triangular prismatic, Black, Smooth	Near symmetric fracture w/ a few asperities
C	25-48	51.030	0.137	2.200	10.543	Rectangular prismatic, dark brown with black spots, smooth	Fractured into 1 large piece and 2 small pieces
J	25-48	39.322	0.021	1.893	10.979	Rectangular prismatic, Light Gray, smooth	clean fracture with one large and one medium piece
J	25-49	104.780	0.048	1.598	41.022	Platy, Gray with pink spotting, smooth	Large piece and small asperity recovered
J	25-5	33.847	0.045	2.200	6.993	Spherical, Gray, angular, rough	Two small pieces. Fine remnants

Table F-1 Continued

Label	Particle number	Peak Load (N)	Displacement of DVRT (mm)	d_L (mm)	Tensile Strength (MPa)	Pre-break description	Post break description
C	25-5	99.262	0.025	1.500	44.102	Platy, dark brown-red, smooth, shiny	Fractured into 1 large piece and 2 small pieces
C	25-50	6.708	0.065	2.000	1.677	Spherical, black and brown, rough, angular	Fractured into multiple small pieces and asperities
J	25-50	128.374	0.126	3.177	12.721	Platy, Gray with tan spotting, smooth	Fractured into one large piece and two medium pieces
C	25-6	3.552	0.006	1.900	0.984	Platy, black-brown, angular, rough	Fractured into 1 medium piece and 1 small piece
J	25-6	129.982	0.051	1.791	40.500	Platy, Lt. Gray w/white spotting, smooth	Fractured in the middle. Some asperities created
C	25-7	9.902	0.015	1.000	9.902	Platy, red-brown, rough, shiny	Fractured into 1 large piece and 1 medium piece

Table F-1 Continued

Label	Particle number	Peak Load (N)	Displacement of DVRT (mm)	d_L (mm)	Tensile Strength (MPa)	Pre-break description	Post break description
J	25-7	59.500	0.019	1.799	18.391	Platy, Brown, Smooth	Fractured into three med size pieces and on small piece
C	25-8	39.008	0.092	2.400	6.772	Angular, black with white, rough	Fractured into 1 large piece and 1 medium piece
C	25-9	35.031	0.058	1.700	12.122	Spherical, grey with white lines, rough, angular, shiny	Fractured into 1 large piece, 1 medium piece, 1 small piece, and asperities
J	25-9	127.636	0.044	1.198	88.932	Triangular prismatic, black, smooth, shiny	fine pieces remain

APPENDIX G

Table G-1. The label (C or J), particle number, peak load (N), Compressive displacement (mm), d_L (mm), tensile strength (MPa), fracture mode, and particle description prior to and post fracture for white/tan (major and secondary compounds: quartz, plagioclase feldspar, potassium feldspar, and mica (muscovite)) particles retained by sieve #10 (2 mm)

Label	**Particle number**	**Peak Load (N)**	**Displacement of DVRT (mm)**	**d_L (mm)**	**Tensile Strength (MPa)**	**Pre-break description**	**Post break description**
C	25-1	22.172	0.016	1.800	6.841	Spherical, dull white with grey spots, rough	Fractured into 1 large piece and 1 medium piece and a few asperities
J	25-1	121.600	0.088	2.700	16.687	Rectangular prismatic, tan, smooth with some pitting	Fractured into two medium pieces, and several small pieces
C	25-10	5.386	0.016	1.900	1.492	Round rectangular prismatic, white with black spot, rough	Fractured into 1 large piece, 1 small piece, and asperities
J	25-11	16.389	0.051	1.997	4.108	platy, tan, rough	Fractured into 1 large piece and many asperities

Table G-1 Continued

Label	Particle number	Peak Load (N)	Displacement of DVRT (mm)	d_L (mm)	Tensile Strength (MPa)	Pre-break description	Post break description
C	25-11	128.594	0.112	2.966	14.622	Rectangular prismatic, white with black marbling, smooth	Fractured into 1 large piece and 1 medium piece
J	25-12	68.102	0.037	2.099	15.451	platy, grayish tan, rough	Fractured into one medium and one small piece
J	25-13	69.821	0.092	2.395	12.172	Triangular prismatic, tan, smooth	Fractured into two approximately uniform small pieces
C	25-13	53.486	0.065	1.750	17.465	Platy rectangle, bright white, smooth	Fractured into 1 large piece and asperities
J	25-14	47.213	0.107	2.497	7.570	platy, tan , rough	Fractured into a several pieces of various size

Table G-1 Continued

Label	Particle number	Peak Load (N)	Displacement of DVRT (mm)	d_L (mm)	Tensile Strength (MPa)	Pre-break description	Post break description
C	25-15	34.354	0.036	2.000	8.592	Platy triangular prismatic, white with red, rough	Fractured into 4 small pieces and asperities
J	25-15	69.843	0.035	1.645	25.820	spherical, white, angular, rough	Fractured into two approximately uniform small pieces w/ one asperity
C	25-16	13.680	0.010	1.800	4.223	Platy rectangle, bright white, rough, angular	Fractured into 2 medium pieces and asperities
C	25-17	118.725	0.036	2.750	15.699	Rectangular prismatic, cream with black spots, smooth	Fractured into 2 large pieces
C	25-18	91.123	0.023	1.900	25.247	Platy rectangle, cream, smooth	Fractured into 1 medium piece and 3 nearly equal small pieces

Table G-1 Continued

Label	Particle number	Peak Load (N)	Displacement of DVRT (mm)	d_L (mm)	Tensile Strength (MPa)	Pre-break description	Post break description
C	25-19	39.531	0.069	2.000	9.882	Platy angular, creamy yellow, rough	Fractured into 1 large piece, 1 medium piece, 1 small piece, and asperities
J	25-2	42.648	0.166	1.716	14.482	Platy, blend of tan and white spotting, rough	Fractured into one small piece with several asperities
C	25-2	81.650	0.031	1.900	22.624	Spherical platy, cream with black and red spots, rough	Fractured into 1 large piece and 1 small piece
C	25-20	64.115	0.027	1.783	20.158	Platy rectangle, white with yellow, smooth	Fractured into 1 medium piece and asperities
C	25-21	47.109	0.031	2.300	8.905	Spherical, white with light brown, rough	Fractured into 2 medium pieces and asperities

Table G-1 Continued

Label	Particle number	Peak Load (N)	Displacement of DVRT (mm)	d_L (mm)	Tensile Strength (MPa)	Pre-break description	Post break description
C	25-22	51.327	0.021	2.000	12.834	Rectangular prismatic, cream white, rough, angular	Fractured into at least 1 large piece and 1 small pieces
C	25-23	52.495	0.061	2.200	10.847	Platy rectangular prismatic, cream with grey lines, rough	Fractured into 1 large piece, 1 medium piece and asperities
C	25-24	18.427	0.019	1.200	12.803	Platy, white with clear and yellow, rough, angular	Fractured into 2 medium pieces, 4 tiny pieces, and asperities
C	25-25	24.981	0.016	1.974	6.411	Platy rectangle, creamy white yellow, rough (grainy), shiny	Fractured into 1 large piece, 1 small piece, and asperities
C	25-26	61.868	0.036	1.500	27.495	Platy, white with light brown, smooth	Fractured into at least 1 large piece with some asperities
C	25-28	65.095	0.014	1.997	16.331	Rectangular prismatic, creamy white with grey, smooth	Fractured into 1 large piece, 2 small pieces, and asperities

Table G-1 Continued

Label	Particle number	Peak Load (N)	Displacement of DVRT (mm)	d_L (mm)	Tensile Strength (MPa)	Pre-break description	Post break description
C	25-29	115.740	0.045	2.199	23.934	Spherical platy, cream with red, smooth	Fractured into 3 large piece
J	25-3	37.471	0.156	2.792	4.808	Spherical w/platy bottom, tan w/white spotting/bottom	Fractured into 1 large piece and 1 small piece with some asperities
C	25-3	126.446	0.041	1.600	49.393	Rectangular prismatic platy, white with pink marbling, smooth, shiny	Fractured into 3 medium size pieces with many small and tiny pieces as well as asperities
C	25-30	40.247	0.030	2.150	8.708	Platy, white with red spots, smooth	Fractured into 2 medium pieces and asperities
C	25-31	28.483	0.083	2.800	3.633	Spherical, white with black lines, rough	Fractured into 1 large piece and 2 small pieces

Table G-1 Continued

Label	Particle number	Peak Load (N)	Displacement of DVRT (mm)	d_L (mm)	Tensile Strength (MPa)	Pre-break description	Post break description
C	25-33	12.799	0.014	1.900	3.546	Spherical, white with black spots, rough, angular	Fractured into 2 medium pieces, 1 small piece and asperities
C	25-34	37.031	0.052	2.099	8.407	Angular, white with brown lines, rough	Fractured into 1 large piece and 1 small piece
C	25-35	21.423	0.016	1.854	6.235	Platy, bright white, smooth, angular	Fractured into 1 large piece and 2 medium piece
C	25-36	61.174	0.023	1.400	31.214	Rectangular prismatic, creamy white yellow, smooth	Fractured into 1 medium piece, 3 small pieces, and asperities
C	25-37	35.400	0.031	1.861	10.227	Spherical, white with grey and red, rough	Fractured into 1 large piece, 1 small piece, and asperities
C	25-38	53.778	0.034	1.899	14.906	Spherical, white with grey spots, angular, smooth	Fractured into 2 medium pieces, and 2 small pieces

Table G-1 Continued

Label	Particle number	Peak Load (N)	Displacement of DVRT (mm)	d_L (mm)	Tensile Strength (MPa)	Pre-break description	Post break description
J	25-4	51.768	0.025	1.899	14.357	platy, tan w/black spotting, smooth	Fractured into at least 1 medium piece with some asperities
C	25-4	125.906	0.041	2.300	23.804	Spherical, white with grey spots, rough	Fractured into 1 large piece and 1 medium piece
C	25-40	70.801	0.055	3.000	7.867	Angular, white with clear and black spots, rough	Fractured into 4 medium pieces
C	25-41	22.073	0.014	1.500	9.810	Platy, white with black lines and spots, smooth, angular	Fractured into 2 large pieces, 1 small piece, and asperities
C	25-42	66.814	0.228	2.500	10.693	Spherical, white with light pink, rough	Fractured into 2 medium pieces

Table G-1 Continued

Label	Particle number	Peak Load (N)	Displacement of DVRT (mm)	d_L (mm)	Tensile Strength (MPa)	Pre-break description	Post break description
C	25-44	81.716	0.058	2.099	18.542	Rectangular prismatic, white with grey, rough, angular	Fractured into 1 large piece, 2 small pieces, and asperities
C	25-45	36.645	0.119	1.927	9.873	Platy, cream with black and red, rough	Fractured into 1 large piece, 3 medium pieces, and 1 tiny piece
C	25-46	127.085	0.063	2.000	31.768	Platy triangle, dull white, smooth, shiny	Fractured into 2 medium pieces, 1 tiny piece, and asperities
C	25-47	35.263	0.147	2.197	7.308	Spherical, yellow-white with black lines, rough	Fractured into 3 medium pieces, multiple tiny pieces, and asperities
C	25-48	115.685	0.038	2.000	28.914	Spherical ,bight white with black, rough, angular	Fractured into 5 medium pieces, and asperities

Table G-1 Continued

Label	Particle number	Peak Load (N)	Displacement of DVRT (mm)	d_L (mm)	Tensile Strength (MPa)	Pre-break description	Post break description
C	25-5	22.756	0.052	2.250	4.495	Platy rounded rectangle, white with black spots, smooth, angular	Fractured into 1 large piece, 1 small piece, and asperities
J	25-5	35.797	0.035	1.748	11.710	platy, tan , rough	Fractured into several small pieces
C	25-50	72.145	0.029	2.099	16.370	Rectangular prismatic, cream white with red lines, smooth	Fractured into two large pieces and multiple small pieces
C	25-6	35.489	0.015	2.250	7.010	Platy, white with red spots, rough, angular	Fractured into 1 large piece and 1 medium pieces
J	25-6	69.055	0.146	2.848	8.515	Triangular prismatic, white, smooth	Fractured into one large piece and one small piece

Table G-1 Continued

Label	Particle number	Peak Load (N)	Displacement of DVRT (mm)	d_L (mm)	Tensile Strength (MPa)	Pre-break description	Post break description
C	25-7	126.688	0.071	3.700	9.256	Rectangular prismatic, white with black spots, rough, angular	Fractured into 1 large piece, 1 medium piece, and 2 small pieces
J	25-7	121.027	0.098	3.098	12.611	Triangular prismatic, cloudy white, smooth	fractured into at least 1 large piece with asperities
C	25-8	21.831	0.016	0.800	34.110	Platy, white with yellow, smooth	Fractured into 1 medium piece and 2 small pieces
C	25-9	29.353	0.023	2.500	4.698	Angular, white with brown spots, rough	Fractured into 1 large piece, 1 small piece, and asperities
J	25-9	117.833	0.028	1.800	36.380	Rectangular prismatic, white, smooth	Fractured into three small pieces, and several tiny

APPENDIX H

Table H-1. The label (C or J), particle number, peak load (N), Compressive displacement (mm), d_L (mm), tensile strength (MPa), fracture mode, and particle description prior to and post fracture for clear/translucent (major and secondary compounds: quartz and plagioclase feldspar) particles retained by sieve #10 (2 mm)

Label	**Particle number**	**Peak Load (N)**	**Displacement of DVRT (mm)**	**d_L (mm)**	**Tensile Strength (MPa)**	**Pre-break description**	**Post break description**
C	25-10	121.930	0.037	3.000	13.546	Spherical, cloudy clear with white spots, rough	2 large pieces, small asperities
J	25-10	106.725	0.041	1.900	29.579	Spherical, translucent, rough	Fractured into two small, uniform pieces
C	25-11	122.536	0.068	2.000	30.636	Platy, clear with gold brown, rough, angular	3 large pieces, multiple small asperities

Table H-1 Continued

Label	Particle number	Peak Load (N)	Displacement of DVRT (mm)	d_L (mm)	Tensile Strength (MPa)	Pre-break description	Post break description
J	25-12	59.412	0.074	1.897	16.518	Triangular prismatic, tannish clear, rough	Fractured into several tiny pieces
C	25-13	59.192	0.014	2.800	7.550	Platy, clear with red brown marbling, smooth	6 medium size pieces
C	25-14	129.122	0.035	3.980	8.152	Rectangular prismatic, cloudy with brown, smooth	3 large pieces and asperities
J	25-14	36.458	0.014	2.000	9.114	Triangular prismatic, tannish clear, smooth	Fractured into two tiny pieces and some fine material
C	25-15	21.765	0.010	3.100	2.265	Platy, clear, smooth, shiny	1 large piece, 1 small piece

Table H-1 Continued

Label	Particle number	Peak Load (N)	Displacement of DVRT (mm)	d_L (mm)	Tensile Strength (MPa)	Pre-break description	Post break description
C	25-18	62.055	0.016	2.798	7.927	Triangular prismatic, cloudy clear with pink, rough	3 medium pieces
J	25-2	62.804	0.019	1.899	17.408	Triangular prismatic, translucent, angular, rough	Fractured into one medium and three small pieces
C	25-2	30.918	0.021	1.200	21.471	Platy, clear, smooth, angular	One large piece and multiple smaller pieces
C	25-20	72.905	0.015	5.000	2.916	Triangular prismatic , clear with brown spots, smooth, shiny	2 large pieces, small asperities

Table H-1 Continued

Label	Particle number	Peak Load (N)	Displacement of DVRT (mm)	d_L (mm)	Tensile Strength (MPa)	Pre-break description	Post break description
C	25-21	65.966	0.035	2.800	8.414	Spherical, clear with brown spots, rough	1 large piece, 1 smaller piece
C	25-23	59.225	0.022	5.000	2.369	Platy, cloudy clear with brown, rough	Fractured into at least 1 large piece
C	25-24	3.084	0.003	2.989	0.345	Angular, cloudy clear, smooth, shiny	Fractured into 2 large pieces and 2 small pieces
C	25-25	103.018	0.034	1.899	28.560	Spherical, transparent brown with black spots, rough	Fractured into 2 larger pieces and 2 small pieces
C	25-26	20.784	0.063	4.500	1.026	Platy, clear with black and brown, rough, angular	Fracture into 2 pieces, and multiple asperities

Table H-1 Continued

Label	Particle number	Peak Load (N)	Displacement of DVRT (mm)	d_L (mm)	Tensile Strength (MPa)	Pre-break description	Post break description
C	25-28	70.074	0.022	2.300	13.246	Platy, clear with white spots, rough, angular	Fracture into 3 pieces, 2 medium and 1 small
C	25-29	104.692	0.028	3.300	9.615	Rectangular prism, cloudy clear, angular, rough	Fractured into at least 1 large piece and 1 small piece
J	25-3	62.177	0.051	1.999	15.561	Spherical, translucent, rough	Fractured into three equally sized (tiny) pieces
C	25-3	63.322	0.019	1.300	37.477	Rectangular prismatic, cloudy clear, rough, angular	Multiple small pieces

Table H-1 Continued

Label	Particle number	Peak Load (N)	Displacement of DVRT (mm)	d_L (mm)	Tensile Strength (MPa)	Pre-break description	Post break description
C	25-30	64.016	0.062	3.100	6.661	Platy, cloudy white with brown lines, smooth	Fractured into multiple small pieces
C	25-31	98.689	0.050	2.000	24.670	Spherical, clear with brown, rough, shiny	Fractured into 1 large piece and 2 small pieces
C	25-32	124.805	0.046	2.200	25.787	Triangular prismatic , clear with pink, angular, shiny, smooth	Explosive fracture, no recovery of particles
C	25-33	53.376	0.014	1.100	44.112	Platy, clear with white, smooth, angular	Fractured into 3 large pieces and asperities

Table H-1 Continued

Label	Particle number	Peak Load (N)	Displacement of DVRT (mm)	d_L (mm)	Tensile Strength (MPa)	Pre-break description	Post break description
C	25-36	103.007	0.030	2.100	23.361	Angular, cloudy white with brown lines, rough	Fractured into at least one large piece
C	25-37	44.509	0.047	1.700	15.400	Triangular prismatic , clear with brown and white, angular, rough	Fractured into at least one large piece and asperities
C	25-38	51.316	0.074	2.799	6.550	Platy, clear with white, smooth, shiny	Fracture into 1 large piece and 1 small piece
C	25-39	106.620	0.053	2.400	18.513	Rectangular prismatic, clear with light brown, smooth	Fractured into at least 2 large pieces and 1 medium piece

Table H-1 Continued

Label	Particle number	Peak Load (N)	Displacement of DVRT (mm)	d_L (mm)	Tensile Strength (MPa)	Pre-break description	Post break description
C	25-4	20.983	0.024	2.750	2.774	Platy, clear with pink marbling, rough, angular	Fractured into two large pieces and multiple asperities
C	25-40	22.381	0.009	1.000	22.381	Platy, clear, smooth, shiny, angular	Fractured into 1 large piece and 1 small piece
C	25-42	96.795	0.049	2.200	20.003	Angular, clear with pink, rough	Fractured into at least 1 large piece and 1 tiny piece
C	25-43	83.038	0.034	1.600	32.437	Platy, clear with pink, rough, angular	Fractured into 1 large piece 1 small piece and asperities

Table H-1 Continued

Label	Particle number	Peak Load (N)	Displacement of DVRT (mm)	d_L (mm)	Tensile Strength (MPa)	Pre-break description	Post break description
C	25-44	20.046	0.008	2.000	5.011	Rectangular prismatic/platy, clear yellow with black spots, rough	Fractured into 1 large piece and 1 tiny piece
C	25-47	33.440	0.039	1.116	26.836	Platy, clear with yellow, rough, shiny	Fractured into 1 large piece and 1 tiny piece
C	25-48	58.090	0.021	1.800	17.937	Platy, cloudy clear with yellow, smooth	Fractured into at least 1 medium piece; fracture occurred between clear and yellow area

Table H-1 Continued

Label	Particle number	Peak Load (N)	Displacement of DVRT (mm)	d_L (mm)	Tensile Strength (MPa)	Pre-break description	Post break description
C	25-49	61.879	0.016	1.900	17.141	Rectangular prismatic, cloudy clear with yellow, rough, shiny	Fractured into at least 2 large pieces
C	25-5	122.745	0.109	4.000	7.673	Spherical, cloudy clear with brown marbling, angular, shiny	Fractured into two large pieces
J	25-5	26.385	0.027	1.600	10.311	Rectangular prismatic, tannish clear, rough	Clean fracture into two uniform pieces
C	25-50	121.787	0.042	2.100	27.623	Spherical with platy bottom, cloudy white, rough	Fractured into at least 1 large piece and asperities

Table H-1 Continued

Label	Particle number	Peak Load (N)	Displacement of DVRT (mm)	d_L (mm)	Tensile Strength (MPa)	Pre-break description	Post break description
J	25-6	53.883	0.016	2.000	13.473	Spherical, clear, rough	Fractured into one small and one tiny piece
C	25-7	4.945	0.003	2.000	1.236	Triangular prismatic , cloudy clear, angular, smooth, shiny	Fractured into 1 large piece and 1 tiny piece
J	25-7	117.161	0.033	1.799	36.185	Spherical, tannish clear, smooth	Fractured into several tiny pieces
J	25-8	48.045	0.022	2.100	10.898	Spherical, tannish clear, smooth	Fractured into two uniform pieces
C	25-8	104.725	0.031	2.200	21.641	Spherical, cloudy clear with brown spots, angular, rough	Fractured into 3 large pieces and multiple small pieces

Table H-1 Continued

Label	Particle number	Peak Load (N)	Displacement of DVRT (mm)	d_L (mm)	Tensile Strength (MPa)	Pre-break description	Post break description
C	25-9	35.224	0.020	0.900	43.487	Platy, clear with dark brown spot, rough, angular	1 large piece, multiple small pieces

APPENDIX I

The Appendix contains tables and figures to supplement the discussion of results.

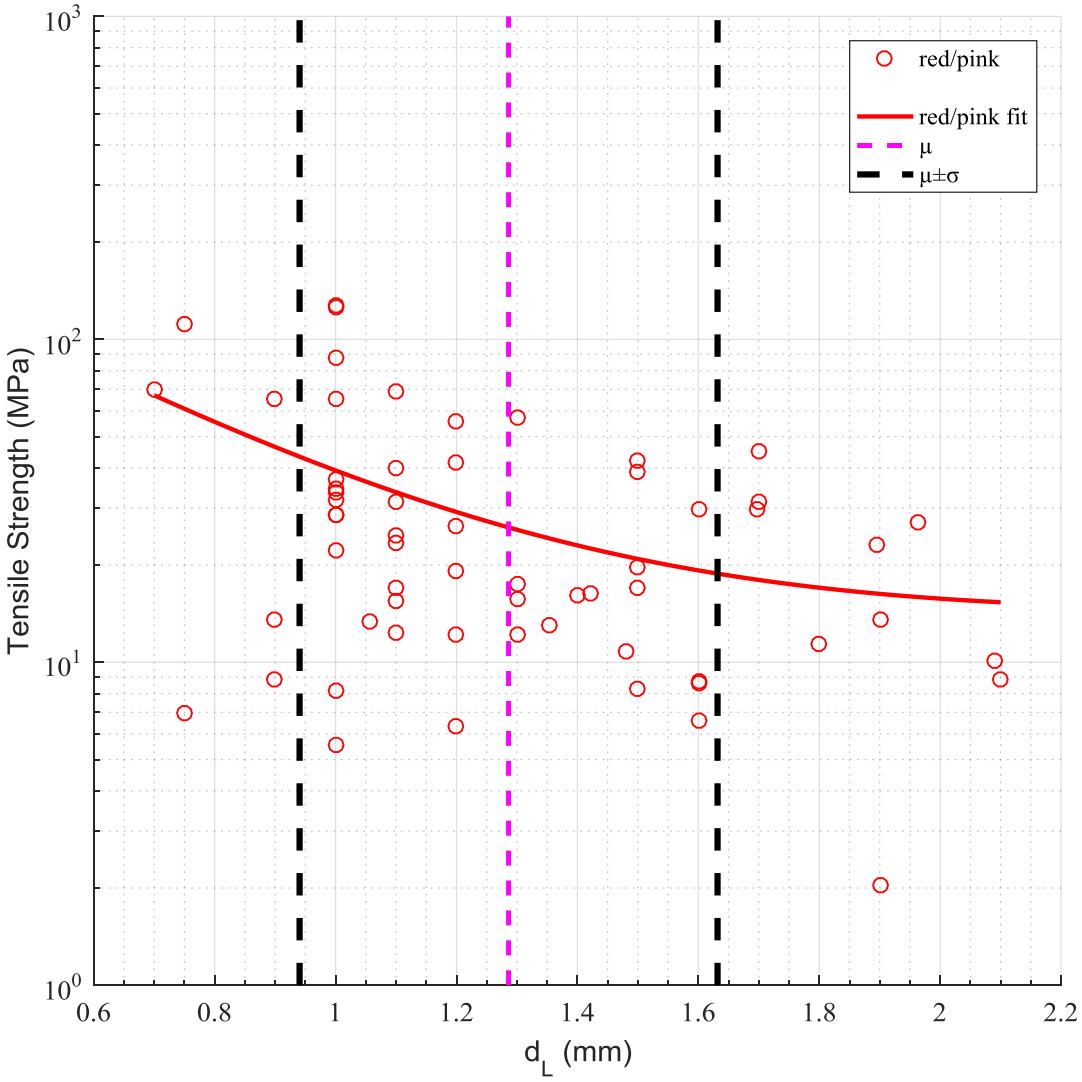


Figure 4-9a. Relationship between tensile strength and d_L for red/pink (major and secondary compounds: quartz, potassium feldspar, and plagioclase feldspar) particles retained between sieve #10 (2 mm) and #20 (0.84 mm).σ

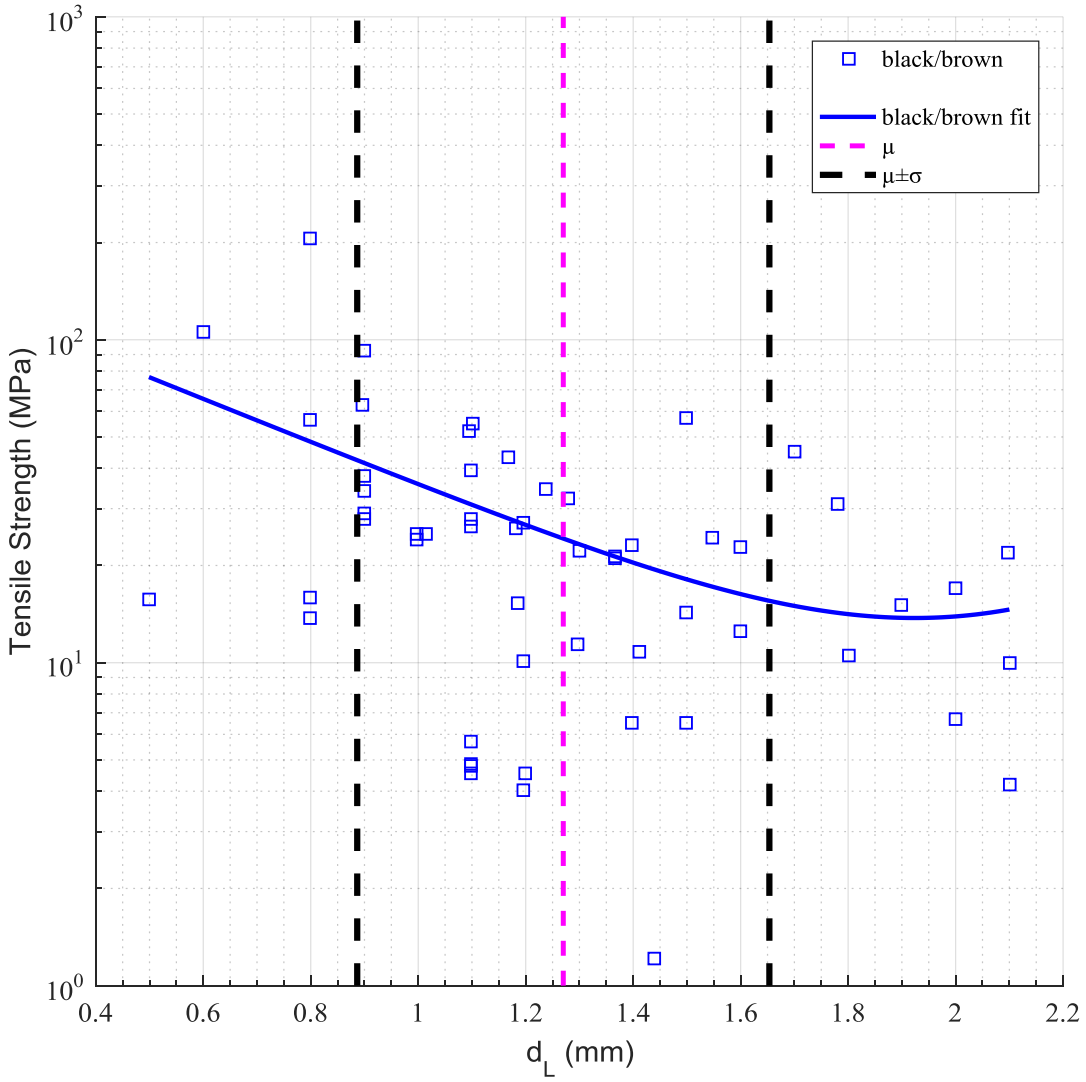


Figure 4-9b. Relationship between tensile strength and d_L for black/brown (major and secondary compounds: quartz, mica (biotite), tridymite, plagioclase feldspar, potassium feldspar, and calcite) particles retained between sieve #10 (2 mm) and #20 (0.84 mm).

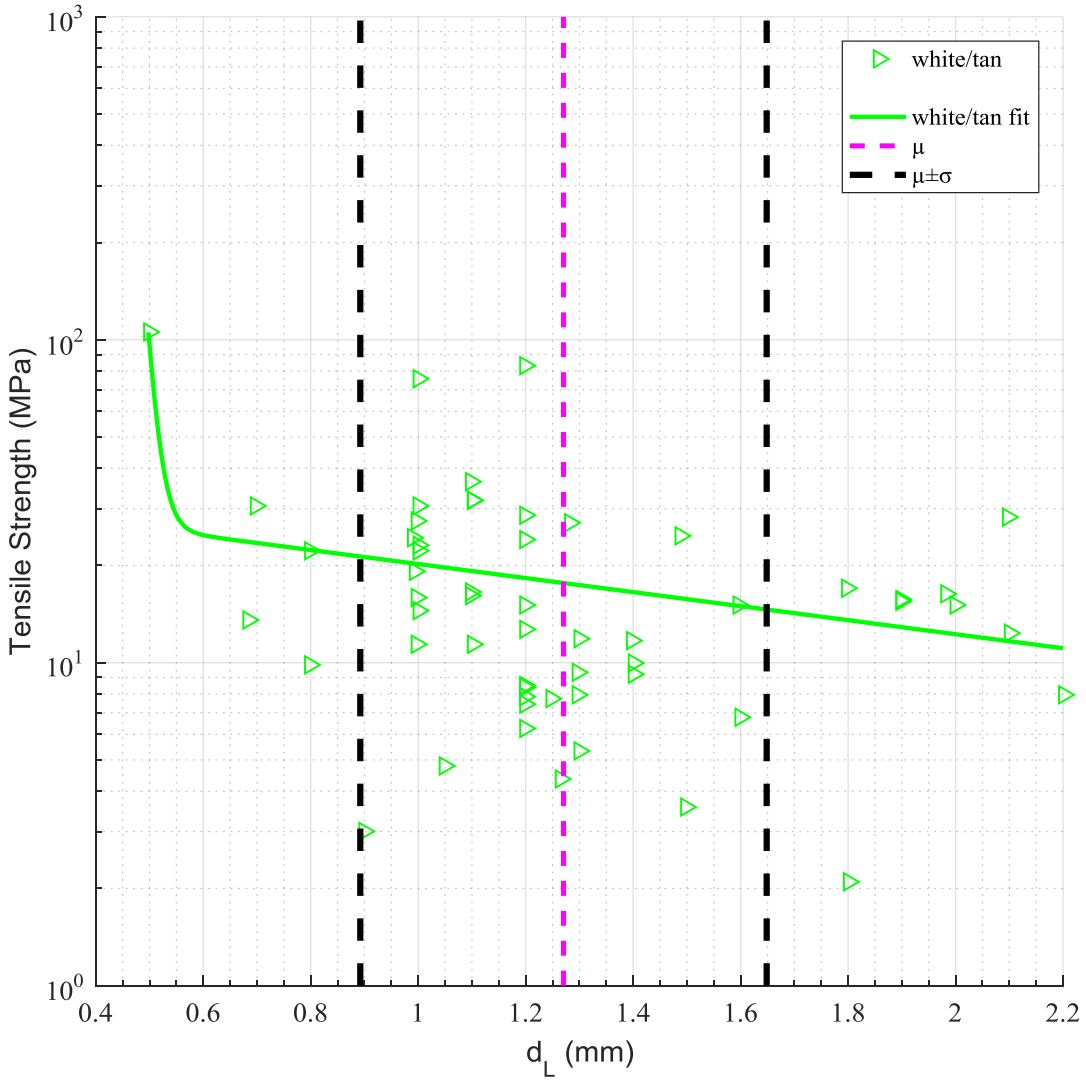


Figure 4-9c. Relationship between tensile strength and d_L for white/tan (major and secondary compounds: quartz, plagioclase feldspar, potassium feldspar, and mica (muscovite)) particles retained between sieve #10 (2 mm) and #20 (0.84 mm).

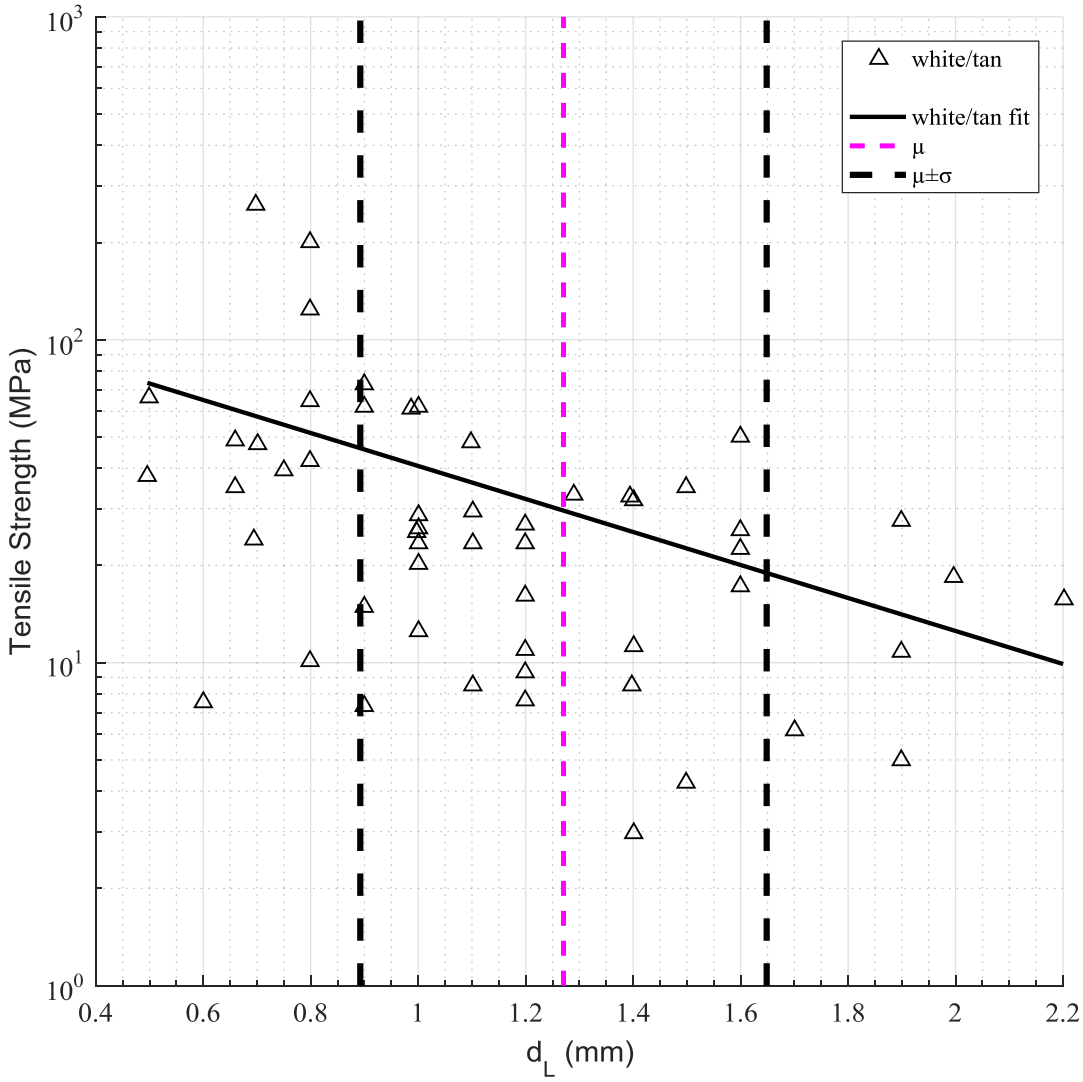


Figure 4-9d. Relationship between tensile strength and d_L for clear/translucent (major and secondary compounds: quartz and plagioclase feldspar) particles retained between sieve #10 (2 mm) and #20 (0.84 mm).

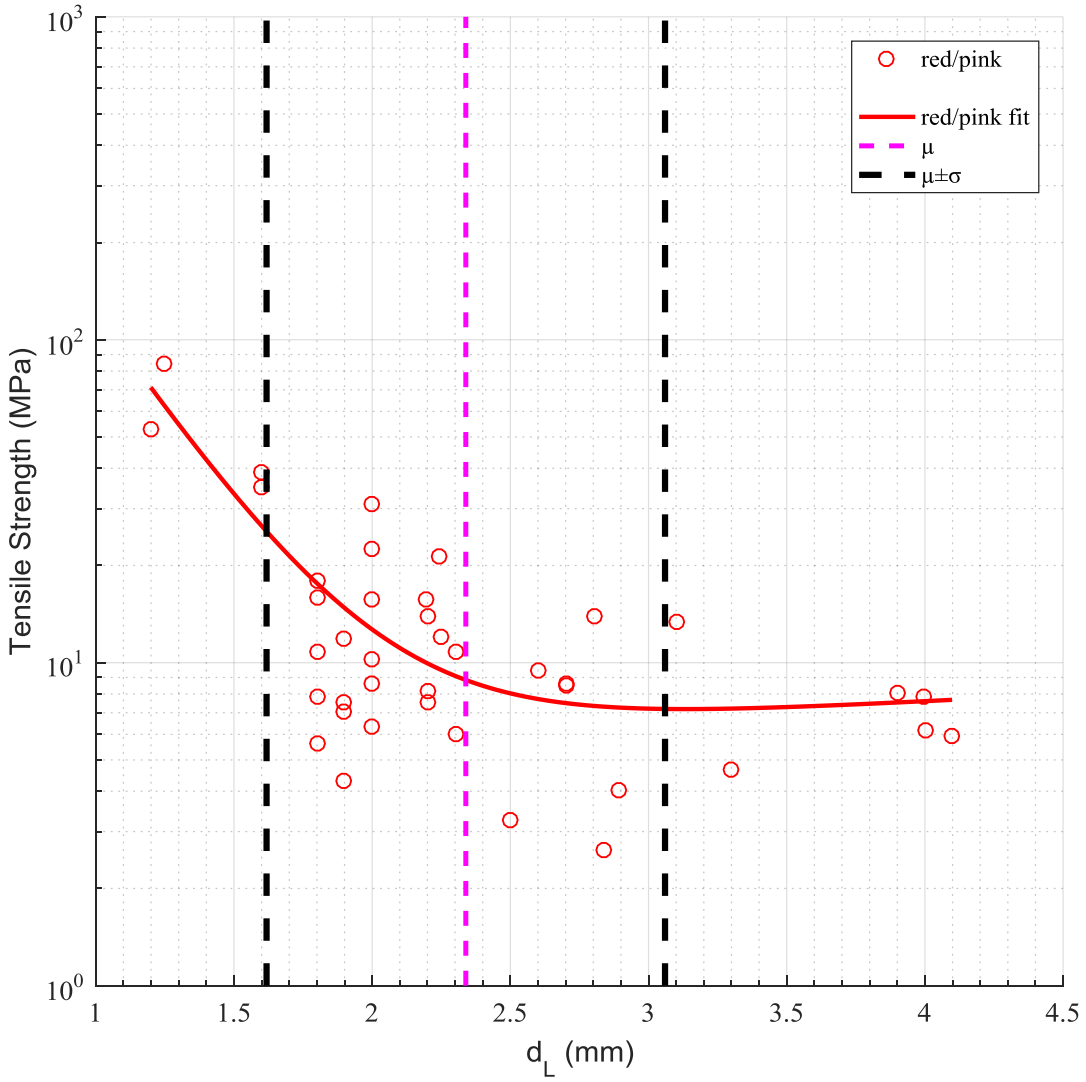


Figure 4-10a. Relationship between tensile strength and d_L for red/pink (major and secondary compounds: quartz, potassium feldspar, and plagioclase feldspar) particles retained by sieve #10 (2 mm).

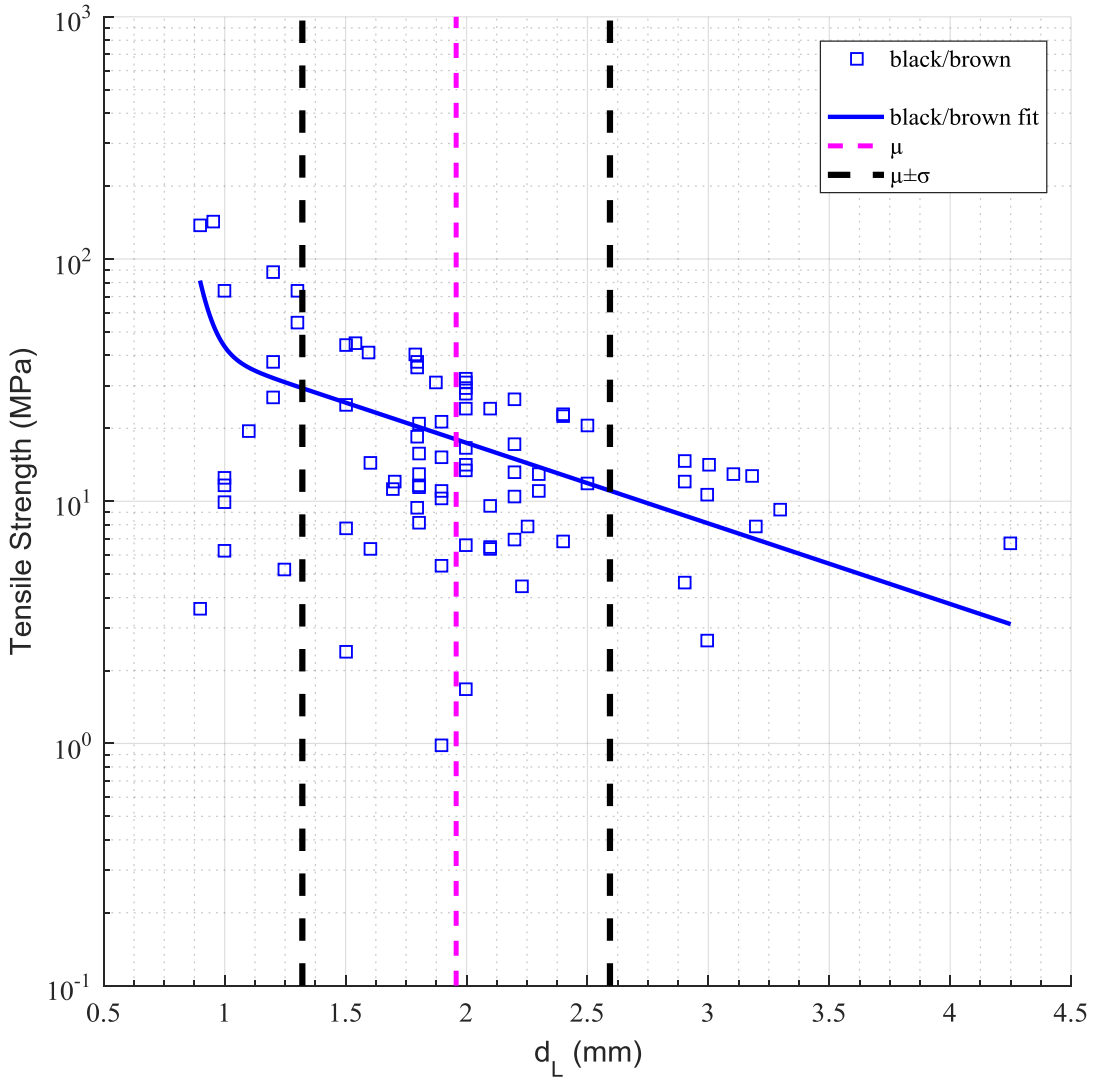


Figure 4-10b. Relationship between tensile strength and d_L for black/brown (major and secondary compounds: quartz, mica (biotite), tridymite, plagioclase feldspar, potassium feldspar, and calcite) particles retained by sieve #10 (2 mm).

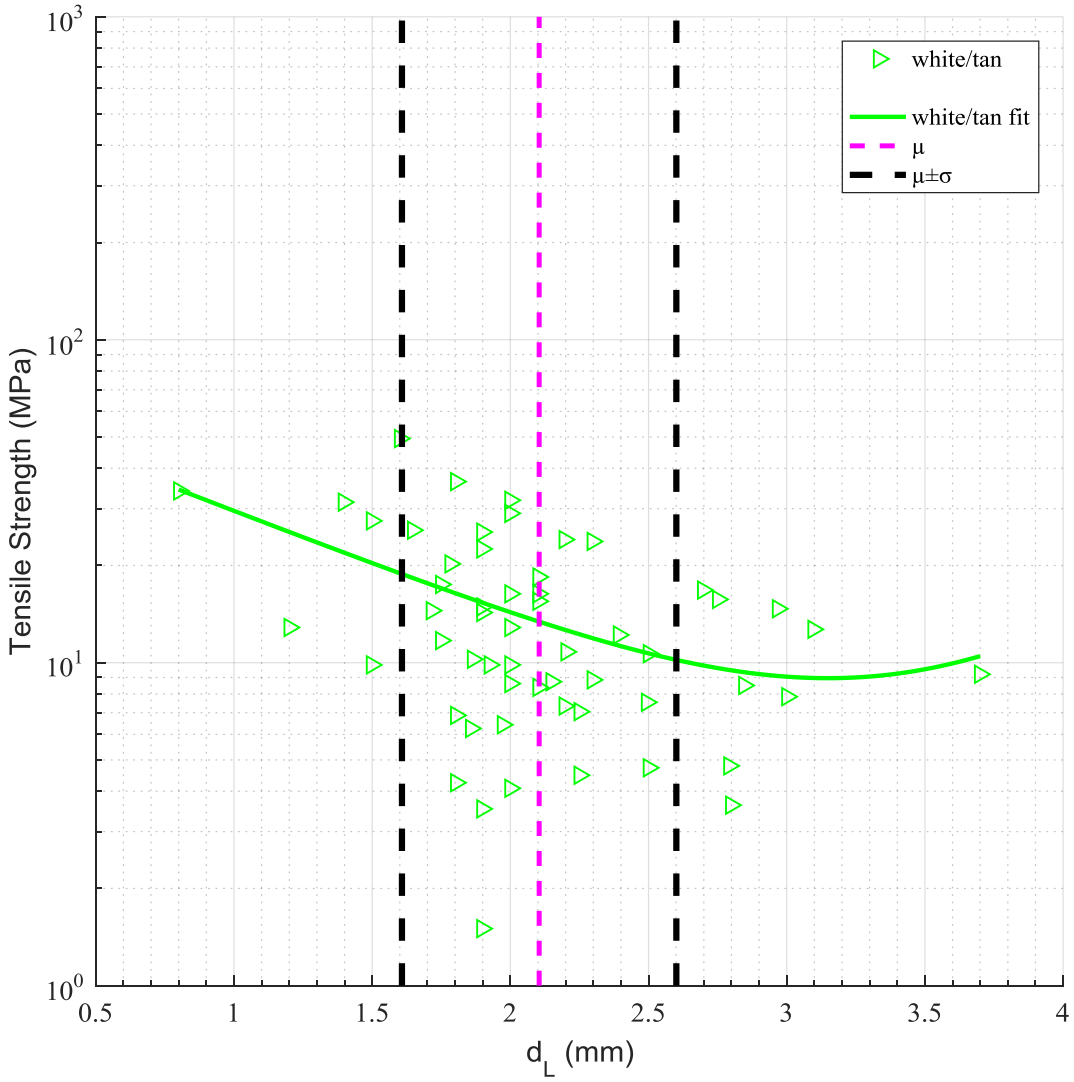


Figure 4-10c. Relationship between tensile strength and d_L for white/tan (major and secondary compounds: quartz, plagioclase feldspar, potassium feldspar, and mica (muscovite)) particles retained by sieve #10 (2 mm).

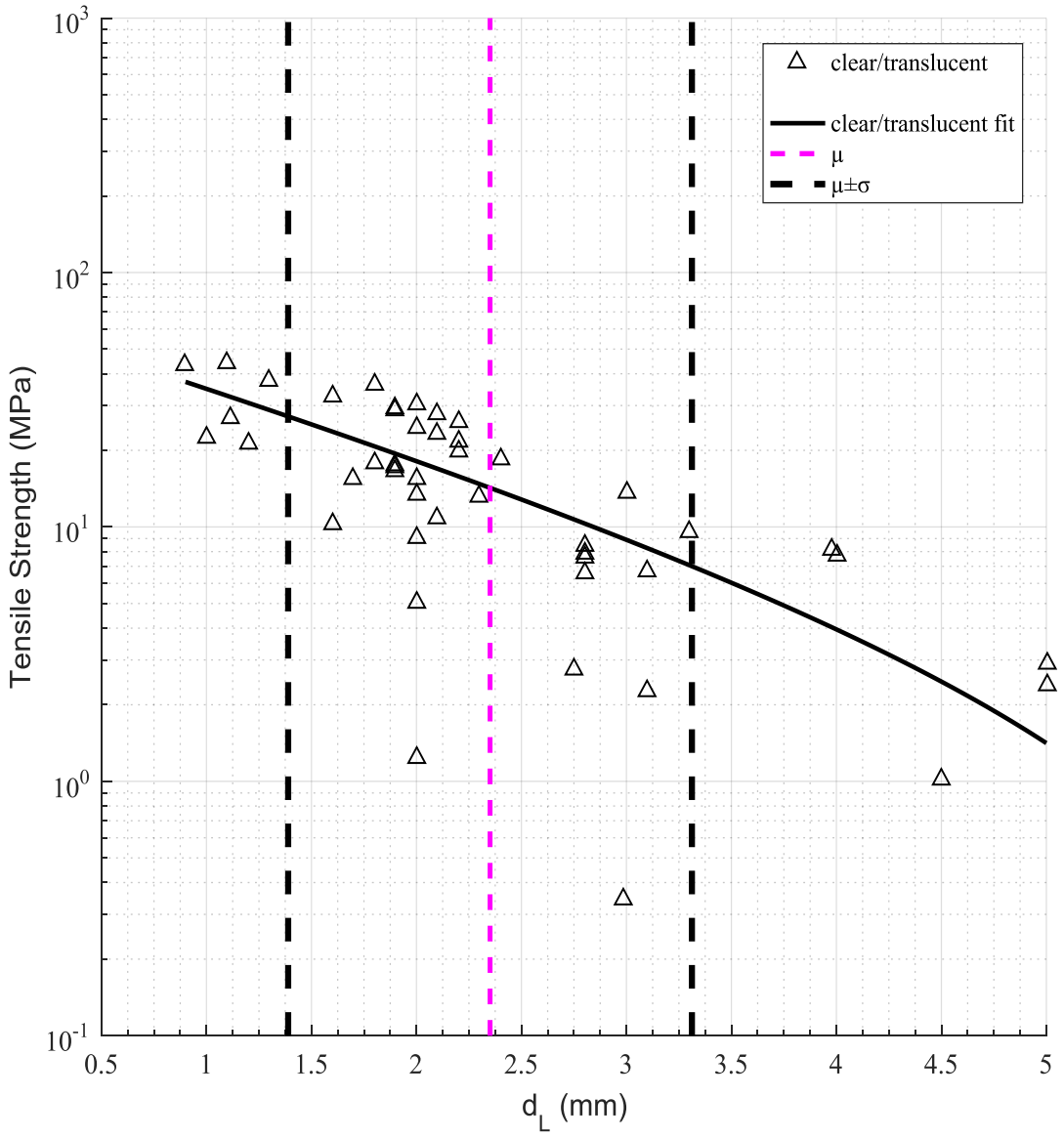


Figure 4-10d. Relationship between tensile strength and d_L for clear/translucent (major and secondary compounds: quartz and plagioclase feldspar) particles retained by sieve #10 (2 mm).

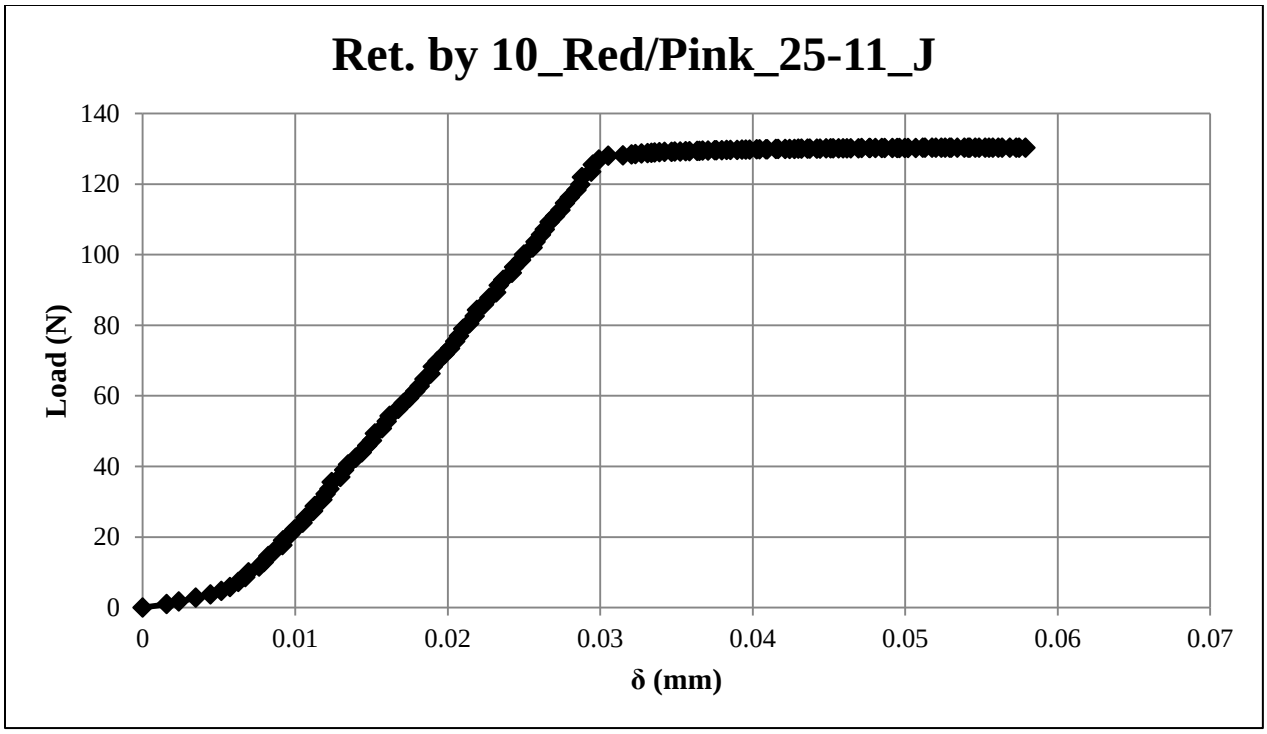


Figure 4-13b.1. The uniaxial compression of particle Red/Pink 25-11_J retained by sieve #10 (2 mm) with a particle diameter in loading direction of 1.25 mm.

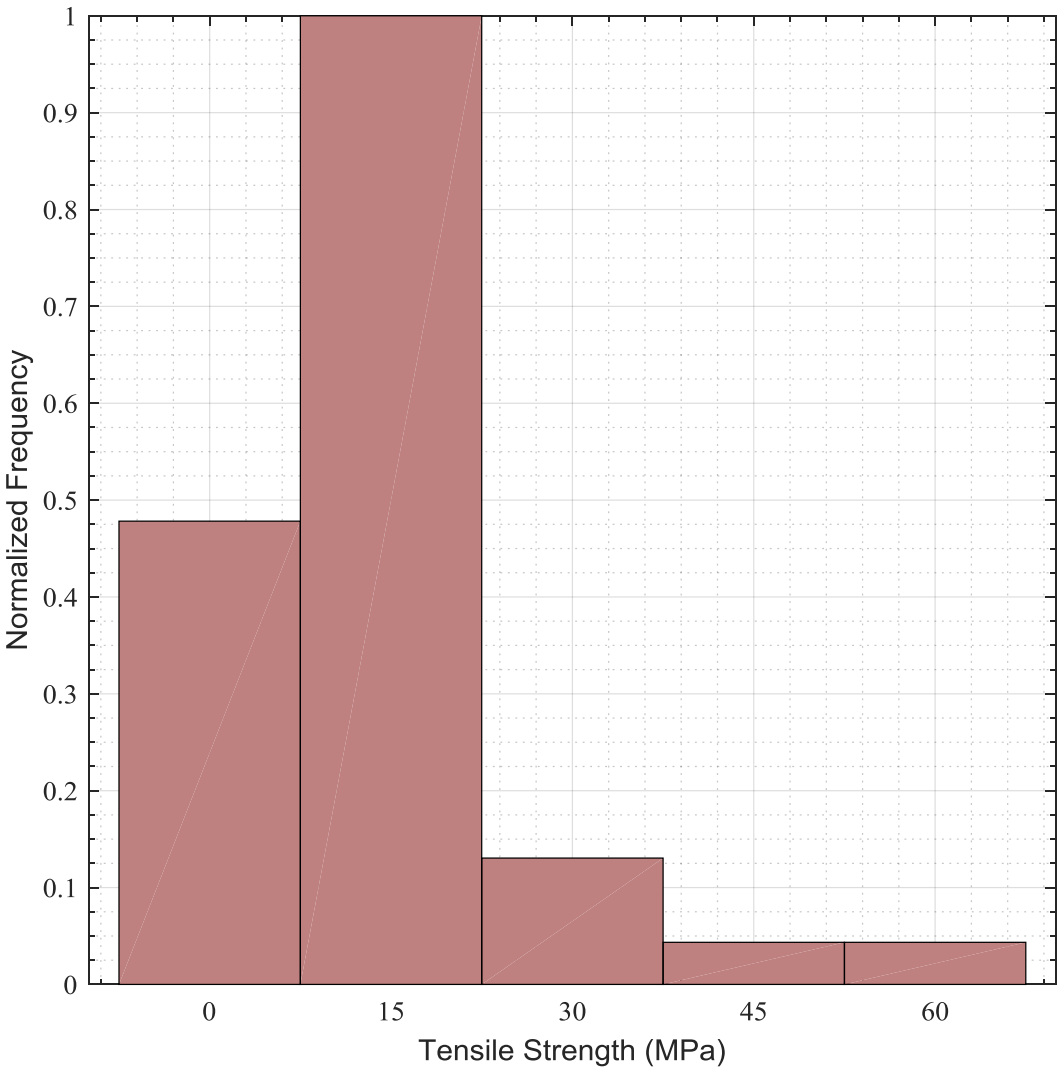


Figure 4-13b.2. The tensile strength histograms for red/pink (major and secondary compounds: quartz, potassium feldspar, and plagioclase feldspar) particles retained by sieve #10 (2 mm) with the exclusion of the outlier.

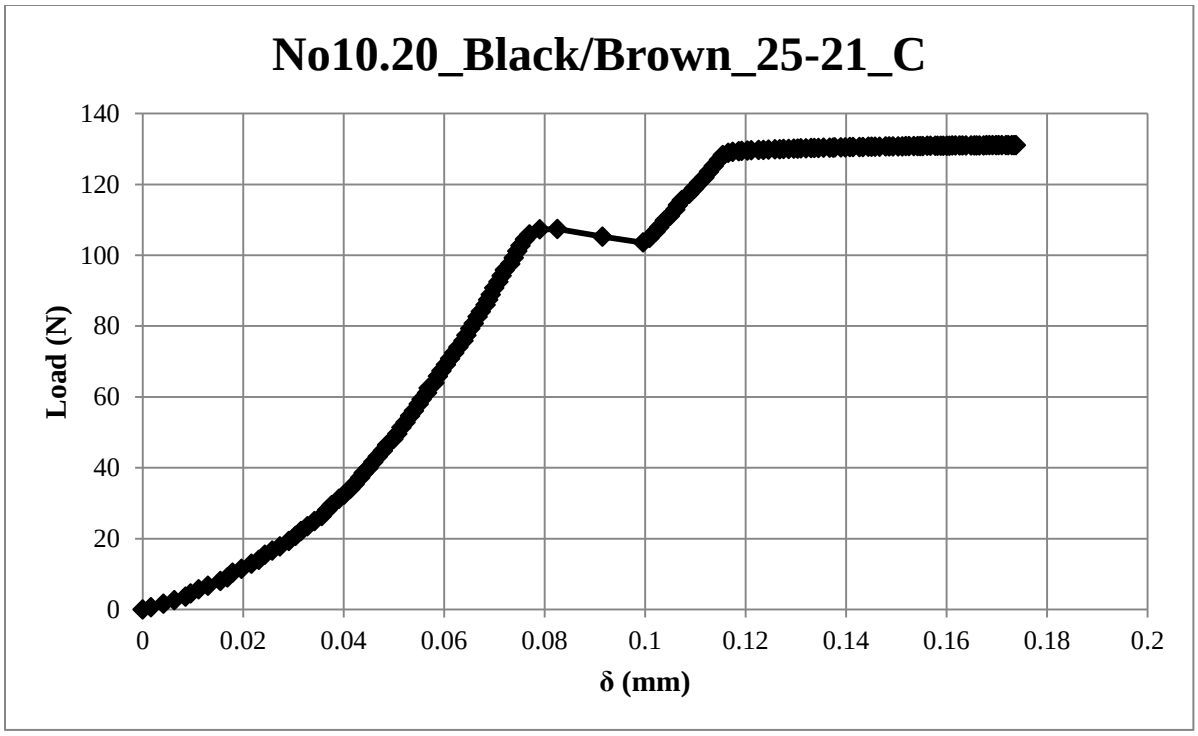


Figure 4-14a.1. The uniaxial compression curve for black/brown particle 25-21_C retained between sieve #10 (2 mm) and #20 (0.84 mm) with a particle diameter in loading direction of 0.80 mm.

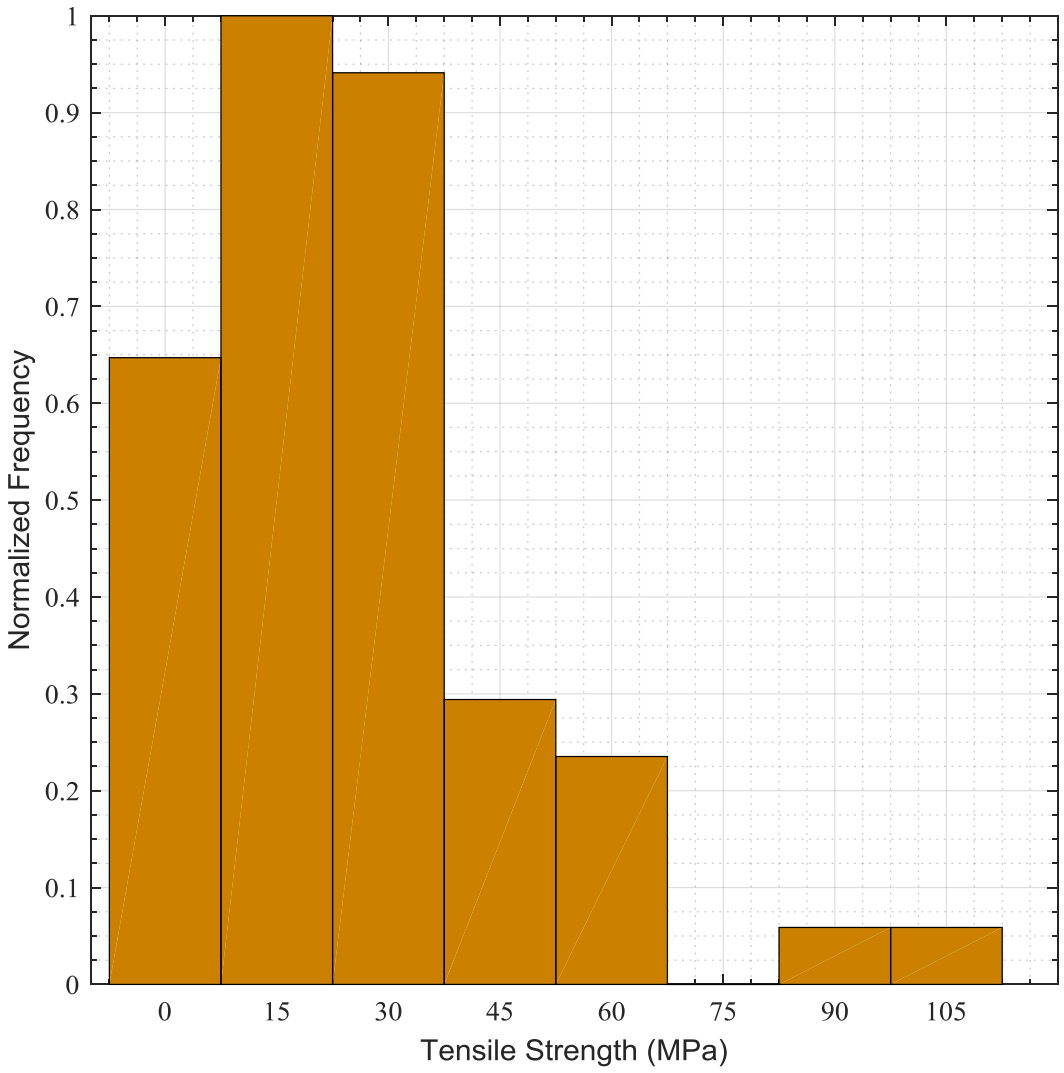


Figure 4-14a.2. The tensile strength histograms for black/brown (major and secondary compounds: quartz, mica (biotite), tridymite, plagioclase feldspar, potassium feldspar, and calcite) particles retained between sieve #10 (2 mm) and #20 (0.84 mm) with the exclusion of the outlier.

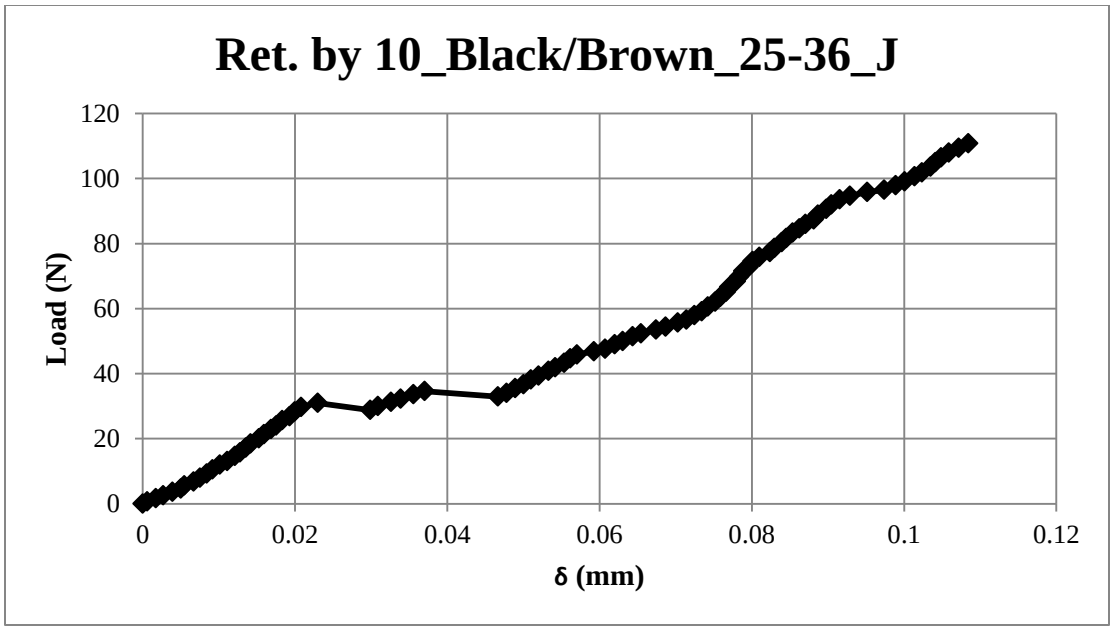


Figure 4-14b.1. The uniaxial compression curve for clear/translucent particle 25-36_J retained by sieve #10 (2 mm) with a particle diameter in loading direction of 0.90 mm.

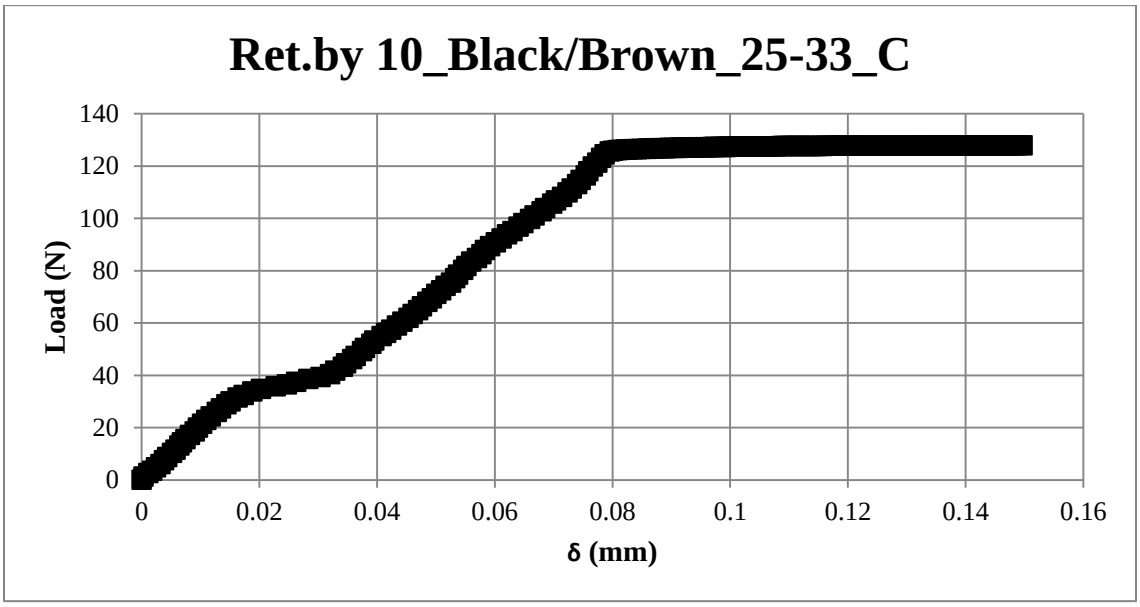


Figure 4-14b.2. The uniaxial compression curve for clear/translucent particle 25-33_C retained by sieve #10 (2 mm) with a particle diameter in loading direction of 0.95 mm.

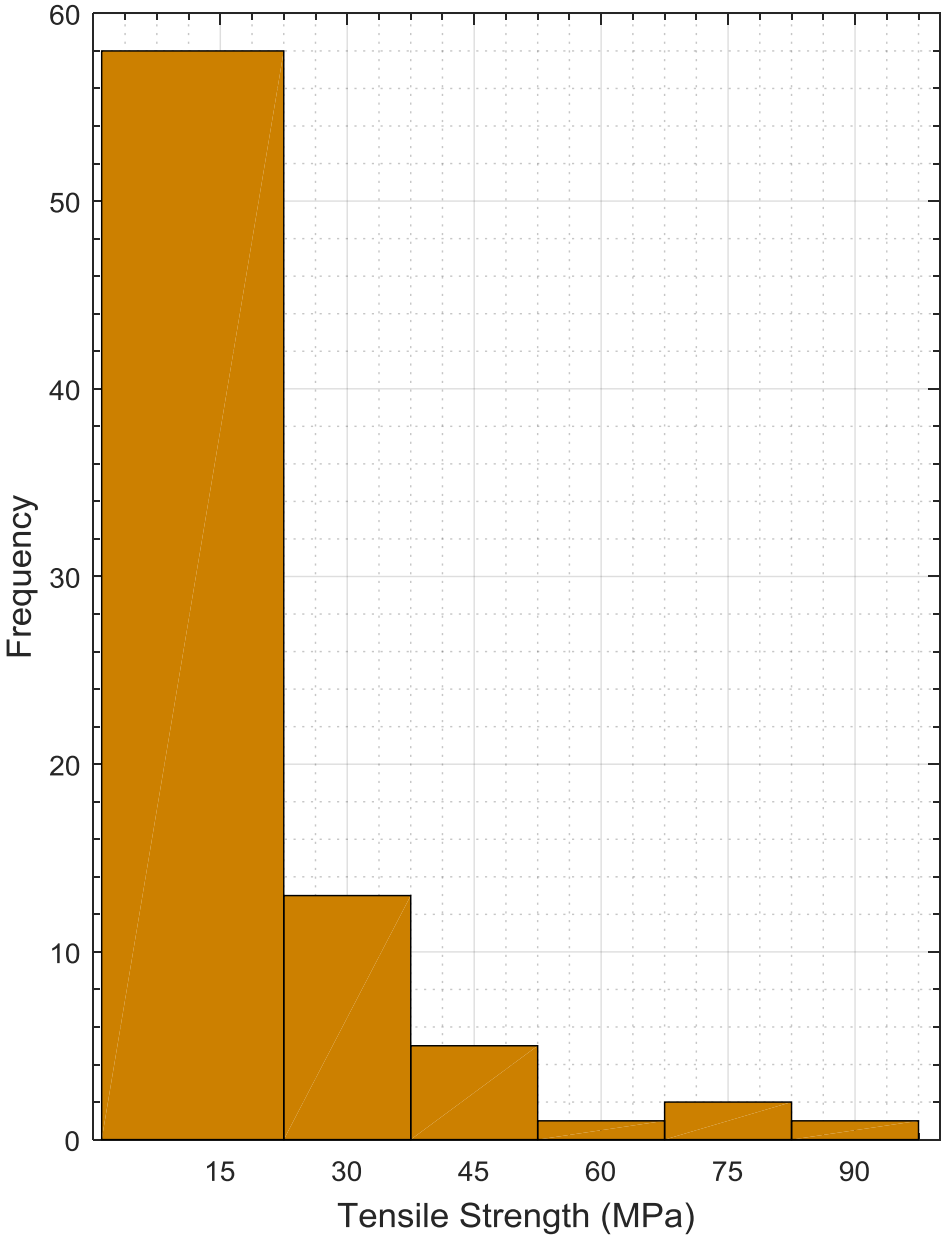


Figure 4-14b.3. The tensile strength histograms for black/brown (major and secondary compounds: quartz, mica (biotite), tridymite, plagioclase feldspar, potassium feldspar, and calcite) particles retained by sieve #10 (2 mm) with the exclusion of outliers.

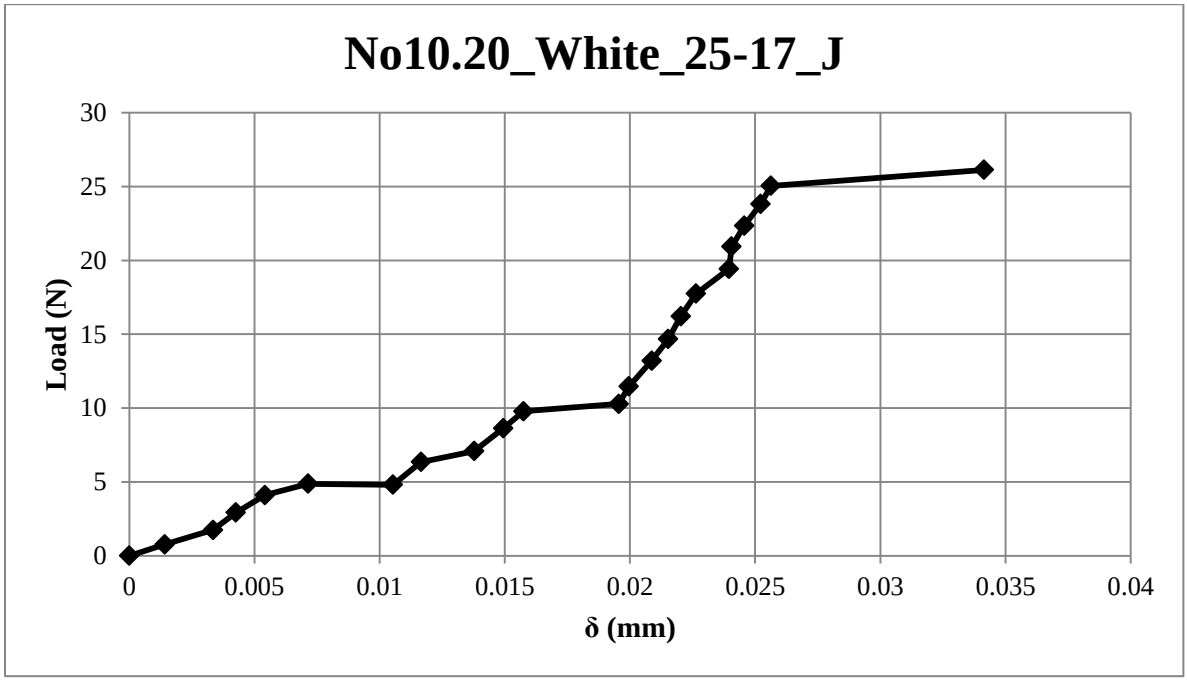


Figure 4-15a.1. The uniaxial compression curve for white/tan particle retained between sieve #10 (2 mm) and #20 (0.84 mm) with a particle diameter in loading direction of 0.50 mm

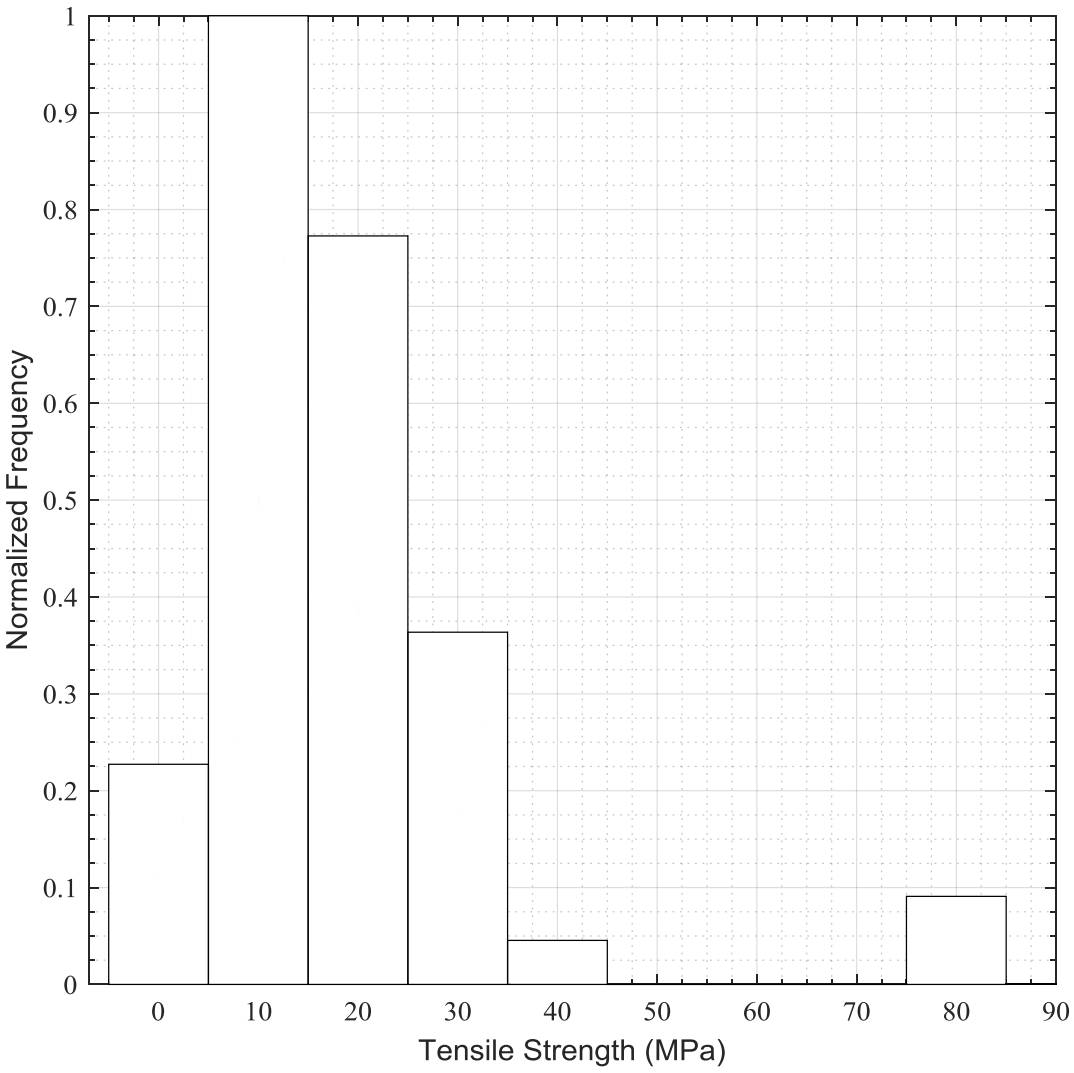


Figure 4-15a.2. The tensile strength histograms for white/tan (major and secondary compounds: quartz, plagioclase feldspar, potassium feldspar, and mica (muscovite)) particles retained between sieve #10 (2 mm) and #20 (0.84 mm) with the exclusion of the outlier.

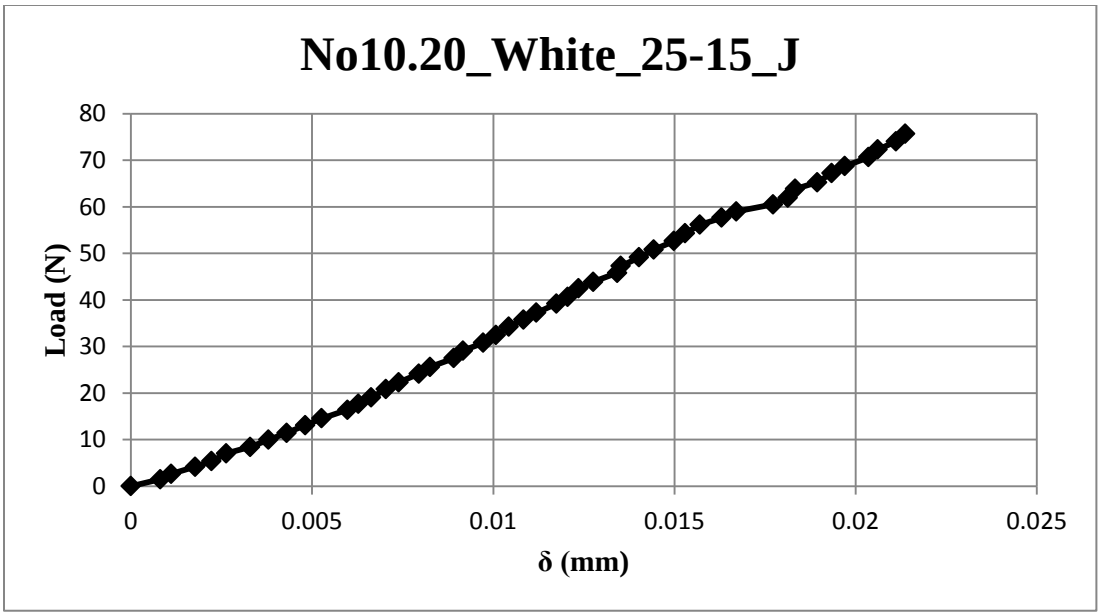


Figure 4-15a.3. The uniaxial compression curve for white/tan particle retained between sieve #10 (2 mm) and #20 (0.84 mm) with a particle diameter in loading direction of 1.00 mm

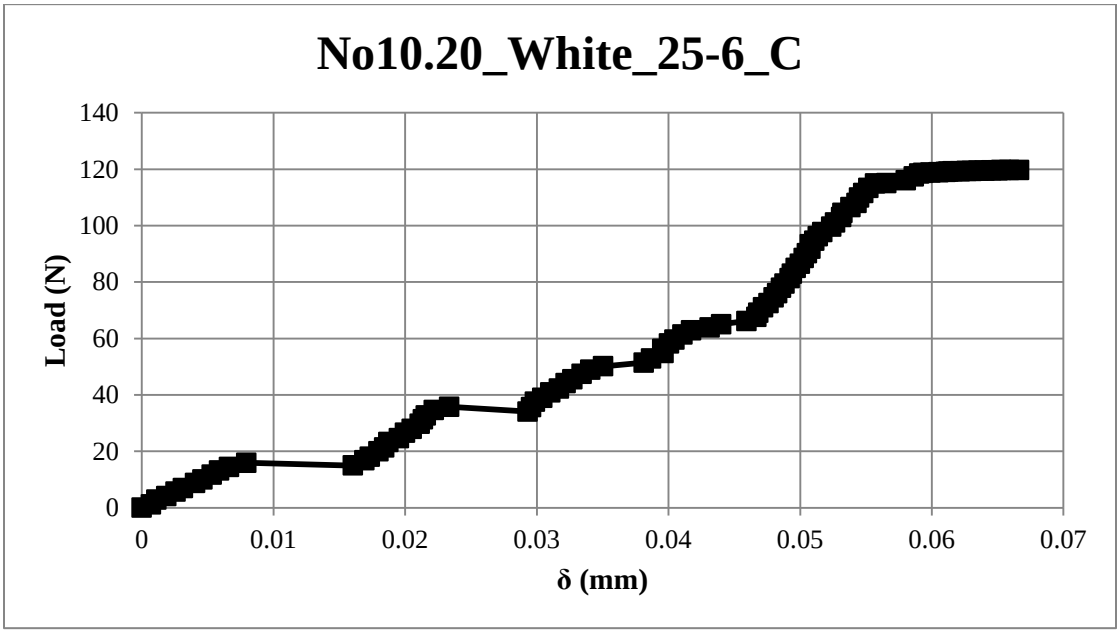


Figure 4-15a.4. The uniaxial compression curve for white/tan particle retained between sieve #10 (2 mm) and #20 (0.84 mm) with a particle diameter in loading direction of 1.20 mm

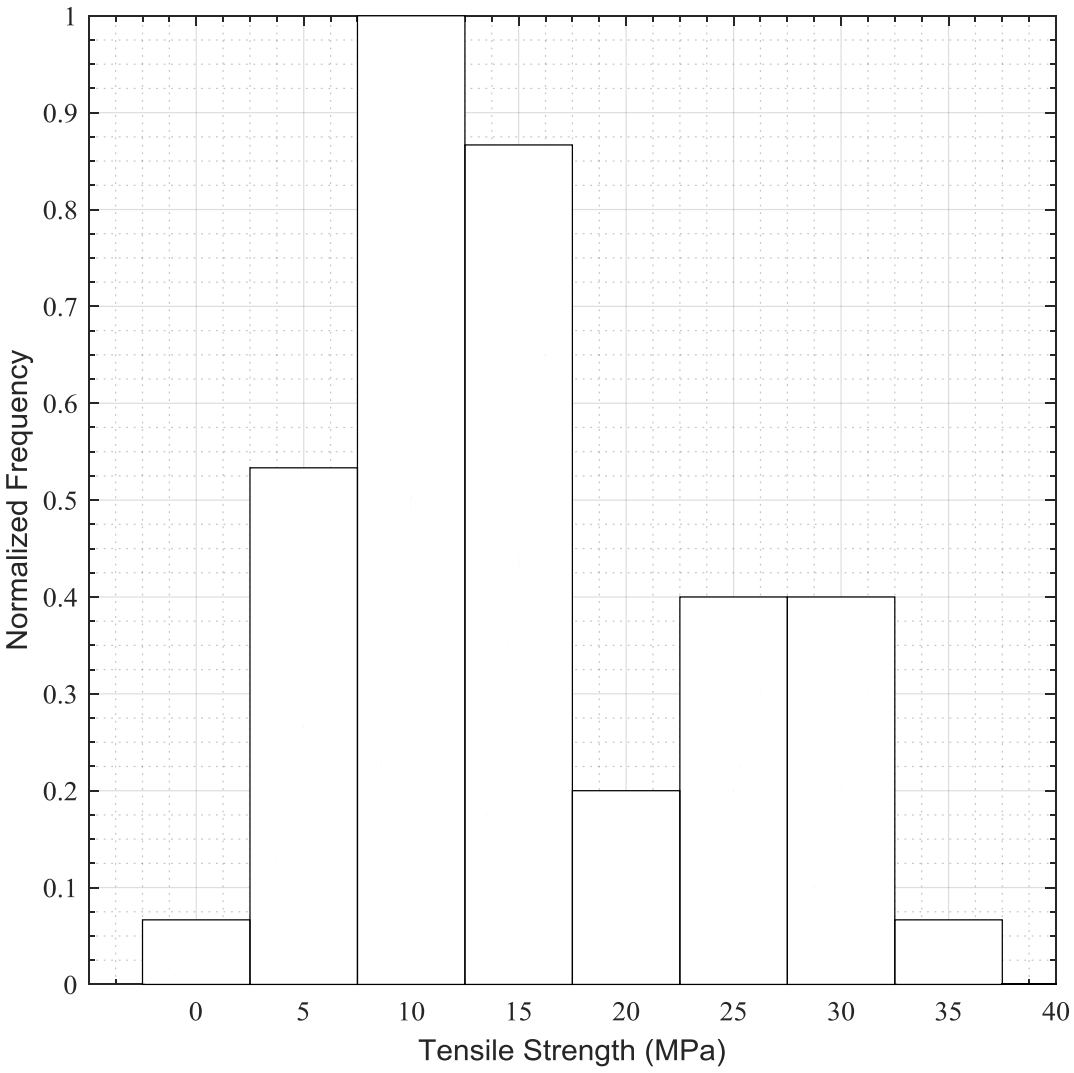


Figure 4-15a.5. The tensile strength histograms for white/tan (major and secondary compounds: quartz, plagioclase feldspar, potassium feldspar, and mica (muscovite)) particles retained between sieve #10 (2 mm) and #20 (0.84 mm) with further exclusions of the outliers.

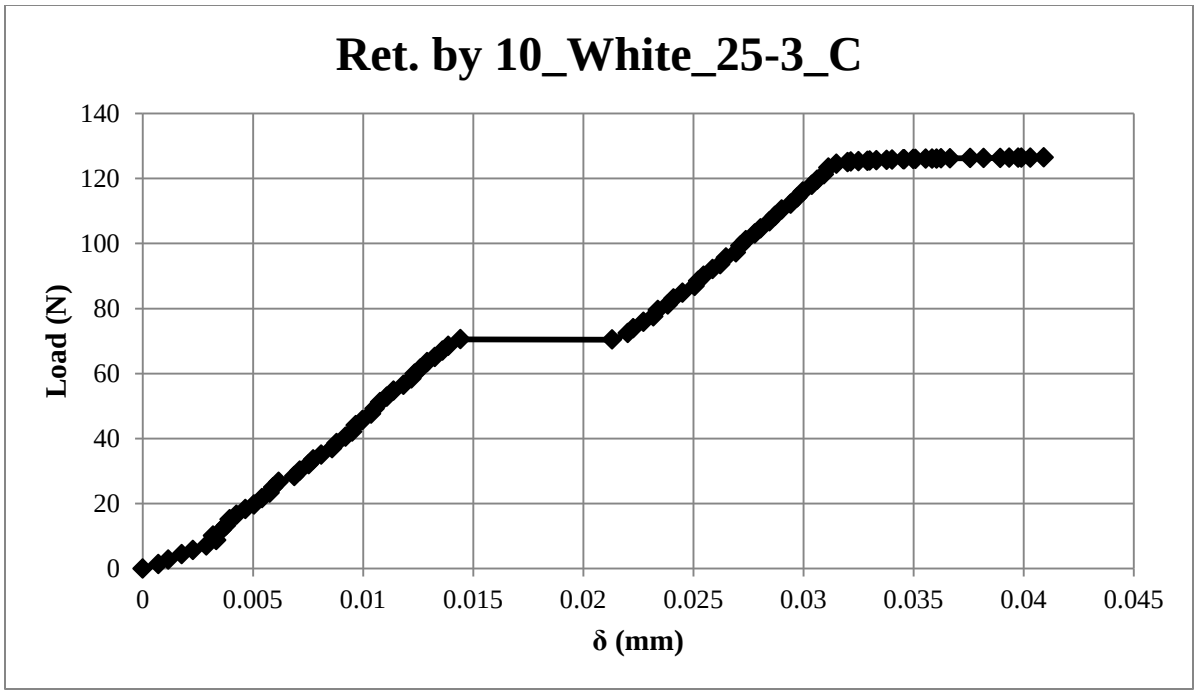


Figure 4-15b.1. The uniaxial compression curve for white/tan particle retained by sieve #10 (2 mm) with a particle diameter in loading direction of 1.60 mm.

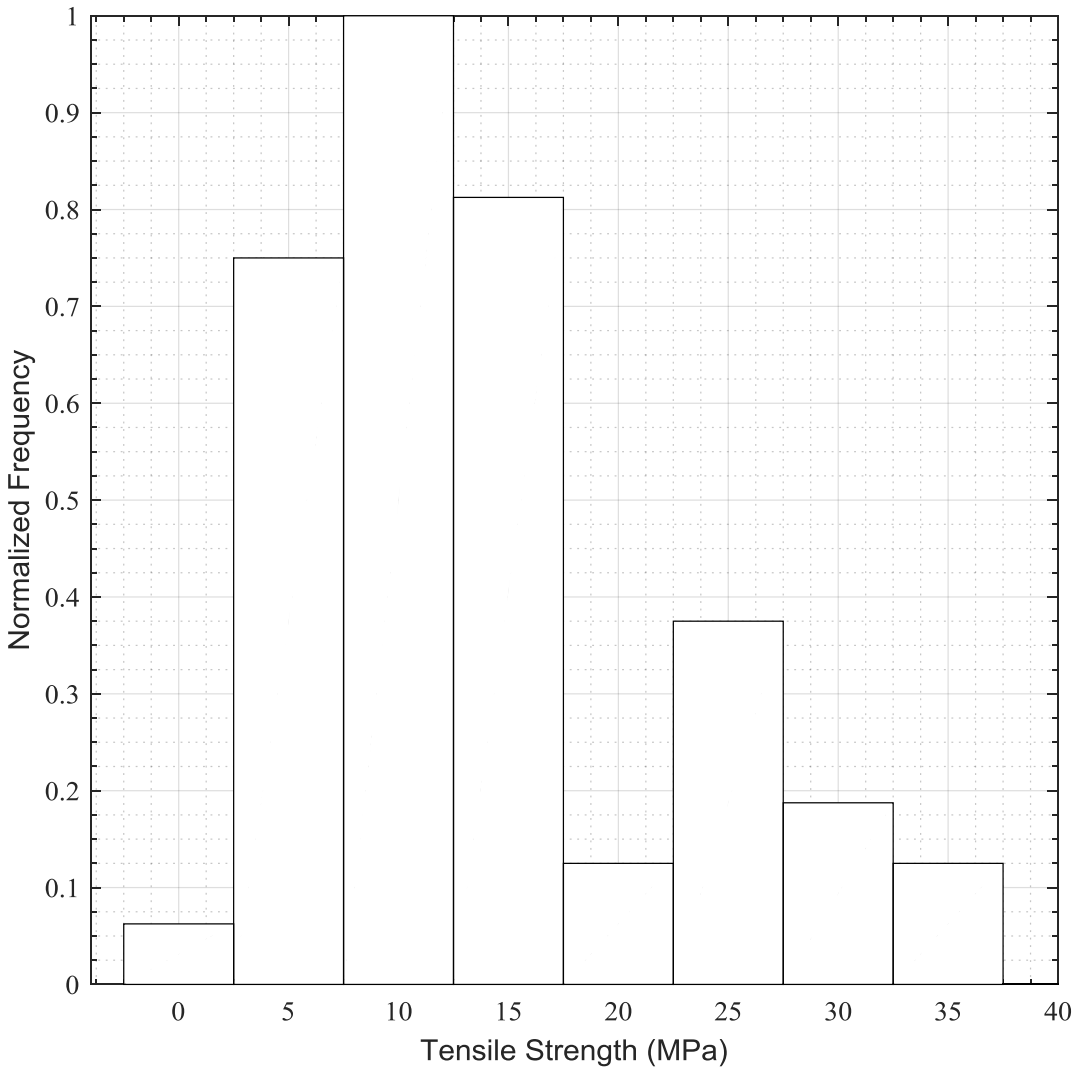


Figure 4-15b.2. The tensile strength histograms for white/tan (major and secondary compounds: quartz, plagioclase feldspar, potassium feldspar, and mica (muscovite)) particles retained by sieve #10 (2 mm) with the exclusion of the outlier.

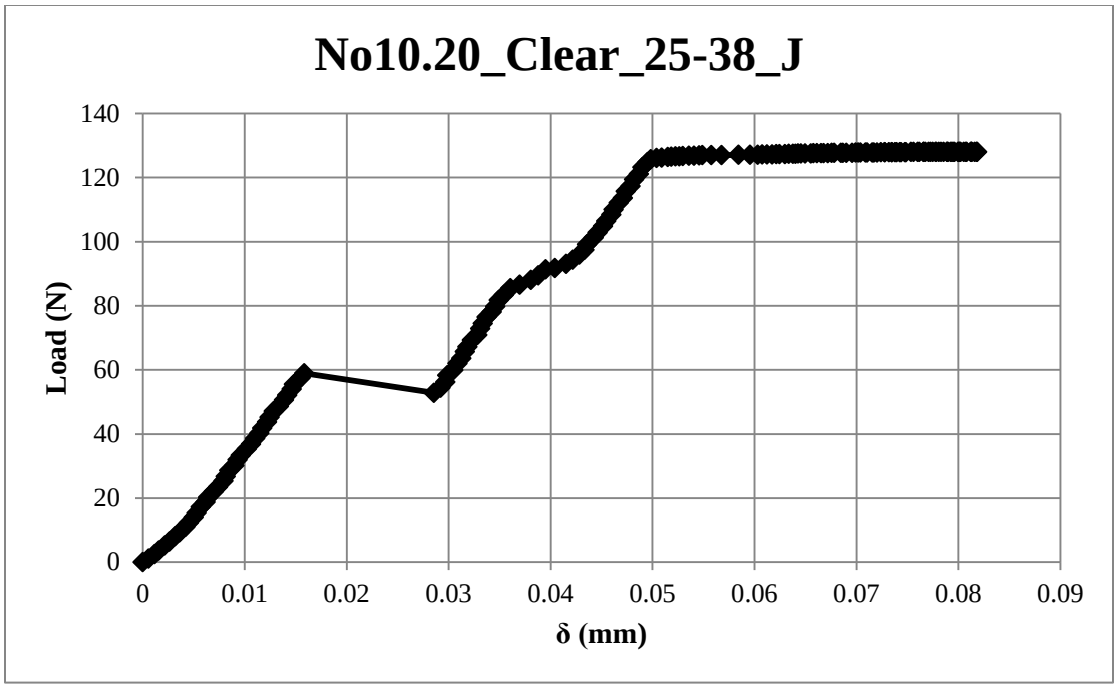


Figure 4-16a.1. The uniaxial compression curve for clear/translucent particle 25-38_J retained between sieve #10 (2 mm) and #20 (0.84 mm) with a particle diameter in loading direction of 0.70 mm.

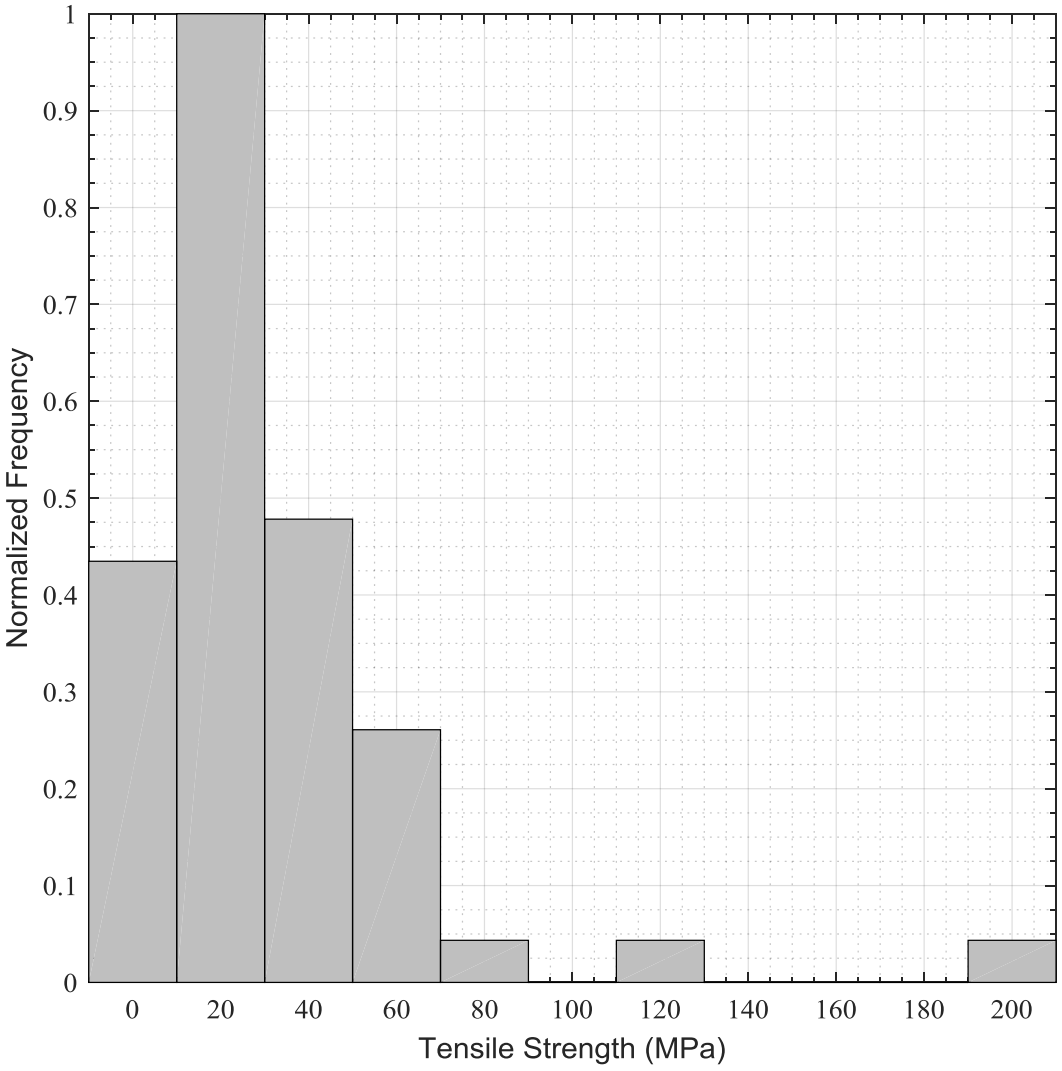


Figure 4-16a.2. The tensile strength histograms for clear/translucent (major and secondary compounds: quartz and plagioclase feldspar) particles retained between sieve #10 (2 mm) and #20 (0.84 mm) with the exclusion of the outlier.

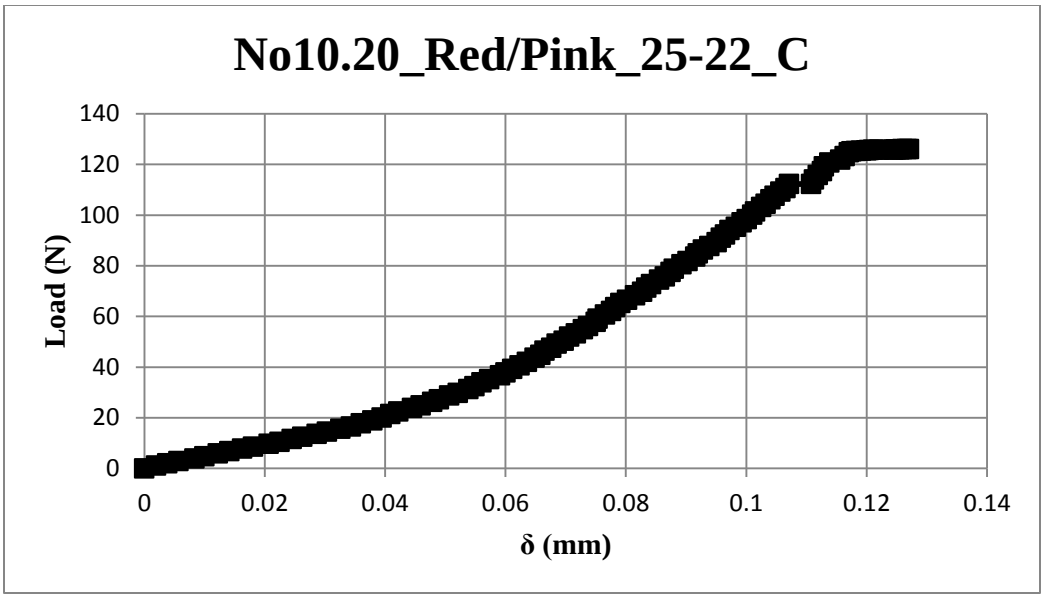


Figure 4-22a.1. The uniaxial compression curve for red/pink particle 25-22_C retained between sieve #10 (2 mm) and #20 (0.84 mm) with a particle diameter in loading direction of 1.00 mm.

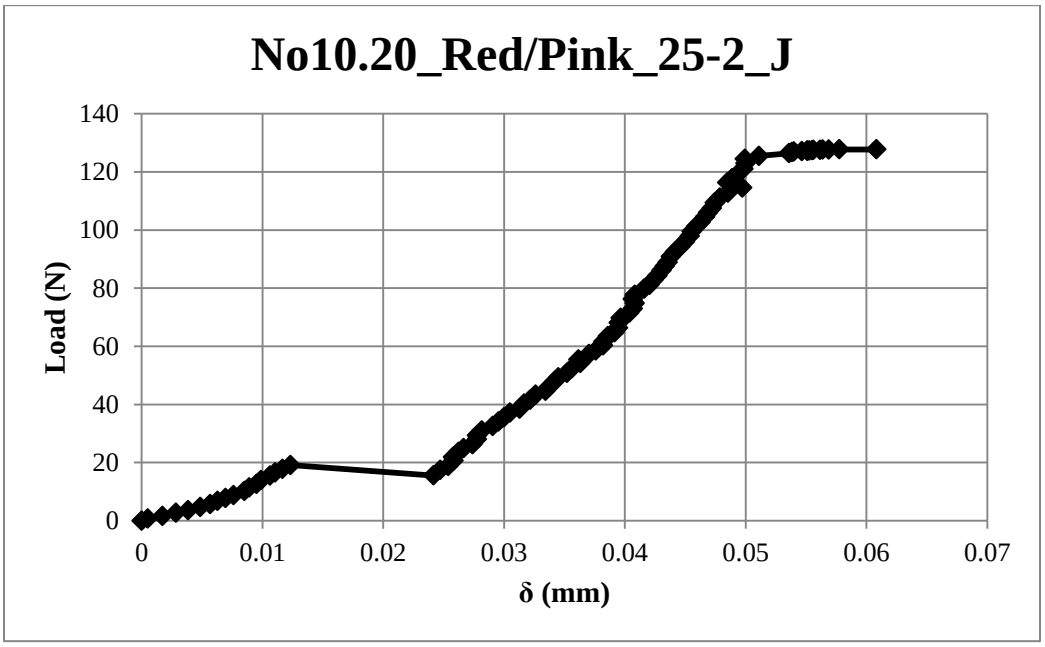


Figure 4-22a.2. The uniaxial compression curve for red/pink particle 25-2_J retained between sieve #10 (2 mm) and #20 (0.84 mm) with a particle diameter in loading direction of 1.00 mm.

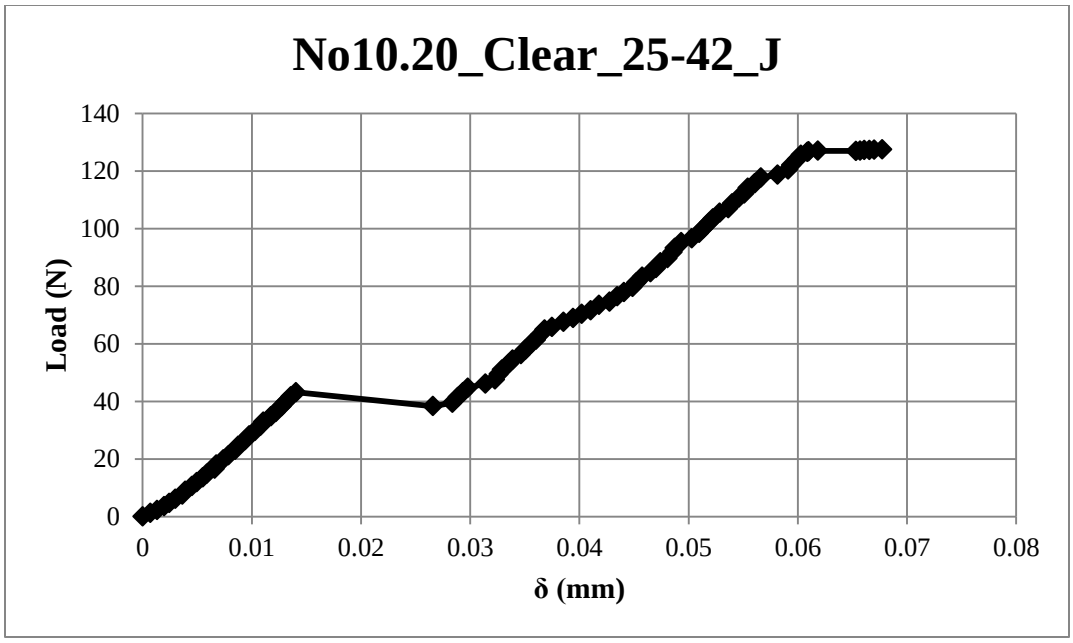


Figure 4-22a.3. The uniaxial compression curve for clear/translucent particle 25-42_J retained between sieve #10 (2 mm) and #20 (0.84 mm) with a particle diameter in loading direction of 0.80 mm.

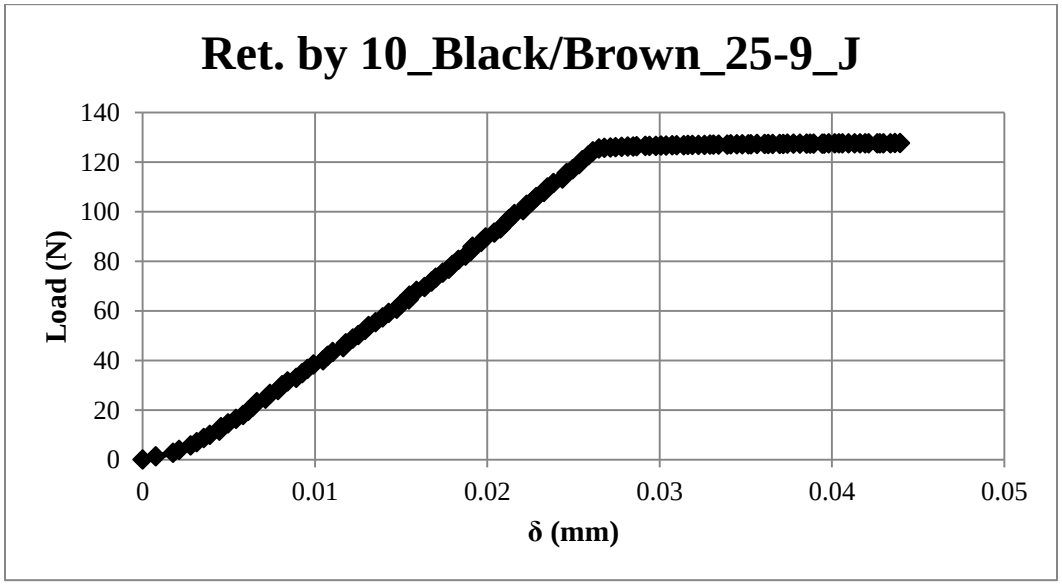


Figure 4-31a.1. The uniaxial compression curve for black/brown particle 25-9_J retained by sieve #10 (2 mm) with a particle diameter in loading direction of 1.20 mm.

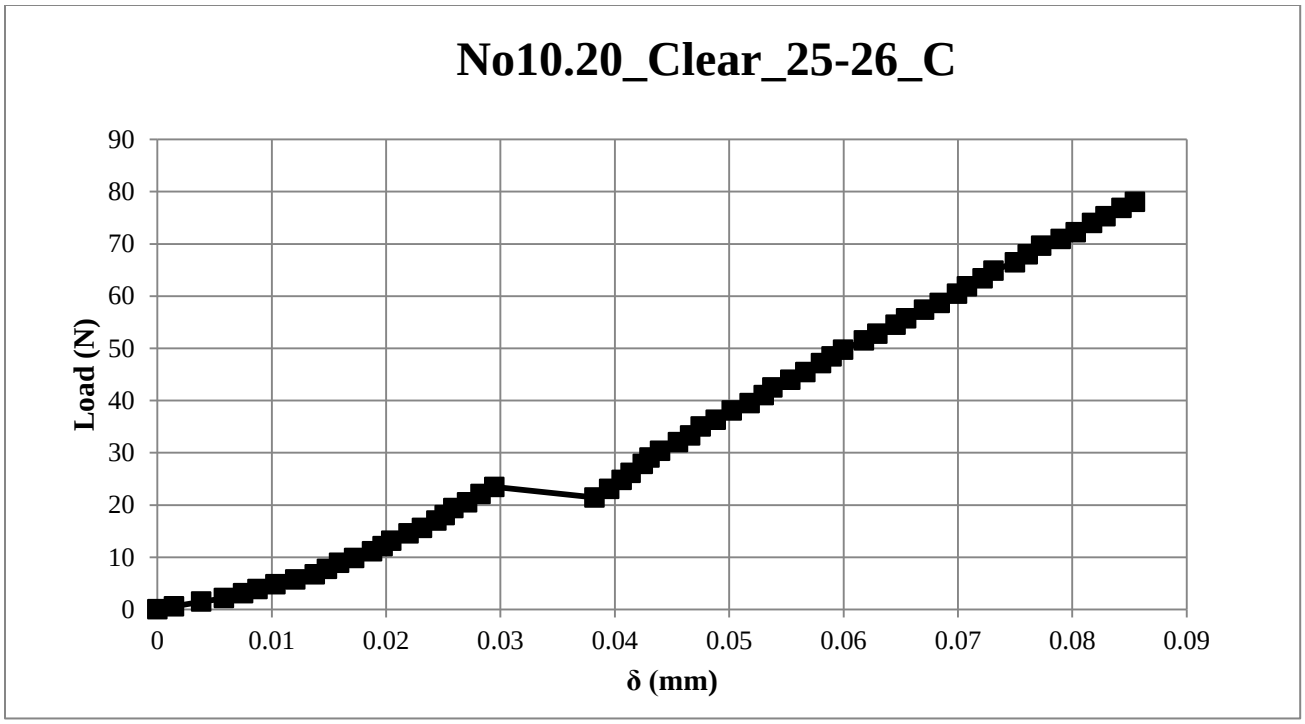


Figure 4-39a.1. The uniaxial compression curve for clear/translucent particle 25-26_C retained between sieve #10 (2 mm) and #20 (0.84 mm) with a particle diameter in loading direction of 0.80 mm.

APPENDIX J

Table J-1. Color, size, label, d_L (mm), fracture load (N), peak load (N), tensile strength (MPa), fracture mode, and internal structure mode for 14 mason sand particles obtained through 3-D x-ray imaging from synchrotron micro-tomography

Color	**Size**	**Label**	**d_L (mm)**	**Fracture Load (N)**	**Peak Load (N)**	**Tensile Strength (MPa)**	**Fracture Mode**	**Internal Structure**
Black/Brown	Ret. By 10	BB_M11	4.47	54.32	98.62	2.72	4	6
Black/Brown	No10.20	BB_M2	3.23	39.15	39.15	3.76	3	5
Black/Brown	Ret. By 10	BB_M9	2.02	445.71	445.71	109.45	4	1
Clear	No10.20	Clear_M1	3.20	17.34	17.34	1.69	1	2
Clear	Ret. By 10	Clear_M10	3.87	81.96	213.51	5.47	3.5	4
Clear	No10.20	Clear_M3	3.13	102.28	102.28	10.42	3	3
Red	Ret. By 10	Red_M10	4.48	162.30	162.30	8.10	4	2
Red	No10.20	Red_M2	2.51	15.58	15.58	2.47	3	5
Red	No10.20	Red_M4	1.63	2.84	5.96	1.07	3	4
Red	Ret. By 10	Red_M9	3.09	649.80	649.80	68.15	4	5

Table J-1 Continued

Color	Size	Label	d_L (mm)	Fracture Load (N)	Peak Load (N)	Tensile Strength (MPa)	Fracture Mode	Internal Structure
White	Ret. By 10	White_M10	3.41	120.44	120.44	10.36	0	3
White	Ret. By 10	White_M11	3.57	79.93	79.93	6.27	3	5
White	No10.20	White_M2	0.35	11.65	52.02	95.46	4	3
White	No10.20	White_M3	2.76	79.25	79.25	10.38	3.5	5

VITA

The author, Thuy Thanh Trieu, was born on Saturday, March 27, 1993, in My Tho a small city in Vietnam. She immigrated with her mother to the United States in 1994 and settled down in Dorchester, Massachusetts for 10 years. In 2003, she moved to Nashville, Tennessee, where she graduated from Martin Luther King Jr. Academic Magnet in 2011. She enrolled in the civil engineering program at the University of Tennessee in Knoxville, Tennessee and pursued a Bachelor's degree in that field of study. She received her Bachelor of Science, with Honors, in Civil Engineering in May, 2015. With her passion for knowledge still burning strong, she decided to continue pursuing her education at the University of Tennessee, Knoxville and enrolled in the Master's Civil Engineering program, with a concentration in geotechnical engineering. As a graduate student, she worked for the Engineering Fundamentals Department as a Graduate Teaching Assistant and performed research work under Dr. Khalid Alshibli with hopes of earning her Master of Science degree in Civil Engineering in May of 2017. Thuy Trieu hopes to pursue her career in civil engineering for a few years as she ponders whether to pursue a Doctorate degree in the future.